# MECHANISTIC STUDIES OF GENOME INTEGRITY, ENVIRONMENTAL HEALTH, AND CANCER ETIOLOGY

EDITED BY: Shan Yan, Robert W. Sobol, Michael G. Kemp and Jianjun Zhao
PUBLISHED IN: Frontiers in Cell and Developmental Biology

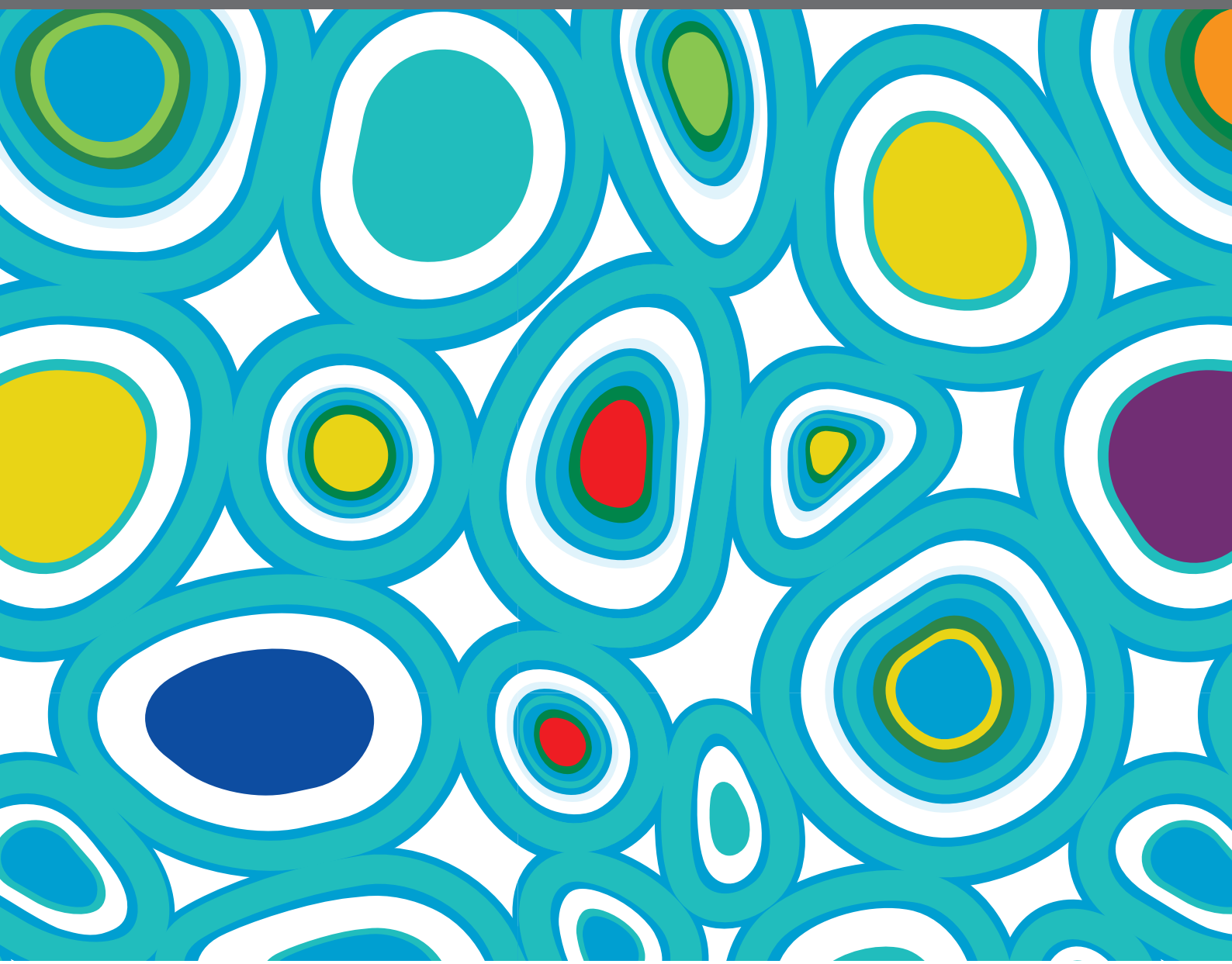

frontiers Research Topics

# frontiers



ISSN 1664-8714
ISBN 978-2-83250-478-9
DOI 10.3389/978-2-83250-478-9

## About Frontiers

Frontiers is more than just an open-access publisher of scholarly articles: it is a pioneering approach to the world of academia, radically improving the way scholarly research is managed. The grand vision of Frontiers is a world where all people have an equal opportunity to seek, share and generate knowledge. Frontiers provides immediate and permanent online open access to all its publications, but this alone is not enough to realize our grand goals.

## Frontiers Journal Series

The Frontiers Journal Series is a multi-tier and interdisciplinary set of open-access, online journals, promising a paradigm shift from the current review, selection and dissemination processes in academic publishing. All Frontiers journals are driven by researchers for researchers; therefore, they constitute a service to the scholarly community. At the same time, the Frontiers Journal Series operates on a revolutionary invention, the tiered publishing system, initially addressing specific communities of scholars, and gradually climbing up to broader public understanding, thus serving the interests of the lay society, too.

## Dedication to Quality

Each Frontiers article is a landmark of the highest quality, thanks to genuinely collaborative interactions between authors and review editors, who include some of the world's best academicians. Research must be certified by peers before entering a stream of knowledge that may eventually reach the public - and shape society; therefore, Frontiers only applies the most rigorous and unbiased reviews.
Frontiers revolutionizes research publishing by freely delivering the most outstanding research, evaluated with no bias from both the academic and social point of view. By applying the most advanced information technologies, Frontiers is catapulting scholarly publishing into a new generation.

## What are Frontiers Research Topics?

Frontiers Research Topics are very popular trademarks of the Frontiers Journals Series: they are collections of at least ten articles, all centered on a particular subject. With their unique mix of varied contributions from Original Research to Review Articles, Frontiers Research Topics unify the most influential researchers, the latest key findings and historical advances in a hot research area! Find out more on how to host your own Frontiers Research Topic or contribute to one as an author by contacting the Frontiers Editorial Office: frontiersin.org/about/contact

# MECHANISTIC STUDIES OF GENOME INTEGRITY, ENVIRONMENTAL HEALTH, AND CANCER ETIOLOGY

Topic Editors:
**Shan Yan,** University of North Carolina at Charlotte, United States
**Robert W. Sobol,** Brown University, United States
**Michael G. Kemp,** Wright State University, United States
**Jianjun Zhao,** Lerner Research Institute, Cleveland Clinic, United States

*Robert W. Sobol is a scientific consultant for Canal House Biosciences, LLC. All other co-editors declare no conflicts of interest.*

**Citation:** Yan, S., Sobol, R. W., Kemp, M. G., Zhao, J., eds. (2022). Mechanistic Studies of Genome Integrity, Environmental Health, and Cancer Etiology. Lausanne: Frontiers Media SA. doi: 10.3389/978-2-83250-478-9

# Table of Contents

frontiers | Frontiers in Cell and Developmental Biology

TYPE Editorial
PUBLISHED 28 September 2022
DOI 10.3389/fcell.2022.1026326



OPEN ACCESS

EDITED AND REVIEWED BY
Ramani Ramchandran,
Medical College of Wisconsin,
United States

*CORRESPONDENCE
Shan Yan,
shan.yan@uncc.edu
Jianjun Zhao,
zhaoj4@ccf.org
Michael Kemp,
mike.kemp@wright.edu
Robert W. Sobol,
rwsobol@brown.edu

†PRESENT ADDRESS
Robert W. Sobol,
Department of Pathology and Laboratory Medicine, Warrant Alpert Medical School & Legorreta Cancer Center, Brown University, Providence, RI, United States

SPECIALTY SECTION
This article was submitted to Molecular and Cellular Pathology, a section of the journal Frontiers in Cell and Developmental Biology

RECEIVED 23 August 2022
ACCEPTED 07 September 2022
PUBLISHED 28 September 2022

CITATION
Yan S, Zhao J, Kemp M and Sobol RW (2022), Editorial: Mechanistic studies of genome integrity, environmental health, and cancer etiology.
*Front. Cell Dev. Biol.* 10:1026326.
doi: 10.3389/fcell.2022.1026326



# Editorial: Mechanistic studies of genome integrity, environmental health, and cancer etiology

Shan Yan[1]*, Jianjun Zhao[2]*, Michael Kemp[3]* and Robert W. Sobol[4]*†

[1]Department of Biological Sciences, University of North Carolina at Charlotte, Charlotte, NC, United States, [2]Department of Cancer Biology, Lerner Research Institute, Cleveland Clinic, Cleveland, OH, United States, [3]Department of Pharmacology and Toxicology, Wright State University, Dayton, OH, United States, [4]Mitchell Cancer Institute and Department of Pharmacology, University of South Alabama, Mobile, AL, United States

KEYWORDS

**genome integrity, environmental health, cancer etiology, DNA repair, DNA damage response**

Editorial on the Research Topic
Mechanistic studies of genome integrity, environmental health, and cancer etiology

Genomic DNA in all cell types is exposed to insults from endogenous sources, such as oxidative stress, as well as exogenous sources, including environmental genotoxins and anti-cancer therapeutics. Deficiencies in genome integrity maintenance pathways have been implicated in the etiology of cancer and other disease states. To mitigate the debilitating genomic lesions, cells have evolved many different pathways to sense, repair, and signal in response to such challenges. Research studies focused on understanding genome integrity mechanisms have utilized a variety of model organisms and cutting-edge technologies at the molecular, cellular, organismal, and ecological levels. Mechanistic studies that help define the process of genome integrity maintenance, the impact of such mechanisms on environmental health, and their role in cancer etiology are highly significant and have led to new ways of diagnosing and treating cancers and other human diseases. Because of the many advances in this area of research over the past few years, this Research Topic intends to provide the latest insights on the field of genome integrity and to discuss the trends of current and future studies aimed at improving our understanding of disease pathogenesis and treatment. Here, we provide an editorial to summarize these seven research articles and two review articles.

Oxidative stress is a cellular process that is aggravated with aging, by consumption of certain diets, or under chemotherapeutic treatment, and results in damage to the DNA of the cells (Pizzino et al., 2017). Oxidative DNA damage is mainly repaired through the base excision repair (BER) pathway (Maynard et al., 2009). Here, Burchat et al. identified a novel function of human 8-oxoguanine DNA glycosylase-1 (OGG1) beyond its conventional DNA repair function as an initiator of BER-mediated DNA repair

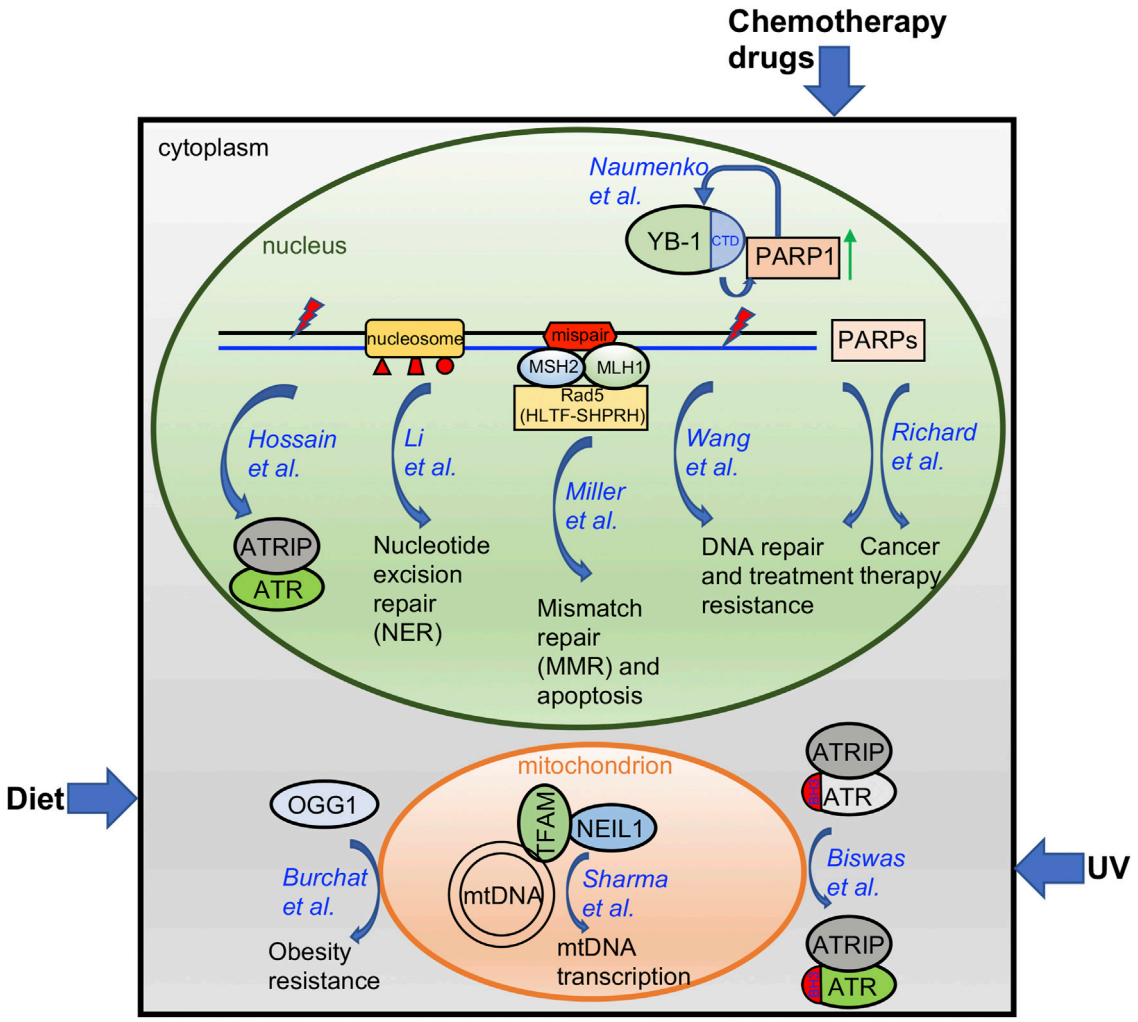


FIGURE 1
A diagram summarizing the findings from papers included in this Research Topic. Please see text for more details.

related to an increase in tissue mitochondrial content (Figure 1). Further, they reported for the first time that OGG1-mediated obesity resistance in both the Agouti obese (Ay/a) mouse model and the diet-induced obesity (DIO) model requires maternal transmission of the hOGG1 transgene. This novel finding of a critical role for OGG1 in modulating energy balance will open a new research field to connect the conventional DNA repair machinery with mitochondrial function in tissues.

Whereas the BER protein Apurinic/Apyrimidinic endonuclease 2 (APE2) has been implicated in the Ataxia-telangectasia and Rad3 related (ATR)-Checkpoint kinase 1 (Chk1) DNA damage response (DDR) pathway in the *Xenopus* system (Willis et al., 2013; Wallace et al., 2017; Lin et al., 2018; Lin et al., 2021), Hossain et al. here provide evidence in pancreatic cancer cells that APE2 is a general regulator of the ATR-Chk1 DDR in response to different stress conditions including oxidative stress, DNA replication stress, and DNA double-strand breaks (DSBs) (Figure 1). A small molecule compound named Celastrol was reported as the first-known APE2 inhibitor that specifically impairs APE2 exonuclease activity by inhibiting its binding to single-stranded DNA (ssDNA). Sensitizing pancreatic cancer cell viability to chemotherapy drugs via APE2-knockdown or exposure to the APE2 inhibitor Celastrol supports the idea that targeting APE2 can provide novel insight into new cancer treatments.

In addition to its well-known checkpoint function in the nucleus, cytoplasmic ATR is converted from *trans*-into a *cis*-isomeric conformation at the Ser428-Pro429 motif within the BH3 domain in a Pin1/DAPK1-regulated manner to suppress apoptosis in mitochondria following ultraviolet (UV) damage (Hilton et al., 2015). Biswas et al. provides the structural basis of the mitochondrial isoform of ATR using a mass spectrometry-

based foot printing approach (Figure 1). Two biotin-modified residues K459 and K469 within the BH3 domain of *cis*-ATR are not accessible in *trans*-ATR, suggesting a conformation change around the BH3 domain between *cis*- and *trans*-ATR. Furthermore, cis-ATR with the accessible BH3 domain, but not trans-ATR, is able to associate with tBid. These findings suggest that the isomerization-induced structural changes of mitochondrial specific cis-ATR are essential for its role in cell survival and the DDR pathway.

In recent years, PARP inhibitors (PARPi) targeting PARP1 and PARP2 have been developed as a novel targeted cancer therapeutic due to their roles in DNA damage repair (Javle and Curtin, 2011; Lord and Ashworth, 2017). But many other members of the PARP protein family with a catalytic domain similar to PARP1 and PARP2 are understudied regarding their function on DNA damage repair and tumor initiation (Jubin et al., 2016). Richard et al. comprehensively reviews the current knowledge of the potential functions of PARP isoforms 4 and 6-16 and discusses the roles these proteins may play in DNA damage repair and as targets for cancer therapeutics (Figure 1). This review also points out the future research directions and further research needs to be conducted.

Following the initial treatment of radiation and chemotherapy, cancer recurrence and acquired resistance are major problems in the clinic. Using pairs of same patient-derived primary and recurrent oral cancer cell lines, Wang et al. identified PARP1 upregulation in the recurrent but not primary oral tumor cells and such PARP1 upregulation was augmented by the chemotherapy drugs cisplatin and 5-fluorouracil (Figure 1). Ectopic overexpression of PARP1 rendered the primary cancer cells resistant to chemotherapy drugs and PARP1 inhibitors sensitized recurrent cancer cells to chemotherapy drugs *in vitro* and *in vivo*. Thus, PARP1 upregulation in recurrent oral cancers suggests that targeting PARP1 can be expanded to recurrent oral cancer treatment.

Y-box binding protein 1 (YBX1, YB-1) is a cold shock domain protein that binds both DNA and RNA and is implicated in numerous cellular processes including transcription, translation, mRNA packaging, pre-mRNA splicing and DNA repair. The involvement of YB-1 in these myriad mechanisms are mediated via numerous protein-protein interactions. Similarly, its role in DNA repair involves interactions with MSH2, DNA polymerase delta, Ku80 and WRN (Gaudreault et al., 2004), RAD21 (Panigrahi et al., 2012), BARD1 and BRCA1 (Woods et al., 2012). Recently, YB-1 was identified among proteins proximal to trapped PARP1 (Krastev et al., 2022). This new report by Naumenko et al. provides more detail on the interaction between YB-1 and PARP1 and the role of YB-1 in regulating poly-ADP-ribose (PAR) synthesis via the interaction between the disordered YB-1 C-terminal domain (CTD) and PAR (Figure 1). Overall, they suggest that YB-1 CTD-like domains may be considered PAR "readers" similar to other known PAR-binding modules.

Nucleotide excision repair (NER) plays an essential role in the removal of bulky DNA lesions induced by UV radiation and other genotoxins. Though biochemical studies have defined the NER mechanism on naked DNA *in vitro*, the packaging of DNA into histones and higher order chromatin structures in the cell *in vivo* likely impacts the ability of the NER machinery to do its job. In this perspective, Li et al. provides a comprehensive summary of how different post-translational modifications to histones by specific classes of enzymes impact NER function *in vivo* (Figure 1).

Proteins of the mismatch repair (MMR) pathway function to correct replication errors including base-base mispairs and small insertion/deletion mispairs (Jiricny, 2006; Li, 2008; Fishel, 2015). In addition, the MMR pathway recognizes DNA damage induced mispairs to trigger apoptosis, such as that induced by the $O^6$-methylguanine:thymidine mispairs that arises after exposure to SN1 alkylators (Fu et al., 2012; Soll et al., 2017; Fujii et al., 2022). While the core proteins for MMR have been well defined (Modrich, 2016), additional proteins that complex with MMR proteins and that may regulate the MMR pathway are anticipated. Here, Miller et al. identified Rad5 (*Saccharomyces cerevisiae*) as an Mlh1 and Msh2 interacting protein (Figure 1). Further, they show that the human counterparts of Rad5 (HLTF and SHPRH) interact with MSH2 and MLH1, respectively. This novel finding will form the basis for future studies to uncover the detailed functional role of these and other MMR interacting proteins.

In response to constant endogenous and/or exogenous sources of DNA damaging agents, it is essential for cells to maintain the stability of the 16.5 kb mitochondrial DNA (mtDNA) in humans, in addition to the nuclear genome (Copeland and Longley, 2014). Sharma et al. here reported and characterized the interaction between the BER protein Nei-like DNA Glycosylase 1 (NEIL1) and mitochondrial transcription factor A (TFAM) which requires the presence of DNA/RNA (Figure 1). Interestingly, NEIL1 is necessary for efficient transcription by TFAM upon alkylating agent induced DNA damage. The regulation of the NEIL1-TFAM interaction by salt concentrations, protein availability, nucleic acids, and the presence of DNA damage suggests a transient, dynamic, and functional association to maintain mtDNA stability.

Overall, the research and review articles in this Research Topic have identified and/or characterized several distinct mechanisms of how cells respond to environmental factors, such as diet, UV, and chemotherapy drugs, and how nuclear genome and epigenome integrity and mitochondria stability are maintained (Figure 1). Future studies in the field to consider include 1) how different environmental factors including but not limited to air pollutants, viruses, and pesticides affect genomic and/or epigenomic integrity; 2) how distinct DNA repair and DDR pathways sense and signal environmental and intrinsic insults; 3) how cutting-edge omics technologies are applied to

better understand genome integrity and public health; and 4) how our novel knowledge in genome/epigenome integrity provides better strategies for cancer therapeutics.

## Author contributions

All authors listed have made a substantial, direct, and intellectual contribution to the work and approved it for publication.

## Funding

SY laboratory is supported by grants from the NIH/NCI (R01CA225637, R01CA263897, and R01CA251141-subaward) and the NIH/NIEHS (R21ES032966) and funds from UNC Charlotte. JZ laboratory is supported by grants from the NIH/NCI (R01CA251141) and the NIH/NINDS (R01NS124081), V Foundation Scholar Award, ASH bridge award, and two Velosano Grants. MK laboratory is supported by grants from the National Institute of General Medical Sciences (GM130583), Ohio Cancer Research Associates (#5020), the Veterans Administration (I01CX002241). RWS is an Abraham A. Mitchell Distinguished Investigator. Research in the Sobol lab on DNA repair, the analysis of DNA damage and the impact of genotoxic exposure is funded by grants from the NIH (ES029518, CA148629, ES014811, ES028949, CA238061, CA236911, AG069740 and ES032522), from the NSF (NSF-1841811) and a grant from the DOD (GRANT11998991, DURIP-Navy). Support is also provided by grants from the Breast Cancer Research Foundation of Alabama, from the Abraham A. Mitchell Distinguished Investigator Fund, and from the Mitchell Cancer Institute Molecular & Metabolic Oncology Program Development fund (to RWS).

## Acknowledgments

We thank all the authors and reviewers who made contributions to this exciting Research Topic.

## Conflict of interest

RWS is a scientific consultant for Canal House Biosciences, LLC. The authors declare that the research was conducted in the absence of any commercial or financial relationships that could be construed as a potential conflict of interest.

## Publisher's note



## References

Copeland, W. C., and Longley, M. J. (2014). Mitochondrial genome maintenance in health and disease. *DNA Repair (Amst)* 19, 190–198. doi:10.1016/j.dnarep.2014.03.010

Fishel, R. (2015). Mismatch repair. *J. Biol. Chem.* 290, 26395–26403. doi:10.1074/jbc.R115.660142

Fu, D., Calvo, J. A., and Samson, L. D. (2012). Balancing repair and tolerance of DNA damage caused by alkylating agents. *Nat. Rev. Cancer* 12, 104–120. doi:10.1038/nrc3185

Fujii, S., Sobol, R. W., and Fuchs, R. P. (2022). Double-strand breaks: When DNA repair events accidentally meet. *DNA Repair (Amst)* 112, 103303. doi:10.1016/j.dnarep.2022.103303

Gaudreault, I., Guay, D., and Lebel, M. (2004). YB-1 promotes strand separation *in vitro* of duplex DNA containing either mispaired bases or cisplatin modifications, exhibits endonucleolytic activities and binds several DNA repair proteins. *Nucleic Acids Res.* 32, 316–327. doi:10.1093/nar/gkh170

Hilton, B. A., Li, Z., Musich, P. R., Wang, H., Cartwright, B. M., Serrano, M., et al. (2015). ATR plays a direct antiapoptotic role at mitochondria, which is regulated by prolyl isomerase Pin1. *Mol. Cell* 60, 35–46. doi:10.1016/j.molcel.2015.08.008

Javle, M., and Curtin, N. J. (2011). The role of PARP in DNA repair and its therapeutic exploitation. *Br. J. Cancer* 105, 1114–1122. doi:10.1038/bjc.2011.382

Jiricny, J. (2006). The multifaceted mismatch-repair system. *Nat. Rev. Mol. Cell Biol.* 7, 335–346. doi:10.1038/nrm1907

Jubin, T., Kadam, A., Jariwala, M., Bhatt, S., Sutariya, S., Gani, A. R., et al. (2016). The PARP family: Insights into functional aspects of poly (ADP-ribose) polymerase-1 in cell growth and survival. *Cell Prolif.* 49, 421–437. doi:10.1111/cpr.12268

Krastev, D. B., Li, S., Sun, Y., Wicks, A. J., Hoslett, G., Weekes, D., et al. (2022). The ubiquitin-dependent ATPase p97 removes cytotoxic trapped PARP1 from chromatin. *Nat. Cell Biol.* 24, 62–73. doi:10.1038/s41556-021-00807-6

Li, G. M. (2008). Mechanisms and functions of DNA mismatch repair. *Cell Res.* 18, 85–98. doi:10.1038/cr.2007.115

Lin, Y., Bai, L., Cupello, S., Hossain, M. A., Deem, B., McLeod, M., et al. (2018). APE2 promotes DNA damage response pathway from a single-strand break. *Nucleic Acids Res.* 46, 2479–2494. doi:10.1093/nar/gky020

Lin, Y., McMahon, A., Driscoll, G., Bullock, S., Zhao, J., and Yan, S. (2021). Function and molecular mechanisms of APE2 in genome and epigenome integrity. *Mutat. Res. Rev. Mutat. Res.* 787, 108347. doi:10.1016/j.mrrev.2020.108347

Lord, C. J., and Ashworth, A. (2017). PARP inhibitors: Synthetic lethality in the clinic. *Science* 355, 1152–1158. doi:10.1126/science.aam7344

Maynard, S., Schurman, S. H., Harboe, C., de Souza-Pinto, N. C., and Bohr, V. A. (2009). Base excision repair of oxidative DNA damage and association with cancer and aging. *Carcinogenesis* 30, 2–10. doi:10.1093/carcin/bgn250

Modrich, P. (2016). Mechanisms in *E. coli* and human mismatch repair (nobel lecture). *Angew. Chem. Int. Ed. Engl.* 55, 8490–8501. doi:10.1002/anie.201601412

Panigrahi, A. K., Zhang, N., Otta, S. K., and Pati, D. (2012). A cohesin-RAD21 interactome. *Biochem. J.* 442, 661–670. doi:10.1042/BJ20111745

Pizzino, G., Irrera, N., Cucinotta, M., Pallio, G., Mannino, F., Arcoraci, V., et al. (2017). Oxidative stress: Harms and benefits for human health. *Oxid. Med. Cell. Longev.* 2017, 8416763. doi:10.1155/2017/8416763

Soll, J. M., Sobol, R. W., and Mosammaparast, N. (2017). Regulation of DNA alkylation damage repair: Lessons and therapeutic opportunities. *Trends biochem. Sci.* 42, 206–218. doi:10.1016/j.tibs.2016.10.001

Wallace, B. D., Berman, Z., Mueller, G. A., Lin, Y., Chang, T., Andres, S. N., et al. (2017). APE2 Zf-GRF facilitates 3'-5' resection of DNA damage following oxidative stress. *Proc. Natl. Acad. Sci. U. S. A.* 114, 304–309. doi:10.1073/pnas.1610011114

Willis, J., Patel, Y., Lentz, B. L., and Yan, S. (2013). APE2 is required for ATR-Chk1 checkpoint activation in response to oxidative stress. *Proc. Natl. Acad. Sci. U. S. A.* 110, 10592–10597. doi:10.1073/pnas.1301445110

Woods, N. T., Mesquita, R. D., Sweet, M., Carvalho, M. A., Li, X., Liu, Y., et al. (2012). Charting the landscape of tandem BRCT domain-mediated protein interactions. *Sci. Signal.* 5, rs6. doi:10.1126/scisignal.2002255

frontiers in Cell and Developmental Biology

ORIGINAL RESEARCH
published: 15 September 2021
doi: 10.3389/fcell.2021.718962

# Maternal Transmission of Human OGG1 Protects Mice Against Genetically- and Diet-Induced Obesity Through Increased Tissue Mitochondrial Content

*Natalie Burchat[1], Priyanka Sharma[1], Hong Ye[1], Sai Santosh Babu Komakula[1,2], Agnieszka Dobrzyn[1,2], Vladimir Vartanian[3], R. Stephen Lloyd[3,4] and Harini Sampath[1,5,6]**

*[1] Rutgers Center for Lipid Research, New Jersey Institute for Food, Nutrition, and Health, Rutgers University, New Brunswick, NJ, United States, [2] Laboratory of Cell Signaling and Metabolic Disorders, Nencki Institute of Experimental Biology, Warsaw, Poland, [3] Oregon Institute of Occupational Health Sciences, Oregon Health and Science University, Portland, OR, United States, [4] Department of Molecular and Medical Genetics, Oregon Health and Science University, Portland, OR, United States, [5] Department of Nutritional Sciences, Rutgers University, New Brunswick, NJ, United States, [6] Center for Microbiome, Nutrition, and Health, New Jersey Institute for Food, Nutrition, and Health, Rutgers University, New Brunswick, NJ, United States*

OPEN ACCESS

**Edited by:**
*Jianjun Zhao, Lerner Research Institute, United States*

**Reviewed by:**
*Youliang Wang, Beijing Institute of Technology, China*
*Rahul N. Kanadia, University of Connecticut, United States*

***Correspondence:**
*Harini Sampath*
*harini.sampath@rutgers.edu*

**Specialty section:**
*This article was submitted to Molecular and Cellular Pathology, a section of the journal Frontiers in Cell and Developmental Biology*

**Received:** *01 June 2021*
**Accepted:** *09 August 2021*
**Published:** *15 September 2021*

**Citation:**
*Burchat N, Sharma P, Ye H, Komakula SSB, Dobrzyn A, Vartanian V, Lloyd RS and Sampath H (2021) Maternal Transmission of Human OGG1 Protects Mice Against Genetically- and Diet-Induced Obesity Through Increased Tissue Mitochondrial Content. Front. Cell Dev. Biol. 9:718962. doi: 10.3389/fcell.2021.718962*

Obesity and related metabolic disorders are pressing public health concerns, raising the risk for a multitude of chronic diseases. Obesity is multi-factorial disease, with both diet and lifestyle, as well as genetic and developmental factors leading to alterations in energy balance. In this regard, a novel role for DNA repair glycosylases in modulating risk for obesity has been previously established. Global deletion of either of two different glycosylases with varying substrate specificities, Nei-like endonuclease 1 (NEIL1) or 8-oxoguanine DNA glycosylase-1 (OGG1), both predispose mice to diet-induced obesity (DIO). Conversely, enhanced expression of the human *OGG1* gene renders mice resistant to obesity and adiposity. This resistance to DIO is mediated through increases in whole body energy expenditure and increased respiration in adipose tissue. Here, we report that *hOGG1* expression also confers resistance to genetically-induced obesity. While Agouti obese ($A^y/a$) mice are hyperphagic and consequently develop obesity on a chow diet, *hOGG1* expression in $A^y/a$ mice ($A^y/a^{Tg}$) prevents increased body weight, without reducing food intake. Instead, obesity resistance in $A^y/a^{Tg}$ mice is accompanied by increased whole body energy expenditure and tissue mitochondrial content. We also report for the first time that OGG1-mediated obesity resistance in both the $A^y/a$ model and DIO model requires maternal transmission of the *hOGG1* transgene. Maternal, but not paternal, transmission of the *hOGG1* transgene is associated with obesity resistance and increased mitochondrial content in adipose tissue. These data demonstrate a critical role for OGG1 in modulating energy balance through changes in adipose tissue function. They also demonstrate the importance of OGG1 in modulating developmental programming of mitochondrial content and quality, thereby determining metabolic outcomes in offspring.

**Keywords: DNA repair, metabolic syndrome (in offspring), obesity, developmental origins of disease, mitochondrial function**

# INTRODUCTION

Oxidatively-induced damage to both nuclear and mitochondrial DNA is repaired *via* the base-excision repair (BER) pathway, initiated by DNA glycosylases. The most commonly formed oxidative lesion, 8-oxoguanine (8-oxoG), is recognized and cleaved by the enzyme, 8-oxoG DNA glycosylase (OGG1). OGG1 initiates repair of 8-oxoG in both the nuclear and mitochondrial genome and has been shown to play a role in diverse pathologies, including neurodegenerative disease, various cancers, and metabolic dysfunction (Sampath et al., 2012a; Vartanian et al., 2017; Sampath and Lloyd, 2019). We have previously demonstrated that mice lacking endogenous OGG1 ($Ogg1^{-/-}$) are prone to diet-induced obesity (DIO) and its sequelae, including insulin resistance, ectopic lipid accumulation in liver and skeletal muscle, gut dysbiosis, and chronic inflammation (Sampath et al., 2012b; Vartanian et al., 2017; Simon et al., 2020). Conversely, enhanced expression of human *OGG1* downstream of a constitutive mitochondrial targeting sequence protects mice from DIO, insulin resistance, and adipose tissue inflammation (Komakula et al., 2018). This metabolic protection in *hOGG1* transgenic mice ($Ogg1^{Tg}$) was accompanied by increases in whole body energy expenditure and increased mitochondrial content and respiration in white adipose tissue (WAT) (Komakula et al., 2018). Thus, our previous studies reported this novel role for OGG1 in modulating energy balance in the context of a hypercaloric high-fat diet (HFD). In the current study, we sought to explore whether *hOGG1* expression could confer protection against genetically-induced obesity. Several models of genetically-induced obesity become obese due to chronic hyperphagia (Robinson et al., 2000; Ellacott and Cone, 2006; Chang et al., 2018). In most of these models, obesity develops spontaneously on a chow diet, without requiring the use of a hypercaloric HFD. We therefore asked the question of whether *hOGG1* expression would be protective in the context of genetically-induced obesity. To address this question, we transferred the gene expressing human *OGG1* downstream of a constitutive mitochondrial targeting sequence ($Ogg1^{Tg}$) (Wang et al., 2011; Komakula et al., 2018) into the $A^y/a$ obese mouse ($A^y/a$). The $A^y/a$ model develops hyperphagia and consequent obesity and insulin resistance due to ectopic overexpression of the Agouti protein, an antagonist of the melanocortin receptor (Klebig et al., 1995; Moussa and Claycombe, 1999; Tschöp and Heiman, 2001). Interestingly, our studies indicate an important function for OGG1 in protecting against genetically-induced obesity. Further, they also uncover a critical role for maternal OGG1 genotype in determining obesity resistance both in the context of genetically-induced as well as DIO.

# EXPERIMENTAL APPROACH

## Animals

Age-matched mice on the C57BL6J background were used in all studies. The generation of *hOGG1*-expressing mice ($Ogg1^{Tg}$) has been previously described (Wang et al., 2011). $A^y/a$ mice were obtained from Jackson Labs (stock #000021) (Siracusa et al., 1987; Klebig et al., 1995). $A^y/a$ mice expressing the *hOGG1* transgene are designated as $A^y/a^{Tg}$ and were bred in house by mating $A^y/a$ or $A^y/a^{Tg}$ animals with $Ogg1^{Tg}$ animals. Cohort sizes were as follows: males– $A^y/a$: 10; $A^y/a^{Tg}$: 11; females – $A^y/a$: 10; $A^y/a^{Tg}$ 11; $A^y/a^{Tg-dad}$: 5; all HFD studies—$n = 5$–9 males per cohort. For studies using $A^y/a$ mice, body weights were measured weekly from week 4 onward, and food intake was measured weekly between weeks 10–22 for males and 18–22 for females. At 50 weeks of age, body composition was measured by NMR (Echo Medical Systems, Houston, TX, United States) and energy expenditure and physical activity were measured *via* open circuit indirect calorimetry (CLAMS Comprehensive Lab Animal Monitoring System, Columbus Instruments, Columbus, OH, United States). Following an acclimation period of 24 h, oxygen consumption ($VO_2$) and carbon dioxide production ($VCO_2$) were recorded every minute for 48 h, with a room air reference taken following each cycle of measurements. Beam breaks on the X, Y, and Z axes were tallied for voluntary physical activity measurements. Gonadal WAT, subscapular brown adipose tissue (BAT), liver, and gastrocnemius were collected at 52 weeks of age. For HFD feeding studies, 8-week old male mice were individually housed and given *ad libitum* access to a 60% HFD for 12 weeks, and body weights and food intake were measured weekly. Body composition was assessed, and tissues were collected at 20 weeks of age. All mice were euthanized between 9 and 11 am by isoflurane overdose followed by exsanguination *via* cardiac puncture. For all *in vivo* procedures, every effort was made to minimize discomfort and suffering, in accordance with the protocols approved by the Animal Care and Use Committee of Rutgers University, New Brunswick, New Jersey under protocol No. 201900077.

## Hepatic Lipids

Hepatic lipids were extracted and separated by thin-layer chromatography, as we have previously described (Komakula et al., 2018).

## DNA and RNA Analyses

RNA was isolated using QIAzol Lysis Reagent and the Qiagen RNeasy kit. Superscript III first-strand synthesis system (Invitrogen, Carlsbad, CA, United States) was used to synthesize cDNA from 1 μg of RNA. Quantitative real-time PCR (qPCR) was performed on a QuantStudio 3 Real-Time PCR System (Applied Biosystems, Foster City, CA, United States) with gene-specific primers. Data were normalized to the expression of RNA18SN5 and quantification was done using the $2^{-\Delta\Delta Ct}$ method. Relative copy number was quantified by qRT-PCR amplification of hOGG1 from 10 ng genomic DNA and normalized to expression of GAPDH.

## Protein Analyses

Whole cell lysates were prepared from frozen tissue using HEPES homogenization buffer (50 mM pH7.4 HEPES, 150 mM NaCl, 10 mM Na-pyrophosphate, 2 mM EDTA, 1% NP-40, 10% Glycerol) with EDTA-free protease and phosphatase inhibitors. Samples are representative of 3–7 animals, and lysate protein concentrations were determined *via* Bradford assay. Equal

amounts of protein were separated by SDS-PAGE and transferred to nitrocellulose membranes. Ponceau total protein staining was performed to confirm uniform loading and transfer of proteins. Following this, membranes were blocked with 5% non-fat dried milk in Tris-buffered saline (TBS, 150 mM NaCl, 50 mM Tris–HCl, pH 7.4) with 0.1% Tween 20 at room temperature with shaking for an hour. The membranes were then incubated overnight at 4°C with primary antibody. Primary antibodies used were as follows: VDAC (Pierce Biotechnology, Waltham, MA, United States), COXIV (Abcam, Cambridge, United Kingdom), PGC-1α (Novus Biologicals, Littleton, CO, United States), HSP60, SIRT1, and GAPDH (all from Cell Signaling Technology, Danvers, MA, United States). Membranes were incubated with HRP- or Alexa-fluor conjugated secondary antibodies and signal was detected using enhanced chemiluminescence or fluorescence imaging, respectively, on an Azure c600 imaging system (Azure Biosystems, United States).

## Statistical Analyses

Data are expressed as mean ± SEM for biological replicates; statistical comparisons were carried out by student's *t*-test for 2-group comparisons and by two−way ANOVA for multi−group comparisons, followed by post−hoc analysis (Bonferroni) in Graph Pad Prism (version 8.2.0 for Windows, GraphPad Software, La Jolla, CA, United States).

# RESULTS

## *hOGG1* Expression Attenuates Body Weight in $A^y/a$ Obese Mice

$A^y/a$ yellow obese mice are a genetic model of obesity resulting from antagonism of the melanocortin receptor and consequent hyperphagia (Moussa and Claycombe, 1999; Tschöp and Heiman, 2001). Unlike other common models of obesity such as the leptin-deficient ob/ob or leptin-receptor deficient db/db mice, $A^y/a$ mice express both a functional leptin gene and a leptin receptor. However, these mice develop insulin and leptin resistance, and are hence a valuable model to study genetically-induced obesity in a clinically relevant manner (Klebig et al., 1995; Miltenberger et al., 1997; Tschöp and Heiman, 2001; Rahmouni et al., 2002; Miyazaki et al., 2009). Melanocortin receptor antagonism in $A^y/a$ mice results in chronic hyperphagia and consequent obesity, which is apparent starting at about 16 weeks on a standard rodent chow diet. To determine the potential impact of *hOGG1* expression on body weight in this model, we introduced the *hOGG1* transgene into $A^y/a$ mice to generate $A^y/a$; $Ogg1^{Tg}$ ($A^y/a^{Tg}$) mice. Body weights were measured from weaning until 48 weeks of age on a standard chow diet in male and female $A^y/a$ and $A^y/a^{Tg}$ littermates. Female $A^y/a^{Tg}$ mice had significantly lower body weights than $A^y/a$ counterparts, starting as early as 5 weeks of age. Male $A^y/a^{Tg}$ mice also had significantly lower body weights than their $A^y/a$ counterparts, starting at 21 weeks of age (**Figures 1A,B**).

Unlike in DIO, which is characterized by increases in fat mass, genetically-induced obesity in $A^y/a$ mice results in increases in both lean and fat masses (Miltenberger et al., 1997). Body composition analyses at 52 weeks of age indicated that reductions in body weight in $A^y/a^{Tg}$ mice were reflected in decreases in both lean and fat masses (**Figures 1C,D**). Thus, *hOGG1* expression in this model attenuates aberrant increases in both lean and fat compartments of $A^y/a$ mice. Increased body weight in $A^y/a$ mice is a consequence of chronic hyperphagia. Interestingly, both female and male $A^y/a^{Tg}$ had higher food intakes than their $A^y/a$ counterparts (**Figures 1E,F**). This suggested that rather than due to attenuation of food intake, peripheral mechanisms may mediate the observed reductions in body weight in $A^y/a^{Tg}$ mice.

## *hOGG1* Expression Increases Energy Expenditure and Mitochondrial Content in $A^y/a$ Obese Mice

Given the similarities between male and female animals, we focused our downstream studies on female mice due to their larger sample size. Energy expenditure analyses were carried out using open circuit indirect calorimetry. $A^y/a^{Tg}$ mice had a trend for elevated $O_2$ consumption and $CO_2$ respiration (**Figures 2A,B**); however, this was not statistically significant. These data suggested that the reduction in body weights in $A^y/a^{Tg}$ mice may be due to physiologically relevant elevations in energy expenditure. Respiratory exchange ratios (RER) were unchanged by genotype (**Figure 2C**), indicating no differences in whole body substrate utilization. Physical activity was not significantly different between genotypes (**Figure 2D**).

To investigate metabolic changes that contribute to this lean phenotype and elevated energy expenditure, we evaluated markers of mitochondrial content and energy sensing across multiple metabolically active tissues in $A^y/a$ and $A^y/a^{Tg}$ mice (**Figure 3**). Markers of mitochondrial content, including heat-shock protein 60 (HSP60), voltage-dependent anion channel (VDAC), and cytochrome c oxidase IV (COX4) were significantly elevated in WAT of $A^y/a^{Tg}$ mice, relative to $A^y/a$ counterparts. HSP60 and VDAC were increased in BAT and gastrocnemius of $A^y/a^{Tg}$ mice (**Figures 3A–F**). In addition, expression of peroxisome proliferator-activated receptor gamma coactivator-1-alpha (PGC-1α), a master regulator of mitochondrial biogenesis, was elevated across tissues in $A^y/a^{Tg}$ mice (NS in gastrocnemius) (**Figures 3A–F**). Expression of the deacetylase, Sirtuin 1 (SIRT1), which activates PGC-1α, was also significantly increased in WAT of $A^y/a^{Tg}$ mice. The elevation in SIRT1 and PGC-1α are consistent with the observed increases in mitochondrial content in these animals. They are also consistent with prior reports from our lab and others indicating a role for OGG1 in altering tissue mitochondrial content and function (Rachek et al., 2002, 2006a,b; Yuzefovych et al., 2013; Vartanian et al., 2017; Komakula et al., 2018). Further, most of the significant changes related to mitochondrial function and content were observed in WAT, rather than in other tissues of $A^y/a^{Tg}$ mice. These data are consistent with our prior observations of an important role for WAT remodeling in mediating the metabolic phenotypes of Ogg1Tg mice (Komakula et al., 2018). We thus propose that *hOGG1* expression increases mitochondrial content in $A^y/a^{Tg}$ mice, particularly in WAT, resulting in elevated

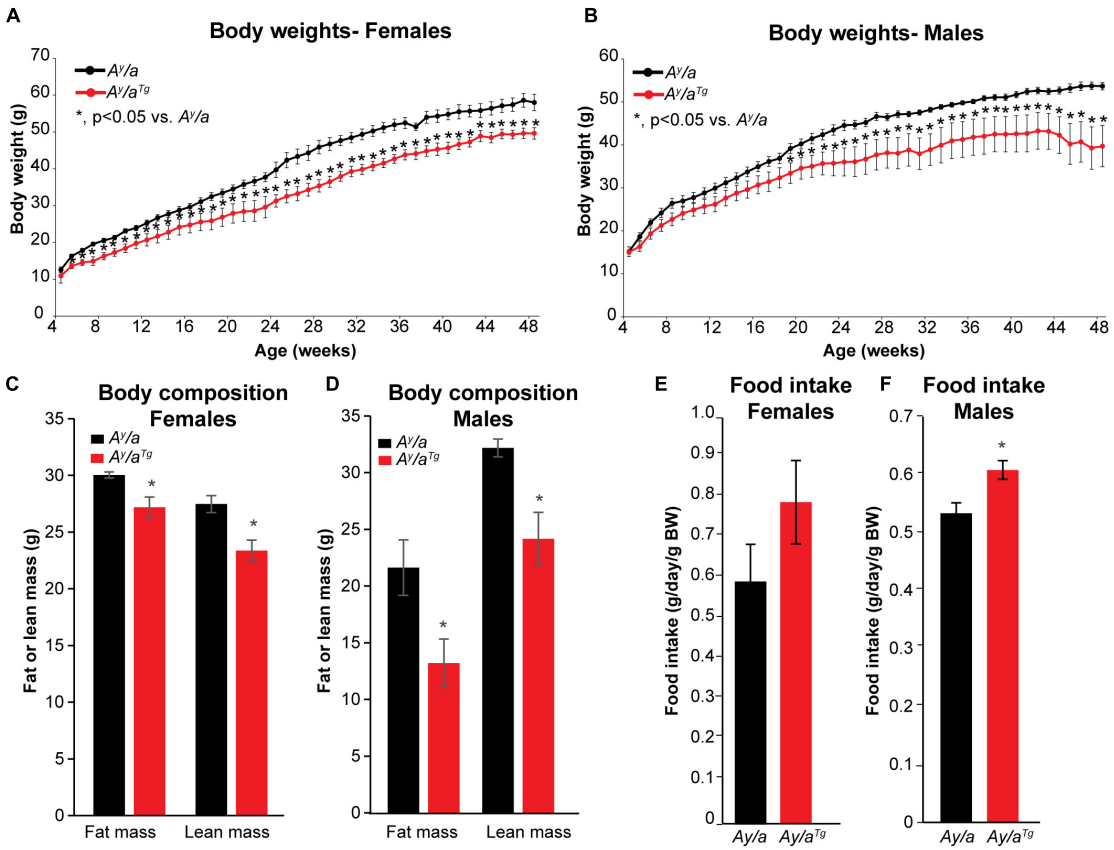


**FIGURE 1 |** Body weights, body composition, and food intake. **(A,B)** Body weights were reduced in $A^y/a^{Tg}$ mice, relative to $A^y/a$ obese counterparts. **(C,D)** Reductions in both lean and fat mass were apparent in $A^y/a^{Tg}$ mice. **(E,F)** Food intake was measured weekly between weeks 10–22 for males and 18–22 for females; food intake was slightly increased in $A^y/a^{Tg}$ mice (NS in females). Averages ± SEM. *$p < 0.05$ vs. sex-matched $A^y/a$.

energy expenditure and attenuation of body weight, relative to $A^y/a$ littermates.

## Maternal Transmission of the *hOGG1* Transgene Is Necessary for Obesity Resistance

Breeding of $A^y/a$ mice is inherently challenging, as the $A^y/a$ mutation reduces fecundity and is embryonically lethal in offspring of homozygous mutants. Thus, animals used in the studies above were derived from parents where one parent transmitted the $A^y/a$ mutation, with the female parent carrying the *hOGG1* transgene. However, during colony expansion, we generated a limited number of offspring where the *hOGG1* transgene was transmitted solely by the male parent ($A^y/a^{Tg-dad}$), since the female parent did not carry the *hOGG1* transgene. Intriguingly, we noticed that offspring from this mating were not protected from obesity, relative to $A^y/a$ controls. Thus, while offspring of female $A^y/a^{Tg}$ mice were protected from agouti-induced obesity, offspring of male $A^y/a^{Tg}$ mice were not (**Figure 4**). Regrettably, these mice were euthanized at 24 weeks, hence longer term body weight curves were not generated for this colony.

Since $A^y/a^{Tg}$ females were lighter than $A^y/a$ animals at breeding age (8 weeks), we sought to determine if the differences in offspring phenotype were simply a function of maternal body weight during pregnancy. We therefore established breeding colonies in our non-$A^y/a$ colony, such that either the female or male parent was *hOGG1* transgenic ($Ogg1^{Tg-mom}$ or $Ogg1^{Tg-dad}$, respectively). Under chow-fed conditions, WT and $Ogg1^{Tg}$ mice do not differ in body weights or litter sizes. WT and $Ogg1^{Tg}$ offspring from all breeding pairs were placed on a 12-week HFD, starting at 8 weeks of age. Mice with maternal transmission of the *hOGG1* transgene ($Ogg1^{Tg-mom}$) were significantly protected from HFD-induced body weight gain, relative to WT littermates, as we have previously reported (**Figure 5A**). However, mice that received the transgene solely from the male parent ($Ogg1^{Tg-dad}$) had body weights that were indistinguishable from WT littermates when fed a HFD (**Figure 5A**). Body composition analyses revealed that fat mass was significantly reduced in $Ogg1^{Tg-mom}$ mice, relative to WT counterparts (**Figure 5B**). Additionally, lean mass was increased in $Ogg1^{Tg-mom}$ mice, relative to WT controls. In contrast, fat and lean masses in $Ogg1^{Tg-dad}$ mice were indistinguishable from WT controls and significantly higher than $Ogg1^{Tg-mom}$ animals (**Figure 5B**). Hepatic lipid accumulation is a distinct

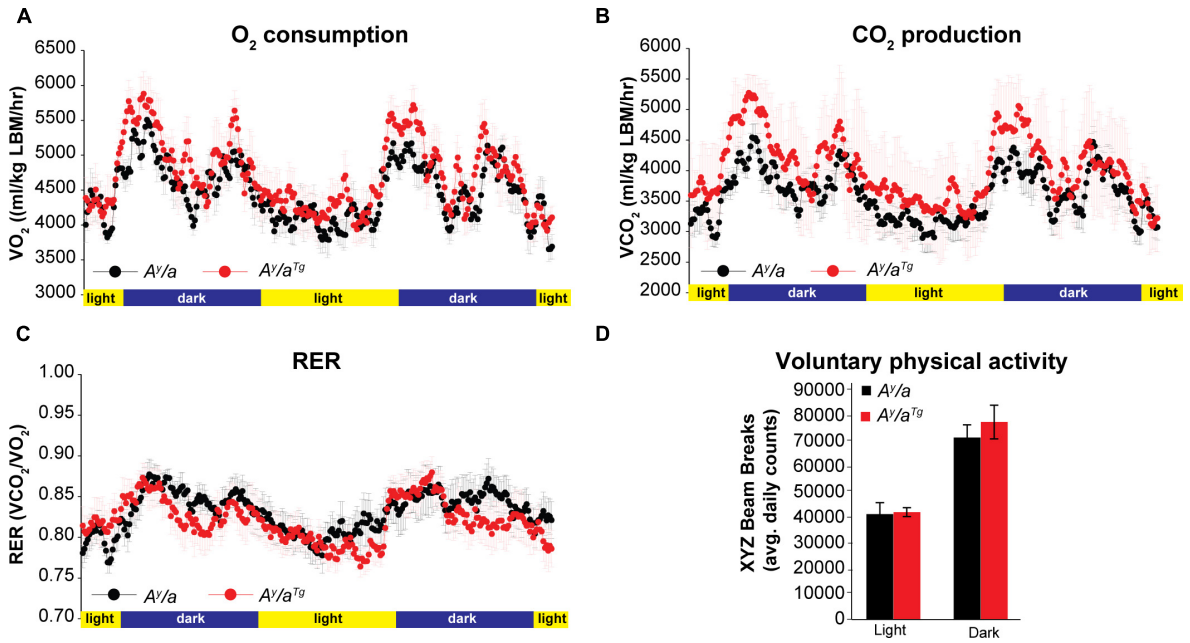


**FIGURE 2 |** Energy expenditure. **(A)** $O_2$ consumption and **(B)** $CO_2$ respiration were measured by indirect calorimetry in female mice. **(C)** Respiratory exchange ratios (RER) were calculated during indirect calorimetry measurements. **(D)** Voluntary physical activity was measured during indirect calorimetry. $n = 6$. Averages ± SEM.

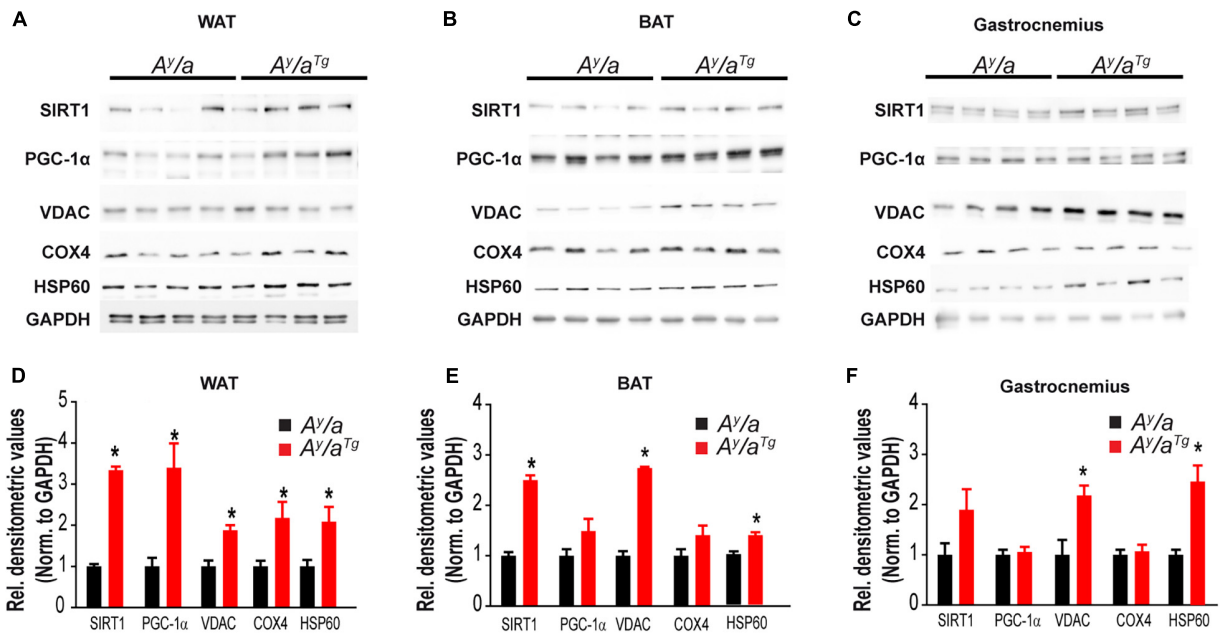


**FIGURE 3 |** Tissue mitochondrial content. Tissue expression of mitochondrial markers was measured by immunoblotting in **(A,D)** WAT, **(B,E)** BAT, and **(C,F)** Gastrocnemius. BAT, brown adipose tissue, COX4, cytochrome c oxidase; GAPDH, glyceraldehyde 3-phosphate dehydrogenase; HSP60, heat shock protein-60; PGC-1α, peroxisome proliferator-activated receptor gamma coactivator 1-alpha; SIRT1, Sirtuin 1; VDAC, voltage-dependent anion channel; WAT, white adipose tissue.

risk factor for further metabolic dysfunction, and we have previously shown that while OGG1 deficiency increases hepatic lipid storage, OGG1-overexpression significantly reduces hepatic lipids (Sampath et al., 2012b; Komakula et al., 2018). Here we discovered that while stored hepatic lipids such as triglycerides (TG) and cholesterol esters (CE) were significantly reduced in $Ogg1^{Tg-mom}$ mice, no such reduction was apparent in $Ogg1^{Tg-dad}$ livers (**Figure 5C**). Thus, transgene inheritance

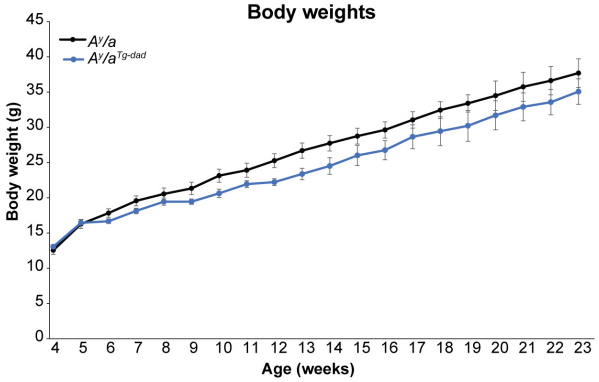


**FIGURE 4 |** Body weights following paternal transmission of *hOGG1*. Body weights were measured at weekly intervals in female mice. Averages ± SEM. *$p < 0.05$ vs. $A^y/a$.

from the female parent was both required and sufficient to confer protection against HFD-induced weight gain, whole body adiposity, and hepatic lipid accumulation.

## Increased Mitochondrial Content in WAT Requires Maternal Transmission of the *hOGG1* Transgene

Inheritance of the *hOGG1* transgene from the male or female parent did not alter the relative transgene copy number nor gene expression of *hOGG1* (**Figures 5D,E**). This led us to conclude that differences in obesity resistance were not a function of unexpected differences in copy number or *hOgg1* expression levels in the offspring. We have previously shown that in the context of HFD-induced obesity, changes in mitochondrial content and function in WAT may mediate obesity resistance in $Ogg1^{Tg}$ mice. Consistent with these previous reports, we discovered that $Ogg1^{Tg-mom}$ mice had increased mitochondrial content, reflected in significantly increased content of VDAC in WAT. However, $Ogg1^{Tg-dad}$ animals did not have a similar increase in mitochondrial content, consistent with the lack of obesity resistance in these mice (**Figure 5F**). Similar increases in mitochondrial content were not observed in BAT or gastroc of $Ogg1^{Tg}$ mice (**Figure 5F**). These findings are consistent with our previous reports (Komakula et al., 2018) and suggest that differences in metabolic phenotypes in $Ogg1^{Tg}$ mice may stem from alterations in WAT mitochondrial content and function. Overall, our results indicate that maternal transmission of the *hOGG1* transgene confers resistance not only to genetically-induced obesity (**Figure 4**), but also to HFD-induced obesity.

# DISCUSSION

We demonstrate for the first time that enhanced expression of the human *OGG1* gene confers protection against genetically-induced obesity. The Agouti yellow mouse obesity syndrome is a result of dominant mutations at the Agouti locus (Moussa and Claycombe, 1999). Ectopic expression of Agouti in multiple tissues in these mice results in a yellow coat color, chronic hyperphagia, obesity, increased linear growth, leptin and insulin resistance, and hyperglycemia. Mechanisms mediating hyperphagia and obesity in this model involve antagonism of the melanocortin receptor, and similar phenotypes have been described in mice overexpressing Agouti-Related protein (AGRP), a potent antagonist of the melanocortin receptors-3 and -4 (Moussa and Claycombe, 1999; Small et al., 2001). Human obesity is also frequently associated with resistance to both leptin and insulin, and genome-wide association studies have implicated mutations near the melanocortin receptor-4 in the development of obesity and insulin resistance (Chambers et al., 2008; Loos et al., 2008). Thus, our results indicating a role for OGG1 in attenuating body weights in the $A^y/a$ obese model (**Figure 1**) are particularly relevant from a translational standpoint. As *hOGG1* expression lowered body weight without lowering food intake (**Figure 1**), body weight reduction in $A^y/a^{Tg}$ mice likely results from alterations in peripheral tissues. Consistently, we observed increases in whole body energy expenditure (**Figure 2**) and mitochondrial content in several metabolically important tissues, particularly in WAT of $A^y/a^{Tg}$ mice (**Figure 3**).

An intriguing discovery of these studies is that of obesity resistance being determined by the maternal OGG1 genotype. Male $Ogg1^{Tg}$ parents were unable to transmit obesity resistance to their $Ogg1^{Tg}$ offspring. Female $Ogg1^{Tg}$ mice, conversely, could transmit this metabolically beneficial phenotype to both male and female (not shown) offspring. These data are strongly suggestive of the mitochondrial genome, which is inherited solely from the female parent, as being a critical determinant of the obesity resistance phenotype in $Ogg1^{Tg}$ mice.

Studies examining the developmental origins of disease have established a strong link between maternal obesity and adverse metabolic outcomes in offspring (Das et al., 2021). For instance, in both human and rodent studies, maternal obesity is associated not only with increased risk of pregnancy complications such as gestational diabetes, but also with adverse outcomes in the offspring, including increased risk of obesity and diabetes. The mechanisms underlying these effects are not completely known but likely involve hormonal regulation, epigenetic changes, oxidative stress in the uterine environment, and dysregulated gut microbiota, among other factors (Saben et al., 2016; Das et al., 2021). While these links between maternal obesity and fetal outcomes have been extensively studied in animal models, relatively few studies have examined a link between maternal obesity resistance and metabolic outcomes in the offspring. Our studies indicate that maternal, but not paternal, OGG1 genotype influences tissue mitochondrial content and energy balance in both male and female $Ogg1^{Tg}$ offspring. These findings clearly implicate a role for mitochondrial quality in determining obesity resistance phenotypes in offspring. They also raise intriguing questions about interactions between the intrauterine environment, which is influenced by maternal genotype, and offspring genotype. Prior studies have reported roles for increased maternal oxidative stress and DNA damage in impacting comparable stress in the fetus and offspring

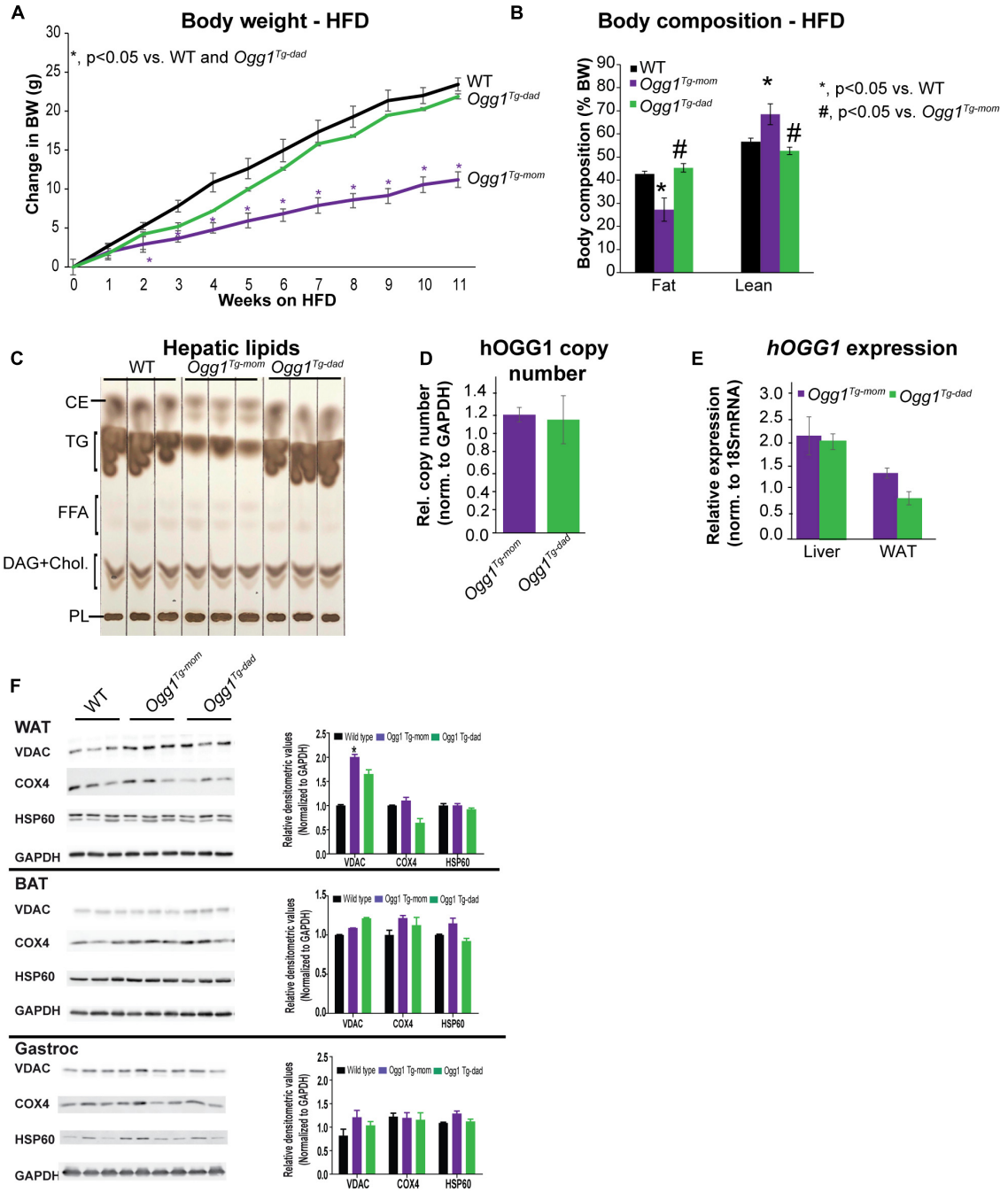


**FIGURE 5 |** Maternal vs. paternal transmission of *hOGG1* influences metabolic phenotype and mitochondrial content of WAT. **(A)** $Ogg1^{Tg\text{-}mom}$ or $Ogg1^{Tg\text{-}dad}$ animals were placed on high-fat diets (HFDs) at 8 weeks of age, and body weights were measured weekly. **(B)** Body composition was measured at the end of 11 weeks of HFD feeding. **(C)** Hepatic lipids were extracted and separated by thin-layer chromatography. **(D)** Relative hOGG1 copy number and **(E)** *hOGG1* gene expression were measured by qPCR. **(F)** Tissue expression of mitochondrial markers was measured by immunoblotting. CE, cholesterol esters; DAG, diacylglycerols; FFA, free fatty acids; PL, phospholipids; TG, triglycerides.

(Luo et al., 2006; Simmons, 2006; Raicević et al., 2010; Rodríguez-Rodríguez et al., 2018). Further, epigenetic modifications during development have been shown to be influenced by an adverse fetal environment and to, in turn, impair metabolic outcomes in adult offspring (Seki et al., 2012; Houde et al., 2013; Ruchat et al., 2013; Marchlewicz et al., 2016; Zhu et al., 2019). In this regard, 8-oxoG itself may serve as an epigenetic mark, thereby altering promoter transcription rates *via* the recruitment of OGG1 to sites of oxidation (Perillo et al., 2008; Ruchko et al., 2009; Zarakowska et al., 2014; Allgayer et al., 2016;

Fleming et al., 2017a,b; Hao et al., 2020). In addition to being recruited to 8-oxoG sites, OGG1 activity influences DNA methylation, as oxidized guanines in CpG sequences are resistant to the action of DNA methyltransferases (Weitzman et al., 1994; Valinluck et al., 2004; Maltseva et al., 2009; Ba and Boldogh, 2018). Thus, oxidative stress and OGG1 activity are both critical determinants of epigenetic programming, although their roles in the uterine environment have not been investigated. We observed that protection from DIO required both the female parent and offspring to carry the hOGG1 transgene. Thus, it is possible that reduced uterine oxidative stress in an $Ogg1^{Tg}$ female may result in altered metabolic programming in $Ogg1^{Tg}$ offspring. The mechanisms mediating these interactions between maternal or *in utero* genotype with offspring genotype require further investigation.

These studies also suggested that among markers of mitochondrial content, which can directly influence energy expenditure, increased mitochondrial content in WAT was consistent with obesity resistance in $Ogg1^{Tg-mom}$ but not $Ogg1^{Tg-dad}$ mice (**Figure 5F**). These data further support our working hypothesis that the improved metabolic phenotype in $Ogg1^{Tg}$ mice is a consequence of increased mitochondrial content and improved function in WAT (Komakula et al., 2018). In further support of a role for OGG1 in modulating adipocyte behavior, we recently showed that OGG1 genotype corresponds with adipocyte differentiation capacity (Komakula et al., 2021). Preadipocytes lacking OGG1 differentiated faster and accumulated more lipids than WT cells, while *hOGG1* expression significantly blunted adipocyte differentiation and lipid accretion. These phenotypes in isolated preadipocytes and 3T3 cells correspond with obesity predisposition or resistance in $Ogg1^{-/-}$ and $Ogg1^{Tg}$ animals, respectively (Komakula et al., 2021). They also indicate an important cell-intrinsic role for OGG1 in the adipocyte, as supported by our current studies.

In summary, we show here for the first time that *hOGG1* expression is protective against obesity resulting not only from HFD consumption, but also from genetically-induced obesity. In both models, *hOGG1* expression alters tissue mitochondrial content, particularly in WAT, and enhances overall energy expenditure. Importantly, maternal transmission of the transgene is both necessary and sufficient to confer resistance to obesity. These data have important implications to our understanding of the etiology of obesity and the role that DNA damage and repair may play in the process. They also establish an important role for interactions between the *in utero* environment, shaped by maternal genotype, with offspring genotype in impacting developmental programming and influencing metabolic outcomes in adult animals.

## DATA AVAILABILITY STATEMENT

The original contributions presented in the study are included in the article/supplementary material, further inquiries can be directed to the corresponding author.

## ETHICS STATEMENT

The animal study was reviewed and approved by Animal Care and Use Committee of Rutgers University, New Brunswick, NJ, United States.

## AUTHOR CONTRIBUTIONS

NB, RL, and HS contributed to conceptualization and design of the study. NB, PS, HY, SK, VV, and HS carried out experiments and analyzed data. NB, PS, and HS prepared figures and wrote the first draft of the manuscript. AD, RL, and HS edited the manuscript and obtained funding. All authors have read and approved the submitted version.

## FUNDING

This work was supported by NIH grants DK100640 (HS) and DK075974 (RL), a grant from European Union's Horizon 2020 research and innovation program under the Marie Sklodowska Curie COFUND grant agreement no. 665735 (Bio4Med) to AD and HS, by funding from the Polish Ministry of Science and Higher Education as part of 2016–2020 funds for the implementation of international projects (agreement no. 548/H2020/COFUND/2016/2) to AD and HS, funds from the Oregon Institute of Occupational Health Sciences at Oregon Health and Science University *via* funds from the Division of Consumer and Business Services of the State of Oregon (ORS 656.630) to RL, and funds from Rutgers University to HS. The funders had no role in study design, data collection and analysis, decision to publish, or preparation of the manuscript.

## ACKNOWLEDGMENTS

We would like to thank Dr. Lars Eide (University of Oslo) for the gift of $Ogg1^{Tg}$ animals.

## REFERENCES

Allgayer, J., Kitsera, N., Bartelt, S., Epe, B., and Khobta, A. (2016). Widespread transcriptional gene inactivation initiated by a repair intermediate of 8-oxoguanine. *Nucleic Acids Res.* 44, 7267–7280.

Ba, X., and Boldogh, I. (2018). 8-Oxoguanine DNA glycosylase 1: beyond repair of the oxidatively modified base lesions. *Redox Biol.* 14, 669–678. doi: 10.1016/j.redox.2017.11.008

Chambers, J. C., Elliott, P., Zabaneh, D., Zhang, W., Li, Y., Froguel, P., et al. (2008). Common genetic variation near MC4R is associated with waist circumference and insulin resistance. *Nat. Genet.* 40, 716–718. doi: 10.1038/ng.156

Chang, J. Y., Park, J. H., Park, S. E., Shon, J., and Park, Y. J. (2018). The fat mass-and obesity-associated (FTO) gene to obesity: lessons from mouse models. *Obesity* 26, 1674–1686. doi: 10.1002/oby.22301

Das, M., Sauceda, C., and Webster, N. J. G. (2021). Mitochondrial dysfunction in obesity and reproduction. *Endocrinology* 162:bqaa158.

Ellacott, K. L., and Cone, R. D. (2006). The role of the central melanocortin system in the regulation of food intake and energy homeostasis: lessons from mouse models. *Philos. Trans. R. Soc. Lond. B Biol. Sci.* 361, 1265–1274. doi: 10.1098/rstb.2006.1861

Fleming, A. M., Ding, Y., and Burrows, C. J. (2017a). Oxidative DNA damage is epigenetic by regulating gene transcription via base excision repair. *Proc. Natl. Acad. Sci.* 114, 2604–2609. doi: 10.1073/pnas.1619809114

Fleming, A. M., Zhu, J., Ding, Y., and Burrows, C. J. (2017b). 8-Oxo-7,8-dihydroguanine in the context of a gene promoter G-Quadruplex is an on-off switch for transcription. *ACS Chem. Biol.* 12, 2417–2426. doi: 10.1021/acschembio.7b00636

Hao, W., Wang, J., Zhang, Y., Wang, C., Xia, L., Zhang, W., et al. (2020). Enzymatically inactive OGG1 binds to DNA and steers base excision repair toward gene transcription. *FASEB J.* 34, 7427–7441. doi: 10.1096/fj.201902243r

Houde, A.-A., Hivert, M.-F., and Bouchard, L. (2013). Fetal epigenetic programming of adipokines. *Adipocyte* 2, 41–46. doi: 10.4161/adip.22055

Klebig, M. L., Wilkinson, J. E., Geisler, J. G., and Woychik, R. P. (1995). Ectopic expression of the agouti gene in transgenic mice causes obesity, features of type II diabetes, and yellow fur. *Proc. Natl. Acad. Sci. U.S.A.* 92:4728. doi: 10.1073/pnas.92.11.4728

Komakula, S. S. B., Tumova, J., Kumaraswamy, D., Burchat, N., Vartanian, V., Ye, H., et al. (2018). The DNA repair protein OGG1 protects against obesity by altering mitochondrial energetics in white adipose tissue. *Sci. Rep.* 8:14886.

Komakula, S. S., Blaze, B., Ye, H., Dobrzyn, A., and Sampath, H. A. (2021). Novel role for the DNA repair enzyme 8-Oxoguanine DNA glycosylase in adipogenesis. *Int. J. Mol. Sci.* 22:1152. doi: 10.3390/ijms22031152

Loos, R. J., Lindgren, C. M., Li, S., Wheeler, E., Zhao, J. H., Prokopenko, I., et al. (2008). Common variants near MC4R are associated with fat mass, weight and risk of obesity. *Nat. Genet.* 40, 768–775.

Luo, Z. C., Fraser, W. D., Julien, P., Deal, C. L., Audibert, F., Smith, G. N., et al. (2006). Tracing the origins of "fetal origins" of adult diseases: programming by oxidative stress? *Med. Hypotheses* 66, 38–44. doi: 10.1016/j.mehy.2005.08.020

Maltseva, D. V., Baykov, A. A., Jeltsch, A., and Gromova, E. S. (2009). Impact of 7,8-dihydro-8-oxoguanine on methylation of the CpG site by Dnmt3a. *Biochemistry* 48, 1361–1368. doi: 10.1021/bi801947f

Marchlewicz, E. H., Dolinoy, D. C., Tang, L., Milewski, S., Jones, T. R., Goodrich, J. M., et al. (2016). Lipid metabolism is associated with developmental epigenetic programming. *Sci. Rep.* 6:34857.

Miltenberger, R. J., Mynatt, R. L., Wilkinson, J. E., and Woychik, R. P. (1997). The role of the agouti gene in the yellow obese syndrome. *J. Nutr.* 127, 1902S–1907S.

Miyazaki, M., Sampath, H., Liu, X., Flowers, M. T., Chu, K., Dobrzyn, A., et al. (2009). Stearoyl-CoA desaturase-1 deficiency attenuates obesity and insulin resistance in leptin-resistant obese mice. *Biochem. Biophys. Res. Commun.* 380, 818–822. doi: 10.1016/j.bbrc.2009.01.183

Moussa, N. M., and Claycombe, K. J. (1999). The yellow mouse obesity syndrome and mechanisms of agouti-induced obesity. *Obes. Res.* 7, 506–514. doi: 10.1002/j.1550-8528.1999.tb00440.x

Perillo, B., Ombra, M. N., Bertoni, A., Cuozzo, C., Sacchetti, S., Sasso, A., et al. (2008). DNA oxidation as triggered by H3K9me2 demethylation drives estrogen-induced gene expression. *Science* 319, 202–206. doi: 10.1126/science.1147674

Rachek, L. I., Grishko, V. I., Ledoux, S. P., and Wilson, G. L. (2006a). Role of nitric oxide-induced mtDNA damage in mitochondrial dysfunction and apoptosis. *Free Radic. Biol. Med.* 40, 754–762. doi: 10.1016/j.freeradbiomed.2005.09.028

Rachek, L. I., Grishko, V. I., Musiyenko, S. I., Kelley, M. R., Ledoux, S. P., and Wilson, G. L. (2002). Conditional targeting of the DNA repair enzyme hOGG1 into mitochondria. *J. Biol. Chem.* 277, 44932–44937. doi: 10.1074/jbc.m208770200

Rachek, L. I., Thornley, N. P., Grishko, V. I., Ledoux, S. P., and Wilson, G. L. (2006b). Protection of INS-1 cells from free fatty acid-induced apoptosis by targeting hOGG1 to mitochondria. *Diabetes* 55, 1022–1028. doi: 10.2337/diabetes.55.04.06.db05-0865

Rahmouni, K., Haynes, W. G., Morgan, D. A., and Mark, A. L. (2002). Selective resistance to central neural administration of leptin in agouti obese mice. *Hypertension* 39, 486–490. doi: 10.1161/hy0202.102836

Raicević, S., Cubrilo, D., Arsenijević, S., Vukcević, G., Zivković, V., Vuletić, M., et al. (2010). Oxidative stress in fetal distress: potential prospects for diagnosis. *Oxid. Med. Cell. Longev.* 3, 214–218. doi: 10.4161/oxim.3.3.12070

Robinson, S. W., Dinulescu, D. M., and Cone, R. D. (2000). Genetic models of obesity and energy balance in the mouse. *Annu. Rev. Genet.* 34, 687–745. doi: 10.1146/annurev.genet.34.1.687

Rodríguez-Rodríguez, P., Ramiro-Cortijo, D., Reyes-Hernández, C. G., López de Pablo, A. L., González, M. C., and Arribas, S. M. (2018). Implication of oxidative stress in fetal programming of cardiovascular disease. *Front. Physiol.* 9:602. doi: 10.3389/fphys.2018.00602

Ruchat, S.-M., Hivert, M.-F., and Bouchard, L. (2013). Epigenetic programming of obesity and diabetes by in utero exposure to gestational diabetes mellitus. *Nutr. Rev.* 71(suppl_1), S88–S94.

Ruchko, M. V., Gorodnya, O. M., Pastukh, V. M., Swiger, B. M., Middleton, N. S., Wilson, G. L., et al. (2009). Hypoxia-induced oxidative base modifications in the VEGF hypoxia-response element are associated with transcriptionally active nucleosomes. *Free Radic. Biol. Med.* 46, 352–359. doi: 10.1016/j.freeradbiomed.2008.09.038

Saben, J. L., Boudoures, A. L., Asghar, Z., Thompson, A., Drury, A., Zhang, W., et al. (2016). Maternal metabolic syndrome programs mitochondrial dysfunction via germline changes across three generations. *Cell Rep.* 16, 1–8. doi: 10.1016/j.celrep.2016.05.065

Sampath, H., and Lloyd, R. S. (2019). Roles of OGG1 in transcriptional regulation and maintenance of metabolic homeostasis. *DNA Repair* 81:102667. doi: 10.1016/j.dnarep.2019.102667

Sampath, H., McCullough, A. K., and Lloyd, R. S. (2012a). Regulation of DNA glycosylases and their role in limiting disease. *Free Radic. Res.* 46, 460–478. doi: 10.3109/10715762.2012.655730

Sampath, H., Vartanian, V., Rollins, M. R., Sakumi, K., Nakabeppu, Y., and Lloyd, R. S. (2012b). 8-Oxoguanine DNA glycosylase (OGG1) deficiency increases susceptibility to obesity and metabolic dysfunction. *PLoS One* 7:17. doi: 10.1371/journal.pone.0051697

Seki, Y., Williams, L., Vuguin, P. M., and Charron, M. J. (2012). Minireview: epigenetic programming of diabetes and obesity: animal models. *Endocrinology* 153, 1031–1038. doi: 10.1210/en.2011-1805

Simmons, R. A. (2006). Developmental origins of diabetes: the role of oxidative stress. *Free Radic. Biol. Med.* 40, 917–922. doi: 10.1016/j.freeradbiomed.2005.12.018

Simon, H., Vartanian, V., Wong, M. H., Nakabeppu, Y., Sharma, P., Lloyd, R. S., et al. (2020). OGG1 deficiency alters the intestinal microbiome and increases intestinal inflammation in a mouse model. *PLoS One* 15:e0227501. doi: 10.1371/journal.pone.0227501

Siracusa, L. D., Russell, L. B., Eicher, E. M., Corrow, D. J., Copeland, N. G., and Jenkins, N. A. (1987). Genetic organization of the agouti region of the mouse. *Genetics* 117, 93–100. doi: 10.1093/genetics/117.1.93

Small, C. J., Kim, M. S., Stanley, S. A., Mitchell, J. R. D., Murphy, K., Morgan, D. G. A., et al. (2001). Effects of chronic central nervous system administration of agouti-related protein in pair-fed animals. *Diabetes* 50:248. doi: 10.2337/diabetes.50.2.248

Tschöp, M., and Heiman, M. L. (2001). Rodent obesity models: an overview. *Exp. Clin. Endocrinol. Diabetes* 109, 307–319. doi: 10.1055/s-2001-17297

Valinluck, V., Tsai, H. H., Rogstad, D. K., Burdzy, A., Bird, A., and Sowers, L. C. (2004). Oxidative damage to methyl-CpG sequences inhibits the binding of the methyl-CpG binding domain (MBD) of methyl-CpG binding protein 2 (MeCP2). *Nucleic Acids Res.* 32, 4100–4108. doi: 10.1093/nar/gkh739

Vartanian, V., Tumova, J., Dobrzyn, P., Dobrzyn, A., Nakabeppu, Y., Lloyd, R. S., et al. (2017). 8-oxoguanine DNA glycosylase (OGG1) deficiency elicits coordinated changes in lipid and mitochondrial metabolism in muscle. *PLoS One* 12:e0181687. doi: 10.1371/journal.pone.0181687

Wang, W., Esbensen, Y., Kunke, D., Suganthan, R., Rachek, L., Bjørås, M., et al. (2011). Mitochondrial DNA damage level determines neural stem cell

differentiation fate. *J. Neurosci.* 31, 9746–9751. doi: 10.1523/jneurosci.0852-11.2011

Weitzman, S. A., Turk, P. W., Milkowski, D. H., and Kozlowski, K. (1994). Free radical adducts induce alterations in DNA cytosine methylation. *Proc. Natl. Acad. Sci.* 91, 1261–1264. doi: 10.1073/pnas.91.4.1261

Yuzefovych, L., Schuler, A., Chen, J., Alvarez, D., Eide, L., Ledoux, S., et al. (2013). Alteration of mitochondrial function and insulin sensitivity in primary mouse skeletal muscle cells isolated from transgenic and knockout mice: role of OGG1. *Endocrinology* 154, 2640–2649. doi: 10.1210/en.2013-1076

Zarakowska, E., Gackowski, D., Foksinski, M., and Olinski, R. (2014). Are 8-oxoguanine (8-oxoGua) and 5-hydroxymethyluracil (5-hmUra) oxidatively damaged DNA bases or transcription (epigenetic) marks? *Mutat. Res. Genet. Toxicol. Environ. Mutagen.* 76, 58–63. doi: 10.1016/j.mrgentox.2013.09.002

Zhu, Z., Cao, F., and Li, X. (2019). Epigenetic programming and fetal metabolic programming. *Front. Endocrinol.* 10:764. doi: 10.3389/fendo.2019.00764

**Conflict of Interest:** The authors declare that the research was conducted in the absence of any commercial or financial relationships that could be construed as a potential conflict of interest.

**Publisher's Note:** All claims expressed in this article are solely those of the authors and do not necessarily represent those of their affiliated organizations, or those of the publisher, the editors and the reviewers. Any product that may be evaluated in this article, or claim that may be made by its manufacturer, is not guaranteed or endorsed by the publisher.

frontiers in Cell and Developmental Biology

ORIGINAL RESEARCH
published: 02 November 2021
doi: 10.3389/fcell.2021.738502

# APE2 Is a General Regulator of the ATR-Chk1 DNA Damage Response Pathway to Maintain Genome Integrity in Pancreatic Cancer Cells

*Md Akram Hossain[1], Yunfeng Lin[1], Garrett Driscoll[1], Jia Li[1], Anne McMahon[1], Joshua Matos[1], Haichao Zhao[1], Daisuke Tsuchimoto[2], Yusaku Nakabeppu[2], Jianjun Zhao[3] and Shan Yan[1]**

*[1] Department of Biological Sciences, University of North Carolina at Charlotte, Charlotte, NC, United States, [2] Division of Neurofunctional Genomics, Department of Immunobiology and Neuroscience, Medical Institute of Bioregulation, Kyushu University, Fukuoka, Japan, [3] Department of Cancer Biology, Lerner Research Institute, Cleveland Clinic, Cleveland, OH, United States*

OPEN ACCESS

**Edited by:**
*Michael Dwinell, Medical College of Wisconsin, United States*

**Reviewed by:**
*Tangliang Li, Shandong University, China*
*Ciaran Morrison, National University of Ireland Galway, Ireland*

***Correspondence:**
*Shan Yan*
*Shan.Yan@uncc.edu*

**Specialty section:**
*This article was submitted to Molecular and Cellular Pathology, a section of the journal Frontiers in Cell and Developmental Biology*

**Received:** *08 July 2021*
**Accepted:** *14 October 2021*
**Published:** *02 November 2021*

**Citation:**
*Hossain MA, Lin Y, Driscoll G, Li J, McMahon A, Matos J, Zhao H, Tsuchimoto D, Nakabeppu Y, Zhao J and Yan S (2021) APE2 Is a General Regulator of the ATR-Chk1 DNA Damage Response Pathway to Maintain Genome Integrity in Pancreatic Cancer Cells. Front. Cell Dev. Biol. 9:738502. doi: 10.3389/fcell.2021.738502*

The maintenance of genome integrity and fidelity is vital for the proper function and survival of all organisms. Recent studies have revealed that APE2 is required to activate an ATR-Chk1 DNA damage response (DDR) pathway in response to oxidative stress and a defined DNA single-strand break (SSB) in *Xenopus laevis* egg extracts. However, it remains unclear whether APE2 is a general regulator of the DDR pathway in mammalian cells. Here, we provide evidence using human pancreatic cancer cells that APE2 is essential for ATR DDR pathway activation in response to different stressful conditions including oxidative stress, DNA replication stress, and DNA double-strand breaks. Fluorescence microscopy analysis shows that APE2-knockdown (KD) leads to enhanced γH2AX foci and increased micronuclei formation. In addition, we identified a small molecule compound Celastrol as an APE2 inhibitor that specifically compromises the binding of APE2 but not RPA to ssDNA and 3′-5′ exonuclease activity of APE2 but not APE1. The impairment of ATR-Chk1 DDR pathway by Celastrol in *Xenopus* egg extracts and human pancreatic cancer cells highlights the physiological significance of Celastrol in the regulation of APE2 functionalities in genome integrity. Notably, cell viability assays demonstrate that APE2-KD or Celastrol sensitizes pancreatic cancer cells to chemotherapy drugs. Overall, we propose APE2 as a general regulator for the DDR pathway in genome integrity maintenance.

**Keywords: ATR-Chk1, DNA damage response, DNA double-strand breaks, DNA single- strand breaks, genome integrity, APE2**

## INTRODUCTION

Cells undergo continuous bombardments of exogenous and endogenous factors that can lead to genomic instability. It is critical for a cell to maintain genome integrity and fidelity for proper cellular function and survival in stress conditions. This task is daunting due to constant insults on the DNA by genotoxic agents, nucleotide mis-incorporation or deprivation during DNA replication, and the intrinsic biochemical instability of the DNA itself (Lindahl, 1993). Both

exogenous and endogenous sources can result in DNA replication stress and/or DNA lesions that include DNA double-strand breaks (DSB), DNA single-strand breaks (SSBs), and oxidative DNA damage (Ciccia and Elledge, 2010; Yan et al., 2014; Tubbs and Nussenzweig, 2017). Although cells have evolved several different DNA repair pathways to resolve DNA lesions, deficiency in DNA repair pathways or failure to resolve replication stress may result in blockage or collapse of replication and transcription machinery, leading to cellular cytotoxicity, mutagenesis, and/or cell death (Friedberg, 2003; Yan et al., 2014). In humans, DNA lesions are involved in numerous genetically inherited disorders, aging and carcinogenesis (Friedberg, 2003; Tubbs and Nussenzweig, 2017). In response to DNA damage, cells have also evolved the DNA damage response (DDR) pathways to coordinate DNA repair, transcription activation, cell cycle progression, and cell death (Jackson and Bartek, 2009; Ciccia and Elledge, 2010). ATM (Ataxia telangiectasia mutated) and ATR (ATM and Rad3-related) kinases are the key regulators in DDR pathways. Whereas ATM-mediated DDR pathway is primarily activated in response to DSBs, ATR-mediated DDR pathway is triggered by several types of stressful conditions, including DNA replication stress, oxidative stress, SSBs, and DSBs (Cimprich and Cortez, 2008; Marechal and Zou, 2013; Paull, 2015). The ATR DDR pathway is critical for duplicating DNA under stressful conditions (Saldivar et al., 2017), and ATR inhibitors as either monotherapy or combination therapy have been in different phases of clinical trials of cancer patients (Karnitz and Zou, 2015; Bradbury et al., 2020).

Depending on the nature and context of DNA damage or replication stress, the ATR DDR pathway is activated by different regulatory mechanisms. It has been proposed that single-strand DNA (ssDNA) coated with RPA (i.e., RPA-ssDNA) together with a 5′-ssDNA/dsDNA junction may serve as a platform to recruit ATR DDR complexes including ATR, ATRIP, TopBP1, and the Rad9-Rad1-Hus1 (9-1-1) complex for ATR activation (Cimprich and Cortez, 2008; Marechal and Zou, 2015). In DNA replication stress, stalled DNA replication forks induced by aphidicolin or gemcitabine (GEM) uncouple helicase and DNA polymerases, generating RPA-ssDNA for ATR activation (Byun et al., 2005; Yan and Michael, 2009; Fredebohm et al., 2013). In response to DSBs induced by γ-radiation, Topoisomerase I inhibitor Camptothecin (CPT), and Topoisomerase II inhibitor Etoposide (ETO), ATR can also be activated by ssDNA derived from bidirectional DSB end resection by different endonucleases and exonucleases such as Mre11 and Exo1 (Shiotani and Zou, 2009; Symington, 2014; Daley et al., 2015). Oxidative DNA damage induced by hydrogen peroxide ($H_2O_2$) also activates ATR DDR pathway by generating ssDNA at oxidative damage sites (Willis et al., 2013; Wallace et al., 2017). Recent studies have demonstrated that defined SSB structures can activate the ATR DDR pathway via a distinct 3′-5′ end resection mechanism that generates necessary short ssDNA (Hossain et al., 2018; Lin et al., 2018).

APE2 (Apurinic/apyrimidinic endonuclease-2, also known as APEX2 or APN2) is an evolutionarily conserved protein with strong 3′-phosphodiesterase and 3′-5′ exonuclease activities but weak AP endonuclease activity and has been implicated in genome and epigenome integrity maintenance (Burkovics et al., 2009; Chaudhari et al., 2021; Lin et al., 2021). Prior studies using different model systems have shown that APE2 plays crucial roles in DNA repair pathways including the base excision repair (BER) pathway, SSB repair pathway, DSB generation and DSB repair pathway, DDR pathways including the ATR-Chk1 DDR pathway and p53-dependent DDR pathway, immune responses including immunoglobulin somatic hypermutation (SHM) and class switch recombination (CSR), and active DNA demethylation (Unk et al., 2001; Burkovics et al., 2006, 2009; Guikema et al., 2007; Dan et al., 2008; Sabouri et al., 2009; Willis et al., 2013; Li et al., 2018; Lin et al., 2018, 2020; Cupello et al., 2019; Yan, 2019; Alvarez-Quilon et al., 2020). Furthermore, APE2 has been implicated in development and growth as well as cancer etiology. A prior study has shown that APE2-knock out (KO) mice are viable but display growth retardation (Ide et al., 2004). Accumulating evidence has shown genomic alterations and abnormal expression of APE2 expression in multiple cancer tissues, including pancreatic cancer and multiple myeloma (MM), and APE2 is proposed to function as an oncogene in liver cancer (Kumar et al., 2018; Jensen et al., 2020; Zheng et al., 2020). Although the underlying molecular mechanism remains to be determined, recent genetic screens identified APE2 as a synthetic lethal target in BRCA1- or BRCA2-deficient human colon cancer cell line DLD-1, human ovarian cancer cell line PEO1, or engineered human epithelial cell line RPE1-hTERT under unperturbed conditions (Mengwasser et al., 2019; Alvarez-Quilon et al., 2020). It has been demonstrated in recent series of studies using *Xenopus* egg extracts that APE2 is critical for the ATR-Chk1 DDR pathway in response to oxidative DNA damage and defined SSB structures (Willis et al., 2013; Wallace et al., 2017; Lin et al., 2018). Mechanistically, APE2 is recruited to oxidative stress-derived SSB sites or defined SSB structures for a distinct 3′-5′ SSB end resection via its 3′-5′ exonuclease activity, leading to RPA-ssDNA, assembly of the ATR DDR complex including ATR, ATRIP, TopBP1, and the 9-1-1 complex, and activation of the ATR DDR pathway (Willis et al., 2013; Wallace et al., 2017; Hossain et al., 2018; Lin et al., 2018). Moreover, APE2 recruitment and activation require its interaction with ssDNA via its C-terminal Zf-GRF motif and two modes of association with PCNA via its Zf-GRF motif and PCNA-Interacting Protein box (PIP) (Wallace et al., 2017; Lin et al., 2018). APE2 directly associates with and brings Chk1 to the activated ATR for phosphorylation (Willis et al., 2013). However, it remains largely unknown whether and how APE2 regulates the ATR DDR pathway in response to different stressful conditions in mammalian cells.

With a ∼9% 5-year survival rate for all stages combined, pancreatic cancer ranks the fourth most common form of cancer-related deaths in the United States, with nearly 57,600 estimated new cases and over 55,000 estimated deaths in 2020 (Siegel et al., 2020). Although GEM has been the standard treatment of pancreatic cancer, the clinical effect of GEM monotherapy remains limited such as low overall survival months and efficacy (Merl et al., 2010). In contrast, new therapy regimen such as a modified FOLFIRINOX regimen (a combination of fluorouracil, leucovorin, irinotecan, and oxaliplatin) as an adjuvant therapy after surgical resection of pancreatic cancer is still developing

(Conroy et al., 2018). A combination of GEM with radiotherapy or other chemotherapy drugs such as ATR inhibitor AZD6738 shows great promise in pancreatic cancer regression (Wallez et al., 2018). Because targeting ATR has emerged as a new area of research for cancer treatment (Fokas et al., 2012; Karnitz and Zou, 2015; Bradbury et al., 2020), it is reasonable to investigate and explore innovative therapy via targeting the ATR-Chk1 DDR pathway's regulatory mechanisms to increase efficacy and/or reduce the toxicity of chemotherapy drugs in pancreatic cancer treatment.

This study provides evidence using pancreatic cancer cell lines that activation of the ATR-Chk1 DDR pathway induced by hydrogen peroxide ($H_2O_2$), GEM, CPT, and ETO is compromised when APE2 is down-regulated via siRNA. Furthermore, siRNA-mediated APE2-knockdown (KD) leads to a higher percentage of γH2AX-positive cells and micronuclei-positive cells. These results suggest that APE2 is a general regulator of the ATR-Chk1 DDR pathway to maintain genome integrity. In addition, we found that Celastrol, a natural compound derived from thunder god vine *Tripterygium wilfordii* (Lu et al., 2020), impaired APE2 interaction with ssDNA and APE2 3′-5′ exonuclease activity *in vitro* and also compromised the defined SSB-induced ATR-Chk1 DDR pathway in *Xenopus* egg extracts. Notably, the ATR-Chk1 DDR pathway activation induced by $H_2O_2$, GEM, CPT, and ETO in pancreatic cancer cells was compromised by the addition of Celastrol. Cell viability assays demonstrated that APE2 suppression via siRNA-mediated KD or the addition of Celastrol sensitized pancreatic cancers to chemotherapy drugs. Our evidence suggests that APE2 regulates the ATR DDR pathway in pancreatic cancer cells and that targeting the novel function of APE2 in ATR DDR may open a new avenue for future therapeutics in pancreatic cancers.

# MATERIALS AND METHODS

## Cell Culture, Treatments and Cell Lysate Preparation

PANC1 and MiaPaCa2 cells were purchased from ATCC (Cat#CRL-1469 and CRL-1420) and cultured in complete media [DMEM (Corning) supplemented with 10% FBS (Atlanta Biologicals) and 1% penicillin/streptomycin (Gibco)] for PANC1 or completed media with 2.5% Horse Serum (Sigma) for MiaPaCa2, respectively. Cells were treated with $H_2O_2$ (Sigma Cat#HX0635), Gemcitabine (GEM, Sigma Cat#G6423) Camptothecin (CPT, Calbiochem Cat#208925), Etoposide (ETO, Calbiochem Cat#341205), VE-822 (Selleckchem Cat#S7102), KU55933 (EMD Millipore Cat#118500), or Celastrol (Sigma Cat#219465) to the final concentrations and incubated for the times as indicated in the individual experiments. GEM, CTP, ETO, VE-822, KU55933, and Celastrol were dissolved in DMSO and stored at −20°C.

Briefly, cells were washed with phosphate-buffered saline, PBS (Gibco Cat#10010023) and trypsinized (Corning Cat#25-053-CI). The cells were collected by centrifugation and resuspended in ice-cold PBS followed by centrifugation. Cultured cells were lysed with in lysis buffer (20 mM Tris–HCL pH 8.0, 150 mM NaCl, 2 mM EDTA, 0.5% Non-idet P-40, 0.5 mM $Na_3V0_4$, 5 mM NaF, 5 μg/mL of Aprotinin, and 10 μg/mL of Leupeptin). Lysates were centrifugated at 13,000 rpm for 30 min at 4°C. The supernatants were transferred into fresh tubes for measuring protein concentrations via Bradford assays (BIO-RAD Cat#5000205) and subsequent immunoblotting analysis.

## Transfection and siRNA-Mediated APE2-KD Assays

For siRNA experiments, APEX2 siRNA (Dharmacon-HorizonDiscovery ON-TARGETplus Human APE2 siRNA Cat#L-013730-01-0005) or control siRNA (Dharmacon-HorizonDiscovery ON-TARGETplus non-targeting siRNA Cat#D-001810-01-05) was mixed with Lipofectamine$^R$ RNAiMAX (Thermo Fisher Scientific Cat#13778100) in Opti-MEM I Reduced Serum Medium (Gibco Cat#31985070) and incubated for 3–5 days according to the manufacture's protocol. The target sequences of the Dharmacon APE2 siRNA include 5′-GAGCCAUGUGAUGCGUA-3′, 5′-CAACAAUCAAACCCGGGUA-3′, 5′-GGACGAGCUGGAUG CGGAU-3′, and 5′-GAGAAGGAGUUACGGACCU-3′, whereas the non-targeting siRNA sequence is 5′-UGGUUUACAUGUCGACUAA-3′. For the rescue experiments in **Figure 1B** and **Supplementary Figure 1A**, after siRNA-mediated APE2-KD, transfecting control plasmid pcDNA3-YFP (Addgene Cat#13033) or pcDNA3-YFP-xAPE2 with Lipofectamine 2000 (Thermo Fisher Scientific Cat#116680019) in Opti-MEM I Reduced Serum Medium. After different treatment and incubation, cells were imaged via fluorescence microscopy to ensure YFP or YFP-xAPE2 was expressed in cells.

## Immunofluorescence Analysis

Cells were fixed in 3% formaldehyde solution for 15 min at room temperature and permeabilized with 2% Triton-X 100. Cells were then incubated with antibodies again γH2AX (EMD Millipore Cat#05-636-AF488, anti-phospho Histone H2AX Ser139-Alexa Fluor 488 conjugate) or APE2 (GeneTex Cat#GTX80642) overnight at 4°C. For APE2 experiment, goat anti-rabbit IgG H&L-conjugated with Alexa Fluor 594 (Abcam Cat#ab150080) was probed as the secondary antibodies. Then cells were mounted with ProLong Gold Antifade Mountant with DAPI (Invitrogen Cat#36941) before immunofluorescence imaging by confocal laser scanning microscope (Olympus FluoView FV1000) or upright fluorescence microscope (Leica DM6 B) analyses.

## Cell Viability Assays

Cell viability assay was carried out to assess percentage of viable cells via CellTiter-GLO 2.0 assays (in experiments in **Figures 2B,E**, and **Supplementary Figure 4G**) or MTT (Thiazolyl blue tetrazolium bromide) assays (other cell viability assay experiments). We performed both of the techniques and got similar results by analyzing the raw data of absorbance values (in MTT) or luminescence values (in CellTiter-GLO 2.0) using Microsoft Excel Spreadsheet. Pancreatic cells were

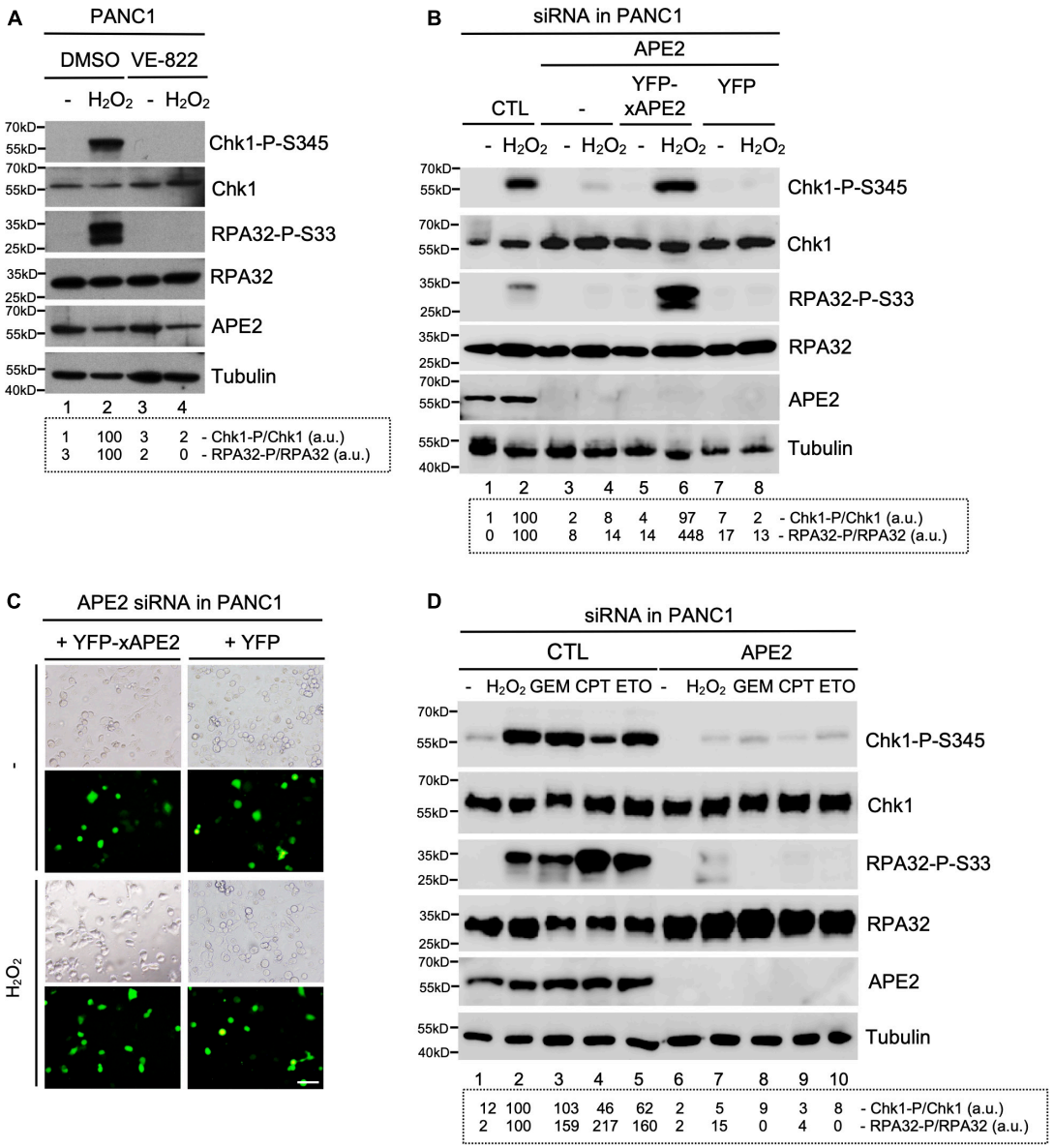


**FIGURE 1 |** APE2 is important for the activation of the ATR-Chk1 DDR pathway in pancreatic cancer cells. **(A)** After 1-h pretreatment of VE-822 (5 μM), PANC1 cells were added with or without $H_2O_2$ (1 mM) for 4 h. Cell lysates were examined via immunoblotting analysis as indicated. **(B)** Transfecting YFP-xAPE2 but not YFP can rescue the Chk1 and RPA32 phosphorylation induced by $H_2O_2$ in APE2-KD PANC1 cells. The ATR-Chk1 DDR pathway analysis of cell lysates from different samples were examined via immunoblotting as indicated. **(C)** Fluorescence microscopy analysis shows that YFP-xAPE2 or YFP was expressed similarly in APE2-KD PANC1 cells with or without treatment of $H_2O_2$. Scale bar, 100 μm. **(D)** The ATR DDR signaling in cell lysates of PANC1 cells with control (CTL) or APE2 siRNAs after treatment of various DNA damaging condition was examined via immunoblotting analysis as indicated. Cells were treated with $H_2O_2$ (1 mM), GEM (50 μM), CPT (5 μM), or ETO (50 μM) for 4 h. Quantifications of Chk1-P/Chk1 (a.u.) and RPA32-P/RPA32 (a.u.) were shown in a dashed box under the immunoblots. The immunoblotting analysis results are representative from two independent experiments.

seeded at 3,000 cells/well in transparent 96-well plates for MTT assays or Opaque 96-well plates for CellTitreGLO-2.0 assays. After different treatment as indicated in different experiments, cells are incubated for 72 h before cell viability assays. For MTT assays, each well with cells (in 100 μl) was added 20 μl of MTT reagent (5 mg/mL, Acros Organics Cat#158992500) and incubated at 37°C for 3.5 h. After cell medium was removed, 150 μl of MTT solvent (VWR Chemicals, Isopropyl ethanol and 37 M Hydrochloric acid) was added to each well for a 10-min incubation with rocking and a subsequent 5-min incubation without rocking. For CellTiter-GLO assays, 100 μl of CellTiter-GLO 2.0 reagent (Promega Cat#G9241) was added to each well with cells (100 μl) followed by incubation at room temperature for 10 min. MTT (absorbance, abs) and CellTiter-GLO 2.0 (luminescence, lum) values were determined by SpectraMAX iD5 Multiplate Reader

(Thermo Fisher Scientific). The MTT/CellTiter-GLO 2.0 values were calculated based on Percentage (%) = [100 × (sample abs/lum)/(control abs/lum)]. MTT/CellTiter-GLO 2.0 assay analyses using Microsoft Excel and GraphPad PRISM software were performed in triplicates ($n$ = 3). Data are presented as mean ± SD for the error bars and normalized with no treatment group.

## Recombinant DNA, Plasmid DNA, FAM-Labeled DNA Structures, and Recombinant Proteins

pcDNA3-YFP was a gift from Doug Golenbock (Addgene plasmid Cat#13033; http://n2t.net/addgene:13033; RRID:Addgene_13033). Recombinant pcDNA3-YFP-xAPE2 was prepared by subcloning the full-length of xAPE2 into pcDNA3-YFP at EcoR1 and *Xho*I sites. Briefly, the coding region of xAPE2 was amplified by PCR with a forward oligo (5′-GGGGGGAATTCATGAAGATTGTGAGCTGGAACATCAAT G-3′) and a reverse oligo (5′-GGGGGCTCGAGGTCCTCA CATCCAGCTTTTTTGGTGAG-3′). Purified PCR product and pCDNA3-YFP were catalyzed by *Eco*RI (New England Biolabs Cat#R3101) and *Xho*I (New England Biolabs Cat#R0146) and ligated together by T4 DNA ligase (New England Biolabs Cat#m0202). After transformation into DH5alpha *E. coli*, plasmids were prepared via QIAprep Spin Miniprep Kit (QIAGEN Cat#27106) following vendor's protocol. In addition, the control (CTL) plasmid, SSB plasmid, FAM-labeled 70-nt ssDNA, and FAM-labeled 70-bp dsDNA with a gap or nicked structure in **Figure 3** were described previously (Lin et al., 2018, 2019, 2020). The pET32a-hAPE2 was described previously (Tsuchimoto et al., 2001). The expression and purification of recombinant protein GST-xAPE1, GST-Zf-GRF, GST-xAPE2, His-tagged xPCNA, and His-tagged RPA complex in **Figure 3** and **Supplementary Figure 3** has been described recently (Willis et al., 2013; Acevedo et al., 2016; Lin et al., 2018; Lin et al., 2020). The His-tagged human APE2 recombinant protein was expressed and purified as described previously (Tsuchimoto et al., 2001).

## Electrophoretic Mobility Shift Assays

For the Electrophoretic mobility shift assays (EMSA) assays in **Figures 3D,F**, similar method has been described previously (Lin et al., 2018, 2020). Briefly, different concentrations of purified recombinant proteins were incubated with 0.15 μM of FAM-labeled 70-nt ssDNA in EMSA Reaction Buffer (10 mM Tris pH 8.0, 50 mM NaCl, 0.2 mM TCEP, 5% glycerol) with or without Celastrol for 3 h at 4°C. Reaction samples were resolved on TBE native gel and virtualized on a BioRad imager.

## Protein-DNA Interaction Assays and *in vitro* Exonuclease Assay

A similar method for the ssDNA-bead binding assays in **Figures 3C**, 4A was described recently (Lin et al., 2018). The Input and Bead-bound fractions were analyzed via immunoblotting analysis as indicated. Similar methods for the *in vitro* exonuclease assay of APE2 (**Figure 3E**) and APE1 (**Figure 3G**) were described previously (Lin et al., 2018). Briefly, FAM-labeled 70-bp dsDNA with a gap structure (0.5 μM) was incubated with purified recombinant GST or GST-APE2/His-PCNA with different concentrations of Celastrol in Exonuclease Assay Buffer (50 mM HEPES, pH 7.5, 20 mM KCl, 10 mM $MgCl_2$, 2 mM DTT). Similarly, FAM-labeled 70-bp dsDNA with a nick structure (0.5 μM) was incubated with purified recombinant GST or GST-APE1 (4 μM) in Exonuclease Assay Buffer. After 1 h-incubation at 37°C, exonuclease assay reactions were quenched with equal volume of TBE-Urea Sample Buffer and denatured at 95°C for 5 min. Samples were resolved on TBE–urea PAGE and imaged on a BioRad imager.

## Experimental Procedures for *Xenopus* Egg Extracts and the SSB-Induced DDR Pathway Assays

The preparation of *Xenopus* HSS and the similar setup of SSB-induced DDR pathway assays for **Figure 3B** were recently described (Willis et al., 2012; Yan and Willis, 2013; DeStephanis et al., 2015; Cupello et al., 2016; Lin et al., 2018, 2019). Briefly, SSB plasmid or control plasmid was added to the HSS to a final concentration of 75 ng/μL and incubated for 30 min at room temperature. Then the samples were examined via immunoblotting analysis.

## Immunoblotting Analysis and Antibodies

Immunoblotting analysis of cell lysates or *Xenopus* egg extracts was carried out similarly as we described previously (Willis et al., 2013; Wallace et al., 2017; Lin et al., 2018, 2020). Primary antibodies against Chk1 (Santa Cruz Biotechnology Cat#sc-8408), Chk1 phosphorylation Ser345 (Cell Signaling Technology Cat#133D3), RPA32 (Thermo Fisher Scientific Cat#MA1-26418), RPA32 phosphorylation Ser33 (Bethyl Laboratories Cat#A300-246A), and Tubulin (Santa Cruz Biotechnology Cat#sc-8035) were purchased from various vendors. Anti-human APE2 antibodies were prepared as described previously (Tsuchimoto et al., 2001).

## Quantification and Statistical Analyses

Intensity of immunoblotting bands such as Chk1-P-S345, Chk1, RPA32-P-S33, and RPA32 was quantified using Image J in **Figures 1**, **4** and **Supplementary Figure 1**. Chk1-P/Chk1 (a.u. indicates arbitrary units) and RPA32-P/RPA32 (a.u.) were calculated when intensity of Chk1-P-S345 or RPA32-P-S33 is normalized to that of Chk1 or RPA32, respectively. Chk1-P/Chk1 (a.u.) and RPA32-P/RPA32 (a.u.) after treatment of hydrogen peroxide were set as 100 a.u. The quantification of γH2AX-positive cells in **Figures 5B,C**, **Supplementary Figures 2B,D** was carried out by eye scoring from three different images for the average percentages and standard deviations. GraphPad PRISM 8 statistical analysis software was used to perform statistical analysis of in **Figures 5B,C,E**, **Supplementary Figures 1D,E,2B,D,F**. Data were presented as mean ± SD from three experiments. A paired two-sided $t$-test was conducted to determine significance of difference.

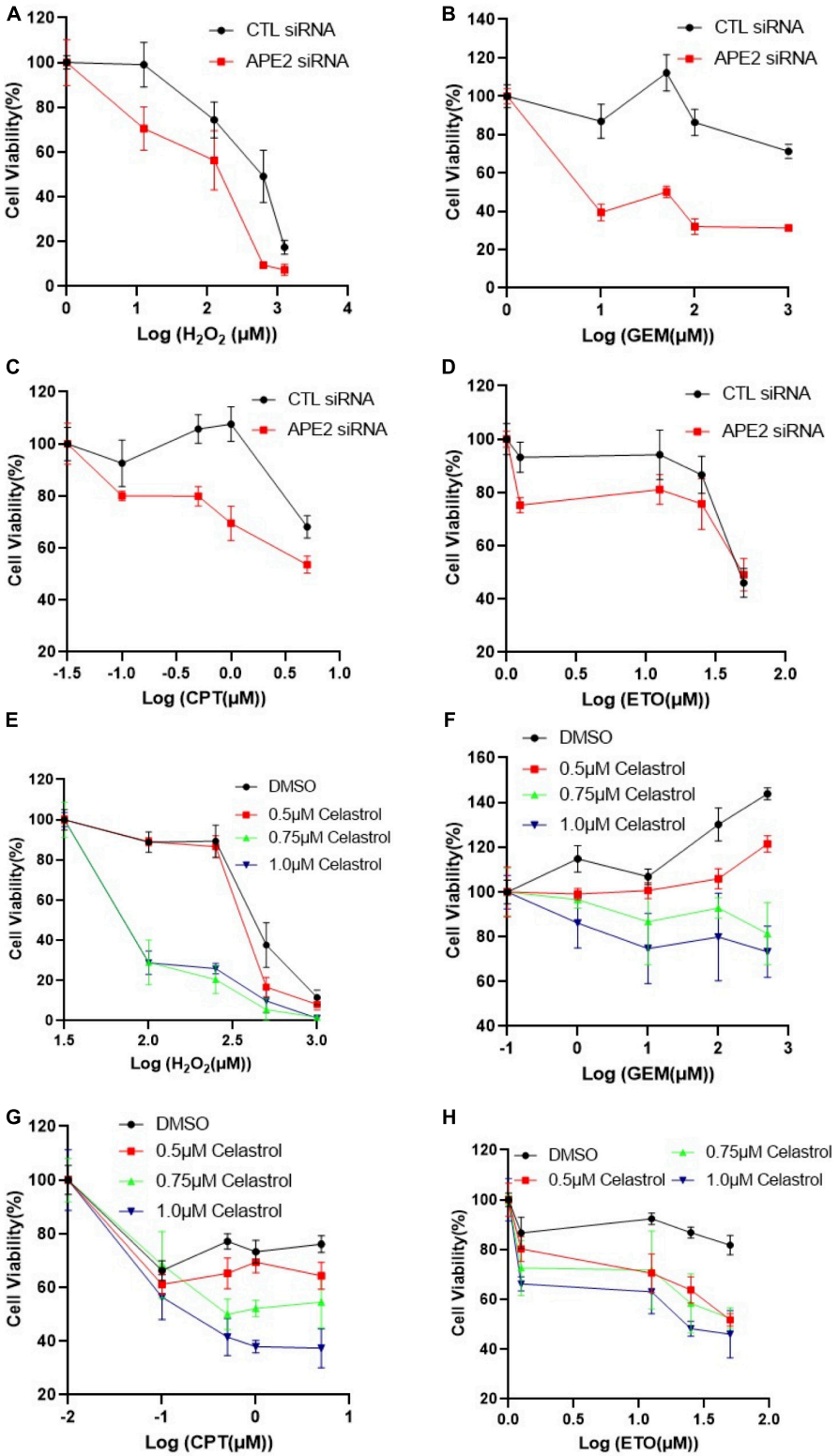


**FIGURE 2 |** APE2 suppression or Celastrol sensitizes PANC1 cells to chemotherapy drugs. **(A–D)** Cell viability assays show that APE2-KD PANC1 cells are more vulnerable to stress conditions [$H_2O_2$ **(A)**, GEM **(B)**, CPT **(C)**, or ETO **(D)**] than Control (CTL) siRNA transfected cells. **(E–H)** Cell viability assays demonstrate that Celastrol (0.5, 0.75, or 1 μM) sensitizes PANC1 cells to $H_2O_2$ **(E)**, GEM **(F)**, CPT **(G)**, or ETO **(H)**. After different treatment as indicated, cells were incubated for 72 h before cell viability assays via CellTiter-GLO method **(B,E)** or MTT method (other experiments).

$p < 0.05$ is considered significant and $p < 0.01$ is considered highly significant.

# RESULTS

## APE2 Is Important for the ATR-Chk1 DDR Pathway in Different Stressful Conditions in Pancreatic Cancer Cells

Our series of studies using *Xenopus* egg extracts have demonstrated that APE2 is important for the ATR DDR pathway in oxidative stress (Willis et al., 2013; Wallace et al., 2017). To determine the role of APE2 in the ATR DDR pathway in pancreatic cancer cells, we first established that $H_2O_2$ triggered Chk1 and RPA32 phosphorylation in human pancreatic cancer PANC1 cells and that ATR-specific inhibitor VE-822 prevented $H_2O_2$-induced Chk1 and RPA32 phosphorylation (**Figure 1A**). Notably, the $H_2O_2$-induced Chk1 phosphorylation and RPA32 phosphorylation were compromised in siRNA-mediated APE2-KD cells compared with control (CTL) siRNA cells (Lane 2 vs. Lane 4, **Figure 1B**). To validate the phenotype of oxidative stress-induced ATR DDR pathway is due to APE2 reduction, we performed complementation assays by transfecting recombinant plasmid of full-length *Xenopus* APE2 tagged with YFP (YFP-xAPE2) or control plasmid of YFP in APE2-KD PANC1 cells (Lane 5–8, **Figure 1B**). Due to the sequence difference between *Xenopus* APE2 and human APE2 in the four targeting regions of APE2-siRNA, YFP-xAPE2 cannot be targeted for protein reduction by APE2-siRNA. Using this siRNA-resistant YFP-xAPE2 approach, we showed that YFP-xAPE2 but not YFP rescued the $H_2O_2$-induced Chk1 and RPA32 phosphorylation in APE2-KD PANC1 cells (Lane 4, 6, and 8, **Figure 1B**). Because anti-human APE2 antibodies do not detect *Xenopus* APE2 protein and anti-*Xenopus* APE2 antibodies do not recognize human APE2 protein, it is a technical difficulty to directly detect and compare endogenous human APE2 and ectopically expressed YFP-xAPE2 via immunoblotting analysis in our rescue experiment. Our control experiment showed that the expression of YFP-xAPE2 and YFP was similar in APE2-KD PANC1 cells regardless of $H_2O_2$ treatment (**Figure 1C**). These observations suggest that APE2 is critical for the ATR-Chk1 DDR pathway in oxidative stress in PANC1 cells. To exclude the possible cell-specific role of APE2 in the ATR DDR pathway, we performed similar experiments in another human pancreatic cancer MiaPaCa2 cells and found that APE2 was also important for the $H_2O_2$-induced ATR-Chk1 DDR pathway in MiaPaCa2 cells (**Supplementary Figures 1A,B**). Thus, the above findings demonstrate the important role of APE2 in the ATR-Chk1 DDR pathway following oxidative stress in human pancreatic cancer cells.

To test whether APE2 is a general regulator in the activation of the ATR-Chk1 DDR pathway, we investigated other stressful conditions such as GEM-induced stalled DNA replication forks and CPT/ETO-induced DSBs. Consistent with the ATR DDR pathway by $H_2O_2$-induced oxidative stress, Chk1 and RPA32 phosphorylation was triggered by GEM, CPT, or ETO in PANC1 cells with the treatment of CTL-siRNA but not APE2-siRNA, suggesting that APE2 plays an important role in ATR DDR under various stressful conditions in PANC1 cells (**Figure 1D**). We also noted similar findings of APE2 in the regulation of the ATR-Chk1 DDR pathway under these different stressful conditions in MiaPaCa2 cells (**Supplementary Figure 1C**). Our control experiments demonstrated that cell viability under unstressed conditions was reduced ∼25–30% in APE2-siRNA cells compared with CTL-siRNA cells in PANC1 and MiaPaCa2 (**Supplementary Figures 1D,E**), which is consistent with previous finding that APE2-knockout in mice leads to abnormal cell proliferation and cell cycle progression (Ide et al., 2004). Overall, our observations suggest that APE2 regulates the ATR DDR pathway in response to different stressful conditions in human pancreatic cancer cells.

## APE2-KD by siRNA Leads to Severe DNA Damage and More Micronuclei in Pancreatic Cancer Cells

To determine the role of APE2 in protecting cells from various stressful conditions, we chose to measure γH2AX status in pancreatic cancer cells under normal or damaging environments (e.g., treatment of $H_2O_2$, GEM, CPT, or ETO). Our fluorescence microscopy analysis shows that the percentage of γH2AX-positive cells in APE2-KD PANC1 cells was higher than that in CTL-siRNA PANC1 cells regardless of the treatment of $H_2O_2$ or GEM (**Figures 5A,B**). We also noted similar observations from the treatment of CPT or ETO (**Figure 5C**). Similarly, we found that APE2-KD by siRNA led to severe γH2AX under normal conditions or after treatment of $H_2O_2$, CPT, or ETO in MiaPaCa2 cells (**Supplementary Figures 2A–D**). These observations suggest that APE2 may protect pancreatic cancer cells from DNA damage such as SSBs and DSBs derived from both endogenous and exogenous sources.

A recent study has shown the critical function of APE2 in the regulation of homologous recombination (HR)-mediated DSB repair in MM (Kumar et al., 2018). Micronuclei, a common feature of chromosome instability, are formed due to mitotic errors that mis-segregate intact chromosomes, errors in DNA replication, or repair defects that generate acentric chromosome fragments (Terradas et al., 2010; Guo et al., 2021). To further validate the critical role of APE2 in DSB repair, we examined the micronuclei formation in pancreatic cancer cells under normal or DSB-generating conditions. Our microscopy analysis demonstrated that more percentage of micronuclei-positive cells were observed in APE2-KD PANC1 cells regardless of the treatment of CPT or ETO (**Figures 5D–E**). We also observed similar results on the role of APE2 in micronuclei formation in MiaPaCa2 cells (**Supplementary Figures 2E–F**). These observations of severe γH2AX and micronuclei formation in APE2-KD cells suggest the important functions of APE2 in resolving the stressful environments, consistent with its role in DNA repair of DSBs and SSBs (Kumar et al., 2018; Cupello et al., 2019).

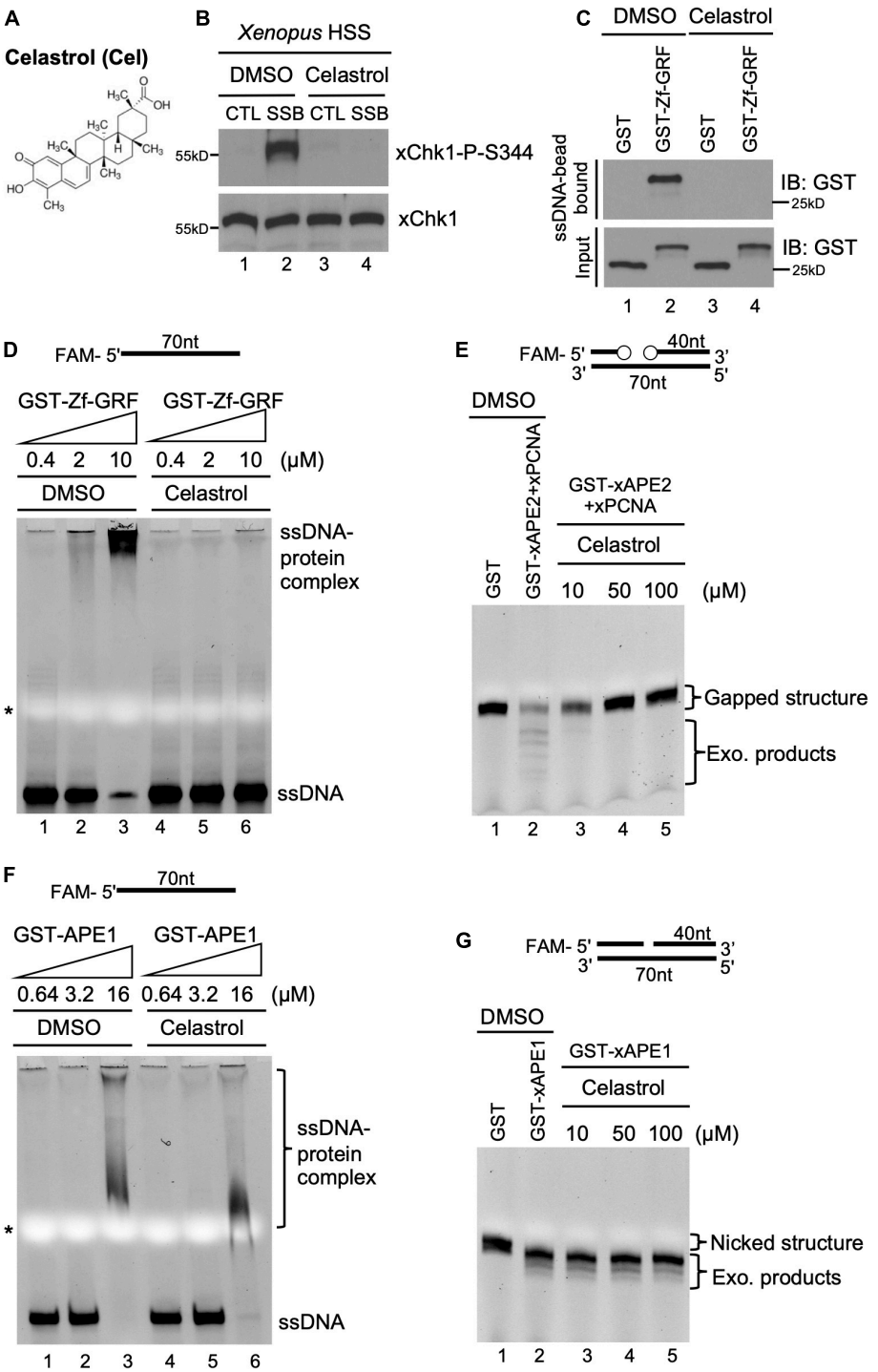


**FIGURE 3 |** A small molecule inhibitor Celastrol impairs APE2 function in the SSB-induced ATR DDR pathway in the *Xenopus* system. **(A)** Chemical structure of a small molecule inhibitor compound Celastrol. **(B)** Celastrol (1 mM) compromises Chk1 phosphorylation induced by SSB plasmid but not CTL plasmid in the *Xenopus* HSS system via immunoblotting analysis. **(C)** The binding of recombinant GST-Zf-GRF but not GST to Dynabead coupled with ssDNA was impaired by Celastrol in GST-pulldown assays. **(D)** The binding of GST-Zf-GRF to ssDNA was impaired by Celastrol in EMSA assays. **(E)** The PCNA-stimulated 3′-5′ exonuclease activity of xAPE2 on a gapped DNA structure *in vitro* was inhibited by Celastrol in TBE-Urea gel electrophoresis. **(F)** EMSA assays show that Celastrol almost had no effect on the binding of GST-xAPE1 to 70nt-ssDNA *in vitro*. **(G)** Celastrol was dispensable for the 3′-5′ exonuclease activity of GST-xAPE1 on a nicked DNA structure in TBE-Urea gel electrophoresis *in vitro*.

## Function of APE2 in the SSB-Induced ATR DDR Pathway Is Compromised by a Distinct APE2 Inhibitor Celastrol in *Xenopus* Egg Extracts

To potentially translate the basic mechanisms of APE2 function in the DDR pathway into future cancer therapy, we sought to identify small molecule inhibitors of APE2 functions. From an unbiased screen of 9,195 compounds, four small-molecule compounds (Dihydrocelastryl, Anthothecol, Erysolin, and MARPIN) were identified to selectively inhibit Chk1 phosphorylation induced by stalled DNA replication forks in p53-deficient cells (Kawasumi et al., 2014). However, the underlying mechanism of how these identified compounds inhibit Chk1 phosphorylation directly or indirectly remains unclear. Dihydrocelastryl is structurally similar to Celastrol, which is a natural compound derived from *thunder god vine* and has been implicated in therapies for cancers such as pancreatic cancer and prostate cancer as an HSP90 modulator and/or proteasome inhibitor (**Figure 3A**; Hieronymus et al., 2006; Zhang et al., 2008). We recently characterized the requirement of APE2 in the ATR-Chk1 DDR pathway activation in response to defined SSB structures in the *Xenopus* high-speed supernatant (HSS) system (Willis et al., 2012; Cupello et al., 2016; Lin et al., 2018, 2019). First, we intended to test whether Celastrol affects the SSB-induced ATR-Chk1 DDR pathway. As expected, Chk1 phosphorylation was induced by defined SSB plasmid but not control (CTL) plasmid in the *Xenopus* HSS system. Importantly, the SSB-induced Chk1 phosphorylation in the HSS system was compromised by the addition of Celastrol (**Figure 3B**).

Next, we sought to elucidate how Celastrol regulates the ATR-Chk1 DDR pathway. Due to the significance of the C-terminal Zf-GRF motif of APE2 in the SSB-induced ATR DDR pathway, we tested whether Celastrol affects the binding of APE2 Zf-GRF motif to ssDNA. Our GST-pulldown experiments show that GST-Zf-GRF but not GST associated the beads coupled with ssDNA (**Figure 3C**), consistent with the APE2 Zf-GRF-ssDNA interaction from previous studies (Wallace et al., 2017; Lin et al., 2018). Notably, the binding of GST-Zf-GRF to ssDNA was compromised by Celastrol (**Figure 3C**). Furthermore, EMSA assays demonstrated that GST-Zf-GRF but not GST associated with 70-nt ssDNA in a dose-dependent manner *in vitro* (**Supplementary Figure 3A**), and that such Zf-GRF-ssDNA association was compromised by Celastrol (**Figure 3D**). To determine the potential role of Celastrol in the regulation of APE2 functions, we turned to the PCNA-mediated APE2 exonuclease activity (**Figure 3E**; Burkovics et al., 2009; Lin et al., 2018). Notably, Celastrol impaired the 3′-5′ end resection of dsDNA with a gapped structure by recombinant *Xenopus* APE2 and PCNA in a dose-dependent manner *in vitro* exonuclease assays, suggesting that APE2 3′-5′ exonuclease activity is inhibited by Celastrol (**Figure 3E**).

To test the specificity of the negative regulation of Celastrol in APE2 Zf-GRF binding to ssDNA and its exonuclease activity, we performed a couple of control experiments. RPA protein complex includes RPA14, RPA32, and RPA70 and has been demonstrated to preferentially associate with ssDNA (Marechal and Zou, 2015; Acevedo et al., 2016). Our EMSA assays showed that Celastrol had almost no effect on the binding of recombinant His-tagged RPA complex to a 70nt-ssDNA (**Supplementary Figure 3B**). Despite some structure and function similarities, APE1 and APE2 display distinct exonuclease and AP endonuclease activities (Li and Wilson, 2014; Lin et al., 2021). Our EMSA assays demonstrated almost no difference on the association of GST-APE1 with a 70nt-ssDNA by Celastrol in comparison to DMSO (**Figure 3F**). Furthermore, Celastrol had almost no noticeable effect on the 3′-5′ SSB end resection of dsDNA with a nicked structure by recombinant GST-xAPE1 *in vitro* exonuclease assays (**Figure 3G**). Overall, our data suggest that Celastrol is a previously uncharacterized small molecule inhibitor of APE2 for its function in SSB end resection and SSB signaling pathway in the *Xenopus* system.

## Celastrol Impairs the ATR-Chk1 DDR Pathway in Pancreatic Cancer Cells

Next, we tested whether Celastrol affects the ATR-Chk1 DDR pathway in human pancreatic cancer cells. First, we found that the binding of recombinant human APE2 protein to ssDNA was also compromised by Celastrol (**Figure 4A**), suggesting that Celastrol may also affect APE2 functions in human cells. Second, we examined the role of Celastrol for cell viability after 3 days and found that $IC_{50}$ of Celastrol was ∼3.054 and ∼3.032 μM in PANC1 and MiaPaCa2 cells, respectively (**Figures 4B,C**). Notably, Chk1 phosphorylation and RPA32 phosphorylation induced by $H_2O_2$, GEM, CPT, or ETO were impaired by 1-h pretreatment of Celastrol (2.5 μM) in PANC1 and MiaPaCa2 cells (**Figures 4D,E**). Our data here support the role of Celastrol in the suppression of the ATR-Chk1 DDR pathway under stress conditions via inhibiting APE2 in human pancreatic cancer cells.

## APE2-KD by siRNA or APE2 Inhibition by Celastrol Sensitizes Pancreatic Cancer Cells to Chemotherapy Drugs

Previous studies show that ATR inhibitor VE-822 sensitizes cancer cells to radiation or chemotherapy drugs such as CPT (Fokas et al., 2012; Josse et al., 2014), and that Chk1-KD by siRNA or Chk1 inhibition by small molecule inhibitor AZD7762 has been shown to function in a synthetically lethal manner with GEM in pancreatic cancers (Venkatesha et al., 2012). Our findings on APE2 in the ATR-Chk1 DDR pathway in both the *Xenopus* system and pancreatic cancer cells prompt us to target the function and regulatory mechanism of APE2 in the ATR DDR pathway for cancer therapy. To directly test whether targeting APE2 functions may sensitize cancer cells to chemotherapy drugs, we took advantage of two strategies developed in this study: APE2 suppression by siRNA-mediated knockdown and APE2 inhibitor Celastrol. Notably, cell viability assays showed that APE2-KD PANC1 cells were more sensitive to $H_2O_2$, GEM, CPT, or ETO than CTL-KD PANC1 cells, suggesting that APE2 suppression sensitizes PANC1 cells to DNA damaging conditions (**Figures 2A–D**). Similarly, APE2 inhibition by Celastrol also sensitized PANC1 cells to $H_2O_2$-induced oxidative stress and

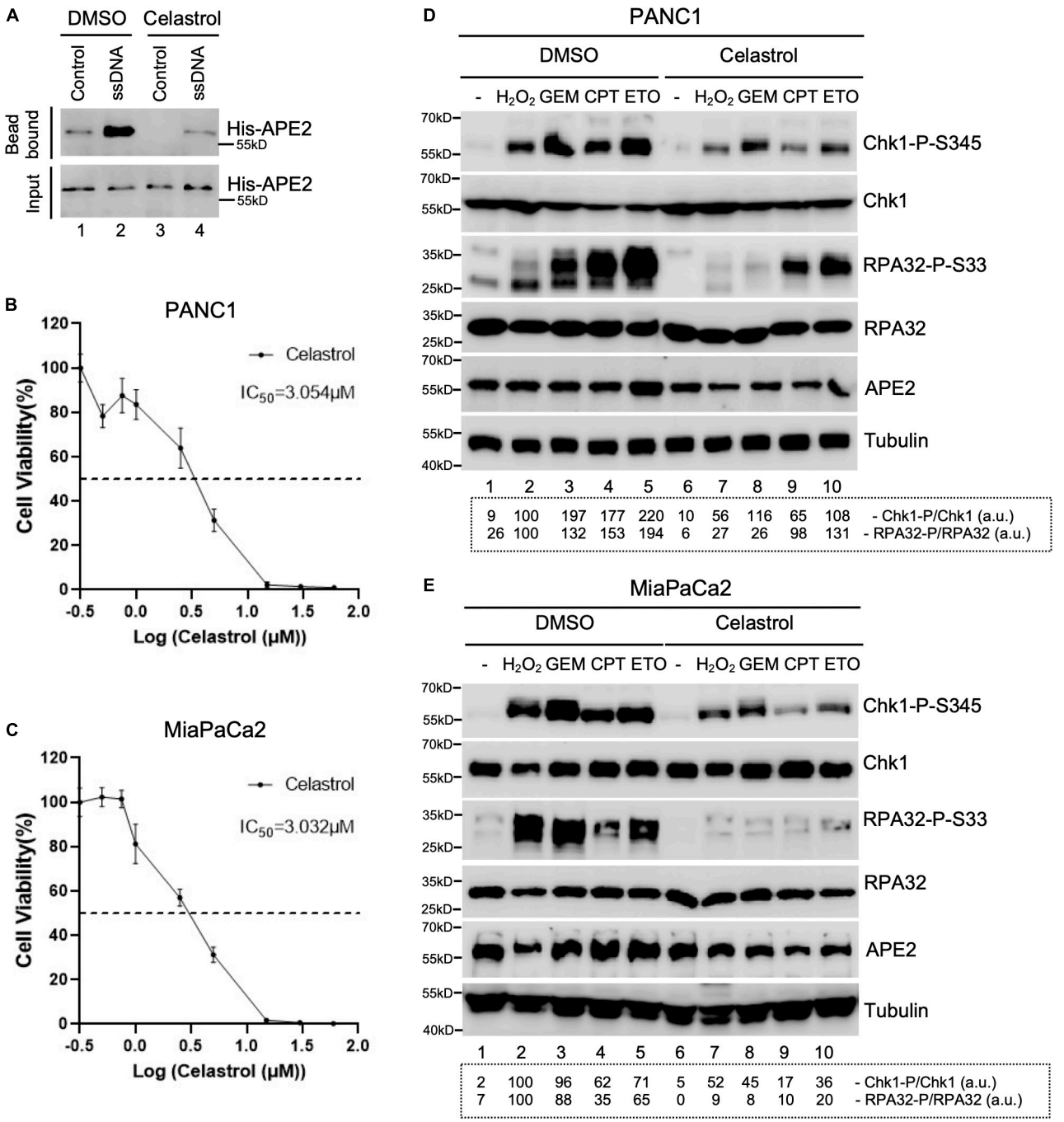


**FIGURE 4 |** Celastrol compromises the ATR-Chk1 DDR pathway activation in pancreatic cancer cells. **(A)** The binding of recombinant His-tagged human APE2 protein to beads coupled with ssDNA was compromised by the addition of Celastrol (100 ng/μl). **(B,C)** Cell viability assays show the toxicity of Celastrol in PANC1 **(B)** or MiaPaCa2 **(C)** cells after 3-day treatment. **(D,E)** PANC1 **(D)** or MiaPaCa2 **(E)** cells were pretreated with Celastrol (2.5 μM) for 1 h followed by 4-h treatment of $H_2O_2$ (1 mM), GEM (50 μM), CPT (5 μM), or ETO (50 μM), respectively. Cell lysates were then extracted and examined via immunoblotting analysis as indicated. Quantifications of Chk1-P/Chk1 (a.u.) and RPA32-P/RPA32 (a.u.) were shown in a dashed box under the immunoblots. The immunoblotting analysis results are representative from two independent experiments.

chemotherapy drugs GEM, CPT, and ETO in a dose-dependent manner (0.5, 0.75, and 1 μM) (**Figures 2E–H**). Similarly, APE2 suppression by siRNA-mediated reduction or Celastrol-mediated inhibition also sensitized MiaPaCa2 cells to oxidative stress or chemotherapy drugs to some extent (**Supplementary Figures 4A–H**). These observations suggest that pancreatic cancer cells may need APE2-mediated ATR DDR pathway and DNA repair mechanisms to protect from various different

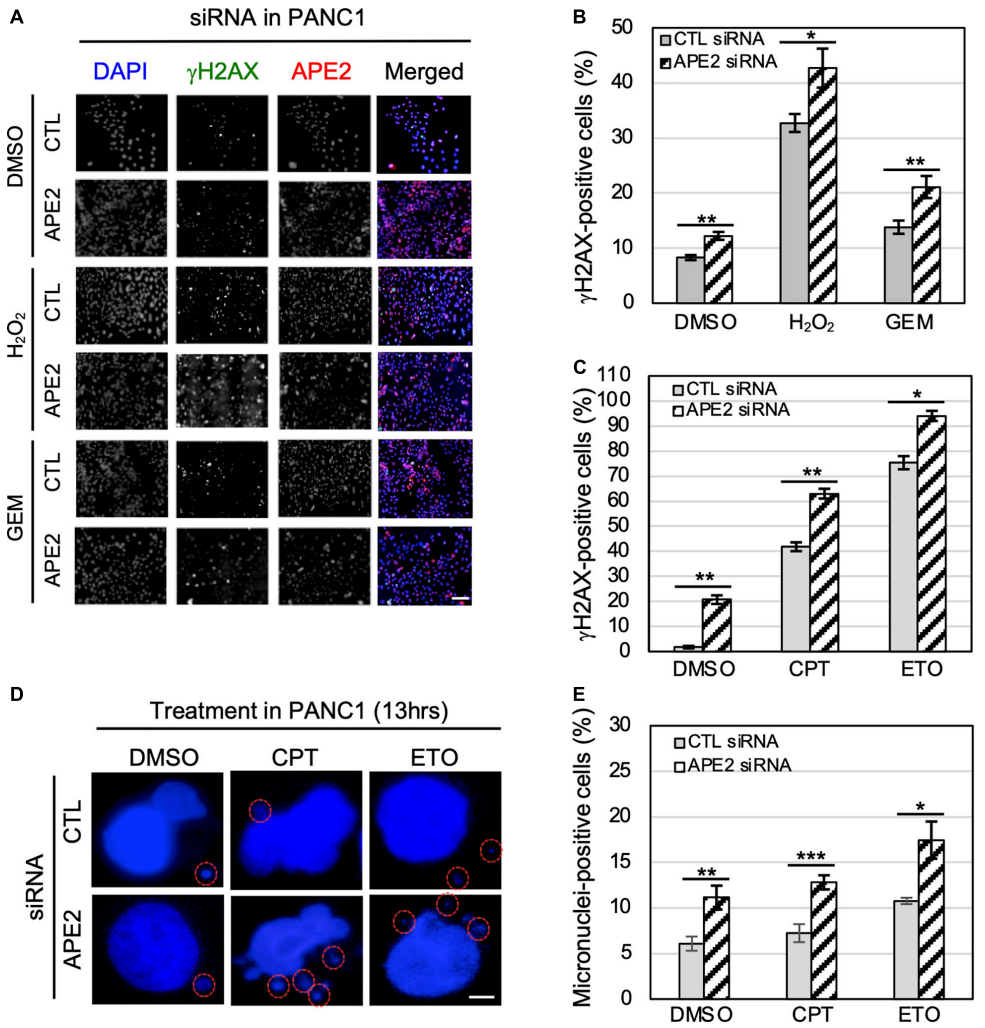


**FIGURE 5 |** APE2-KD induces substantially more γH2AX foci and micronuclei under normal or stress conditions in PANC1 cells. **(A)** Immunofluorescence microscopy analysis shows γH2AX and APE2 foci after DMSO or treatment of $H_2O_2$ (1 mM for 5 h) or GEM (100 μM for 5 h) in PANC1 cells with CTL or APE2 siRNA in a slide view. Scale bar, 100 μm. **(B,C)** Percentage of γH2AX-positive PANC1 cells after treatment of $H_2O_2$/GEM or CPT/ETO. **(D)** Microscopy analysis shows micronuclei (circled with red) after DAPI staining in PANC1 cells after treatment of CPT (1 μM for 13 h) or ETO (20 μM for 13 h) with CTL or APE2 siRNA. Scale bar, 5 μm. **(E)** Percentage of micronuclei-positive PANC1 cells after treatment of CPT or ETO with CTL or APE2 siRNA was quantified. **(B,C,E)*** indicates $p < 0.05$; ** indicates $p < 0.01$; *** indicates $p < 0.001$; $n = 3$.

stressful conditions including chemotherapy drugs, replication stress or oxidative stress.

# DISCUSSION

## Role of APE2 in the DNA Damage Response

Accumulating evidence suggests that APE2 plays various critical roles in maintaining genome and epigenome integrity (Lin et al., 2021). However, it remains unclear whether APE2 is required for the ATR DDR pathway in mammalian cells. This study demonstrated that APE2 is important for the ATR-Chk1 DDR pathway in response to different stress conditions including oxidative stress, DNA replication stress, and DSBs in pancreatic cancer cells (**Figure 1** and **Supplementary Figure 1**). Fluorescence microscopy analysis shows that APE2-KD by siRNA leads to a higher percentage of γH2AX and more micronuclei under normal or stress conditions in pancreatic cancer cells (**Figure 5** and **Supplementary Figure 2**). Furthermore, we identified a small molecule Celastrol as the first APE2 inhibitor that prevents the binding of APE2 Zf-GRF to ssDNA, APE2's 3′-5′ exonuclease activity, and the SSB-induced ATR-Chk1 DDR pathway in the *Xenopus* HSS system (**Figure 3** and **Supplementary Figure 3**). Notably, Celastrol treatment impairs the ATR-Chk1 DDR pathway in pancreatic cancer cells (**Figure 4**). Finally, APE2 suppression by siRNA-mediated knockdown or APE2 inhibition by small molecule inhibitor Celastrol can sensitize pancreatic cancer cells to chemotherapy drugs including GEM, CPT, and ETO (**Figure 2**

and **Supplementary Figure 4**). These observations from this study indicate the important role of APE2 in the DNA damage response to maintain genome integrity in mammalian cells. Here, we propose a working model how APE2 especially its exonuclease activity contributes to genome stability in pancreatic cancer cells: (**I**) in APE2-proficient cells, APE2 may process oxidative DNA damage, DSBs, and stalled forks to generate longer region of ssDNA coated with RPA for ATR DDR activation, leading to Chk1 phosphorylation and RPA32 phosphorylation; and (**II**) in APE2-deficient cells, siRNA-mediated APE2-KD or Celastrol-mediated APE2 inhibition (e.g., via ssDNA interaction and exonuclease activity) results in defects of RPA-ssDNA formation and ATR DDR activation, leading to more DNA damage, increased micronuclei, and decreased cell viability (**Figure 6**).

Previous studies have demonstrated that APE2 is required for the ATR DDR pathway in response to oxidative stress and defined SSB structures in *Xenopus* egg extracts (Willis et al., 2013; Wallace et al., 2017; Lin et al., 2018). Our observations in this study support the important role of APE2 in the ATR-Chk1 DDR pathway in response to hydrogen peroxide-induced oxidative stress, GEM-induced DNA replication stress and CPT/ETO-induced DSBs in human pancreatic cancer cell. These studies collectively support the upstream role of APE2 in the ATR DDR pathway during evolution, although future studies are needed to directly test whether the role of APE2 in the ATR DDR pathway is conserved in other cell types or under other DNA damaging conditions. It is noted that a recent genome-wide CRIPR/Cas9 screen identified APE2 as one of the 117 genes whose mutation leads to hypersensitivity to ATR inhibitors (Hustedt et al., 2019). Although different cell lines and experimental approaches may partially explain the discrepancy with the findings in this study, it is also possible that APE2 contributes to genome integrity via multiple mechanisms in addition to the ATR DDR pathway. Consistent with this speculation, it has been reported that APE2 is important for the HR-mediated DSB repair in MM cells (Kumar et al., 2018). It is interesting to test whether targeting APE2 via small molecule inhibitor such as Celastrol can sensitize cancer cells to ATR inhibitors.

## Role of APE2 in the Maintenance of Genome Integrity

What are the phenotypes of APE2-KD? A prior APE2-knockout (KO) mice study demonstrated that the S and G2/M phases of the cell cycle were significantly increased in APE2-KO thymocytes compared with the wild type (Ide et al., 2004). Similarly, the G2/M phase was arrested in proliferating but not unstimulated APE2-KO splenocytes compared with the wild type (Ide et al., 2004). Consistent with these cell cycle phenotypes of APE2-KO, expression of 74 cell cycle related genes was altered in APE2-KO thymus (Dan et al., 2008). Although exact underlying mechanisms of APE2 in cell cycle regulation need further investigation, an independent group recently reported that APE2 is positively correlated with cell cycle and MYC pathway, and that APE2-KD can suppress CCNB1 and MYC expression likely at the transcription level (Zheng et al., 2020).

Our data demonstrate the critical function of APE2 in the protection of pancreatic cancer cells from DNA damaging conditions (**Figure 5**). Previous studies have shown that APE2 is critical for the SSB repair pathway in *Xenopus* egg extracts, and HR-mediated DSB repair pathway in MM cells (Kumar et al., 2018; Cupello et al., 2019). A recent CRISPR/Cas9-mediated genetic screen identified APE2 as a synthetic lethal target of BRCA2 in human colon epithelial cell line DLD-1 cells and human ovarian cancer cells PEO1 cells (Mengwasser et al., 2019). Although the underlying mechanism remains unknown, more γH2AX was observed in APE2-knockout (KO) PEO1 cells under unperturbed condition (Mengwasser et al., 2019). Nonetheless, this study is consistent with our observation of increased γH2AX and micronuclei in APE2-KD PANC1 and MiaPaCa2 cells under unperturbed and stress conditions (**Figure 5** and **Supplementary Figure 2**). Furthermore, the function of APE2 in protecting cells from DNA damage and micronuclei under different stress conditions (**Figure 5**) is in line with its role in SSB repair and DSB repair mechanisms to promote survival in cancer cells. Alternatively, the protection of cancer cells from DNA damaging conditions by APE2 may be mediated from its critical function in the ATR-Chk1 DDR pathway indirectly due to the role of ATR in genome integrity.

## Distinct Role of Celastrol as APE2 Inhibitor

Small molecule inhibitors targeting multi-function protein APE1 in DNA repair and redox signaling (e.g., Methoxyamine, AR03, APE1 inhibitor III, and E3330/APX3330) have been identified and characterized, and E3330/APX3330 as APE1 redox inhibitor has entered and completed Phase I clinical trials in patients with advanced solid tumors (NCT03375086) (Shahda et al., 2019; Caston et al., 2021). However, there is no any specific and/or non-specific small molecule inhibitor targeting APE2 functions from the literature. To the best of our knowledge, Celastrol is the first characterized APE2 inhibitor that impairs APE2's function in the ATR DDR pathway both in the *Xenopus* system and pancreatic cancer cells via negative regulation of ssDNA binding and catalytic function of APE2.

Our recent studies have shown that APE1 and APE2 as well as their exonuclease but not AP endonuclease activity are important for the SSB-induced Chk1 phosphorylation in the *Xenopus* system (Lin et al., 2018, 2020). Our data in this study demonstrate the inhibitory effect of Celastrol on the ssDNA binding of APE2 Zf-GRF, but not APE1 nor RPA (**Figure 3** and **Supplementary Figure 3**). Furthermore, exonuclease activity of APE2 but not APE1 was compromised by Celastrol, which may explain the suppression of SSB-induced Chk1 phosphorylation by Celastrol in the *Xenopus* system (**Figure 3**). More importantly, Celastrol treatment can sensitize pancreatic cancer cells to chemotherapy drugs including GEM, CPT, and ETO, which is similar to the phenotype of APE2-KD cells as expected (**Figure 2** and **Supplementary Figure 4**). Although it is not possible to rule out the possibility that other Celastrol targets other than APE2 may also contribute partially to the decreased cell viability, at least

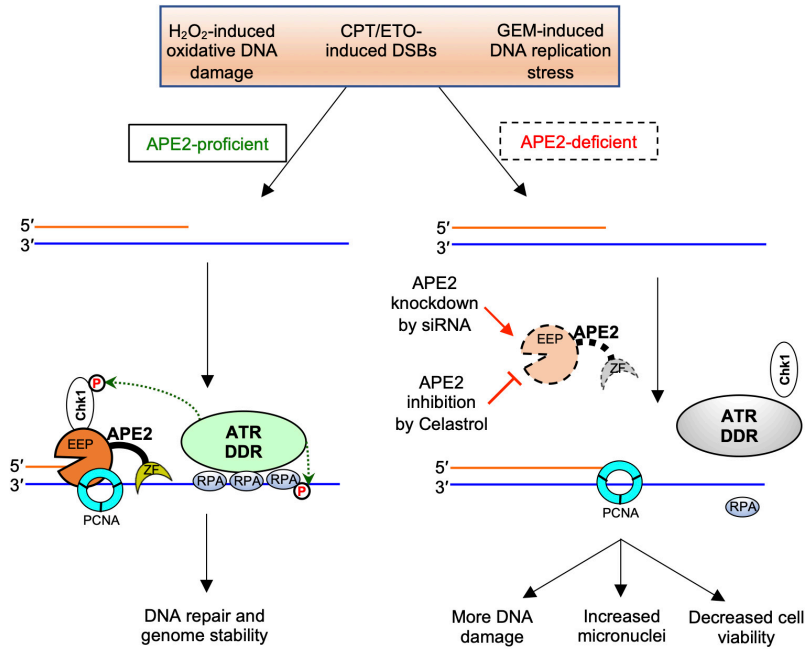


**FIGURE 6 |** A working model of the general regulator function of APE2 in the ATR-Chk1 DDR pathway. EEP, endonuclease/exonuclease/phosphatase; ZF, Zf-GRF motif; DDR, DNA damage response. See text for more details.

the impairment of the ATR DDR pathway via Celastrol-mediated APE2 inhibition is one of the underlying mechanisms.

Although Celastrol exhibits anti-cancer and anti-inflammation activities in previous studies, the translational implication of Celastrol remains limited due to toxicity and narrow therapeutic window as a single agent (Cascao et al., 2017; Chen et al., 2018). Of note, Celastrol (0.5–1 μM) at lower micromolar concentrations than $IC_{50}$ (∼3 μM) can sensitize cancer cells to chemotherapy drugs. Due to the inhibitory effect of Celastrol in the ATR DDR pathway, it will be interesting to test in future studies whether cancer cells with deficiency in ATM or BRCA1/2 are more vulnerable to Celastrol, and whether Celastrol in combination with other small molecules such as PARP1 inhibitors can sensitize cancer cells synergistically. Future follow-up studies are also warranted to identify the possible direct binding site (s) of Celastrol within APE2 and to characterize the APE2 interaction and inhibition by structural approaches. In addition, Celastrol may be further developed and optimized to more specific and efficient APE2 inhibitors in future studies.

## Targeting ATR and Its Regulators in the DNA Damage Response Pathway for Cancer Therapy

Whereas ATR inhibitors with combinations of radiotherapy or chemotherapy have synergistic effects in cancer therapies (Josse et al., 2014; Wallez et al., 2018; Bradbury et al., 2020), regulators/modulators of the ATR-Chk1 DDR pathway have also been targets for cancer therapy. For example, a negative selection RNAi screen from over 10,000 genes in pancreatic cancer BxPC-3 cells identified Rad17, an important regulator of the ATR-Chk1 DDR pathway (Zou et al., 2002; Cimprich and Cortez, 2008), as the most significant synthetic lethal target with GEM treatment, and validation experiments showed that Rad17-KD sensitizes pancreatic cancer cells including BxPC-3, MiaPaCa2, and JoPaca-1 to GEM (Fredebohm et al., 2013). Whereas TopBP1 is a well-established regulator of the ATR-Chk1 DDR pathway (Cimprich and Cortez, 2008; Yan and Michael, 2009), recent studies have demonstrated that TopBP1 promotes prostate cancer progression and that down-regulation of TopBP1 significantly suppressed the proliferation of prostate cancer 22RV1 and LNCaP cells via an apoptosis-mediated mechanism (Li et al., 2020). Rad9-KD via siRNA enhanced sensitivity of breast cancer cell MCF-7 and MDA-MB-231 to doxorubicin that induces DSBs (Yun et al., 2014). Therefore, our findings from this study on the enhanced sensitivity of pancreatic cancer cells to chemotherapy drugs by siRNA-mediated APE2-KD or Celastrol-mediated APE2 inhibition is in with the overall concept that suppressing regulators of the ATR DDR pathway can enhance efficacy of chemotherapies.

## Targeting APE2 in the DNA Damage Response for Future Studies in Cancer Therapy

Does APE2 overexpress in cancer cells compared with normal cells? A pan-cancer analysis from TCGA database and cBioPortal has identified APE2 overexpression at mRNA level in tumor tissues compared with adjacent non-malignant tissues from kidney cancer, breast cancer, lung cancer, liver cancer, and

prostate cancer (Jensen et al., 2020). Similarly, APE2 in the MM patient group was overexpressed at mRNA level in comparison to control group monoclonal gammopathy of undetermined significance (MGUS) (Kumar et al., 2018). Furthermore, APE2 overexpression at protein level was also observed in MM cell lines compared with normal cell lines (Kumar et al., 2018). Another independent bioinformatics analysis validated APE2 overexpression in liver cancer and further demonstrated that APE2-high liver cancer patients had a lower overall survival rate compared with APE2-low liver cancer patients regardless of the cancer stages and the hepatitis infection status (Kumar et al., 2018). Thus, APE2 was suggested as an oncogene in liver cancer and could serve as a potential biomarker for cancer screening in the future.

In addition, APE2 was recently identified as a synthetic lethality target in BRCA1/2-deficient cells from a couple of CRISPR-mediated genetic screens, although the exact underlying mechanism remains to be elucidated (Mengwasser et al., 2019; Alvarez-Quilon et al., 2020). Our finding in this study on the critical role of APE2 in the ATR DDR pathway in pancreatic cancer cells provides vital knowledge for future translational studies targeting APE2 functions in various mice models with different genetic backgrounds such as deficiency of ATM or BRCA1/2. Notably, a recent study has shown that chemotherapy drug cisplatin increases APE2 abundance and provokes mitochondrial fragmentation and acute kidney injury (Hu et al., 2021). Thus, targeting APE2 at its expression level or inhibiting its catalytic function via small molecule inhibitor such as Celastrol will provide additional avenues for cancer therapy. While APE2-KD via siRNA or APE2 inhibition via Celastrol sensitizes PANC1 cells or MiaPaCa2 cells to chemotherapy drugs (**Figure 2** and **Supplementary Figure 4**), future investigation is needed to test whether adding back wild type or various mutant hAPE2 to shRNA-mediated APE2-KD or CRISPR/Cas9-mediated APE2-knockout stable cell lines can rescue the phenotype of APE2 deficiency. Anticipated findings from these experiments are expected to elucidate the exact functional domains of APE2 critical for cancer cells' sensitivity to chemotherapy drugs.

Overall, we have demonstrated the important function of APE2 in the ATR-Chk1 DDR pathway in pancreatic cancer cells, which can be targeted for future combination or synthetic lethality therapies for cancers.

## DATA AVAILABILITY STATEMENT

The original contributions presented in the study are included in the article/**Supplementary Material**, further inquiries can be directed to the corresponding author/s.

## ETHICS STATEMENT

The animal study was reviewed and approved by The Institutional Animal Care and Use Committee (IACUC) at University of North Carolina at Charlotte.

## AUTHOR CONTRIBUTIONS

MAH, YL, and SY designed the experiments. MAH, YL, GD, JL, AM, JM, HZ, and SY performed the experiments. DT and YN provided the critical reagents. MAH, YL, and SY analyzed the data. MAH and SY wrote the manuscript. MAH, YL, GD, DT, YN, JZ, and SY revised the manuscript with input from all authors.

## FUNDING

This Yan lab was supported, in part, by grants from the NIH/NCI (R01CA225637 and R01CA251141), NIH/NIEHS (R21ES032966) and NIH/NIGMS (R15GM114713), and funds from UNC Charlotte. MAH was supported by the Graduate School Summer Fellowship (GSSF) & GASP program at UNC Charlotte. JM was supported by the Diversity Supplements program at the NIH/NCI (R01CA225637).

## ACKNOWLEDGMENTS

We thank Pinku Muhkerjee, Matthew Michael, and Doug Golenbock for reagents. We are grateful for the assistance by Didier Dréau, Christine Richardson, Paola Lopez-Duarte, Donna Goodenow, and David Gray for FACS as well as confocal and fluorescence microscopy analysis.

## SUPPLEMENTARY MATERIAL

The Supplementary Material for this article can be found online at: https://www.frontiersin.org/articles/10.3389/fcell.2021.738502/full#supplementary-material

**Supplementary Figure 1 |** Important function of APE2 in ATR-Chk1 DDR pathway in pancreatic cancer cells. **(A)** MiaPaCa2 cells were treated with CTL siRNA or APE2 siRNA for 7 days. Plasmid expressing YFP-xAPE2 or YFP was transfected to APE2-KD MiaPaCa2 cells after 3 days of siRNA-mediated knockdown. After 4-h treatment of $H_2O_2$ (1 mM), total cell lysates were extracted and analyzed via immunoblotting as indicated. **(B)** Fluorescence microscopy analysis shows that the YFP-xAPE2 and YFP was expressed similarly in APE2-KD MiaPaCa2 cells. Scale bar, 100 μm. **(C)** The ATR DDR signaling in cell lysates of MiaPaCa2 cells with control (CTL) or APE2 siRNAs after treatment of various DNA damaging condition was examined via immunoblotting analysis as indicated. Cells were treated with $H_2O_2$ (1 mM), GEM (50 μM), CPT (5 μM), or ETO (50 μM) for 4 h. **(D,E)** Cell viability assays show cell proliferations after 3 days of APE2 siRNA vs. CTL siRNA transfected PANC1 cells **(D)** or MiaPaCa2 cells **(E)**. * indicates $p < 0.05$; ** indicates $p < 0.01$, $n = 4$.

**Supplementary Figure 2 |** APE2-KD induces substantially more γH2AX and micronuclei in MiaPaCa2 cells. **(A,C)** Immunofluorescence analysis was performed in MiaPaCa2 cells after CTL siRNA or APE2 siRNA with or without treatment of $H_2O_2$ (625 μM for 5 h), CPT (5 μM for 5 h), or ETO (50 μM for 5 h). DAPI, γH2AX, APE2, and merged images from presentative cells were shown in a slide view. Scale bars, 100 μm. **(B,D)** Percentage of γH2AX-positive cells from **(A)** or **(C)** was quantified in **(B)** and **(D)**, respectively. **(E)** Micronuclei formation of MiaPaCa2 after CTL siRNA or APE2 siRNA with or without 5-h treatment of CPT (5 μM) or ETO (50 μM) was examined via microscopy analysis. Red-dotted circles indicated the micronuclei. Scale bar, 5 μm. **(F)** Percentage of micronuclei-positive MiaPaCa2 cells after treatment of CPT or ETO with CTL or APE2 siRNA from **(E)** was quantified. **(B,D,F)** * indicates $p < 0.05$; ** indicates $p < 0.01$; *** indicates $p < 0.001$.

**Supplementary Figure 3 |** *In vitro* EMSA assays. **(A)** EMSA assays show that the binding of GST-Zf-GRF but not GST can form ssDNA (70nt)-protein complex. **(B)** EMSA assays demonstrate that the recombinant His-tagged RPA complex associated with 70nt-ssDNA and that Celastrol had almost no effect on the association of 70nt-ssDNA and RPA complex.

**Supplementary Figure 4 |** APE2-KD or Celastrol sensitized MiaPaCa2 cells to chemotherapy drugs. **(A–D)** Cell viability assays show that APE2-KD MiaPaCa2 cells were more vulnerable to stress conditions ($H_2O_2$, GEM, CPT, or ETO) compared to CTL siRNA transfected cells. **(E–H)** Cell viability assays demonstrate that Celastrol sensitized MiaPaCa2 cells to $H_2O_2$, GEM, CPT, and ETO.

## REFERENCES


Acevedo, J., Yan, S., and Michael, W. M. (2016). Direct Binding to Replication Protein A (RPA)-coated Single-stranded DNA Allows Recruitment of the ATR Activator TopBP1 to Sites of DNA Damage. *J. Biol. Chem.* 291, 13124–13131. doi: 10.1074/jbc.M116.729194

Alvarez-Quilon, A., Wojtaszek, J. L., Mathieu, M. C., Patel, T., Appel, C. D., Hustedt, N., et al. (2020). Endogenous DNA 3′ blocks are vulnerabilities for BRCA1 and BRCA2 deficiency and are reversed by the APE2 nuclease. *Mol. Cell* 78, 1152–1165e1158. doi: 10.1016/j.molcel.2020.05.021

Bradbury, A., Hall, S., Curtin, N., and Drew, Y. (2020). Targeting ATR as Cancer Therapy: A new era for synthetic lethality and synergistic combinations? *Pharmacol. Ther.* 207:107450. doi: 10.1016/j.pharmthera.2019.107450

Burkovics, P., Hajdu, I., Szukacsov, V., Unk, I., and Haracska, L. (2009). Role of PCNA-dependent stimulation of 3′-phosphodiesterase and 3′-5′ exonuclease activities of human Ape2 in repair of oxidative DNA damage. *Nucleic Acids Res.* 37, 4247–4255. doi: 10.1093/nar/gkp357

Burkovics, P., Szukacsov, V., Unk, I., and Haracska, L. (2006). Human Ape2 protein has a 3′-5′ exonuclease activity that acts preferentially on mismatched base pairs. *Nucleic Acids Res.* 34, 2508–2515. doi: 10.1093/nar/gkl259

Byun, T. S., Pacek, M., Yee, M. C., Walter, J. C., and Cimprich, K. A. (2005). Functional uncoupling of MCM helicase and DNA polymerase activities activates the ATR-dependent checkpoint. *Genes Dev.* 19, 1040–1052. doi: 10.1101/gad.1301205

Cascao, R., Fonseca, J. E., and Moita, L. F. (2017). Celastrol: A Spectrum of Treatment Opportunities in Chronic Diseases. *Front. Med.* 4:69. doi: 10.3389/fmed.2017.00069

Caston, R. A., Gampala, S., Armstrong, L., Messmann, R. A., Fishel, M. L., and Kelley, M. R. (2021). The multifunctional APE1 DNA repair-redox signaling protein as a drug target in human disease. *Drug Discov. Today* 26, 218–228. doi: 10.1016/j.drudis.2020.10.015

Chaudhari, S., Ware, A. P., Jayaram, P., Gorthi, S. P., El-Khamisy, S. F., and Satyamoorthy, K. (2021). Apurinic/Apyrimidinic Endonuclease 2 (APE2): An ancillary enzyme for contextual base excision repair mechanisms to preserve genome stability. *Biochimie* 190, 70–90. doi: 10.1016/j.biochi.2021.07.006

Chen, S. R., Dai, Y., Zhao, J., Lin, L., Wang, Y., and Wang, Y. (2018). A Mechanistic Overview of Triptolide and Celastrol, Natural Products from Tripterygium wilfordii Hook F. *Front. Pharmacol.* 9:104. doi: 10.3389/fphar.2018.00104

Ciccia, A., and Elledge, S. J. (2010). The DNA damage response: making it safe to play with knives. *Mol. Cell* 40, 179–204. doi: 10.1016/j.molcel.2010.09.019

Cimprich, K. A., and Cortez, D. (2008). ATR: an essential regulator of genome integrity. *Nat. Rev. Mol. Cell Biol.* 9, 616–627. doi: 10.1038/nrm2450

Conroy, T., Hammel, P., Hebbar, M., Ben Abdelghani, M., Wei, A. C., Raoul, J. L., et al. (2018). FOLFIRINOX or Gemcitabine as Adjuvant Therapy for Pancreatic Cancer. *N. Engl. J. Med.* 379, 2395–2406. doi: 10.1056/NEJMoa1809775

Cupello, S., Lin, Y., and Yan, S. (2019). Distinct roles of XRCC1 in genome integrity in Xenopus egg extracts. *Biochem. J.* 476, 3791–3804.doi: 10.1042/BCJ20190798

Cupello, S., Richardson, C., and Yan, S. (2016). Cell-free Xenopus egg extracts for studying DNA damage response pathways. *Int. J. Dev. Biol.* 60, 229–236. doi: 10.1387/ijdb.160113sy

Daley, J. M., Niu, H., Miller, A. S., and Sung, P. (2015). Biochemical mechanism of DSB end resection and its regulation. *DNA Repair* 32, 66–74. doi: 10.1016/j.dnarep.2015.04.015

Dan, Y., Ohta, Y., Tsuchimoto, D., Ohno, M., Ide, Y., Sami, M., et al. (2008). Altered gene expression profiles and higher frequency of spontaneous DNA strand breaks in APEX2-null thymus. *DNA Repair* 7, 1437–1454. doi: 10.1016/j.dnarep.2008.05.003

DeStephanis, D., Mcleod, M., and Yan, S. (2015). REV1 is important for the ATR-Chk1 DNA damage response pathway in Xenopus egg extracts. *Biochem. Biophys. Res. Commun.* 460, 609–615. doi: 10.1016/j.bbrc.2015.03.077

Fokas, E., Prevo, R., Pollard, J. R., Reaper, P. M., Charlton, P. A., Cornelissen, B., et al. (2012). Targeting ATR in vivo using the novel inhibitor VE-822 results in selective sensitization of pancreatic tumors to radiation. *Cell Death Dis.* 3:e441. doi: 10.1038/cddis.2012.181

Fredebohm, J., Wolf, J., Hoheisel, J. D., and Boettcher, M. (2013). Depletion of RAD17 sensitizes pancreatic cancer cells to gemcitabine. *J. Cell Sci.* 126, 3380–3389. doi: 10.1242/jcs.124768

Friedberg, E. C. (2003). DNA damage and repair. *Nature* 421, 436–440. doi: 10.1038/nature01408

Guikema, J. E., Linehan, E. K., Tsuchimoto, D., Nakabeppu, Y., Strauss, P. R., Stavnezer, J., et al. (2007). APE1- and APE2-dependent DNA breaks in immunoglobulin class switch recombination. *J. Exp. Med.* 204, 3017–3026. doi: 10.1084/jem.20071289

Guo, X., Dai, X., Wu, X., Cao, N., and Wang, X. (2021). Small but strong: Mutational and functional landscapes of micronuclei in cancer genomes. *Int. J. Cancer* 148, 812–824. doi: 10.1002/ijc.33300

Hieronymus, H., Lamb, J., Ross, K. N., Peng, X. P., Clement, C., Rodina, A., et al. (2006). Gene expression signature-based chemical genomic prediction identifies a novel class of HSP90 pathway modulators. *Cancer Cell* 10, 321–330. doi: 10.1016/j.ccr.2006.09.005

Hossain, M. A., Lin, Y., and Yan, S. (2018). Single-strand break end resection in genome integrity: mechanism and regulation by APE2. *Int. J. Mol. Sci.* 19:2389. doi: 10.3390/ijms19082389

Hu, Y., Yang, C., Amorim, T., Maqbool, M., Lin, J., Li, C., et al. (2021). Cisplatin-Mediated Upregulation of APE2 Binding to MYH9 Provokes Mitochondrial Fragmentation and Acute Kidney Injury. *Cancer Res.* 81, 713–723. doi: 10.1158/0008-5472.CAN-20-1010

Hustedt, N., Alvarez-Quilon, A., Mcewan, A., Yuan, J. Y., Cho, T., Koob, L., et al. (2019). A consensus set of genetic vulnerabilities to ATR inhibition. *Open Biol.* 9:190156. doi: 10.1098/rsob.190156

Ide, Y., Tsuchimoto, D., Tominaga, Y., Nakashima, M., Watanabe, T., Sakumi, K., et al. (2004). Growth retardation and dyslymphopoiesis accompanied by G2/M arrest in APEX2-null mice. *Blood* 104, 4097–4103. doi: 10.1182/blood-2004-04-1476

Jackson, S. P., and Bartek, J. (2009). The DNA-damage response in human biology and disease. *Nature* 461, 1071–1078. doi: 10.1038/nature08467

Jensen, K. A., Shi, X., and Yan, S. (2020). Genomic alterations and abnormal expression of APE2 in multiple cancers. *Sci. Rep.* 10:3758.doi: 10.1038/s41598-020-60656-5

Josse, R., Martin, S. E., Guha, R., Ormanoglu, P., Pfister, T. D., Reaper, P. M., et al. (2014). ATR inhibitors VE-821 and VX-970 sensitize cancer cells to topoisomerase i inhibitors by disabling DNA replication initiation and fork elongation responses. *Cancer Res.* 74, 6968–6979. doi: 10.1158/0008-5472.CAN-13-3369

Karnitz, L. M., and Zou, L. (2015). Molecular Pathways: Targeting ATR in Cancer Therapy. *Clin. Cancer Res.* 21, 4780–4785. doi: 10.1158/1078-0432.CCR-15-0479

Kawasumi, M., Bradner, J. E., Tolliday, N., Thibodeau, R., Sloan, H., Brummond, K. M., et al. (2014). Identification of ATR-Chk1 pathway inhibitors that selectively target p53-deficient cells without directly suppressing ATR catalytic activity. *Cancer Res.* 74, 7534–7545. doi: 10.1158/0008-5472.CAN-14-2650

Kumar, S., Talluri, S., Pal, J., Yuan, X., Lu, R., Nanjappa, P., et al. (2018). Role of apurinic/apyrimidinic nucleases in the regulation of homologous recombination in myeloma: mechanisms and translational significance. *Blood Cancer J.* 8:92. doi: 10.1038/s41408-018-0129-9

Li, J., Liang, W., Li, Y., and Qian, W. (2018). Apurinic/apyrimidinic endonuclease 2 and Zinc finger DNA 3′-phosphoesterase play overlapping roles in the maintenance of epigenome and genome stability. *Plant Cell* 30, 1954–1970. doi: 10.1105/tpc.18.00287

Li, K., Peng, S., Li, Z., Lai, Y., Wang, Q., Tao, Y., et al. (2020). Topoisomerase II-binding protein 1 promotes the progression of prostate cancer via ATR-CHK1 signaling pathway. *Aging* 12, 9948–9958. doi: 10.18632/aging.103260

Li, M., and Wilson, D. M. III (2014). Human apurinic/apyrimidinic endonuclease 1. *Antioxid. Redox Signal.* 20, 678–707. doi: 10.1089/ars.2013.5492

Lin, Y., Bai, L., Cupello, S., Hossain, M. A., Deem, B., Mcleod, M., et al. (2018). APE2 promotes DNA damage response pathway from a single-strand break. *Nucleic Acids Res.* 46, 2479–2494. doi: 10.1093/nar/gky020

Lin, Y., Ha, A., and Yan, S. (2019). Methods for studying DNA single-strand break repair and signaling in Xenopus laevis egg extracts. *Methods Mol. Biol.* 1999, 161–172. doi: 10.1007/978-1-4939-9500-4_9

Lin, Y., Mcmahon, A., Driscoll, G., Bullock, S., Zhao, J., and Yan, S. (2021). Function and molecular mechanisms of APE2 in genome and epigenome integrity. *Mutat. Res.* 787:108347. doi: 10.1016/j.mrrev.2020.108347

Lin, Y., Raj, J., Li, J., Ha, A., Hossain, M. A., Richardson, C., et al. (2020). APE1 senses DNA single-strand breaks for repair and signaling. *Nucleic Acids Res.* 48, 1925–1940. doi: 10.1093/nar/gkz1175

Lindahl, T. (1993). Instability and decay of the primary structure of DNA. *Nature* 362, 709–715. doi: 10.1038/362709a0

Lu, Y., Liu, Y., Zhou, J., Li, D., and Gao, W. (2020). Biosynthesis, total synthesis, structural modifications, bioactivity, and mechanism of action of the quinone-methide triterpenoid celastrol. *Med. Res. Rev.* 41, 1022–1060. doi: 10.1002/med.21751

Marechal, A., and Zou, L. (2013). DNA damage sensing by the ATM and ATR kinases. *Cold Spring Harb. Perspect. Biol.* 5:a012716. doi: 10.1101/cshperspect.a012716

Marechal, A., and Zou, L. (2015). RPA-coated single-stranded DNA as a platform for post-translational modifications in the DNA damage response. *Cell Res.* 25, 9–23. doi: 10.1038/cr.2014.147

Mengwasser, K. E., Adeyemi, R. O., Leng, Y., Choi, M. Y., Clairmont, C., D'andrea, A. D., et al. (2019). Genetic screens reveal FEN1 and APEX2 as BRCA2 synthetic lethal targets. *Mol. Cell* 73, 885–899e886. doi: 10.1016/j.molcel.2018.12.008

Merl, M. Y., Abdelghany, O., Li, J., and Saif, M. W. (2010). "First-line treatment of metastatic pancreatic adenocarcinoma: can we do better?," in *Highlights from the "2010 ASCO Annual Meeting"*, Vol. 11, (Chicago, IL: ASCO), 317–320.

Paull, T. T. (2015). Mechanisms of ATM Activation. *Annu. Rev. Biochem.* 84, 711–738. doi: 10.1146/annurev-biochem-060614-034335

Sabouri, Z., Okazaki, I. M., Shinkura, R., Begum, N., Nagaoka, H., Tsuchimoto, D., et al. (2009). Apex2 is required for efficient somatic hypermutation but not for class switch recombination of immunoglobulin genes. *Int. Immunol.* 21, 947–955. doi: 10.1093/intimm/dxp061

Saldivar, J. C., Cortez, D., and Cimprich, K. A. (2017). The essential kinase ATR: ensuring faithful duplication of a challenging genome. *Nat. Rev. Mol. Cell Biol.* 18, 622–636. doi: 10.1038/nrm.2017.67

Shahda, S., Lakhani, N. J., O'neil, B., Rasco, D. W., Wan, J., Mosley, A. L., et al. (2019). A phase I study of the APE1 protein inhibitor APX3330 in patients with advanced solid tumors. *J Clin. Oncol.* 37, 3097–3097. doi: 10.1200/JCO.2019.37.15_suppl.3097

Shiotani, B., and Zou, L. (2009). Single-stranded DNA orchestrates an ATM-to-ATR switch at DNA breaks. *Mol. Cell* 33, 547–558. doi: 10.1016/j.molcel.2009.01.024

Siegel, R. L., Miller, K. D., and Jemal, A. (2020). Cancer statistics, 2020. *CA Cancer J. Clin.* 70, 7–30. doi: 10.3322/caac.21590

Symington, L. S. (2014). End resection at double-strand breaks: mechanism and regulation. *Cold Spring Harb. Perspect. Biol.* 6:a016436. doi: 10.1101/cshperspect.a016436

Terradas, M., Martin, M., Tusell, L., and Genesca, A. (2010). Genetic activities in micronuclei: is the DNA entrapped in micronuclei lost for the cell? *Mutat. Res.* 705, 60–67. doi: 10.1016/j.mrrev.2010.03.004

Tsuchimoto, D., Sakai, Y., Sakumi, K., Nishioka, K., Sasaki, M., Fujiwara, T., et al. (2001). Human APE2 protein is mostly localized in the nuclei and to some extent in the mitochondria, while nuclear APE2 is partly associated with proliferating cell nuclear antigen. *Nucleic Acids Res.* 29, 2349–2360. doi: 10.1093/nar/29.11.2349

Tubbs, A., and Nussenzweig, A. (2017). Endogenous DNA Damage as a Source of Genomic Instability in Cancer. *Cell* 168, 644–656. doi: 10.1016/j.cell.2017.01.002

Unk, I., Haracska, L., Prakash, S., and Prakash, L. (2001). 3′-phosphodiesterase and 3′–>5′ exonuclease activities of yeast Apn2 protein and requirement of these activities for repair of oxidative DNA damage. *Mol. Cell Biol.* 21, 1656–1661. doi: 10.1128/MCB.21.5.1656-1661.2001

Venkatesha, V. A., Parsels, L. A., Parsels, J. D., Zhao, L., Zabludoff, S. D., Simeone, D. M., et al. (2012). Sensitization of pancreatic cancer stem cells to gemcitabine by Chk1 inhibition. *Neoplasia* 14, 519–525. doi: 10.1593/neo.12538

Wallace, B. D., Berman, Z., Mueller, G. A., Lin, Y., Chang, T., Andres, S. N., et al. (2017). APE2 Zf-GRF facilitates 3′-5′ resection of DNA damage following oxidative stress. *Proc. Natl. Acad. Sci. U S A.* 114, 304–309. doi: 10.1073/pnas.1610011114

Wallez, Y., Dunlop, C. R., Johnson, T. I., Koh, S. B., Fornari, C., Yates, J. W. T., et al. (2018). The ATR Inhibitor AZD6738 Synergizes with Gemcitabine In Vitro and In Vivo to Induce Pancreatic Ductal Adenocarcinoma Regression. *Mol. Cancer Ther.* 17, 1670–1682. doi: 10.1158/1535-7163.MCT-18-0010

Willis, J., Destephanis, D., Patel, Y., Gowda, V., and Yan, S. (2012). Study of the DNA damage checkpoint using Xenopus egg extracts. *J. Vis. Exp.* 2012:e4449. doi: 10.3791/4449

Willis, J., Patel, Y., Lentz, B. L., and Yan, S. (2013). APE2 is required for ATR-Chk1 checkpoint activation in response to oxidative stress. *Proc. Natl. Acad. Sci. U S A.* 110, 10592–10597. doi: 10.1073/pnas.1301445110

Yan, S. (2019). Resolution of a complex crisis at DNA 3′ termini. *Nat. Struct. Mol. Biol.* 26, 335–336. doi: 10.1038/s41594-019-0215-0

Yan, S., and Michael, W. M. (2009). TopBP1 and DNA polymerase-alpha directly recruit the 9-1-1 complex to stalled DNA replication forks. *J. Cell Biol.* 184, 793–804. doi: 10.1083/jcb.200810185

Yan, S., and Willis, J. (2013). WD40-repeat protein WDR18 collaborates with TopBP1 to facilitate DNA damage checkpoint signaling. *Biochem. Biophys. Res. Commun.* 431, 466–471. doi: 10.1016/j.bbrc.2012.12.144

Yan, S., Sorrell, M., and Berman, Z. (2014). Functional interplay between ATM/ATR-mediated DNA damage response and DNA repair pathways in oxidative stress. *Cell. Mol. Life Sci.* 71, 3951–3967. doi: 10.1007/s00018-014-1666-4

Yun, H., Shi, R., Yang, Q., Zhang, X., Wang, Y., Zhou, X., et al. (2014). Over expression of hRad9 protein correlates with reduced chemosensitivity in breast cancer with administration of neoadjuvant chemotherapy. *Sci. Rep.* 4:7548. doi: 10.1038/srep07548

Zhang, T., Hamza, A., Cao, X., Wang, B., Yu, S., Zhan, C. G., et al. (2008). A novel Hsp90 inhibitor to disrupt Hsp90/Cdc37 complex against pancreatic cancer cells. *Mol. Cancer Ther.* 7, 162–170. doi: 10.1158/1535-7163.MCT-07-0484

Zheng, R., Zhu, H. L., Hu, B., Ruan, X., and Cai, H. (2020). Identification of APEX2 as an oncogene in liver cancer. *World J. Clin. Cases* 8, 2917–2929. doi: 10.12998/wjcc.v8.i14.2917

Zou, L., Cortez, D., and Elledge, S. J. (2002). Regulation of ATR substrate selection by Rad17-dependent loading of Rad9 complexes onto chromatin. *Genes Dev.* 16, 198–208. doi: 10.1101/gad.950302

**Conflict of Interest:** The authors declare that the research was conducted in the absence of any commercial or financial relationships that could be construed as a potential conflict of interest.

**Publisher's Note:** All claims expressed in this article are solely those of the authors and do not necessarily represent those of their affiliated organizations, or those of the publisher, the editors and the reviewers. Any product that may be evaluated in this article, or claim that may be made by its manufacturer, is not guaranteed or endorsed by the publisher.

frontiers in Cell and Developmental Biology

ORIGINAL RESEARCH
published: 05 January 2022
doi: 10.3389/fcell.2021.804962

# PARP1 Upregulation in Recurrent Oral Cancer and Treatment Resistance

*Feifei Wang, Odjo G. Gouttia, Ling Wang and Aimin Peng**

*Department of Oral Biology, University of Nebraska Medical Center, Lincoln, NE, United States*

First-line treatments for oral cancer typically include surgery, radiation, and in some cases, chemotherapy. Radiation and oral cancer chemotherapeutics confer cytotoxicity largely by inducing DNA damage, underscoring the importance of the cellular DNA damage repair and response pathways in cancer therapy. However, tumor recurrence and acquired resistance, following the initial response to treatment, remains as a major clinical challenge. By analyzing oral tumor cells derived from the primary and recurrent tumors of the same patient, our study revealed upregulated PARP1 expression in the recurrent tumor cells. Cisplatin and 5-fluorouracil treatment further augmented PARP1 expression in the recurrent, but not the primary, tumor cells. Post-treatment upregulation of PARP1 was dependent on the catalytic activities of PARP and CDK7. Consistent with the established function of PARP1 in DNA repair, we showed that overexpression of PARP1 rendered the primary tumor cells highly resistant to DNA damage treatment. Conversely, PARP inhibition partially reversed the treatment resistance in the recurrent tumor cells; combinatorial treatment using a PARP inhibitor and cisplatin/5-fluorouracil significantly sensitized the tumor response *in vivo*. Taken together, we reported here PARP1 upregulation as a clinically relevant mechanism involved in oral cancer recurrence, and suggested the clinical benefit of PARP inhibitors, currently approved for the treatment of several other types of cancer, in oral cancer.

**Keywords: PARP inhibition, oral cancer, DNA repair, chemotherapy, PARP1**

OPEN ACCESS

***Edited by:***
*Shan Yan,*
*University of North Carolina at Charlotte, United States*

***Reviewed by:***
*Youwei Zhang,*
*Case Western Reserve University, United States*
*Chunzhang Yang,*
*National Cancer Institute, United States*

****Correspondence:***
*Aimin Peng*
*aimin.peng@unmc.edu*

***Specialty section:***
*This article was submitted to Molecular and Cellular Pathology, a section of the journal Frontiers in Cell and Developmental Biology*

***Received:*** *29 October 2021*
***Accepted:*** *10 December 2021*
***Published:*** *05 January 2022*

***Citation:***
*Wang F, Gouttia OG, Wang L and Peng A (2022) PARP1 Upregulation in Recurrent Oral Cancer and Treatment Resistance. Front. Cell Dev. Biol. 9:804962. doi: 10.3389/fcell.2021.804962*

## INTRODUCTION

Oral cancer, including cancers of the mouth and the back of the throat, is the sixth most common cancer worldwide. In the United States, approximately 50,000 new oral cancer cases are diagnosed each year. First-line treatments for oral cancer typically include surgery and radiation, with chemotherapy added to decrease the possibility of metastasis, to eliminate residual tumor cells after surgery, to enhance the efficacy of radiation, and for patients with confirmed distant metastasis (Casiglia and Woo, 2001; Gau et al., 2019; Johnson et al., 2020). Radiation and oral cancer chemotherapeutics, such as cisplatin and 5-fluorouracil (5-FU), confer cytotoxicity largely by inducing DNA damage. Oral cancer caused by HPV generally responds to the existing treatments, with over 80% 5-year survival rate for stage III and IV patients. On the other hand, only 10–20% HPV- oral cancer patients at stage III and IV survive the 5-year period. Moreover, the survival rate of oral cancer has not improved significantly over the past decades. Thus, it is important, and urgent, to discover new mechanisms of treatment resistance, and to develop new therapeutics and combinations to overcome resistance in oral cancer.

The cellular DNA damage response (DDR) pathway plays a crucial role in determining the treatment outcome of radiation and genotoxic chemotherapeutics (Jackson and Bartek, 2009).

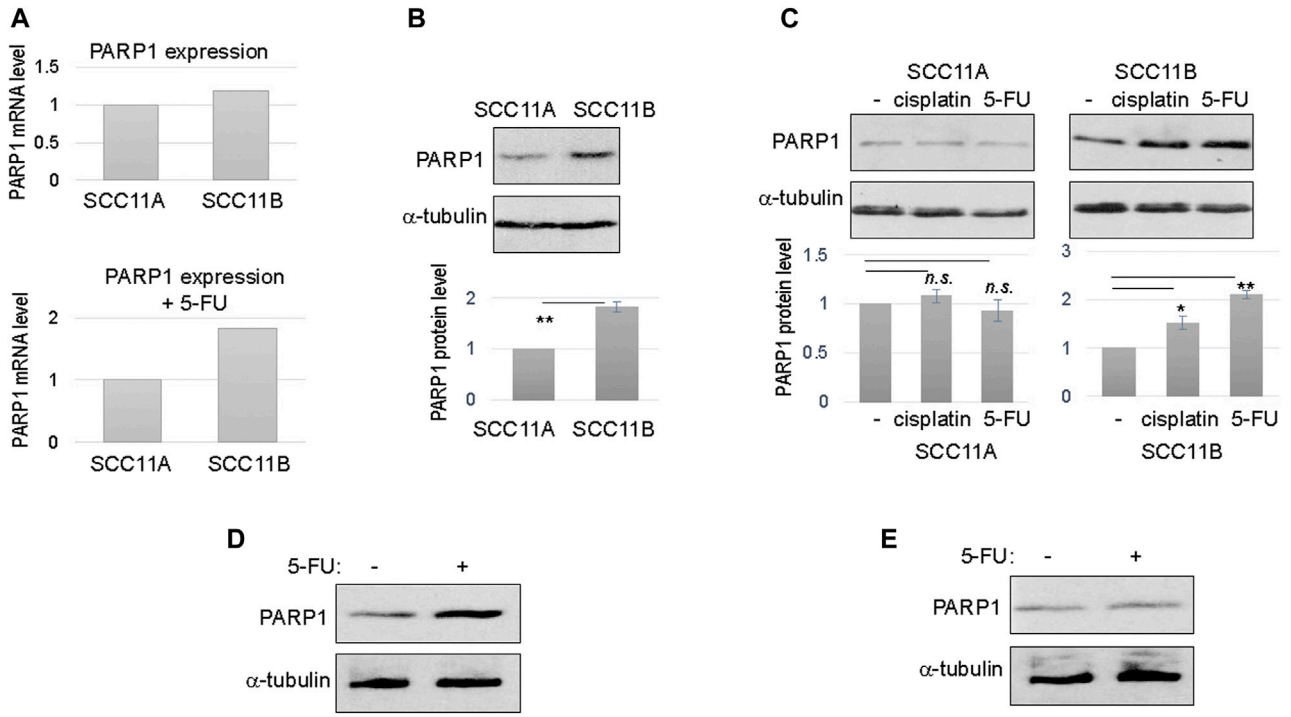


**FIGURE 1 |** Upregulation of PARP1 in recurrent oral cancer cells. **(A)** The levels of PARP1 mRNA in SCC11A and SCC11B cells, without DNA damage **(upper panel)**, or with 5-FU treatment **(lower panel)**. **(B)** SCC11A and SCC11B cells were analyzed by immunoblotting for the protein levels of PARP1 and α-tubulin (loading control). The band intensity was quantified, and the PARP1 to α-tubulin ratio was shown in the lower panel. The relative PARP1 protein level in SCC11B was normalized to that in SCC11A. The average of three independent experiments was shown, with statistical analysis (**$p < 0.01$). **(C)** SCC11A and SCC11B cells were treated with cisplatin (10 μM) or 5-FU (10 μM), as indicated, for 1 day. The treated and untreated cells were analyzed by immunoblotting for PARP1 and α-tubulin. The band intensity was quantified, and the PARP1 to α-tubulin ratio was shown in the lower panel. The relative PARP1 protein level in drug treated cells was normalized to that in untreated cells. The average of three independent experiments was shown, with statistical analysis (*$p < 0.05$, n.s. not significant). **(D)** SCC10B cells were treated with or without 5-FU (10 μM), for 1 day. The cells were then analyzed by immunoblotting for PARP1 and α-tubulin. **(E)** The oral mucosal epithelial cells were treated with or without 5-FU (10 μM), for 1 day. The cells were then analyzed by immunoblotting for PARP1 and α-tubulin.

The DDR encompasses complex signaling pathways that lead to cell cycle arrest and cell death. On the other hand, the DDR employs various DNA repair mechanisms to remove DNA damage, and promote cell survival (Ciccia and Elledge, 2010). Based on these principles, it has been long proposed that targeting certain elements of the DDR can effectively sensitize tumor cells to radiation and other DNA damaging drug treatments (Zhou et al., 2003; Liang et al., 2009; Jalal et al., 2011; Lord and Ashworth, 2012).

Among the most promising new anti-cancer targets are poly (ADP-ribose) polymerases (PARPs). PARPs catalyze the attachment of poly (ADP-ribose) chains to substrate proteins, a process termed PARylation (Luo and Kraus, 2012; Dulaney et al., 2017; Martin-Hernandez et al., 2017; Ray Chaudhuri and Nussenzweig, 2017). In particular, PARP1 accounts for over 90% of DNA damage-induced PARylation, thereby playing an important role in the DDR. PARP1 acts as an early and upstream sensor for a variety of DNA damage, and is required for the recruitment of many downstream repair factors, such as X-ray repair cross-complementing protein 1 (XRCC1) (Luo and Kraus, 2012; Dulaney et al., 2017; Martin-Hernandez et al., 2017; Ray Chaudhuri and Nussenzweig, 2017). Consistent with the function of PARP1 in DNA repair, its inhibition has been considered as a valid approach to enhance the cytotoxic effect of radiation and chemotherapeutics, as well as to exploit synthetic lethality in tumors with defective DSB repair (Dulaney et al., 2017; Lord and Ashworth, 2017). Olaparib, a PARP inhibitor (PARPi), was approved by FDA and EMA in 2014 for the treatment of ovarian cancer with BRCA1 and BRCA2 mutations. The approval was extended also to breast cancer in 2018, and to prostate and pancreatic cancer in 2019. With these emerging successes of PARPi, it is important to investigate the involvement of PARPs in the pathophysiology of oral cancer, and to evaluate the potential application of PARPi in the treatment of oral tumors, particularly those exhibiting resistance to DNA damaging agents. In this study, we revealed upregulation

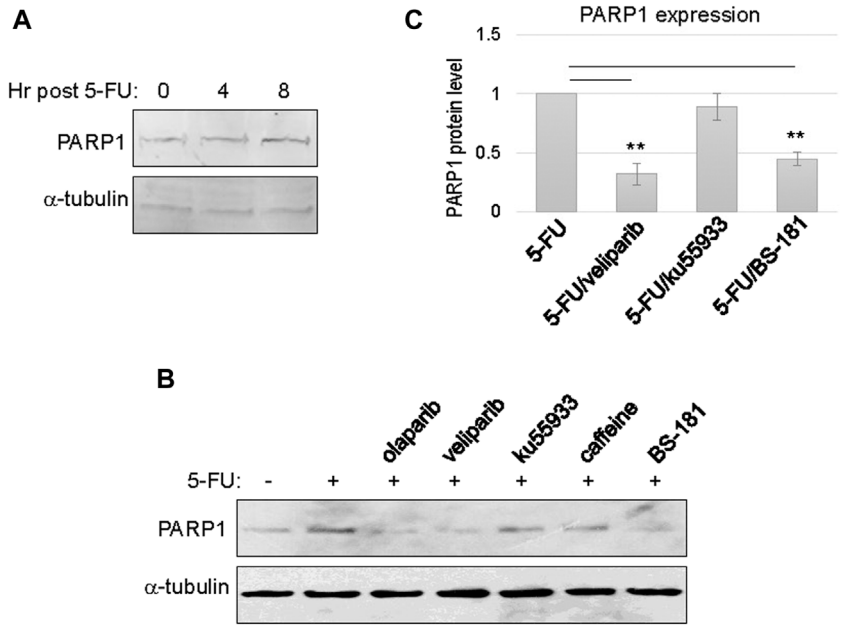


**FIGURE 2 |** PARP1 upregulation upon chemotherapeutic treatments in recurrent oral tumor cells. **(A)** SCC11B cells were treated with or without 5-FU (10 μM), as indicated, for 4 or 8 h. The treated and untreated cells were analyzed by immunoblotting for PARP1 and α-tubulin. **(B)** SCC11B cells were treated with or without 5-FU (10 μM), in combination with olaparib (10 μM), veliparib (10 μM), Ku55933 (10 μM), caffeine (3 mM), and BS-181 (1 μM), as indicated, for 1 day. The treated and untreated cells were analyzed by immunoblotting for PARP1 and α-tubulin. **(C)** Quantification of PARP1 expression in panel **(B)**. The relative PARP1 protein level in cells with combination drug treatments was normalized to that in cells treated with 5-FU alone. The average of three independent experiments was shown, with statistical analysis.

of PARP1 as a mechanism that rendered oral cancer cells resistant to treatment, and PARPi as effective agents that re-sensitized these cells to chemotherapy *in vitro* and *in vivo*.

# RESULTS

## Upregulation of PARP1 in the Recurrent Oral Tumor Cells

To shed new light on oral cancer resistance and recurrence, we obtained a pair of patient-derived, matched, oral cancer cell lines. Of these lines, SCC11A was established from the initial oral tumor, and SCC11B was obtained from the recurrent tumor after treatment with radiation and chemotherapy. The patient expired due to tumor recurrence and the subsequent metastasis. These matched cell lines offer a physiologically relevant model to study molecular events that underlie treatment evasion and tumor recurrence. Interestingly, RNA sequencing analysis of gene expression revealed that SCC11B exhibited an elevated RNA level of PARP1, particularly when cells were treated with 5-FU (**Figure 1A**).

To confirm the RNA sequencing results, we analyzed the protein level of PARP1 in SCC11A and SCC11B cells. In fact, PARP1 protein in SCC11B was approximately two fold more abundant than that in SCC11A (**Figure 1B**). Upon treatment with cisplatin and 5-FU, two chemotherapeutic drugs used for oral cancer, PARP1 expression was further increased in SCC11B, by approximately 50 and 100%, respectively (**Figure 1C**). By comparison, cisplatin and 5-FU did not induce PARP1 expression in SCC11A cells (**Figure 1C**).

Furthermore, we noted a similar fashion of 5-FU-induced PARP1 upregulation in SCC10B, another oral cancer cell line derived from recurrent tumor (**Figure 1D**). PARP1 expression was unchanged in the control, oral mucosal epithelial cells upon 5-FU treatment (**Figure 1E**), confirming that upregulation of PARP1 reflects an acquired, post-treatment mechanism in some tumor cells.

## The Catalytic Activity of PARP1 Mediates its Own Upregulation After DNA Damage

Upregulation of PARP1 expression was observed between 4 and 8 h post 5-FU treatment, possibly reflecting the time frame of PARP1 transcription and translation (**Figure 2A**). Next, we sought to reveal more mechanistic insights into the cellular activities that govern PARP1 upregulation. Interestingly, inhibition of PARP *per se*, using olaparib or veliparib, prevented PARP1 upregulation in the presence of

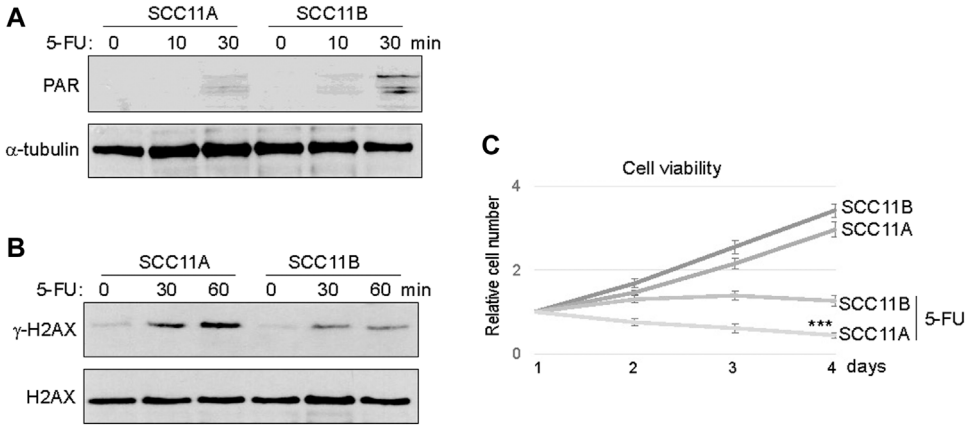


**FIGURE 3 |** SCC11B cells exhibited increased PARylation and cell resistance. **(A)** SCC11A and SCC11B cells were incubated in 5-FU (10 μM), for 10 or 30 min, as indicated. Cells were harvested for immunoblotting. **(B)** SCC11A and SCC11B cells were incubated in 5-FU (10 μM), for 30 or 60 min, as indicated. Cells were harvested for immunoblotting. **(C)** Cell viability assay was performed as in the Materials and Methods. SCC11A and SCC11B cells were incubated for 4 days. 5-FU (10 μM) was added at day 1. The cell numbers at days 2–4 were normalized to that at day 1 (untreated). The mean values and standard derivations, from three independent experiments, were shown.

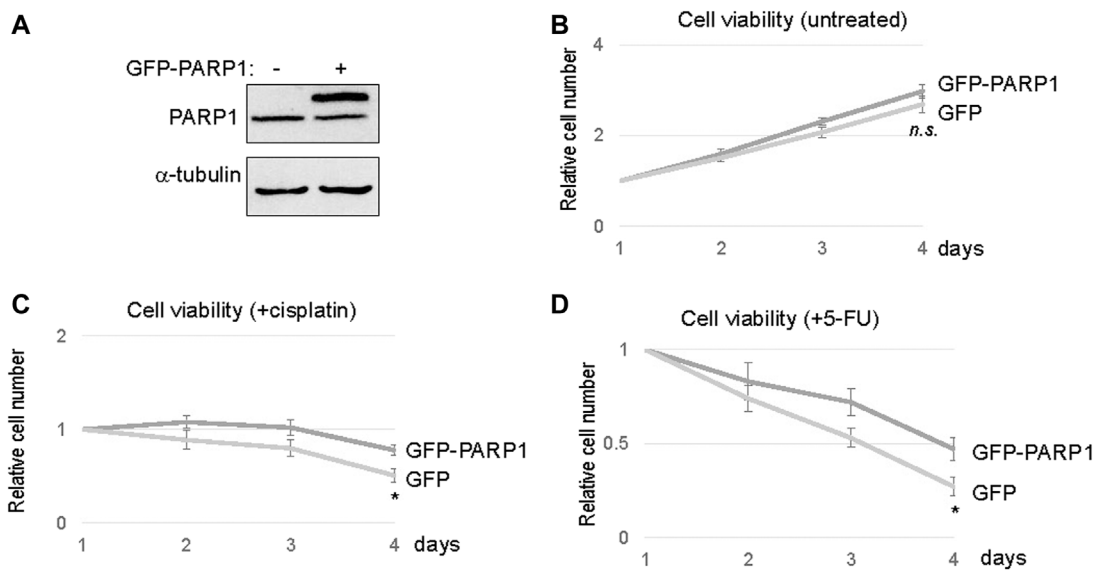


**FIGURE 4 |** PARP1 upregulation rendered SCC11A cells more resistant to chemotherapeutic drugs. **(A)** The expression of recombinant and endogenous PARP1 was shown by immunoblotting. **(B)** SCC11A cells expressing GFP-PARP1 or control GFP vector were incubated for 4 days. Cell viability was determined as described in Materials and Methods, the cell numbers at days 2–4 were normalized to that at day 1. The mean values and standard derivations, from three independent experiments, were shown. **(C)** SCC11A cells expressing GFP-PARP1 or control GFP vector were incubated for 4 days. Cisplatin (10 μM) was added at day 1. The cell numbers at days 2–4 were normalized to that at day 1 (untreated). The mean values and standard derivations, from three independent experiments, were shown. **(D)** SCC11A cells expressing GFP-PARP1 or control GFP vector were incubated for 4 days. 5-FU (10 μM) was added at day 1. The cell numbers at days 2–4 were normalized to that at day 1 (untreated). The mean values and standard derivations, from three independent experiments, were shown.

5-FU treatment (**Figures 2B,C**). By comparison, inhibition of ATM with ku55933, or ATM/ATR with caffeine, did not significantly alter PARP1 upregulation (**Figures 2B,C**). These results indicated that DNA damage-induced PARP1 upregulation does not rely on the conventional signaling pathway initiated via ATM/ATR activation. Moreover, a selective inhibitor of CDK7, BS-181, also reduced PARP1 expression (**Figures 2B,C**).

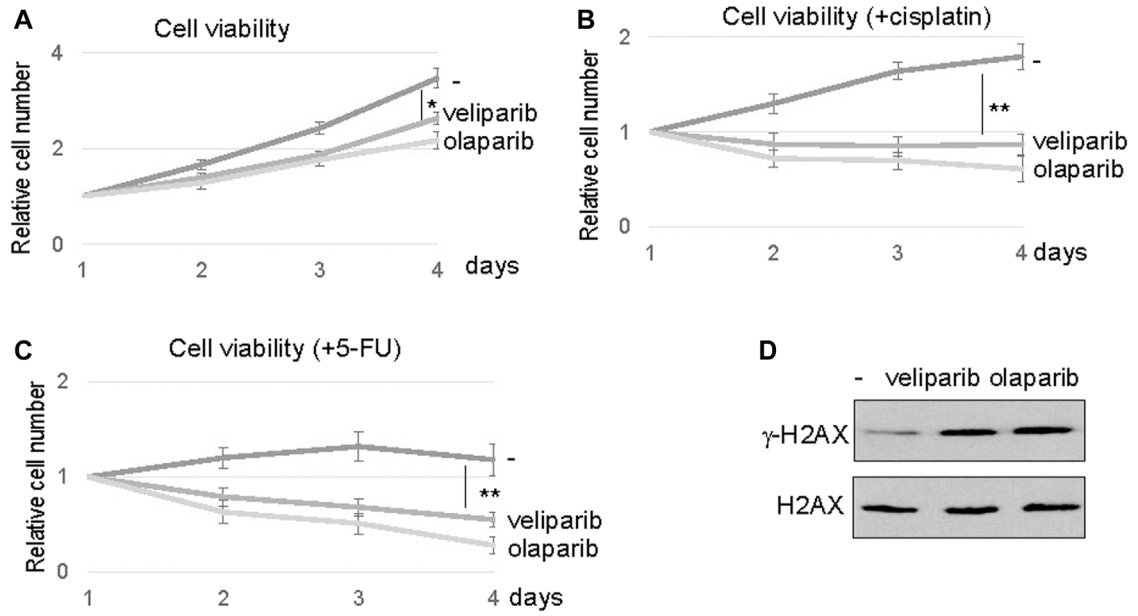


**FIGURE 5 |** PARP inhibition sensitized SCC11B cells to DNA damage. **(A)** SCC11B cells were incubated for 4 days, with or without veliparib and olaparib, as indicated. The cell numbers at days 2–4 were normalized to that at day 1 (untreated). The mean values and standard derivations, from three independent experiments, were shown. **(B)** SCC11B cells were incubated for 4 days, with or without veliparib and olaparib, as indicated. Cisplatin (10 μM) was added at day 1. The cell numbers at days 2–4 were normalized to that at day 1 (untreated). The mean values and standard derivations, from three independent experiments, were shown. **(C)** SCC11B cells were incubated for 4 days, with or without veliparib and olaparib, as indicated. 5-FU (10 μM) was added at day 1. The cell numbers at days 2–4 were normalized to that at day 1 (untreated). The mean values and standard derivations, from three independent experiments, were shown. **(D)** SCC11B cells were treated with or without veliparib and olaparib for 1 day. The cells were harvested and analyzed by immunoblotting for γ-H2AX and H2AX.

## PARP1 Upregulation Renders Oral Cancer Cells Resistant to DNA Damaging Drugs

Consistent with PARP1 upregulation, an elevated level of Poly (ADP-ribosyl)ation (PARylation) was induced in SCC11B cells, compared to SCC11A cells, upon 5-FU treatment (**Figure 3A**). On the other hand, accumulation of γ-H2AX appeared alleviated in SCC11B cells, potentially owing to PARP1-mediated DNA repair (**Figure 3B**). Using a cell viability assay, we confirmed that SCC11B cells exhibited increased resistance to 5-FU treatment (**Figure 3C**). Thus, PARP1 upregulation during oral tumor recurrence correlated with increased PARylation, decreased DNA damage accumulation, and acquired drug resistance.

To directly assess the functional impact of PARP1 upregulation, we expressed recombinant PARP1 in SCC11A cells, to approximately two to three fold over the endogenous level (**Figure 4A**). Compared to the vector control, PARP1 expression alone did not markedly influence the cell viability (**Figure 4B**). However, significant proliferative advantages were observed in PAPR1-expressing cells upon treatment with cisplatin or 5-FU (**Figures 4C,D**). Together, these results indicated that upregulation of PARP1 in SCC11A cells adequately conferred tumor cell resistance to chemotherapeutic drugs.

## PARP1 Targeting in Recurrent Oral Cancer Cells and Tumors

Our findings prompted us to evaluate the potential of PARP1 targeting in enhancing the therapeutic response of oral tumor cells, particularly in SCC11B cells that exhibited PARP1 upregulation. PARP inhibition using two clinically approved inhibitors, veliparib and olaparib, reduced the viability of SCC11B cells, suggesting the possible use of PARPi as monotherapeutic agents (**Figure 5A**). However, a more profound therapeutic benefit was observed, when SCC11B cells were treated with PARPi in combination with cisplatin or 5-FU (**Figures 5B,C**). In these cases, both veliparib and olaparib elicited synergistic effects with cisplatin and 5-FU. Interestingly, veliparib and olaparib increased the induction of γ-H2AX after 5-FU treatment (**Figure 5D**). This finding indicated that inhibition of PARP1 caused increased accumulation of DNA damage, particularly DNA double strand breaks, after therapeutic exposure to 5-FU.

We further confirmed the efficacy of PARP1 targeting using siRNA-mediated PARP1 depletion (**Figure 6A**). Consistent with PARP inhibition, reducing the expression level of PARP1 in SCC11B cells enhanced the therapeutic outcome of 5-FU, as indicated by decreased cell viability (**Figure 6B**). Finally, we

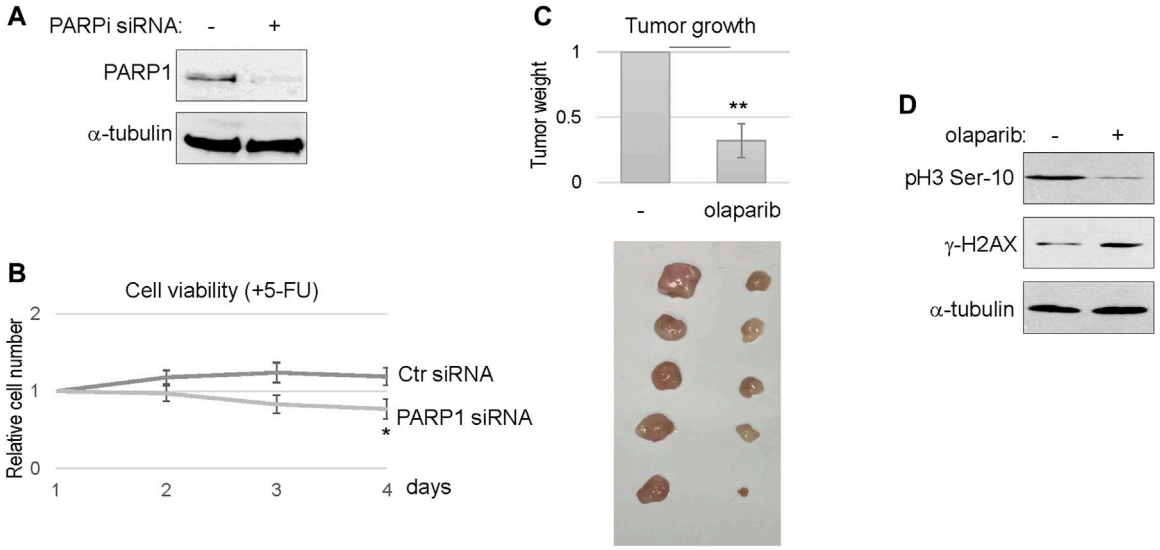


**FIGURE 6 |** PARP targeting sensitized the SCC11B tumor response to chemotherapy. **(A)** SCC11B cells were treated with PARP1 siRNA or control siRNA, as described in Materials and Methods. Cells were analyzed by immunoblotting to confirm PARP1 depletion. **(B)** SCC11B cells were incubated for 4 days, with control or PARP1 siRNA, as indicated. 5-FU (10 μM) was added at day 1. The cell numbers at days 2–4 were normalized to that at day 1 (untreated). The mean values and standard derivations, from three independent experiments, were shown. **(C)** SCC11B cells were implanted into immunodeficient mice to form tumors. As described in Materials and Methods, mice were then treated with cisplatin/5-FU, with or without olaparib. Tumors were excised, and shown in the lower panel. The average tumor weight of olaparib/cisplatin/5-FU-treated group was normalized to that of cisplatin/5-FU. The mean values and standard derivations were shown, statistical significance was determined by Student's t-test ($n$ = 5 per group). **(D)** Tumor samples were processed, as described in Materials and Methods, and analyzed by immunoblotting.

established SCC11B xenograft tumor models in immunodeficient mice, to evaluate the effect of PARPi in chemotherapy. A combination regimen with both cisplatin and 5-FU was used, as in the clinical treatment of head and neck and many other cancers. Compared to chemotherapy alone, combination with olaparib substantially improved the tumor responses, and deceased the final tumor volume by approximately three fold (**Figure 6C**). Biochemical analyses of the tumor samples confirmed that PARPi treatment increased DNA damage accumulation, and decreased cell proliferation, as judged by γ-H2AX and phospho-histone H3, respectively (**Figure 6D**).

# MATERIALS AND METHODS

## Antibodies and Chemicals

Sodium dodecyl sulfate-polyacrylamide gel electrophoresis (SDS-PAGE) and immunoblotting was performed as described previously (Wang et al., 2019a). Anti-PARP1, H2AX, Histone H3 Ser-10, and γ-H2AX antibodies were purchased from Cell Signaling (Danvers, MA); anti-poly (ADP-ribose) polymer antibody was obtained from Santa Cruz Biotechnology (Dallas, TX); α-tubulin antibody was a gift from Dr. James Wahl (University of Nebraska Medical Center). The intensity of band signals was measured using NIH ImageJ software. Cisplatin and 5-fluorouracil were purchased from Sigma (St. Louis, MO); olaparib and veliparib were obtained from Selleckchem (Houston, TX) and Santa Cruz Biotech (Dallas, TX), respectively.

## Cell Culture and Analyses

Human oral squamous-cell carcinoma cell lines SCC11A (UM-SCC-11A), SCC11B (UM-SCC-11B), and SCC10B (UM-SCC-10B) were obtained from the University of Michigan, and characterized genetically and morphologically (Brenner et al., 2010; Wang et al., 2012; Luong et al., 2016). These cells were maintained in Dulbecco's modified Eagle medium (DMEM, Sigma) supplemented with 10% fetal bovine serum (FBS, Sigma). Mouse oral mucosal epithelial cells were purchased from Cell Biologics (Chicago, IL), and maintained in the recommended epithelial medium (Cell Biologics). To measure SCC11A and SCC11B cell sensitivity to cisplatin and 5-FU, cells were treated with cisplatin at indicated concentrations, and incubated for 1–4 days. The numbers of viable cells were counted using a hemocytometer. GFP-PARP1 was described in our previous study (Wang et al., 2019b), and was transfected to SCC11A cells using lipofectamine (Thermo Fisher Scientific, Waltham, MA). Cell pellets were submitted to Genewiz (South Plainfield, NJ) for RNA sequencing analysis. PARP1 siRNA (target sequence UGACUUGGAAGUGAUCGA) were purchased from Integrated DNA Technologies (IDT), and transfected into cells using Lipofectamine RNAiMAX (Thermo) following the protocol recommended by the manufacturer. A non-targeting control, or scramble siRNA was used as a control.

## Mouse Tumor Studies

Athymic nude mice were purchased from the Jackson Laboratory (Bar Harbor, ME) and housed at the animal facility at the UNMC

College of Dentistry. SCC11B cells were implanted into 6-week old mice by a single subcutaneous injection of tumor cells (2–6 × $10^5$ cells in 100 µl of sterile PBS). To test how tumors respond to chemotherapy, once the tumor size reached 50 $mm^3$, cisplatin and 5-FU (5 mg/kg mouse), with or without olaparib (10 mg/kg mouse) were administered intraperitoneally on days 1 and 3. Ten days after the initial treatment, the mice were euthanized, and tumors were removed and weighed.

To prepare tumor lysate for immunoblotting analysis, excised tumor samples were frozen on dry ice, and cut into small pieces. 20 µl/mg of RIPA (20 mM Tris-Cl (pH 7.4) 1 mM EDTA. 0.5 mM EGTA. 1% Triton X-100. 0.1% sodium deoxycholate. 0.1% SDS. 150 mM NaCl) was added, and the samples were homogenized. The samples were then centrifuged, and supernatants were collected for immunoblotting.

## Statistical Analysis

Statistical analyses were performed in cell viability assays and in the tumor weight measurements. Briefly, data were analyzed using an unpaired 2-tailed Student's t test to determine the statistical significance. A *p*-value less than 0.05 is considered as significant.

# DISCUSSION

## Acquired Cancer Resistance in Oral Cancer Is Associated With Altered DDR Pathways

In this study, we reported PARP1 upregulation during the recurrence of oral tumor, using patient-derived cell lines. We showed that the elevated PARP1 expression conferred treatment resistance in the primary oral tumor cells, and that the recurrent tumor cells are highly dependent on PARP activity for treatment evasion. Presumably, the initial clinical treatment using radiation and chemotherapy selected for cells with PARP1 upregulation. Furthermore, in these recurrent oral tumor cells, cisplatin and 5-fluorouracil were capable of inducing the gene expression of PARP1. To our knowledge, this mechanism of treatment-induced PARP1 expression is new. Strikingly, this phenomenon was not seen in the matched primary tumor cells, or in a control oral mucosal epithelial cell line, pointing to specific dysregulation of PARP1 expression that was acquired during tumor recurrence.

Our findings add to the emerging understanding of how tumor resistance and recurrence is driven by specific alterations of the DDR. Deficient DNA damaging signaling, particularly the ATM kinase-mediated pathway, has been observed in oral cancer cells, in correlation with reduced responsiveness to cisplatin (Wang et al., 2012). Other studies revealed polymorphisms of DDR genes as potential risk factors that promote head and neck cancer progression. Altered expression levels of DNA repair genes, including both upregulation and downregulation, have been shown in oral cancer studies (Wang et al., 2007; Jenkins et al., 20132013; Ali et al., 2017; Dylawerska et al., 2017; Psyrri et al., 2021). Thus, detailed functional studies are necessary to further elucidate how these DDR alterations impact the progression and treatment responses of oral cancer.

## PARP1 as an Anti-Cancer Drug Target in Oral Cancer

With the proven clinical benefits of PARPi in other solid tumors, the potential application of PARPi in oral cancer treatment has been enthusiastically proposed (Glorieux et al., 2017; Moutafi et al., 2021). This therapeutic idea was further supported by multiple lines of preclinical studies. For example, PARPi was found effective in head and neck cancer with SMAD4-deficiency (Hernandez et al., 2020). The efficacy of PARPi, in combination with radiation, platinum-based drugs, DNA-PKcs inhibitor, PD-1/PD-L1 blockage agents, and many other drugs, has been suggested (Glorieux et al., 2017; Moutafi et al., 2021). Building on these premises, multiple ongoing clinical trials are evaluating the efficacy of PARPi in monotherapy or combination therapy of oral cancer. Combinatorial treatments using PARPi and conventional chemotherapy attracted particular interests, as potentially promising opportunities to overcome tumor resistance to either PARPi or chemotherapy alone (Lu et al., 2018; Li et al., 2020; McMullen et al., 2020).

Evidence provided in this study supported the use of PARPi in oral cancer therapy, especially in combination with cisplatin or 5-fluorouracil. PARP1 suppressed the induction of DNA double strand breaks following cisplatin or 5-fluorouracil treatment. This is well in line with the role of PARP1 in single strand break repair, and consistent with the observation of increased cell resistance upon PARP1 expression.

## PARP1 Is Upregulated Upon DNA Damage Treatment in Resistant Oral Cancer Cells

Our study revealed upregulation of PARP1 expression in at least some recurrent oral tumor cells, as one of the underlying mechanisms of treatment resistance and tumor recurrence. Thus, the physiological relevance of PARP1 in oral cancer recurrence provides an additional rationale for PARP1 targeting. Unlike the primary oral tumor cells, recurrent tumor cells gained the capability of inducing PARP1 expression upon cisplatin or 5-fluorouracil treatment. This treatment-induced PARP1 expression can potentially serve as a prognostic biomarker that predicts both tumor resistance to DNA damaging agents, and therapeutic benefits of PARPi in combination therapy.

Regulation of PARP1 gene expression remains to be better understood. DNA damage-induced PARP1 expression, as shown in our studies, was not dependent on ATM/ATR kinase activities. PARP1 upregulation was disrupted by inhibitors of CDK7 and PARP. CDK7 is known to be associated with, and phosphorylate, transcription factors (Fisher, 2019); existing evidence also supported a role of PARP1 in transcriptional regulation (Schiewer and Knudsen, 2014). Interestingly, previous studies of mouse PARP1 expression suggested an autoregulatory model in which PARP1 binds to its own promoter region, and suppresses transcription (Vidaković et al., 2009). Thus, it shall be investigated if PARPi influences its own expression by trapping PARP1 in its promoter region, or through additional

transcriptional factors that are directly or indirectly modulated through PARylation.

Taken together, our studies reported PARP1 upregulation as a clinically relevant mechanism of tumor resistance, and suggested PARPi as promising therapeutic intervention, in combination with chemotherapy. Further delineation of the underlying mechanisms will potentially shed new light on the signaling network of tumor recurrence, and uncover additional drug targets to cripple cancer resistance.

## DATA AVAILABILITY STATEMENT

The raw data supporting the conclusion of this article will be made available by the authors, without undue reservation.

## ETHICS STATEMENT

The animal study was reviewed and approved by the UNMC IACUC.

## AUTHOR CONTRIBUTIONS

FW and AP conceived the study. FW, OG, LW, and AP performed the experiments, and analyzed the data. FW and AP contributed to the writing and data presentation of the manuscript. All authors contributed to the article and approved the submitted version.

## FUNDING

AP is supported by funding from the National Institutes of Health (CA233037; DE030427).

## ACKNOWLEDGMENTS

We thank Dr. James Wahl (University of Nebraska Medical Center, United States) for reagents, Mackenzie Zwiener (University of Nebraska Medical Center) for critical reading of the manuscript.

## REFERENCES

Ali, J., Sabiha, B., Jan, H. U., Haider, S. A., Khan, A. A., and Ali, S. S. (2017). Genetic Etiology of Oral Cancer. *Oral Oncol.* 70, 23–28. doi:10.1016/j.oraloncology.2017.05.004

Brenner, J. C., Graham, M. P., Kumar, B., Saunders, L. M., Kupfer, R., Lyons, R. H., et al. (2010). Genotyping of 73 UM-SCC Head and Neck Squamous Cell Carcinoma Cell Lines. *Head Neck* 32, 417–426. doi:10.1002/hed.21198

Casiglia, J., and Woo, S. B. (2001). A Comprehensive Review of Oral Cancer. *Gen. Dent* 49, 72–82.

Ciccia, A., and Elledge, S. J. (2010). The DNA Damage Response: Making it Safe to Play with Knives. *Mol. Cel.* 40, 179–204. doi:10.1016/j.molcel.2010.09.019

Dulaney, C., Marcrom, S., Stanley, J., and Yang, E. S. (2017). Poly(ADP-ribose) Polymerase Activity and Inhibition in Cancer. *Semin. Cel Developmental Biol.* 63, 144–153. doi:10.1016/j.semcdb.2017.01.007

Dylawerska, A., Barczak, W., Wegner, A., Golusinski, W., and Suchorska, W. M. (2017). Association of DNA Repair Genes Polymorphisms and Mutations with Increased Risk of Head and Neck Cancer: a Review. *Med. Oncol.* 34, 197. doi:10.1007/s12032-017-1057-4

Fisher, R. P. (2019). Cdk7: a Kinase at the Core of Transcription and in the Crosshairs of Cancer Drug Discovery. *Transcription* 10, 47–56. doi:10.1080/21541264.2018.1553483

Gau, M., Karabajakian, A., Reverdy, T., Neidhardt, E.-M., and Fayette, J. (2019). Induction Chemotherapy in Head and Neck Cancers: Results and Controversies. *Oral Oncol.* 95, 164–169. doi:10.1016/j.oraloncology.2019.06.015

Glorieux, M., Dok, R., and Nuyts, S. (2017). Novel DNA Targeted Therapies for Head and Neck Cancers: Clinical Potential and Biomarkers. *Oncotarget* 8, 81662–81678. doi:10.18632/oncotarget.20953

Hernandez, A. L., Young, C. D., Bian, L., Weigel, K., Nolan, K., Frederick, B., et al. (2020). PARP Inhibition Enhances Radiotherapy of SMAD4-Deficient Human Head and Neck Squamous Cell Carcinomas in Experimental Models. *Clin. Cancer Res.* 26, 3058–3070. doi:10.1158/1078-0432.ccr-19-0514

Jackson, S. P., and Bartek, J. (2009). The DNA-Damage Response in Human Biology and Disease. *Nature* 461, 1071–1078. doi:10.1038/nature08467

Jalal, S., Earley, J. N., and Turchi, J. J. (2011). DNA Repair: from Genome Maintenance to Biomarker and Therapeutic Target. *Clin. Cancer Res.* 17, 6973–6984. doi:10.1158/1078-0432.ccr-11-0761

Jenkins, G., O'Byrne, K. J., Panizza, B., and Richard, D. J. (20132013). Genome Stability Pathways in Head and Neck Cancers. *Int. J. Genomics* 2013, 464720. doi:10.1155/2013/464720

Johnson, D. E., Burtness, B., Leemans, C. R., Lui, V. W. Y., Bauman, J. E., and Grandis, J. R. (2020). Head and Neck Squamous Cell Carcinoma. *Nat. Rev. Dis. Primers* 6, 92. doi:10.1038/s41572-020-00224-3

Li, H., Liu, Z.-Y., Wu, N., Chen, Y.-C., Cheng, Q., and Wang, J. (2020). PARP Inhibitor Resistance: the Underlying Mechanisms and Clinical Implications. *Mol. Cancer* 19, 107. doi:10.1186/s12943-020-01227-0

Liang, Y., Lin, S.-Y., Brunicardi, F. C., Goss, J., and Li, K. (2009). DNA Damage Response Pathways in Tumor Suppression and Cancer Treatment. *World J. Surg.* 33, 661–666. doi:10.1007/s00268-008-9840-1

Lord, C. J., and Ashworth, A. (2017). PARP Inhibitors: Synthetic Lethality in the Clinic. *Science* 355, 1152–1158. doi:10.1126/science.aam7344

Lord, C. J., and Ashworth, A. (2012). The DNA Damage Response and Cancer Therapy. *Nature* 481, 287–294. doi:10.1038/nature10760

Lu, Y., Liu, Y., Pang, Y., Pacak, K., and Yang, C. (2018). Double-barreled Gun: Combination of PARP Inhibitor with Conventional Chemotherapy. *Pharmacol. Ther.* 188, 168–175. doi:10.1016/j.pharmthera.2018.03.006

Luo, X., and Kraus, W. L. (2012). On PAR with PARP: Cellular Stress Signaling through poly(ADP-Ribose) and PARP-1. *Genes Dev.* 26, 417–432. doi:10.1101/gad.183509.111

Luong, K. V., Wang, L., Roberts, B. J., Wahl III, J. K., and Peng, A. (2016). Cell Fate Determination in Cisplatin Resistance and Chemosensitization. *Oncotarget* 7, 23383–23394. doi:10.18632/oncotarget.8110

Martin-Hernandez, K., Rodriguez-Vargas, J.-M., Schreiber, V., and Dantzer, F. (2017). Expanding Functions of ADP-Ribosylation in the Maintenance of Genome Integrity. *Semin. Cel Developmental Biol.* 63, 92–101. doi:10.1016/j.semcdb.2016.09.009

McMullen, M., Karakasis, K., Madariaga, A., and Oza, A. M. (2020). Overcoming Platinum and PARP-Inhibitor Resistance in Ovarian Cancer. *Cancers (Basel)* 12. doi:10.3390/cancers12061607

Moutafi, M., Economopoulou, P., Rimm, D., and Psyrri, A. (2021). PARP Inhibitors in Head and Neck Cancer: Molecular Mechanisms, Preclinical and Clinical Data. *Oral Oncol.* 117, 105292. doi:10.1016/j.oraloncology.2021.105292

Psyrri, A., Gkotzamanidou, M., Papaxoinis, G., Krikoni, L., Economopoulou, P., Kotsantis, I., et al. (2021). The DNA Damage Response Network in the Treatment of Head and Neck Squamous Cell Carcinoma. *ESMO Open* 6, 100075. doi:10.1016/j.esmoop.2021.100075

Ray Chaudhuri, A., and Nussenzweig, A. (2017). The Multifaceted Roles of PARP1 in DNA Repair and Chromatin Remodelling. *Nat. Rev. Mol. Cel Biol* 18, 610–621. doi:10.1038/nrm.2017.53

Schiewer, M. J., and Knudsen, K. E. (2014). Transcriptional Roles of PARP1 in Cancer. *Mol. Cancer Res.* 12, 1069–1080. doi:10.1158/1541-7786.mcr-13-0672

Vidaković, M., Gluch, A., Qiao, J., Oumard, A., Frisch, M., Poznanović, G., et al. (2009). PARP-1 Expression in the Mouse Is Controlled by an Autoregulatory Loop: PARP-1 Binding to an Upstream S/MAR Element and to a Novel Recognition Motif in its Promoter Suppresses Transcription. *J. Mol. Biol.* 388, 730–750. doi:10.1016/j.jmb.2009.03.032

Wang, F., Wang, L., Fisher, L. A., Li, C., Wang, W., and Peng, A. (2019). Phosphatase 1 Nuclear Targeting Subunit (PNUTS) Regulates Aurora Kinases and Mitotic Progression. *Mol. Cancer Res.* 17, 10–19. doi:10.1158/1541-7786.mcr-17-0670

Wang, F., Zhu, S., Fisher, L. A., Wang, L., Eurek, N. J., Wahl, J. K., 3rd, et al. (2019). Phosphatase 1 Nuclear Targeting Subunit Mediates Recruitment and Function of Poly (ADP-Ribose) Polymerase 1 in DNA Repair. *Cancer Res.* 79, 2526–2535. doi:10.1158/0008-5472.can-18-1673

Wang, L., Mosel, A. J., Oakley, G. G., and Peng, A. (2012). Deficient DNA Damage Signaling Leads to Chemoresistance to Cisplatin in Oral Cancer. *Mol. Cancer Ther.* 11, 2401–2409. doi:10.1158/1535-7163.mct-12-0448

Wang, Y., Spitz, M. R., Lee, J. J., Huang, M., Lippman, S. M., and Wu, X. (2007). Nucleotide Excision Repair Pathway Genes and Oral Premalignant Lesions. *Clin. Cancer Res.* 13, 3753–3758. doi:10.1158/1078-0432.ccr-06-1911

Zhou, B. B. S., Anderson, H. J., and Roberge, M. (2003). Targeting DNA Checkpoint Kinases in Cancer Therapy. *Cancer Biol. Ther.* 2, S16–S22. doi:10.4161/cbt.200

**Conflict of Interest:** The authors declare that the research was conducted in the absence of any commercial or financial relationships that could be construed as a potential conflict of interest.

**Publisher's Note:** All claims expressed in this article are solely those of the authors and do not necessarily represent those of their affiliated organizations, or those of the publisher, the editors and the reviewers. Any product that may be evaluated in this article, or claim that may be made by its manufacturer, is not guaranteed or endorsed by the publisher.

frontiers in Cell and Developmental Biology

REVIEW
published: 14 January 2022
doi: 10.3389/fcell.2021.801200

# Beyond PARP1: The Potential of Other Members of the Poly (ADP-Ribose) Polymerase Family in DNA Repair and Cancer Therapeutics

*Iain A. Richard*[1], *Joshua T. Burgess*[1], *Kenneth J. O'Byrne*[1,2] *and Emma Bolderson*[1]*

[1]Cancer and Ageing Research Program (CARP), Centre for Genomics and Personalised Health (CGPH), Queensland University of Technology (QUT), Brisbane, QLD, Australia, [2]Princess Alexandra Hospital, Brisbane, QLD, Australia

The proteins within the Poly-ADP Ribose Polymerase (PARP) family encompass a diverse and integral set of cellular functions. PARP1 and PARP2 have been extensively studied for their roles in DNA repair and as targets for cancer therapeutics. Several PARP inhibitors (PARPi) have been approved for clinical use, however, while their efficacy is promising, tumours readily develop PARPi resistance. Many other members of the PARP protein family share catalytic domain homology with PARP1/2, however, these proteins are comparatively understudied, particularly in the context of DNA damage repair and tumourigenesis. This review explores the functions of PARP4,6-16 and discusses the current knowledge of the potential roles these proteins may play in DNA damage repair and as targets for cancer therapeutics.

**Keywords: PARP, cancer, DNA damage, DNA repair, genomic stability, tumourigenesis**

OPEN ACCESS

***Edited by:***
*Jianjun Zhao,*
*Lerner Research Institute,*
*United States*

***Reviewed by:***
*Ciler Celik-Ozenci,*
*Koç University, Turkey*
*Hiroaki Wakimoto,*
*Massachusetts General Hospital and Harvard Medical School, United States*
*Jing Luo,*
*Tianjin Medical University Cancer Institute and Hospital, China*

***Correspondence:**
*Emma Bolderson*
*emma.bolderson@qut.edu.au*

***Specialty section:***
*This article was submitted to Molecular and Cellular Pathology, a section of the journal Frontiers in Cell and Developmental Biology*

***Received:*** *25 October 2021*
***Accepted:*** *21 December 2021*
***Published:*** *14 January 2022*

***Citation:***
*Richard IA, Burgess JT, O'Byrne KJ and Bolderson E (2022) Beyond PARP1: The Potential of Other Members of the Poly (ADP-Ribose) Polymerase Family in DNA Repair and Cancer Therapeutics. Front. Cell Dev. Biol. 9:801200. doi: 10.3389/fcell.2021.801200*

## INTRODUCTION

As global populations age, cancer has emerged as the most prominent cause of death worldwide (Lin et al., 2019; Aburto et al., 2020; Sung et al., 2021). Therefore, identifying new therapeutic targets and designing non-invasive molecular mechanisms to inhibit and eliminate cancer growth is a major objective of academic and pharmaceutical teams worldwide. One such protein that has become a new therapeutic cancer target in recent years is Poly (ADP-ribose) Polymerase 1 (PARP1), which belongs to the PARP protein family. The members of this protein family have been associated with DNA repair, genomic instability and as targets for cancer therapy (D'Amours et al., 1999; Amé et al., 2004; Berti et al., 2013; Morales et al., 2014; Schlacher, 2017). Supporting this, PARP1 has emerged as a potent cancer target in ovarian and breast cancers. Since much is known about PARP1-3 (Bryant et al., 2005; Farmer et al., 2005; Murai et al., 2012; Ray Chaudhuri and Nussenzweig, 2017; Alemasova and Lavrik, 2019; Rodriguez-Vargas et al., 2019; Bilokapic et al., 2020) and the Tankyrases (PARP5a/5b) (Lakshmi et al., 2017; Li et al., 2019), this review will focus on the lesser-studied PARP family members, their roles in maintenance of genomic stability and cellular homeostasis, and their potential as cancer targets (Hottiger et al., 2010; Morales et al., 2014; Xu et al., 2020; Challa et al., 2021).

## THE PARP FAMILY

The PARP protein family was initially described in 1963 (Chambon et al., 1963) and the crystal structure of the PARP1 catalytic domain was later elucidated in 1996 (Ruf et al., 1996). This unique

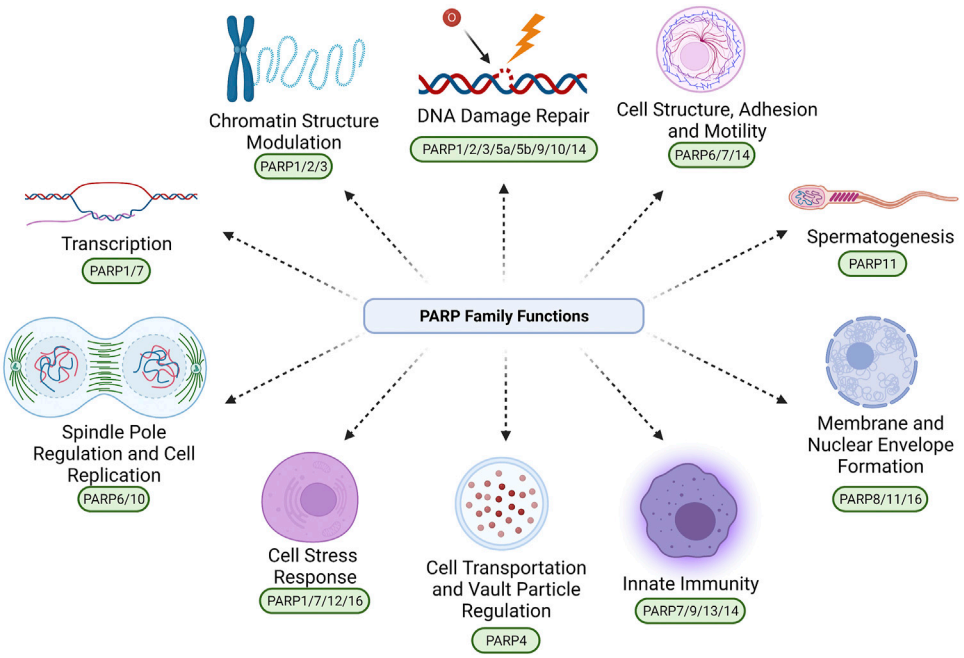


**FIGURE 1 |** The confirmed and proposed diverse roles of the PARP protein family. These roles include: DNA Damage Repair (PARP1/2/3/5a/5b/9/10/14), Cell Structure, Adhesion and Motility (PARP6/7/14), Spermatogenesis (PARP11), Membrane and Nuclear Envelope Formation (PARP8/11/16), Innate Immunity (PARP7/9/13/14), Cell Transportation and Vault Particle Regulation (PARP4), Cell Stress Response (PARP1/7/12/16), Spindle Pole Regulation and Cell Replication (PARP6/10), Transcription (PARP1/7), and Chromatin Structure Modulation (PARP1/2/3). Due to the large diversity of PARP activity, it is likely that PARPs are also involved in biological processes beyond those exemplified in this figure, that are yet to be fully elucidated. Created with BioRender.com.

family consists of 17 proteins to date (Amé et al., 2004; Hottiger et al., 2010; Morales et al., 2014; Challa et al., 2021), excluding the highly diverged PARP homologue tRNA 2′-phosphotransferase 1 (TRPT1) (Hottiger et al., 2010). The full range of functionality of this protein family has not been fully elucidated, however, they have all been shown (with the exception of PARP13) to catalyse the transfer of ADP-ribose (Morales et al., 2014) to substrates, via the use of nicotinamide adenine dinucleotide (NAD+) as a metabolic substrate (Hottiger et al., 2010; Morales et al., 2014; Gupte et al., 2017; Cohen, 2020). This modification is referred to as ADP ribosylation (ADPr). ADPr has so far been identified as important in many cellular processes, including transcription, chromatic structure modulation, replication, recombination, and DNA damage repair (D'Amours et al., 1999; Morales et al., 2014).

PARPs fall into two main categories depending on the (ADPr) modification they produce. These categories are mono-[ADPr] (MAR), and Poly-[ADPr] (PAR) (**Figure 2**). This difference is mechanistically important in biological processes. PAR ribosylation modifications create branched elongated chains that commonly act as signaling molecules (Ruf et al., 1996; Amé et al., 2004; Hottiger et al., 2010; Vyas et al., 2013). Current studies indicate that only PARPs with a H-Y-E amino acid triad domain can produce PAR modifications, due to the glutamic acid residue (E) facilitating the process of producing these elongated ribosylation chains (Hottiger et al., 2010; Challa et al., 2021). However, it is important to note that PARP3 contains a H-Y-E domain motif, but does not produce PAR chains, suggesting that the motif is not the only structural driving factor of PARylation (Hottiger et al., 2010; Vyas et al., 2014; Challa et al., 2021). There is less data surrounding the functional importance of MAR modifications. However, MAR modifications typically inhibit target protein function, which suggests a direct regulatory role (refer to **Table 1** for PARP specific catalytic activity). Despite this fundamental difference, both PAR and MAR modifications utilise NAD+ as a substrate (Corda and Di Girolamo, 2003; Hottiger et al., 2010; Cohen, 2020). The PARP protein family is also involved in the formation of non-membranous structures (Amé et al., 2004; Vyas et al., 2013; Catara et al., 2017; Challa et al., 2021). These structures include: spindle poles, RNA granules, and DNA repair foci (Catara et al., 2017).

PARP1-3 have been identified as regulatory proteins in single-strand break repair pathways (Fisher et al., 2007; Hanzlikova et al., 2018; Rose et al., 2020). In recent years PARP inhibitors (PARPi) have been developed as a novel targeted cancer therapeutic (Dziadkowiec et al., 2016; Rose et al., 2020). These inhibitors work on tumours that are deficient in the double-strand break repair pathway of homologous recombination, caused by the dysfunction of proteins such as *BRCA1/2*, via promotor methylation or gene mutation (Dziadkowiec et al., 2016; Rose et al., 2020). These defects can be used to target tumours using PARPi, that bind to the NAD+ binding domain of several PARPs, predominantly PARP1/2, inhibiting their catalytic activity and trapping them on DNA (Dziadkowiec et al., 2016; Ronson et al., 2018; Rose et al., 2020). This inhibition can be used as a selective target in *BRAC1/2* deficient cancer cells leading to a

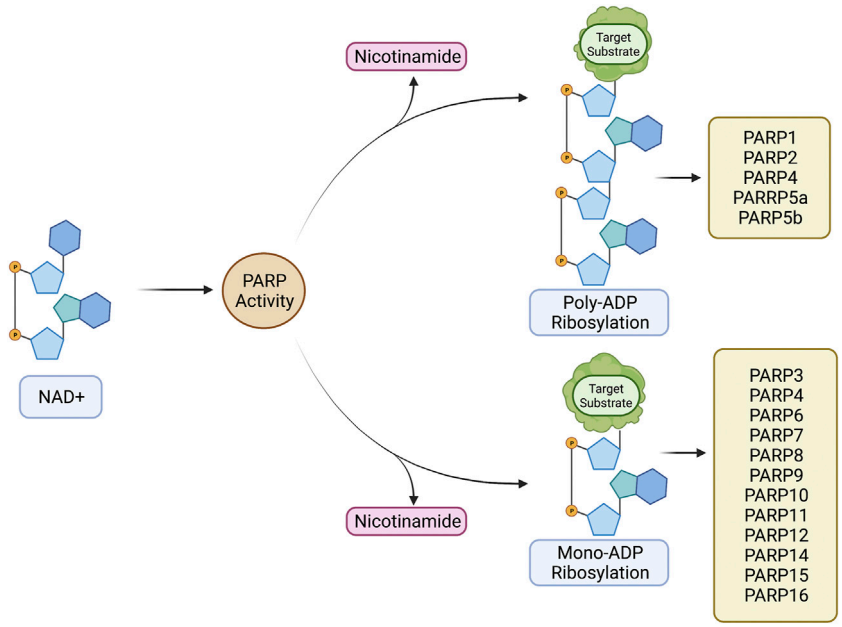


**FIGURE 2 |** PARP family-dependent poly and mono ADP ribosylation. These processes comprise conversion of NAD+ to a ribosylation modification via PARP catalytic activity, producing nicotinamide as a biproduct. PARP1/2/4/5a/5b have been experimentally shown to produce poly-ADP ribosylation modifications. PARP3/4/6/7/8/9/10/11/12/14/15/16 have been experimentally shown to produce mono-ADP ribosylation modifications. Created with BioRender.com.

buildup of highly cytotoxic unrepairable double-strand breaks, resulting in cell death. This review will examine the potential of other members of the PARP family as targets for cancer therapy.

## THE ROLES OF THE PARP FAMILY IN CELLULAR HOMEOSTASIS: IMPLICATIONS FOR TUMOURIGENESIS AND CANCER THERAPY

The proteins within the PARP family function to maintain cellular homeostasis through their involvement in a diverse array of biological pathways, beyond DNA damage repair (**Figure 1**). Through these diverse pathways the upregulation, depletion or mutation of these unique proteins can promote tumourigenesis. Although their catalytic domains share homology, PARP proteins vary widely in size and structure promoting a rich diversity of functions. PARPs range from 36.38 kDa (PARP16) to 202.8 kDa (PARP14) in size (**Table 1**). Their catalytic activity also varies, PARP1-2/4/5a/5b produce PAR modifications, whereas PARP3/4/6-12/14-16 produce MAR modifications (**Figure 2**; **Table 1**).

Due to its MARylation activity (**Figure 2**; **Table 1**), PARP4 has been categorized as a mono-[ADP-ribosyl] transferase (MART), however, PARP4 is not currently included in any PARP sub-family classification (**Figure 3**). Notably, this MART classification is true despite PARP4 having a H-Y-E catalytic triad domain which is commonly associated with PARylation (Vyas et al., 2013; Challa et al., 2021). Being a MART, it is likely that PARP4 is involved in protein regulation and transport (Challa et al., 2021). Supporting this, a study has implicated PARP4 in the regulation of vault ribonucleoprotein particle function (Kickhoefer et al., 1999). Interestingly, PARP4 begins producing PAR chains after re-localising to vault particles (Kickhoefer et al., 1999; Vyas et al., 2014). Vault particles are comparatively large highly conserved biological structures, comprising of hollow barrel structures, around 13 MDa in size, that are believed to be involved in intracellular transport of materials (Kickhoefer et al., 1999; Mossink et al., 2003; Woodward et al., 2015). In relation to cancer, a study found that two PARP4 mutations were found in 43% of their cohort diagnosed with breast and thyroid cancer (Ikeda et al., 2016). Conversely, these mutations were only present in 0.5% of the control cohort. Low PARP4 levels were also associated with poorer prognosis (Ikeda et al., 2016). This suggests that PARP4 may have a role in suppressing tumourigenesis.

Although several of the clinically approved PARP inhibitors also target PARP4, in addition to PARP1-3, it is unclear what the effect of inhibiting PARP4 would have on tumour cells. However, a recent study describes the rational design of a new inhibitor to target PARP4 via its unique threonine residue in the nicotinamide sub-pocket (Kirby et al., 2021). The study found that the AEP07 compound had a 12-fold selectivity for PARP4 over other PARP family members and may form the basis for the further investigation of the activity and development of specific PARP4 inhibitors for therapeutic applications (Kirby et al., 2021).

Like PARP4, PARP6 produces MAR modifications (**Figure 2**; **Table 1**). Due to its unique structure it currently does not belong to any sub-family classification (**Figure 3**). However, recent

**TABLE 1 |** Overview of PARP family structure and basic function.

| Name | Other names | Molecular weight (Da) | Amino acid length | Catalytic triad sequence | Type of ribosylation activity (PAR or MAR) | DNA dependent activation | Inhibitors available—FDA approval status |
|---|---|---|---|---|---|---|---|
| PARP1 | PARP, ARTD1 | 113,084 | 1,014 | H-Y-E Hottiger et al. (2010), Challa et al. (2021) | PAR Ko and Ren (2012) | Yes De Vos et al. (2012), Vyas et al. (2013) | Yes—Approved for prostate cancer, breast cancer, ovarian cancer and gynecologic cancer. Sisay and Edessa (2017), Dal Molin et al. (2018), Cortesi et al. (2021) |
| PARP2 | ARTD2 | 66,206 | 583 | H-Y-E Hottiger et al. (2010), Challa et al. (2021) | PAR Ali et al. (2016) | Yes De Vos et al. (2012), Ali et al. (2016) | Yes - Approved for prostate cancer, breast cancer, ovarian cancer and gynecologic cancer. Sisay and Edessa (2017), Dal Molin et al. (2018), Cortesi et al. (2021) |
| PARP3 | ARTD3 | 60,089 | 533 | H-Y-E Hottiger et al. (2010), Challa et al. (2021) | MAR Rodriguez-Vargas et al. (2019), Challa et al., 2021) | Yes De Vos et al. (2012) | Yes—Approved for ovarian cancer Sisay and Edessa (2017), Dal Molin et al. (2018) |
| PARP4 | vPARP, ARTD4 | 37,288 | 327 | H-Y-E Hottiger et al. (2010), Challa et al. (2021) | MAR (PAR when localised to vault particles) Kickhoefer et al. (1999); Challa et al., 2021) | No | Yes—Not FDA approved Dal Molin et al. (2018), Kirby et al. (2021) |
| PARP5a | TNKS1, ARTD5 | 142,039 | 1,327 | H-Y-E Hottiger et al. (2010), Haikarainen et al. (2014) | PAR Haikarainen et al. (2014) | Postulated (De Vos et al. (2012), Haikarainen et al. (2014) | Yes—Not FDA approved. Sisay and Edessa (2017), Dal Molin et al. (2018), Cortesi et al. (2021) |
| PARP5b | TNKS2, ARTD6 | 126,918 | 1,166 | H-Y-E Hottiger et al. (2010), Haikarainen et al. (2014) | PAR Haikarainen et al. (2014) | Postulated De Vos et al. (2012), Haikarainen et al. (2014) | Yes—Not FDA approved. Sisay and Edessa (2017), Dal Molin et al. (2018), Cortesi et al. (2021) |
| PARP6 | ARTD17 | 71,115 | 630 | H-Y-I Hottiger et al. (2010), Challa et al. (2021) | MAR Challa et al. (2021) | Undetermined | Yes—Not FDA approved. Wang et al. (2018) |
| PARP7 | tiPARP, ARTD14 | 76,227 | 657 | H-Y-I Hottiger et al. (2010), Challa et al. (2021) | MAR Challa et al. (2021) | Undetermined | Yes—Not FDA approved. Gozgit et al. (2021) |
| PARP8 | ARTD16 | 95,871 | 854 | H-Y-I Hottiger et al. (2010), Challa et al. (2021) | MAR Challa et al. (2021) | Undetermined | No |
| PARP9 | BAL1, ARTD9 | 96,343 | 854 | Q-Y-T (Hottiger et al., 2010; Xu et al., 2020; Xing et al., 2021) | MAR Yang et al. (2017) | Undetermined | No |
| PARP10 | ARTD10 | 109,998 | 1,025 | H-Y-I Hottiger et al. (2010), Challa et al. (2021) | MAR Challa et al. (2021) | No Vyas et al. (2013) | Yes—Not FDA approved.Lemke et al. (2020) |
| PARP11 | ARTD11 | 39,597 | 338 | H-Y-I Hottiger et al. (2010), Challa et al. (2021) | MAR Challa et al. (2021) | Undetermined | Yes—Not FDA approved. Kirby et al. (2018) |
| PARP12 | ARTD12 | 79,064 | 701 | H-Y-I Hottiger et al. (2010), Challa et al. (2021) | MAR Challa et al. (2021) | Undetermined | Yes—(Nonselective)—Not approved for PARP12. Dal Molin et al. (2018) |
| PARP13 | ZAP, ARTD13 | 101,431 | 902 | Y-Y-V Hottiger et al. (2010), Morales et al. (2014), Challa et al. (2021) | Catalytically Inactive—MAR Postulated Hottiger et al. (2010), Morales et al. (2014), Challa et al. (2021) | Undetermined | No |
| PARP14 | BAL2, ARTD8 | 202,800 | 1,801 | H-Y-L Hottiger et al. (2010), Challa et al. (2021) | MAR Challa et al. (2021) | Undetermined | Yes—Not FDA approved. Schenkel et al. (2021) |
| PARP15 | BAL3, ARTD4 | 74,576 | 678 | H-Y-L Hottiger et al. (2010), Challa et al. (2021) | MAR Challa et al. (2021) | Undetermined | Yes (Nonselective) - Not FDA approved for PARP15. Dal Molin et al. (2018) |
| PARP16 | ARTD15 | 36,383 | 332 | H-Y-Y Hottiger et al. (2010), Challa et al. (2021) | MAR Challa et al. (2021) | Undetermined | Yes (Nonselective)—Not FDA approved for PARP16. Sisay and Edessa (2017), Dal Molin et al. (2018), Cortesi et al. (2021), Palve et al. (2021) |

*Molecular Weight and Amino Acid Length were derived from UniProt database*

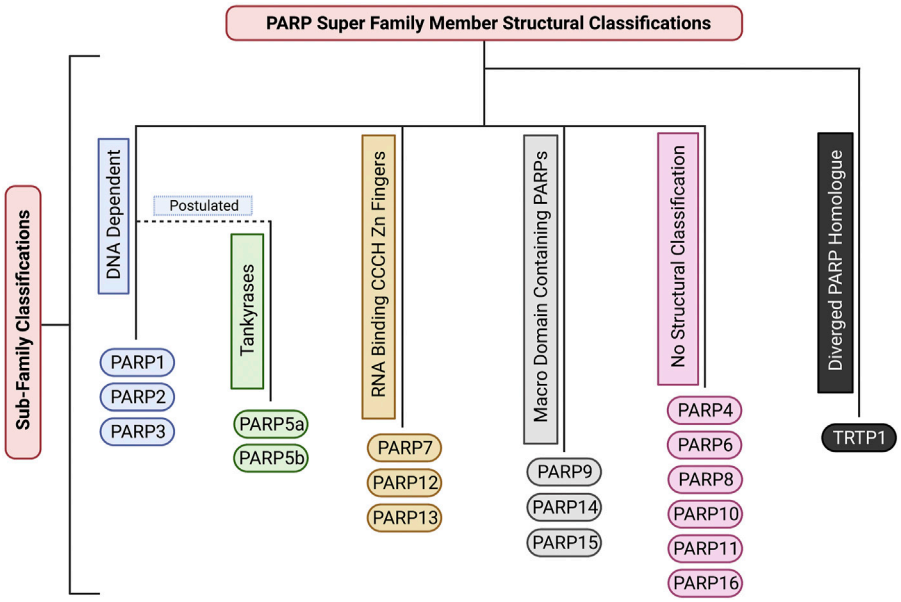


**FIGURE 3 |** The structural sub-classifications of the PARP family. These classifications include: DNA Dependent PARPs (PARP1/2/3), Tankyrases (PARP5a/5b), RNA Binding CCCH Zn Finger PARPs (PARP7/12/13), Macro Domain Containing PARPs (PARP9/14/15), PARPs with no sub-classification (PARP4/6/8/10/11/16), and Diverged PARP Homologues (TRTP1). Created with BioRender.com.

studies have elucidated that PARP6 is involved in some key cellular functions. One study showed that PARP6 enzyme inhibition induces Multi-Polar Spindle (MPS) formation and centrosome defects (Wang et al., 2018). Inhibiting other PARPs such as: PARP1, PARP2, PARP3, PARP5a and PARP5b, did not create the same phenotype, providing strong evidence that PARP6 plays a unique role in the regulation of MPS induction (Wang et al., 2018). Furthermore, a previous study demonstrated that PARP6 is a negative regulator of cell proliferation and that PARP6 expression leads to accumulation of cells in S-phase (Tuncel et al., 2012). While at the time the reason for this was unclear, it is likely that this was caused by PARP6s involvement in MPS induction and centrosome homeostasis (Tuncel et al., 2012; Wang et al., 2018). PARP6 expression levels have been observed to be lower in colorectal cancer compared to neighboring non-cancerous tissue (Qi et al., 2016). It is suggested this may be due to hypermethylation of the PARP6 promotor region (Qi et al., 2016). Additionally, this paper also found that PARP6 expression is negatively correlated to Survivin expression. Survivin is an inhibitor of apoptosis (IAP) family member (Jaiswal et al., 2015). This anti-apoptotic property is largely suggested to be why high expression of Survivin is correlated with cancer and tumourigenesis, implicating PARP6 as a tumour suppressor (Jaiswal et al., 2015). However, a later paper, suggested that PARP6 positively regulates Survivin in gastric cancer, with higher expression of PARP6 showing a strong correlation with increased carcinogenic cell properties including: motility, proliferation, migration and invasion (Sun et al., 2018). These studies suggest contradicting roles for PARP6 in the regulation of Survivin and this may be explained by PARP6 having different regulatory roles in different tissue types. However, further research is required to confirm this. A potent PARP6 inhibitor, AZ0108 has been found to selectively inhibit PARP6 catalytic activity (Wang et al., 2018). This inhibitor has been found to induce MPS error-induced apoptosis in breast cancer cells *in vitro* and inhibition of xenograft tumour growth *in vivo* (Wang et al., 2018). Additionally, via mass spectrometry it was found that Checkpoint Kinase 1 (Chk1) (a protein involved in the regulation of the cell cycle and DNA damage response) is a substrate of PARP6. Inhibiting PARP6 activity with AZ0108 leads to an increase in Chk1 phosphorylation and defects in mitotic signalling (Wang et al., 2018). This provides strong evidence that it could be worthwhile investigating targeting PARP6 for cancer therapy in the future.

PARP7 adds MAR modifications (**Figure 2**; **Table 1**) to its substrates and belongs to the CCCH-Zn finger PARP sub-family (**Figure 3**) (Vyas et al., 2013; Challa et al., 2021). It has been determined that the Zinc finger of PARP7 has a high binding affinity for RNA, suggesting a potential regulatory role in transcription (Rasmussen et al., 2021). Depletion of PARP7 leads to an increase of cells in mitosis, but not reduced viability. This suggests that cells are still able to undergo mitosis, but that mitosis progresses more slowly in the absence of PARP7 (Vyas et al., 2013; Vyas et al., 2014). PARP7 has also been shown to be a regulator of innate immunity, transcription factor activity and stress responses (Xue et al., 2018; Palavalli Parsons et al., 2021; Rasmussen et al., 2021). A recent study has shown that PARP7 is a suppressor of aryl hydrocarbon receptor (AHR) and a positive regulator of Liver X Receptors (LXRs), type I interferons (IFN-Is), and hypoxia-inducible factor I (HIF-1a), suggesting it may have a role in innate immunity. AHR, LXRs, IFN-Is and HIF1a have all been shown to have a direct link to

tumourigenesis (Lin and Gustafsson, 2015; Jun et al., 2017; Xue et al., 2018; Aricò et al., 2019; Rasmussen et al., 2021). PARP7 expression levels are typically increased in a wide range of cancers, such as: colorectal cancer, head and neck cancer, liver cancer and myeloma (Cheng et al., 2019). Whereas low PARP7 expression levels were found in: bladder cancer, cervical cancer, esophageal cancer, leukemia, lung cancer, lymphoma, melanoma, and in particular breast cancer (Cheng et al., 2019). Notably, high PARP7 expression levels in breast cancer have been correlated with improved patient outcome and patients with advanced breast cancer have very low expression of PARP7 (Cheng et al., 2019). Additionally, study of the PARP7 catalytic domain suggests it plays a regulatory role in microtubule control via MARylation modifications. One study found that mutation of the PARP7 catalytic site led to an overall increase in microtubule stability, resulting in slowed growth and migration of ovarian cancer cells (Palavalli Parsons et al., 2021). A recent study identified a potent and selective inhibitor of PARP7, RBN-2397. This compound has shown promising results in lung cancer xenografts, causing tumour regression after treatment (Gozgit et al., 2021). A phase 1 clinical trial on metastatic or advanced-stage solid malignant tumours is underway to assess its efficacy. In addition, another phase 1 clinical trial is underway to examine the efficacy of RBN-2397 against advanced squamous non-small cell lung carcinoma in combination with immunotherapy, highlighting the potential of PARP7 as a cancer therapy target.

PARP8 is catalytically capable of producing MAR modifications (**Figure 2**; **Table 1**) and at present is not catagorised into any structural sub-classification (**Figure 3**) (Hottiger et al., 2010). PARP8 is primarily localised on the nuclear envelope for the majority of the cell cycle but localises to centrosomes and spindle poles during mitosis. Consistent with this, depletion of PARP8 is associated with mitotic and nuclear morphology defects and a decrease in cellular viability, although the mechanism behind this is unknown (Vyas et al., 2013; Vyas et al., 2014; Challa et al., 2021). To date the biological pathways PARP8 is involved in have not been uncovered. Structural modelling and experimental analysis have revealed that PARP8 has MARylation activity, although its substrates have not been identified (Hottiger et al., 2010; Vyas et al., 2014; Challa et al., 2021). To date, a cellular function for PARP8 has not been established and no PARP8 inhibitors have been investigated for anti-cancer activity or clinically developed.

PARP9 was originally suggested to be catalytically inactive due to it's inability to undergo auto-ADP-ribosylation (Vyas et al., 2014), but it was subsequently confirmed to have MAR activity (**Figure 2**; **Table 1**) (Yang et al., 2017). Similarly, to several other PARPs, PARP9 contains macrodomains that bind ADPr and PAR (**Figure 3**). In addition to its proposed role in DNA repair, a recent study showed a function for PARP9 in the detection of RNA viruses (Xing et al., 2021). PARP9 has also been implicated in chemoresistance in prostate cancer and diffuse large B cell lymphoma (Camicia et al., 2013; Bachmann et al., 2014). The levels of PARP9 are also elevated in breast cancer and its depletion inhibited the migration of breast cancer cells (Tang et al., 2018). To the best of our knowledge, no PARP9 inhibitors have been identified or investigated, to date.

PARP10 is a MAR transferase (MART) (**Figure 2**; **Table1**) (Kleine et al., 2008; Vyas et al., 2013; Challa et al., 2021). PARP10 is not structurally categorised in any PARP family sub-classifications (**Figure 3**). Up to 70 substrates have been identified for PARP10 (Feijs et al., 2013), however, it is unclear how many of these are genuine substrates *in vivo*. A subsequent study also showed that PARP10 also promotes cellular transformation, proposed to be through the alleviation of replication stress (Schleicher et al., 2018). Supporting this assertion, PARP10 depletion significantly inhibited tumour growth in a mouse xenograft model (Schleicher et al., 2018). A novel PARP10 inhibitor, A82-(CONHMe)-B354, has recently been developed (Lemke et al., 2020). This inhibitor was found to have an IC50 of 6.0 uM via a histone ADP-ribosylation assay. This study also generated a screen of various proposed PARP10 inhibitory molecules using a PARP10 virtual combinatorial library (VCL) (Lemke et al., 2020). These proposed inhibitors require further study to determine their efficacy against tumour cells and whether clinical development would have therapeutic applications (Lemke et al., 2020).

PARP11 is catalytically capable of producing MAR modifications, but has not been assigned to a structural sub-category (**Figure 3**; **Table 1**) (Hottiger et al., 2010). PARP11 is primarily located at nuclear pores, where it co-localises with Nucleoporin153 (NUP153) (Vyas et al., 2014; Meyer-Ficca et al., 2015). PARP11 is important in cellular processes such as maintaining nuclear envelope stability and nuclear remodeling during spermatogenesis (Vyas et al., 2014; Meyer-Ficca et al., 2015) and its activity is essential for spermatid formation in mice (Meyer-Ficca et al., 2015). The silencing of PARP11 resulted in deformed sperm heads due to improper nuclear envelope formation during spermatogenesis, leading to infertility (Meyer-Ficca et al., 2015). A recent study found that ITK7 is a potent and highly selective inhibitor of PARP11 activity (Kirby et al., 2018). Inhibition resulted in disassociation of PARP11 from the nuclear envelope. Further study is needed to establish a clinical application for this potent inhibitor (Kirby et al., 2018).

PARP12 produces MAR modifications (**Figure 2**; **Table 1**) on target proteins and belongs to the Zinc Finger CCCH Domain-Containing Protein sub-family (**Figure 3**) (Shao et al., 2018; Challa et al., 2021). This protein is localised in the Golgi and is punctate in the cytoplasm during interphase (Vyas et al., 2013; Vyas et al., 2014; Buch-Larsen et al., 2020). There is evidence to support a role for PARP12 in the cellular stress response, through a PARP1-dependent pathway. Following oxidative stress PARP12 is translocated from the Golgi to stress granules via a mechanism dependent upon PARP1 activity (Catara et al., 2017). It is hypothesised that PARP12 may have a function in Golgi maintenance under normal cellular conditions and is required to prevent translation under stress conditions. PARP12 may also have a tumour suppressor function and supporting this, low PARP12 expression levels are associated with tumourigenesis (Shao et al., 2018). One study demonstrated that PARP12 depletion via *in vitro* CRISPR-Cas9 modification in QGY-7703 and Huh7 cells promoted liver cancer cell

migration (Shao et al., 2018). This was further supported by an *in vivo* metastasis assay that showed that PARP12 deficiency in mice promoted hepatocellular carcinoma metastasis via the regulation of the epithelial-mesenchymal transition process (Shao et al., 2018). To date, no studies have reported PARP12 selective inhibitors. Given the roles PARP12 plays in tumourigenesis and maintaining cellular homeostasis, identifying selective inhibitors of its activity may be an effective therapeutic strategy for cancer treatment.

PARP13 has no defined catalytic activity, producing neither PAR nor MAR modifications. However, its structure suggests that it is capable of producing MAR modifications (**Table 1**), although this has yet to be experimentally demonstrated (Hottiger et al., 2010). PARP13 belongs to the Zinc Finger CCCH Domain-Containing Protein sub-family (**Figure 3**) and is localized to punctate structures throughout the cell during interphase and is punctate in the cytoplasm during mitosis (Vyas et al., 2013; Vyas et al., 2014; Buch-Larsen et al., 2020; Challa et al., 2021). Depletion of PARP13 has a strong negative impact on cell viability, although the reason for this has not been determined (Vyas et al., 2013; Vyas et al., 2014). PARP13 is involved in specific anti-viral pathways, including recruiting cellular RNA degradation machineries such as poly(A)- specific ribonuclease (PARN) that removes the poly A tail of the viral mRNA (Todorova et al., 2014; Todorova et al., 2015). To date no PARP13 inhibitors have been reported and the impact of its depletion on tumour cell growth has not been investigated.

PARP14 produces mono-ADP ribosylation (MAR) modifications (**Figure 2**; **Table 1**) on target proteins (Vyas et al., 2013; Vyas et al., 2014; Buch-Larsen et al., 2020; Challa et al., 2021). PARP14 is associated with a multitude of disease states, including; cancer, atherosclerosis and the inflammatory response to allergens (Qin et al., 2019). PARP14 is an actin cytoskeleton-regulating, Macro-domain containing PARP (**Figure 3**) (Vyas et al., 2013; Buch-Larsen et al., 2020; Challa et al., 2021). Depletion of PARP14 leads to actin cytoskeletal defects, and overall cell viability defects. One study found that PARP14 depletion caused a phenotype with elongated processes extending from the cell body in approximately 60% of siRNA transfected cells (Vyas et al., 2013). It was hypothesised that this is due to the cells inability to retract and dismantle actin filaments as the cell moves. This provides strong evidence that PARP14 is important in maintaining cytoskeletal structure and cell motility. In addition to cytoskeletal regulation, PARP14 regulates the expression of B-cell survival factors and represses caspase apoptotic pathways to transduce survival signals in murine primary B cells (Cho et al., 2011; Barbarulo et al., 2013). This implicates PARP14 in promoting tumourigenesis via its role as a downstream effector of JNK2 and inhibiting the JNK1-JNK2 pro-apoptotic pathway (Barbarulo et al., 2013). In support of targeting PARP14 to treat cancer, an inhibitor of PARP14, RBN012759, was shown to lead to an inflammatory response in tumour explants, similarly to that induced by immune checkpoint inhibitors (Schenkel et al., 2021). This compound inhibits PARP14 activity at very low concentrations and displays approximately 300-fold selectivity for PARP14 over other highly homologous PARP family members (Schenkel et al., 2021). This makes targeting PARP14 a promising avenue for developing cancer therapeutics (Schenkel et al., 2021). However, further research needs to be conducted to fully elucidate the mode of action and clinical application of this inhibitor.

PARP15 is a catalytically active PARP that produces MAR modifications (**Figure 2**; **Table 1**) and is a member of the macro-PARP subfamily (**Figure 3**) (Vyas et al., 2013; Challa et al., 2021). PARP15 has low protein expression levels in cells and therefore its localisation and the effects of its depletion are unknown (Vyas et al., 2013). Two single nucleotide polymorphisms (SNPs) of PARP15 (*rs6793271, rs17208928*) have been associated with decreased survival rates in patients with acute myeloid leukemia (Lee et al., 2016). Further study is needed to elucidate whether PARP15 is involved in tumourigenesis and if it would be an appropriate target for tumour therapy. To date, no selective inhibitors of PARP15 have been reported.

PARP16 produces MAR modifications (**Figure 2**; **Table 1**) and is the smallest member of the PARP super-family (**Table 1**) (Hottiger et al., 2010). Notably, PARP16 possesses a tail anchor for attachment to membranous structures, which is a unique characteristic within the PARP protein family and such PARP16 is not categorized into any of the other structural sub-families (**Figure 3**) (Vyas et al., 2013; Yang et al., 2020). During interphase it has a punctate localisation and is within the membrane of the endoplasmic reticulum (ER); during mitosis it is punctate in the cytoplasm (Vyas et al., 2013; Vyas et al., 2014; Buch-Larsen et al., 2020). Depletion of PARP16 is associated with a defective membrane phenotype, with 30% of cells exhibiting completely round cell membrane morphology, suggesting a role in membrane structure. GFP-tagged PARP16 has been observed to localise to the ER membrane (Vyas et al., 2013), further supporting that PARP16 is involved in the maintenance or formation of the ER membrane. Failure to maintain proteostasis due to decreased ER efficiency is considered a driving factor of cellular aging and cancer. PARP16 also positively regulates ER stress sensors (PERK and IRE1) during the unfolded protein response (UPR), which is associated with cellular senescence (Yang et al., 2020). As such, inhibition of PARP16 activity in Angeotensin II (Ang II)-treated mice and vascular cells was found to reduce senescence-associated phenotypes (Yang et al., 2020). Ang II plays a key role in regulating the renin-angiotensin system (RAS), an increase in Ang II causes an increase in blood pressure (Benigni et al., 2010). Due to the critical role of PARP16 in the cellular stress response, it has been speculated that PARP16 maybe an efficient cancer target. Supporting this, treatment of a hepatocellular carcinoma cell line with a small molecule inhibitor of PARP16 in combination with agents that induced ER stress led to enhanced apoptosis (Wang et al., 2017). Further investigation of PARP16 inhibitors is required to explore the utility of their use as a cancer therapeutic. PARP16 has been identified as a potent novel target for cancer therapeutics when inhibited in conjunction with PARP1. For example, silencing PARP16 *in vitro* reduced cancer cell survival when cells were treated with the PARP1 inhibitor Olaparib and the WEE1 inhibitor adavosertib (Palve et al., 2021). In addition, chemical proteomics identified PARP16 as a novel secondary target of

PARP inhibitor talazoparib. This raises the possibility that the off-target inhibitory effects of talazoparib on PARP16 may contribute to its potency as a selective cancer therapeutic and may support targeting PARP16 as an anti-cancer therapy (Palve et al., 2021).

## PARP PROTEIN INVOLVEMENT IN THE DNA DAMAGE RESPONSE

DNA Damage repair, and genetic instability are intrinsically linked as hallmarks of cancer. Many members of the PARP protein family have been found to have strong involvement in these pathways. In contrast, many others are still yet to have their functional involvement in DNA damage fully elucidated.

In terms of a potential role for PARP4 in DNA damage, one study examined whether vault proteins relocalised to UV-induced DNA damage and found that PARP4 did not respond to UV irradiation (Kickhoefer et al., 1999). It is possible that PARP4 may respond to other forms of DNA damage, but to date no other experimental evidence has directly implicated PARP4 in DNA damage repair processes. However, PARP4 does contain a BRCT domain (Perina et al., 2014), which is prevalent in many DNA repair proteins, including PARP1, which may support a role for PARP4 in DNA repair and tumourigenesis (Jean et al., 1999; Perina et al., 2014; Hu et al., 2019).

There is currently no literature supporting a role for PARP6 in the DNA damage response and further study is required to establish what, if any, role it has in this process.

A direct role for PARP7 in DNA repair has not been confirmed experimentally, however a recent study detected several DNA repair proteins (including PARP1, and PARP2) as substrates of PARP7 MARylation, suggesting that PARP7 may have a regulatory role in DNA repair (Palavalli Parsons et al., 2021). PARP7 also undergoes auto-PARylation and has been shown to have affinity for PARP4 as a substrate (Palavalli Parsons et al., 2021). Auto-PARylation is heavily associated with DNA Damage repair related PARPs such as: PARP1. Moreover, the CCCH-type Zinc Finger of PARP7 suggests it may have a high binding affinity for RNA, raising the possibility that PARP7 could be a potential regulator of transcription or RNA-dependent DNA repair. However, more studies need to be conducted to establish these potential roles.

Supporting a role for PARP8 in DNA repair, auto-PARylation of a PARP8 cysteine residue occurs in response to oxidative stress induced by $H_2O_2$ treatment, suggesting that, like PARP1, it may have a role in the oxidative stress response (Buch-Larsen et al., 2020). Further investigation is needed to establish the precise function of PARP8 in the DNA damage response.

PARP9 has been shown to interact with the ubiquitin (Ub) E3 ligase Dtx3L to form a heterodimeric complex, which mediates mono-ubiquitylation of Histone H4 following DNA damage (Camicia et al., 2013; Yan et al., 2013). Expression of GFP-tagged PARP9 macrodomains were shown to be recruited to sites of DNA damage induced by microirradiation, suggesting that PARP9 is likely to have a direct role in the DNA damage response (Yan et al., 2013). Cells depleted of PARP9 or Dtx3L were also shown to have a 50% decrease in DNA double strand break repair via non-homologous end-joining (NHEJ), suggesting that the Dtx3L/PARP9 complex has a direct role in DNA repair (Yan et al., 2013; Yang et al., 2017). However, PARP9 deficient mice were subsequently shown to have functional V(D)J, which requires NHEJ, suggesting that PARP9 may not be essential for NHEJ or that compensatory mechanisms are involved (Robert et al., 2017). Taken together, the roles of PARP9 in DNA repair and tumourigenesis suggest it may be a successful anticancer target, however further investigation is required.

Like several other members of the PARP protein family, depletion of PARP10 results in genomic instability and hypersensitivity to DNA damaging agents. It was also demonstrated that PARP10 has a role in DNA repair and cooperates with the replication-associated Proliferating Cell Nuclear Antigen (PCNA) to mediate translesion synthesis in response to UV-induced lesions (Feijs et al., 2013; Nicolae et al., 2014). A subsequent study also showed that PARP10 also promotes cellular transformation, proposed to be through the alleviation of replication stress (Schleicher et al., 2018). Supporting this assertion, PARP10 depletion significantly inhibited tumour growth in a mouse xenograft model (Schleicher et al., 2018). Given that PARP10 has a role in DNA repair and its depletion inhibits tumour growth, it is suggested that it may be a chemotherapeutic target.

Further study needs to be conducted to determine if PARP11 has a role in DNA damage response pathways and tumourigenesis, to date its roles in these processes have not been established.

The direct involvement of PARP12 in the DNA damage response is yet to be experimentally confirmed. However, its PARP1-dependent response to cellular stress may indicate that it plays a role in the DNA damage response, although further study is required to fully elucidate the roles of PARP12 in this process.

In addition to antiviral responses, PARP13 has also been shown to be a mediator in DNA damage repair (Todorova et al., 2015; Fujimoto et al., 2017) and forms a complex with PARP1 and heat shock transcription factor 1 (HSF1). This complex aids in the facilitation of DNA damage repair via transportation of PARP1 (Fujimoto et al., 2017), which then disassociates from this complex and localises to sites of DNA breaks to promote repair. It is likely that it is via this pathway PARP13 plays a tumour suppressive role. Additionally, one paper hypothesised that the inhibitory effect of PARP13 on TRAILR4 (pro survival receptor) sensitises cells to TRAIL mediated apoptosis, acting as a protective barrier against tumourigenesis (Todorova et al., 2015). For these reasons PARP13 may be a strong novel target for designing cancer therapeutics.

PARP14 has been shown to have a role in DNA repair via an interaction with PCNA at replication forks promoting replication of DNA lesions and fragile sites (Nicolae et al., 2015). Depletion of PARP14 also leads to a decrease in repair of double-strand breaks via homologous recombination and subsequent sensitivity to DNA damaging agents such as

bleomycin and hydroxyurea (Nicolae et al., 2015). The homologous recombination repair protein Rad51 was shown to be MARylated by PARP14. Furthermore, PARP14 also contains a Macro2 domain which enables it to recognise and bind MARylated substrates including Rad51 (Nicolae et al., 2015). This supports a direct role for PARP14 in DNA repair. A link was also observed between high PARP14 expression levels and poorer prognosis in multiple myeloma (Cho et al., 2011; Barbarulo et al., 2013; Iansante et al., 2015; Dhoonmoon et al., 2020). Moreover, another study found that PARP14 promoted cancer cell proliferation in hepatocellular carcinoma by promoting the Warburg effect (Iansante et al., 2015). In light of these studies, it has been suggested that PARP14 may be a novel drug target for several cancer types including diffuse large B-cell lymphoma, multiple myeloma prostate cancer and hepatocellular carcinoma (Qin et al., 2019). The role of PARP14 in DNA repair also suggests its inhibition may sensitise tumours to DNA-damaging chemotherapeutics (Qin et al., 2019).

The involvement of PARP15 and PARP16 in DNA damage repair has not been experimentally shown to date, further research needs to be conducted to determine this.

## CONCLUSION

Studies of PARP family proteins have primarily focused upon PARP1-3 and the Tankyrases. As such, the roles of these prevalent proteins have been well defined in DNA repair, telomere maintenance, tumourigenesis and cancer therapy. In contrast, far less is known about the rest of the PARP family proteins. Here, we have highlighted the diverse and intricate roles the PARP family play within the cellular environment to maintain cellular homeostasis. Given that several of the PARPs discussed here have potential roles in mitosis and DNA repair, it is likely that the other PARP proteins could represent future targets for cancer therapy. The role of these PARPs in DNA repair and cell division may form the focus of subsequent studies and guide the consensus to develop further PARP family members as targets of anti-cancer therapy.

## AUTHOR CONTRIBUTIONS

All the authors contributed to writing and editing the manuscript. IAR made **Table 1** and the figures.

## REFERENCES


Aburto, J. M., Villavicencio, F., Basellini, U., Kjærgaard, S., and Vaupel, J. W. (2020). Dynamics of Life Expectancy and Life Span equality. *Proc. Natl. Acad. Sci. USA* 117 (10), 5250–5259. doi:10.1073/pnas.1915884117

Alemasova, E. E., and Lavrik, O. I. (2019). Poly(ADP-ribosyl)ation by PARP1: Reaction Mechanism and Regulatory Proteins. *Nucleic Acids Res.* 47 (8), 3811–3827. doi:10.1093/nar/gkz120

Ali, S. O., Khan, F. A., Galindo-Campos, M. A., and Yélamos, J. (2016). Understanding Specific Functions of PARP-2: New Lessons for Cancer Therapy. *Am. J. Cancer Res.* 6 (9), 1842–1863.

Amé, J.-C., Spenlehauer, C., and de Murcia, G. (2004). The PARP Superfamily. *Bioessays* 26 (8), 882–893. doi:10.1002/bies.20085

Aricò, E., Castiello, L., Capone, I., Gabriele, L., and Belardelli, F. (2019). Type I Interferons and Cancer: An Evolving Story Demanding Novel Clinical Applications. *Cancers* 11 (12), 1943. doi:10.3390/cancers11121943

Bachmann, S. B., Frommel, S. C., Camicia, R., Winkler, H. C., Santoro, R., and Hassa, P. O. (2014). DTX3L and ARTD9 Inhibit IRF1 Expression and Mediate in Cooperation with ARTD8 Survival and Proliferation of Metastatic Prostate Cancer Cells. *Mol. Cancer* 13, 125. doi:10.1186/1476-4598-13-125

Barbarulo, A., Iansante, V., Chaidos, A., Naresh, K., Rahemtulla, A., Franzoso, G., et al. (2013). Poly(ADP-ribose) Polymerase Family Member 14 (PARP14) Is a Novel Effector of the JNK2-dependent Pro-survival Signal in Multiple Myeloma. *Oncogene* 32 (36), 4231–4242. doi:10.1038/onc.2012.448

Benigni, A., Cassis, P., and Remuzzi, G. (2010). Angiotensin II Revisited: New Roles in Inflammation, Immunology and Aging. *EMBO Mol. Med.* 2 (7), 247–257. doi:10.1002/emmm.201000080

Berti, M., Ray Chaudhuri, A., Thangavel, S., Gomathinayagam, S., Kenig, S., Vujanovic, M., et al. (2013). Human RECQ1 Promotes Restart of Replication forks Reversed by DNA Topoisomerase I Inhibition. *Nat. Struct. Mol. Biol.* 20 (3), 347–354. doi:10.1038/nsmb.2501

Bilokapic, S., Suskiewicz, M. J., Ahel, I., and Halic, M. (2020). Bridging of DNA Breaks Activates PARP2-HPF1 to Modify Chromatin. *Nature* 585 (7826), 609–613. doi:10.1038/s41586-020-2725-7

Bryant, H. E., Schultz, N., Thomas, H. D., Parker, K. M., Flower, D., Lopez, E., et al. (2005). Specific Killing of BRCA2-Deficient Tumours with Inhibitors of poly(ADP-Ribose) Polymerase. *Nature* 434 (7035), 913–917. doi:10.1038/nature03443

Buch-Larsen, S., Hendriks, I., Lodge, J., Rykær, M., Furtwängler, B., Shishkova, E., et al. (2020). Mapping Physiological ADP-Ribosylation Using Activated Ion Electron Transfer Dissociation (AI-ETD). *Cel Rep.* 32, 108176. doi:10.1016/j.celrep.2020.108176

Camicia, R., Bachmann, S. B., Winkler, H. C., Beer, M., Tinguely, M., Haralambieva, E., et al. (2013). BAL1/ARTD9 Represses the Anti-proliferative and Pro-apoptotic IFNγ-STAT1-IRF1-53 Axes in Diffuse Large B-Cell Lymphoma. *J. Cel Sci.* 126 (Pt 9), 1969–1980. doi:10.1242/jcs.118174

Catara, G., Grimaldi, G., Schembri, L., Spano, D., Turacchio, G., Lo Monte, M., et al. (2017). PARP1-produced Poly-ADP-Ribose Causes the PARP12 Translocation to Stress Granules and Impairment of Golgi Complex Functions. *Sci. Rep.* 7 (1), 14035. doi:10.1038/s41598-017-14156-8

Challa, S., Stokes, M. S., and Kraus, W. L. (2021). MARTs and MARylation in the Cytosol: Biological Functions, Mechanisms of Action, and Therapeutic Potential. *Cells* 10 (2), 313. doi:10.3390/cells10020313

Chambon, P., Weill, J. D., and Mandel, P. (1963). Nicotinamide Mononucleotide Activation of a New DNA-dependent Polyadenylic Acid Synthesizing Nuclear Enzyme. *Biochem. Biophys. Res. Commun.* 11, 39–43. doi:10.1016/0006-291x(63)90024-x

Cheng, L., Li, Z., Huang, Y.-Z., Zhang, X., Dai, X.-Y., Shi, L., et al. (2019). TCDD-Inducible Poly-ADP-Ribose Polymerase (TIPARP), A Novel Therapeutic Target of Breast Cancer. *Cancer Manag. Res.* 11, 8991–9004. doi:10.2147/cmar.S219289

Cho, S. H., Ahn, A. K., Bhargava, P., Lee, C.-H., Eischen, C. M., McGuinness, O., et al. (2011). Glycolytic Rate and Lymphomagenesis Depend on PARP14, an ADP Ribosyltransferase of the B Aggressive Lymphoma (BAL) Family. *Proc. Natl. Acad. Sci.* 108 (38), 15972–15977. doi:10.1073/pnas.1017082108

Cohen, M. S. (2020). Interplay between Compartmentalized NAD+ Synthesis and Consumption: a Focus on the PARP Family. *Genes Dev.* 34 (5-6), 254–262. doi:10.1101/gad.335109.119

Corda, D., and Di Girolamo, M. (2003). New Embo Member's Review: Functional Aspects of Protein Mono-ADP-Ribosylation. *Embo J.* 22 (9), 1953–1958. doi:10.1093/emboj/cdg209

Cortesi, L., Rugo, H. S., and Jackisch, C. (2021). An Overview of PARP Inhibitors for the Treatment of Breast Cancer. *Targ Oncol.* 16 (3), 255–282. doi:10.1007/s11523-021-00796-4

Dal Molin, G. Z., Westin, S. N., and Coleman, R. L. (2018). Rucaparib in Ovarian Cancer: Extending the Use of PARP Inhibitors in the Recurrent Disease. *Future Oncol.* 14 (30), 3101–3110. doi:10.2217/fon-2018-0215

D'Amours, D., Desnoyers, S., D'Silva, I., and Poirier, G. G. (1999). Poly(ADP-ribosyl)ation Reactions in the Regulation of Nuclear Functions. *Biochem. J.* 342 (Pt 2), 249–268. doi:10.1042/bj3420249

De Vos, M., Schreiber, V., and Dantzer, F. (2012). The Diverse Roles and Clinical Relevance of PARPs in DNA Damage Repair: Current State of the Art. *Biochem. Pharmacol.* 84 (2), 137–146. doi:10.1016/j.bcp.2012.03.018

Dhoonmoon, A., Schleicher, E. M., Clements, K. E., Nicolae, C. M., and Moldovan, G.-L. (2020). Genome-wide CRISPR Synthetic Lethality Screen Identifies a Role for the ADP-Ribosyltransferase PARP14 in DNA Replication Dynamics Controlled by ATR. *Nucleic Acids Res.* 48 (13), 7252–7264. doi:10.1093/nar/gkaa508

Dziadkowiec, K. N., Gąsiorowska, E., Nowak-Markwitz, E., and Jankowska, A. (2016). PARP Inhibitors: Review of Mechanisms of Action and BRCA1/2 Mutation Targeting. *PM* 4 (4), 215–219. doi:10.5114/pm.2016.65667

Farmer, H., McCabe, N., Lord, C. J., Tutt, A. N. J., Johnson, D. A., Richardson, T. B., et al. (2005). Targeting the DNA Repair Defect in BRCA Mutant Cells as a Therapeutic Strategy. *Nature* 434 (7035), 917–921. doi:10.1038/nature03445

Feijs, K. L., Kleine, H., Braczynski, A., Forst, A. H., Herzog, N., Verheugd, P., et al. (2013). ARTD10 Substrate Identification on Protein Microarrays: Regulation of GSK3β by Mono-ADP-Ribosylation. *Cell Commun Signal* 11 (1), 5. doi:10.1186/1478-811x-11-5

Fisher, A. E. O., Hochegger, H., Takeda, S., and Caldecott, K. W. (2007). Poly(ADP-ribose) Polymerase 1 Accelerates Single-Strand Break Repair in Concert with poly(ADP-Ribose) Glycohydrolase. *Mol. Cel Biol.* 27 (15), 5597–5605. doi:10.1128/mcb.02248-06

Fujimoto, M., Takii, R., Takaki, E., Katiyar, A., Nakato, R., Shirahige, K., et al. (2017). The HSF1-PARP13-PARP1 Complex Facilitates DNA Repair and Promotes Mammary Tumorigenesis. *Nat. Commun.* 8 (1), 1638. doi:10.1038/s41467-017-01807-7

Gozgit, J. M., Vasbinder, M. M., Abo, R. P., Kunii, K., Kuplast-Barr, K. G., Gui, B., et al. (2021). PARP7 Negatively Regulates the Type I Interferon Response in Cancer Cells and its Inhibition Triggers Antitumor Immunity. *Cancer Cell* 39 (9), 1214–1226. doi:10.1016/j.ccell.2021.06.018

Gupte, R., Liu, Z., and Kraus, W. L. (2017). PARPs and ADP-Ribosylation: Recent Advances Linking Molecular Functions to Biological Outcomes. *Genes Dev.* 31 (2), 101–126. doi:10.1101/gad.291518.116

Haikarainen, T., Krauss, S., and Lehtio, L. (2014). Tankyrases: Structure, Function and Therapeutic Implications in Cancer. *CPD* 20 (41), 6472–6488. doi:10.2174/1381612820666140630101525

Hanzlikova, H., Kalasova, I., Demin, A. A., Pennicott, L. E., Cihlarova, Z., and Caldecott, K. W. (2018). The Importance of Poly(ADP-Ribose) Polymerase as a Sensor of Unligated Okazaki Fragments during DNA Replication. *Mol. Cel* 71 (2), 319–331. doi:10.1016/j.molcel.2018.06.004

Hottiger, M. O., Hassa, P. O., Lüscher, B., Schüler, H., and Koch-Nolte, F. (2010). Toward a Unified Nomenclature for Mammalian ADP-Ribosyltransferases. *Trends Biochem. Sci.* 35 (4), 208–219. doi:10.1016/j.tibs.2009.12.003

Hu, W.-F., Krieger, K. L., Lagundžin, D., Li, X., Cheung, R. S., Taniguchi, T., et al. (2019). CTDP1 Regulates Breast Cancer Survival and DNA Repair through BRCT-specific Interactions with FANCI. *Cell Death Discov.* 5, 105. doi:10.1038/s41420-019-0185-3

Iansante, V., Choy, P. M., Fung, S. W., Liu, Y., Chai, J.-G., Dyson, J., et al. (2015). PARP14 Promotes the Warburg Effect in Hepatocellular Carcinoma by Inhibiting JNK1-dependent PKM2 Phosphorylation and Activation. *Nat. Commun.* 6, 7882. doi:10.1038/ncomms8882

Ikeda, Y., Kiyotani, K., Yew, P. Y., Kato, T., Tamura, K., Yap, K. L., et al. (2016). Germline PARP4 Mutations in Patients with Primary Thyroid and Breast Cancers. *Endocr. Relat. Cancer* 23 (3), 171–179. doi:10.1530/erc-15-0359

Mittal, R., Jaiswal, P., and Goel, A. (2015). Survivin: A Molecular Biomarker in Cancer. *Indian J. Med. Res.* 141 (4), 389–397. doi:10.4103/0971-5916.159250

Jean, L., Risler, J. L., Nagase, T., Coulouarn, C., Nomura, N., and Salier, J. P. (1999). The Nuclear Protein PH5P of the Inter-α-inhibitor Superfamily: a Missing Link between poly(ADP-Ribose)polymerase and the Inter-α-inhibitor Family and a Novel Actor of DNA Repair? *FEBS Lett.* 446 (1), 6–8. doi:10.1016/s0014-5793(99)00173-8

Jun, J. C., Rathore, A., Younas, H., Gilkes, D., and Polotsky, V. Y. (2017). Hypoxia-Inducible Factors and Cancer. *Curr. Sleep Med. Rep.* 3 (1), 1–10. doi:10.1007/s40675-017-0062-7

Kickhoefer, V. A., Siva, A. C., Kedersha, N. L., Inman, E. M., Ruland, C., Streuli, M., et al. (1999). The 193-kD Vault Protein, VPARP, Is a Novel poly(ADP-Ribose) Polymerase. *J. Cel Biol.* 146 (5), 917–928. doi:10.1083/jcb.146.5.917

Kirby, I. T., Kojic, A., Arnold, M. R., Thorsell, A.-G., Karlberg, T., Vermehren-Schmaedick, A., et al. (2018). A Potent and Selective PARP11 Inhibitor Suggests Coupling between Cellular Localization and Catalytic Activity. *Cel Chem. Biol.* 25 (12), 1547–1553. doi:10.1016/j.chembiol.2018.09.011

Kirby, I. T., Person, A., and Cohen, M. (2021). Rational Design of Selective Inhibitors of PARP4. *RSC Med. Chem.* 12 (11), 1950–1957. doi:10.1039/d1md00195g

Kleine, H., Poreba, E., Lesniewicz, K., Hassa, P. O., Hottiger, M. O., Litchfield, D. W., et al. (2008). Substrate-Assisted Catalysis by PARP10 Limits its Activity to Mono-ADP-Ribosylation. *Mol. Cel* 32 (1), 57–69. doi:10.1016/j.molcel.2008.08.009

Ko, H. L., and Ren, E. C. (2012). Functional Aspects of PARP1 in DNA Repair and Transcription. *Biomolecules* 2 (4), 524–548. doi:10.3390/biom2040524

Lakshmi, T. V., Bale, S., Khurana, A., and Godugu, C. (2017). Tankyrase as a Novel Molecular Target in Cancer and Fibrotic Diseases. *CDT* 18 (10), 1214–1224. doi:10.2174/1389450117666160715152503

Lee, M. K., Cheong, H. S., Koh, Y., Ahn, K.-S., Yoon, S.-S., and Shin, H. D. (2016). Genetic Association ofPARP15Polymorphisms with Clinical Outcome of Acute Myeloid Leukemia in a Korean Population. *Genet. Test. Mol. Biomarkers* 20 (11), 696–701. doi:10.1089/gtmb.2016.0007

Lemke, M., Ravenscroft, H., Rueb, N. J., Kireev, D., Ferraris, D., and Franzini, R. M. (2020). Integrating DNA-Encoded Chemical Libraries with Virtual Combinatorial Library Screening: Optimizing a PARP10 Inhibitor. *Bioorg. Med. Chem. Lett.* 30 (19), 127464. doi:10.1016/j.bmcl.2020.127464

Li, N., Wang, Y., Neri, S., Zhen, Y., Fong, L. W. R., Qiao, Y., et al. (2019). Tankyrase Disrupts Metabolic Homeostasis and Promotes Tumorigenesis by Inhibiting LKB1-AMPK Signalling. *Nat. Commun.* 10 (1), 4363. doi:10.1038/s41467-019-12377-1

Lin, C.-Y., and Gustafsson, J. A. (2015). Targeting Liver X Receptors in Cancer Therapeutics. *Nat. Rev. Cancer* 15 (4), 216–224. doi:10.1038/nrc3912

Lin, L., Yan, L., Liu, Y., Yuan, F., Li, H., and Ni, J. (2019). Incidence and Death in 29 Cancer Groups in 2017 and Trend Analysis from 1990 to 2017 from the Global Burden of Disease Study. *J. Hematol. Oncol.* 12 (1), 96. doi:10.1186/s13045-019-0783-9

Meyer-Ficca, M. L., Ihara, M., Bader, J. J., Leu, N. A., Beneke, S., and Meyer, R. G. (2015). Spermatid Head Elongation with Normal Nuclear Shaping Requires ADP-Ribosyltransferase PARP11 (ARTD11) in Mice1. *Biol. Reprod.* 92 (3), 80. doi:10.1095/biolreprod.114.123661

Morales, J., Li, L., Fattah, F. J., Dong, Y., Bey, E. A., Patel, M., et al. (2014). Review of Poly (ADP-Ribose) Polymerase (PARP) Mechanisms of Action and Rationale for Targeting in Cancer and Other Diseases. *Crit. Rev. Eukaryot. Gene Expr.* 24 (1), 15–28. doi:10.1615/critreveukaryotgeneexpr.2013006875

Mossink, M. H., van Zon, A., Scheper, R. J., Sonneveld, P., and Wiemer, E. A. (2003). Vaults: a Ribonucleoprotein Particle Involved in Drug Resistance? *Oncogene* 22 (47), 7458–7467. doi:10.1038/sj.onc.1206947

Murai, J., Huang, S.-y. N., Das, B. B., Renaud, A., Zhang, Y., Doroshow, J. H., et al. (2012). Trapping of PARP1 and PARP2 by Clinical PARP Inhibitors. *Cancer Res.* 72, 5588–5599. doi:10.1158/0008-5472.can-12-2753

Nicolae, C. M., Aho, E. R., Vlahos, A. H. S., Choe, K. N., De, S., Karras, G. I., et al. (2014). The ADP-Ribosyltransferase PARP10/ARTD10 Interacts with Proliferating Cell Nuclear Antigen (PCNA) and Is Required for DNA Damage Tolerance. *J. Biol. Chem.* 289 (19), 13627–13637. doi:10.1074/jbc.M114.556340

Nicolae, C. M., Aho, E. R., Choe, K. N., Constantin, D., Hu, H.-J., Lee, D., et al. (2015). A Novel Role for the Mono-ADP-Ribosyltransferase PARP14/ARTD8 in Promoting Homologous Recombination and Protecting against Replication Stress. *Nucleic Acids Res.* 43 (6), 3143–3153. doi:10.1093/nar/gkv147

Palavalli Parsons, L. H., Challa, S., Gibson, B. A., Nandu, T., Stokes, M. S., Huang, D., et al. (2021). Identification of PARP-7 Substrates Reveals a Role for MARylation in Microtubule Control in Ovarian Cancer Cells. *Elife* 10, e60481. doi:10.7554/eLife.60481

Palve, V., Knezevic, C. E., Bejan, D. S., Luo, Y., Li, X., Novakova, S., et al. (2021). The Non-canonical Target PARP16 Contributes to Polypharmacology of the PARP Inhibitor Talazoparib and its Synergy with WEE1 Inhibitors. *Cel Chem. Biol.* doi:10.1016/j.chembiol.2021.07.008

Perina, D., Mikoč, A., Ahel, J., Ćetković, H., Žaja, R., and Ahel, I. (2014). Distribution of Protein poly(ADP-Ribosyl)ation Systems across All Domains of Life. *DNA Repair* 23, 4–16. doi:10.1016/j.dnarep.2014.05.003

Qi, G., Kudo, Y., Tang, B., Liu, T., Jin, S., Liu, J., et al. (2016). PARP6 Acts as a Tumor Suppressor via Downregulating Survivin Expression in Colorectal Cancer. *Oncotarget* 7 (14), 18812–18824. doi:10.18632/oncotarget.7712

Qin, W., Wu, H.-J., Cao, L.-Q., Li, H.-J., He, C.-X., Zhao, D., et al. (2019). Research Progress on PARP14 as a Drug Target. *Front. Pharmacol.* 10, 172. doi:10.3389/fphar.2019.00172

Rasmussen, M., Tan, S., Somisetty, V. S., Hutin, D., Olafsen, N. E., Moen, A., et al. (2021). PARP7 and Mono-ADP-Ribosylation Negatively Regulate Estrogen Receptor α Signaling in Human Breast Cancer Cells. *Cells* 10 (3), 623. doi:10.3390/cells10030623

Ray Chaudhuri, A., and Nussenzweig, A. (2017). The Multifaceted Roles of PARP1 in DNA Repair and Chromatin Remodelling. *Nat. Rev. Mol. Cel Biol.* 18 (10), 610–621. doi:10.1038/nrm.2017.53

Robert, I., Gaudot, L., Yélamos, J., Noll, A., Wong, H.-K., Dantzer, F., et al. (2017). Robust Immunoglobulin Class Switch Recombination and End Joining inParp9-Deficient Mice. *Eur. J. Immunol.* 47 (4), 665–676. doi:10.1002/eji.201646757

Rodriguez-Vargas, J. M., Nguekeu-Zebaze, L., and Dantzer, F. (2019). PARP3 Comes to Light as a Prime Target in Cancer Therapy. *Cell Cycle* 18 (12), 1295–1301. doi:10.1080/15384101.2019.1617454

Ronson, G. E., Piberger, A. L., Higgs, M. R., Olsen, A. L., Stewart, G. S., McHugh, P. J., et al. (2018). PARP1 and PARP2 Stabilise Replication forks at Base Excision Repair Intermediates through Fbh1-dependent Rad51 Regulation. *Nat. Commun.* 9 (1), 746. doi:10.1038/s41467-018-03159-2

Rose, M., Burgess, J. T., O'Byrne, K., Richard, D. J., and Bolderson, E. (2020). PARP Inhibitors: Clinical Relevance, Mechanisms of Action and Tumor Resistance. *Front. Cel Dev. Biol.* 8, 564601. doi:10.3389/fcell.2020.564601

Ruf, A., Mennissier de Murcia, J., de Murcia, G., and Schulz, G. E. (1996). Structure of the Catalytic Fragment of poly(AD-Ribose) Polymerase from Chicken. *Proc. Natl. Acad. Sci.* 93 (15), 7481–7485. doi:10.1073/pnas.93.15.7481

Schenkel, L. B., Molina, J. R., Swinger, K. K., Abo, R., Blackwell, D. J., Lu, A. Z., et al. (2021). A Potent and Selective PARP14 Inhibitor Decreases Protumor Macrophage Gene Expression and Elicits Inflammatory Responses in Tumor Explants. *Cel Chem. Biol.* 28 (8), 1158–1168. doi:10.1016/j.chembiol.2021.02.010

Schlacher, K. (2017). PARPi Focus the Spotlight on Replication fork protection in Cancer. *Nat. Cel Biol.* 19 (11), 1309–1310. doi:10.1038/ncb3638

Schleicher, E. M., Galvan, A. M., Imamura-Kawasawa, Y., Moldovan, G.-L., and Nicolae, C. M. (2018). PARP10 Promotes Cellular Proliferation and Tumorigenesis by Alleviating Replication Stress. *Nucleic Acids Res.* 46 (17), 8908–8916. doi:10.1093/nar/gky658

Shao, C., Qiu, Y., Liu, J., Feng, H., Shen, S., Saiyin, H., et al. (2018). PARP12 (ARTD12) Suppresses Hepatocellular Carcinoma Metastasis through Interacting with FHL2 and Regulating its Stability. *Cell Death Dis.* 9 (9), 856. doi:10.1038/s41419-018-0906-1

Sisay, M., and Edessa, D. (2017). PARP Inhibitors as Potential Therapeutic Agents for Various Cancers: Focus on Niraparib and its First Global Approval for Maintenance Therapy of Gynecologic Cancers. *Gynaecol. Oncol. Res. Pract.* 4, 18. doi:10.1186/s40661-017-0055-8

Sun, X., Zhang, Y., Chu, M., Wang, L., Shen, H., Zhang, Z., et al. (2018). PARP6 Acts as an Oncogene and Positively Regulates Survivin in Gastric Cancer. *Int. J. Clin. Exp. Pathol.* 11 (5), 2364–2371.

Sung, H., Ferlay, J., Siegel, R. L., Laversanne, M., Soerjomataram, I., Jemal, A., et al. (2021). Global Cancer Statistics 2020: GLOBOCAN Estimates of Incidence and Mortality Worldwide for 36 Cancers in 185 Countries. *CA A. Cancer J. Clin.* 71 (3), 209–249. doi:10.3322/caac.21660

Tang, X., Zhang, H., Long, Y., Hua, H., Jiang, Y., and Jing, J. (2018). PARP9 Is Overexpressed in Human Breast Cancer and Promotes Cancer Cell Migration. *Oncol. Lett.* 16 (3), 4073–4077. doi:10.3892/ol.2018.9124

Todorova, T., Bock, F. J., and Chang, P. (2014). PARP13 Regulates Cellular mRNA post-transcriptionally and Functions as a Pro-apoptotic Factor by Destabilizing TRAILR4 Transcript. *Nat. Commun.* 5, 5362. doi:10.1038/ncomms6362

Todorova, T., Bock, F. J., and Chang, P. (2015). Poly(ADP-ribose) Polymerase-13 and RNA Regulation in Immunity and Cancer. *Trends Mol. Med.* 21 (6), 373–384. doi:10.1016/j.molmed.2015.03.002

Tuncel, H., Tanaka, S., Oka, S., Nakai, S., Fukutomi, R., Okamoto, M., et al. (2012). PARP6, a mono(ADP-Ribosyl) Transferase and a Negative Regulator of Cell Proliferation, Is Involved in Colorectal Cancer Development. *Int. J. Oncol.* 41 (6), 2079–2086. doi:10.3892/ijo.2012.1652

Vyas, S., Chesarone-Cataldo, M., Todorova, T., Huang, Y.-H., and Chang, P. (2013). A Systematic Analysis of the PARP Protein Family Identifies New Functions Critical for Cell Physiology. *Nat. Commun.* 4 (1), 2240. doi:10.1038/ncomms3240

Vyas, S., Matic, I., Uchima, L., Rood, J., Zaja, R., Hay, R. T., et al. (2014). Family-wide Analysis of poly(ADP-Ribose) Polymerase Activity. *Nat. Commun.* 5, 4426. doi:10.1038/ncomms5426

Wang, J., Zhu, C., Song, D., Xia, R., Yu, W., Dang, Y., et al. (2017). Epigallocatechin-3-gallate Enhances ER Stress-Induced Cancer Cell Apoptosis by Directly Targeting PARP16 Activity. *Cel Death Discov.* 3 (1), 17034. doi:10.1038/cddiscovery.2017.34

Wang, Z., Grosskurth, S. E., Cheung, T., Petteruti, P., Zhang, J., Wang, X., et al. (2018). Pharmacological Inhibition of PARP6 Triggers Multipolar Spindle Formation and Elicits Therapeutic Effects in Breast Cancer. *Cancer Res.* 78 (23), 6691–6702. doi:10.1158/0008-5472.Can-18-1362

Woodward, C. L., Mendonça, L. M., and Jensen, G. J. (2015). Direct Visualization of Vaults within Intact Cells by Electron Cryo-Tomography. *Cell. Mol. Life Sci.* 72 (17), 3401–3409. doi:10.1007/s00018-015-1898-y

Xing, J., Zhang, A., Du, Y., Fang, M., Minze, L. J., Liu, Y.-J., et al. (2021). Identification of poly(ADP-Ribose) Polymerase 9 (PARP9) as a Noncanonical Sensor for RNA Virus in Dendritic Cells. *Nat. Commun.* 12 (1), 2681. doi:10.1038/s41467-021-23003-4

Xu, H., Chai, S., Wang, Y., Wang, J., Xiao, D., Li, J., et al. (2020). Molecular and Clinical Characterization of PARP9 in Gliomas: A Potential Immunotherapeutic Target. *CNS Neurosci. Ther.* 26 (8), 804–814. doi:10.1111/cns.13380

Xue, P., Fu, J., and Zhou, Y. (2018). The Aryl Hydrocarbon Receptor and Tumor Immunity. *Front. Immunol.* 9, 286. doi:10.3389/fimmu.2018.00286

Yan, Q., Xu, R., Zhu, L., Cheng, X., Wang, Z., Manis, J., et al. (2013). BAL1 and its Partner E3 Ligase, BBAP, Link Poly(ADP-Ribose) Activation, Ubiquitylation, and Double-Strand DNA Repair Independent of ATM, MDC1, and RNF8. *Mol. Cel Biol.* 33 (4), 845–857. doi:10.1128/mcb.00990-12

Yang, C.-S., Jividen, K., Spencer, A., Dworak, N., Ni, L., Oostdyk, L. T., et al. (2017). Ubiquitin Modification by the E3 Ligase/ADP-Ribosyltransferase Dtx3L/Parp9. *Mol. Cel* 66 (4), 503–516. doi:10.1016/j.molcel.2017.04.028

Yang, D., Wang, Q., Wei, G., Wu, J., Zhu, Y. C., Zhu, Q., et al. (2020). Smyd3-PARP16 axis Accelerates Unfolded Protein Response and Vascular Aging. *Aging* 12 (21), 21423–21445. doi:10.18632/aging.103895

**Conflict of Interest:** The authors declare competing financial interests; EB and KO'B. are founders of Carpe Vitae Pharmaceuticals. EB, KO'B, and JB are inventors on provisional patent applications filed by Queensland University of Technology.

**Publisher's Note:** All claims expressed in this article are solely those of the authors and do not necessarily represent those of their affiliated organizations, or those of the publisher, the editors, and the reviewers. Any product that may be evaluated in this article, or claim that may be made by its manufacturer, is not guaranteed or endorsed by the publisher.

frontiers | Frontiers in Cell and Developmental Biology

REVIEW
published: 08 April 2022
doi: 10.3389/fcell.2022.847051

# Epigenetic Regulation of Nucleotide Excision Repair

*Wentao Li*, Kyle Jones, Tyler J. Burke, Md Akram Hossain and Leah Lariscy*

*Department of Environmental Health Science, College of Public Health, University of Georgia, Athens, GA, United States*

Genomic DNA is constantly attacked by a plethora of DNA damaging agents both from endogenous and exogenous sources. Nucleotide excision repair (NER) is the most versatile repair pathway that recognizes and removes a wide range of bulky and/or helix-distorting DNA lesions. Even though the molecular mechanism of NER is well studied through *in vitro* system, the NER process inside the cell is more complicated because the genomic DNA in eukaryotes is tightly packaged into chromosomes and compacted into a nucleus. Epigenetic modifications regulate gene activity and expression without changing the DNA sequence. The dynamics of epigenetic regulation play a crucial role during the *in vivo* NER process. In this review, we summarize recent advances in our understanding of the epigenetic regulation of NER.

**Keywords: epigenetics, nucleotide excision repair, DNA damage, histone modifications, genome architecture, chromatin remodeler**

OPEN ACCESS

***Edited by:***
*Michael G. Kemp,*
*Wright State University, United States*

***Reviewed by:***
*Sheera Adar,*
*Hebrew University of Jerusalem, Israel*
*John Wyrick,*
*Washington State University, United States*

****Correspondence:***
*Wentao Li*
*wentao.li@uga.edu*

***Specialty section:***
*This article was submitted to Molecular and Cellular Pathology, a section of the journal Frontiers in Cell and Developmental Biology*

***Received:*** *01 January 2022*
***Accepted:*** *24 March 2022*
***Published:*** *08 April 2022*

***Citation:***
*Li W, Jones K, Burke TJ, Hossain MA and Lariscy L (2022) Epigenetic Regulation of Nucleotide Excision Repair. Front. Cell Dev. Biol. 10:847051. doi: 10.3389/fcell.2022.847051*

## INTRODUCTION

The genome is essential for the survival of all living organisms and its integrity is critical for accurate transmission of genetic information to offspring. However, genomic DNA is constantly attacked by a plethora of DNA damaging agents both from endogenous and exogenous sources; For example, the reactive oxygen species (e.g., superoxide) produced in cellular metabolic processes, environmental carcinogens such as ultraviolet (UV) light, polycyclic aromatic hydrocarbons (PAHs) and mycotoxins, and high-frequency ionizing radiation like X-rays and gamma rays can directly distort the structure of DNA double helix and/or break the DNA strand(s) (Hoeijmakers, 2001). DNA lesions can block genome transcription and replication, which threatens the viability of damaged cells, or the whole organism, and eventually leads to mutations or chromosomal aberrations if not repaired in a timely and efficient manner. To deal with DNA lesions, organisms have evolved a complex system including DNA damage response and a variety of DNA repair pathways. There are five major DNA repair mechanisms: direct reversal repair, base excision repair, nucleotide excision repair (NER), mismatch repair, and double-strand break repair.

Among the five major repair mechanisms, NER is the most versatile one as it recognizes and removes a wide range of bulky and/or helix-distorting DNA lesions such as UV-induced cyclobutane pyrimidine dimers (CPDs) and (6-4) pyrimidine-pyrimidone photoproducts [(6-4)PPs] (Sancar, 2016). The basic NER process involves DNA lesion recognition, dual incision bracketing the lesion, release of excision product, repair synthesis, and ligation (Hu et al., 2017). NER consists of two subpathways: global genomic repair and transcription-coupled repair (TCR). Global genomic repair removes DNA lesions throughout the whole genome, while TCR acts only on the transcribed strand of actively transcribed genes (Mellon et al., 1987; Hanawalt and Spivak, 2008). They differ at the step of DNA lesion recognition but share the same repair machinery for the following repair process. The biochemical basics of global genomic repair were reconstituted *in vitro* for both prokaryotes and eukaryotes (Sancar, 2016). Six repair proteins, UvrA, UvrB, UvrC, UvrD, DNA Pol I, and DNA

ligase, are required for global genomic repair in *E. coli* (Sancar and Rupp, 1983; Husain et al., 1985; Sancar and Tang, 1993). For global genomic repair in humans, six core repair factors, RPA, XPA, XPC, TFIIH, XPG, and XPF-ERCC1, are essential for damage recognition, dual incision, and release of the excision product in an *in vitro* system (Aboussekhra et al., 1995; Mu et al., 1995). Then, DNA Pol δ/ε and DNA ligase I or XRCC1-ligase III complex perform the repair synthesis and ligation respectively (Sancar, 1996; Wood, 1997). In contrast, even though TCR mechanism in *E. coli* has been elucidated *in vitro* (Selby and Sancar, 1993), TCR reaction in eukaryotes has not been reconstituted with purified protein components because of its complexity. The stalling of elongating RNA polymerase II (RNAP II) at a DNA lesion triggers TCR (Li et al., 2014b), and cockayne syndrome group B (CSB), the human homolog of yeast Rad26, binds to the lesion-stalled RNAP II and sequentially recruits CSA, UVSSA, and TFIIH to initiate NER in a cooperative manner (van der Weegen et al., 2020). Besides the above TCR factors, a variety of factors such as Sen1 (Li et al., 2016), Spt4/5 (Li et al., 2014a) and PFAc (Tatum et al., 2011), which directly interact with RNAP II, have been discovered to either facilitate or repress TCR in yeast (Li and Li, 2017). Recently, another elongation factor, ELOF1 (Prather et al., 2005), was found to facilitate TCR through promoting UVSSA and TFIIH recruitment (Olivieri et al., 2020; Geijer et al., 2021; van der Weegen et al., 2021). Genetic defects in NER genes are associated with a broad range of human diseases including xeroderma pigmentosum (XP), cockayne syndrome (CS), UV-sensitive syndrome ($UV^{S}S$) (Cleaver and Thomas, 1993), and trichothiodystrophy (TTD).

Even though the mode of dual incision *in vivo* for NER is the same as *in vitro* studies (Kemp et al., 2012; Hu et al., 2013), the NER process in cells is far more complicated than that of *in vitro* experiments. The reason lies in the fact that genomic DNA in eukaryotes is tightly packaged into chromosomes and compacted into a nucleus, while *in vitro* system uses naked DNA template and purified repair proteins. It is much easier for repair proteins to access damage site in naked DNA than it is to access that in nucleosomal DNA (Schieferstein and Thoma, 1998; Hara et al., 2000; Liu and Smerdon, 2000). The human genome in a diploid cell contains around 6 billion DNA base pairs (bp) with a length of 3 m, and about 146 bp DNA is wrapped around a histone octamer (H3, H4, H2A, H2B) to form a nucleosome core particle (NCP), the fundamental repeating unit of the chromatin (Luger et al., 1997). NCPs are connected by linker DNA (10–70 bp) to form a 11 nm diameter "beads on a string" array. With the addition of linker histones (H1 and H5), which bind the nucleosome at the entry/exit sites of the linker DNA, the nucleosomal array is further consolidated into a 30 nm diameter chromatin fiber (Li and Reinberg, 2011). The arrangement of chromatin fiber in three-dimensional (3D) space within the nucleus is not random. Instead, chromatin fiber is folded into a hierarchy of loops and coils with the aid of scaffold proteins in different nuclear regions, forming specific territories such as topologically associating domains (TADs) and lamina-associated domains (LADs). In this way, the entire human genome is compacted into 23 pairs of chromosomes. Each chromosome occupies a unique part of the nuclear space termed chromosome territory (Meaburn and Misteli, 2007). The presence of nucleosomes, chromatin fiber, and higher-order spatial organization chromatin domains poses barriers to the NER repair proteins because the NER process requires the repair machinery to have access to DNA lesions to allow the sequential assembly and actions of repair complexes (**Figure 1**). Not only that, but epigenetic regulation, which modulates gene expression without changing the DNA sequence, can also affect the entire *in vivo* NER process (Li, 2012). In its broadest definition, which includes both heritable and non-heritable changes in gene activity and expression, epigenetic regulation consists of histone modifications, chromatin remodeling, nucleosome positioning, DNA modifications, and non-coding RNA. It is complex, dynamic, and important for transcription, DNA replication, and DNA repair. Meanwhile, DNA damage formation and repair can also affect epigenetic activities.

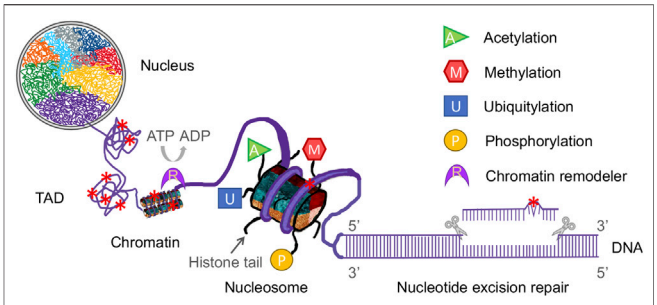


**FIGURE 1 |** Diagrammatic representation of the complex components of epigenetics and nucleotide excision repair in a eukaryotic nucleus. Eukaryotic genomic DNA is wrapped around a histone octamer to form a nucleosome, which is the repeating unit of the chromatin. Chromatin fiber is folded into a hierarchy of loops and coils to form topologically associating domains (TADs). In this way, eukaryotic DNA is compacted into chromosomes in a nucleus. Each chromosome has its own territory (shown as different colors) in the nucleus. Nucleotide excision repair (NER) removes a wide range of DNA damage (denoted as red star) in cellular DNA and NER machinery requires access to damaged DNA in chromatin. Modifications of histone tails, such as acetylation, methylation, ubiquitylation and phosphorylation (shown as various colored shapes), and chromatin remodeling catalyzed by remodelers (shown as a purple crescent) affect the genome architecture and thus regulate the NER process.

The dynamics of epigenetic regulation, which induces alterations of DNA lesion accessibility for repair machinery controlled by changes in spatial genome architecture, play a crucial role during the *in vivo* NER process (Dinant et al., 2008; Deem et al., 2012; Papamichos-Chronakis and Peterson, 2013; Karakaidos et al., 2020). In recent years, newly developed methodologies derived from next-generation sequencing (NGS) technology have been used for epigenomic profiling (Mehrmohamadi et al., 2021), genome-wide mapping of DNA damage and repair (Li and Sancar, 2020), and capturing spatial genome organization (Oluwadare et al., 2019). In addition, structural studies using cutting-edge cryo-electron microscopy (cryo-EM) and computer simulation modeling have revealed key insights into the NER process (Xu et al., 2017; Yan et al., 2021). In this review, we summarize recent advances in the epigenetic regulation of NER, focusing on insights into how the dynamics of genome architecture affect NER.

## DIVERSE ROLES OF HISTONE MODIFICATIONS IN NER

Through a hierarchy of compaction, the entire human genomic DNA is tightly packaged within a nucleus with a diameter of 5–10 μm (Misteli, 2007). In contrast to *in vitro* reconstitution assay system, the cellular NER machinery must overcome obstacles introduced by DNA packaging to gain access to DNA lesions before and during the occurrence of NER. Furthermore, the spatial genome architecture must be restored upon completion of repair (Smerdon, 1991; Polo et al., 2006; Tiwari et al., 2017). The HIRA (histone regulator A) complex, a replication-independent histone chaperone, has been shown to play important roles in chromatin restoration and transcription recovery after DNA damage and repair (Bouvier et al., 2021; Caron et al., 2021). The genome organization at different hierarchical levels can affect DNA damage formation as well. For example, at the single-nucleosome level, distribution of CPDs shows a striking 10.3-base periodicity (Gale et al., 1987) and (6-4) PPs are enriched in nucleosome linker regions (Mitchell et al., 1990). Recent studies have revealed that CPDs formation is significantly higher at "out" rotational settings in a nucleosome (Mao et al., 2016; Mao et al., 2017). Histone modifications, the covalent post-translational modifications (PTMs) of both histone tails and the core of the histone octamer, have been shown to play diverse roles in NER by altering chromatin structure (Li, 2012; Mao and Wyrick, 2016). These modifications include acetylation, methylation, phosphorylation, ubiquitylation, sumoylation, ADP-ribosylation, neddylation, and citrullination. Distinct histone modifications act alone or in combination to form the so-called "histone code" (Jenuwein and Allis, 2001). They regulate most, if not all, chromatin-templated cellular processes, such as gene transcription, DNA replication, DNA repair, and chromosome condensation, by disrupting chromatin contacts and/or recruiting nonhistone factors to chromatin (Kouzarides, 2007). There are additional histone modifications that are still being discovered. Here, we focus on the four major modifications (acetylation, methylation, ubiquitylation and phosphorylation) and their effects on NER (**Figure 1**).

### Histone Acetylation and NER

Histone acetylation, one of the most important and highly studied histone modifications, is the covalent addition of an acetyl group to the lysine residue within histones. It is mediated via histone acetyltransferases (HATs), which are divided into three families: GNAT (GCN5 related *N*-acetyltransferase), MYST (MOZ, YBF2/SAS3, SAS2, TIP60), and P300/CBP (Hodawadekar and Marmorstein, 2007). Histone deacetylation, on the other hand, is catalyzed by histone deacetylases (HDACs). Based on function and sequence homology to yeast original proteins, the 18 HDAC enzymes in humans are classified into four classes (Seto and Yoshida, 2014). The class I HDACs, homologous to yeast Rpd3 (reduced potassium dependency 3), include HDAC1, HDAC2, HDAC3, and HDAC8. The class II HDACs comprise HDAC4, HDAC5, HDAC6, HDAC7, HDAC9, and HDAC10 and share homology with yeast Hda1 (histone deacetylase 1). SIRT1, SIRT2, SIRT3, SIRT4, SIRT5, SIRT6, and SIRT7 belong to the class III and have homology to yeast Sir2 (silent information regulator 2), an $NAD^+$-dependent enzyme. HDAC11 is assigned to the class IV as it is homologous to neither Rpd3 nor Hda1 yeast enzymes. Histone acetylation generally promotes open chromatin and gene activation because the addition of acetyl groups neutralizes the positive charge of histone lysine residues and thus reduces the strong electrostatic histone-DNA interaction, leading to a more open chromatin structure favorable for the transcriptional machinery. Histone acetylation can also be "read" by bromodomain-containing proteins which recruit positive elongation factors (Roth et al., 2001).

Seminal studies in the 1980s showed that histone hyperacetylation induced by sodium butyrate, an inhibitor of histone HDAC, stimulates NER in UV treated human fibroblasts (Smerdon et al., 1982; Ramanathan and Smerdon, 1989) and that a hyperacetylation phase, followed by a hypoacetylation phase, occurred immediately after UV irradiation (Ramanathan and Smerdon, 1986). Yeast Gcn5, a subunit of the SAGA (Spt-Ada-Gcn5 Acetyltransferase) transcriptional coactivator complex, was then identified to be responsible for H3 (K9 and K14) acetylation and global genomic repair at certain loci but not the whole genome (Teng et al., 2002; Yu et al., 2005). It was later found that Rad16, together with Rad7, mediate the UV-dependent H3 (K9 and K14) acetylation by increasing the occupancy of Gcn5 in chromatin after UV treatment (Teng et al., 2008; Yu et al., 2011). Intriguingly, histone variant Htz1 (H2A.Z in humans) promotes H3 acetylation for efficient NER by using the same way as Rad16 (Yu et al., 2013). Like H3 acetylation, histone H4 acetylation also increases in response to UV irradiation and NuA4 (nucleosome acetyltransferase of histone H4) HAT is important for efficient NER in yeast (Irizar et al., 2010; Hodges et al., 2019). Human GCN5, homologous to the yeast Gcn5, was also found to be involved in H3 acetylation and NER in UV-damaged chromatin by physically interacting with the transcription factor E2F1 (Guo et al., 2010; Guo et al., 2011). Another two transcription coactivators in mammalian cells, CBP (CREB-binding protein) and p300, were shown to participate in NER through their HAT activities and physical interactions with repair proteins such as p53, DDB2, CSB and PCNA (Datta et al., 2001; Hasan et al., 2001; Rubbi and Milner, 2003). H3K56 acetylation, catalyzed by P300/CBP in mammals and by Rtt109 (homolog of P300/CBP) in yeast, plays an important role in genome stability (Driscoll et al., 2007; Han et al., 2007). However, it is dispensable for NER and responsible for the restoration of chromatin structure after completion of NER (Battu et al., 2011). Similarly, H3K14 acetylation, on its own, was found to have no effect on the repair of UV damaged DNA in an elegant *in vitro* study. However, it could facilitate UV damage repair in the presence of RSC (Remodeling the Structure of Chromatin), a chromatin remodeler, by enhancing the interaction between RSC and nucleosome (Duan and Smerdon, 2014). Besides acetylating histones, P300/CBP also interacts and acetylates nonhistone NER factor XPG in a PCNA-p21 dependent manner, which makes the 3′ incision on the damaged DNA strand during dual incision (Tillhon et al., 2012). Thus, P300/CBP may promote NER by acetylating both histones and the essential

NER factor XPG. Recently, it was reported that GCN5/PCAF (P300/CBP-associated factor) mediated acetylation of RPA1 (replication protein A1) and acetylation of XPF by TIP60 promote NER (He et al., 2017; Zhao et al., 2017; Wang et al., 2020). Like HATs, HDACs can deacetylate both histones and nonhistone NER factors. For example, HDAC3 deacetylates H3K14 after UV irradiation and this deacetylation of H3K14 facilitates the recruitment of XPC during NER (Kakumu et al., 2017; Nishimoto et al., 2020). Interestingly, HDAC4 itself was recently discovered to bind XPC directly for efficient NER (Li et al., 2020). A previous study has shown that XPA, a rate limiting NER factor, is deacetylated by SIRT1 and this deacetylation is required for optimal NER (Fan and Luo, 2010). However, it was later found that only a small fraction of XPA is acetylated and downregulation of SIRT1 has no measurable effect on overall rate of NER. Instead, XPA and hence NER is regulated by circadian clock at the transcriptional level (Kang et al., 2010; Kang et al., 2011).

With the development of NGS-based methods for genome-wide mapping of DNA damage and repair (Sloan et al., 2018; Li and Sancar, 2020), our understanding of DNA damage formation and repair in diverse chromatin environments has increased significantly. With the aid of XR-seq (Hu et al., 2015; Hu et al., 2019), which purely measures ongoing repair by isolating and sequencing the excision products released during NER, a genome-wide comparison of chromatin states, histone modifications, gene expression and UV damage repair kinetics was performed (Adar et al., 2016). It was found that the earliest repair occurs in active and open chromatin regions, while repair in repressed heterochromatin regions is relatively slow. Regions with H3K27 acetylation, which is associated with active promoters and enhancers, have high levels of early repair. Indeed, UV damage repair super hotspots, which are defined as the earliest-repair sites in the genome, are significantly enriched in both frequently interacting regions (FIREs) and super enhancers (Jiang et al., 2021).

## Histone Methylation and NER

Histone methylation, catalyzed by histone methyltransferases (HMTs), is the process of adding one, two, or three methyl groups to lysine and arginine residues in histone proteins. Methyl groups can also be removed from histone residues by histone demethylases. Depending on which residues are methylated and how many methyl groups are added, histone methylation can either increase or decrease gene transcription activity (Greer and Shi, 2012). The most extensively studied methylation of H3K9, H3K27 and H4K20 is associated with repressed transcription, whereas methylation of H3K4, H3K36, and H3K79 is linked to active transcription. Like histone acetylation, methylation events, which can weaken electrostatic attractions between histone and DNA, lead to unwinding of the DNA followed by recruitment of transcriptional machinery, and thus increase transcription activity. Some histone methylations, however, trigger chromatin compaction and inhibit the access of transcriptional machinery to DNA. For example, H3K9 methylation can recruit HP1 (heterochromatin protein 1) and bind to the highly conserved chromodomain of HP1, resulting in chromatin compaction and gene silencing (Jacobs and Khorasanizadeh, 2002). In *Drosophila melanogaster*, a global decrease of H3K9 trimethylation after UV irradiation was discovered in salivary gland cells (Palomera-Sanchez et al., 2010).

In contrast to histone acetylation, which has been known to function in NER for a long time, the involvement of histone methylation in NER was only recently revealed, and one histone methylation, H3K79, was found to function in NER (Bostelman et al., 2007; Chaudhuri et al., 2009; Tatum and Li, 2011; Zhu et al., 2018). In yeast, the H3K79 methylation is catalyzed by Dot1 with its HMT activity. Both Dot1 and H3K79 methylation are required for efficient global genomic repair but not for TCR (Tatum and Li, 2011). It was found that the role of H3K79 methylation in global genomic repair was unlikely achieved through activating cell cycle checkpoints or regulating the expression of NER genes. Rather, it may serve as a docking site for the recruitment of the NER machinery required for global genomic repair (Gsell et al., 2020). It was later found that DOT1L mediated H3K79 methylation is indeed essential for XPC recruitment and efficient NER after UV irradiation in mammalian cells (Zhu et al., 2018). Nevertheless, another study in mouse embryonic fibroblasts suggested that DOT1L is not implicated in global genomic repair, and that it mainly facilitates the reactivation of RNAP II transcription initiation by securing an open chromatin structure (Oksenych et al., 2013). The difference may be explained by the fact that global genomic repair in rodents is significantly slower than that in humans (van der Horst et al., 1997) and that embryonic stem cells primarily eliminate cells containing massively damaged DNA through apoptosis rather than NER (Li et al., 2019). Besides its role in NER, DOT1L is also critical for transcription elongation, DNA damage response, normal development, and formation of heterochromatin (Wysocki et al., 2005; Wood et al., 2018; Ljungman et al., 2019).

H3K4 trimethylation (H3K4me3) and H3K4 monomethylation (H3K4me1) are associated with actively transcribed promoters and active enhancers, respectively. It was found that DDB2, a DNA damage-binding protein, interacts with and recruits the histone methyltransferase ASH1L (Absent, Small or Homeotic discs 1) to UV lesions leading to deposition of H3K4me3. Similar to H3K79 methylation, H3K4me3 facilitates the stable docking of XPC to DNA damage sites enabling the recruitment of downstream NER proteins by XPC (Balbo Pogliano et al., 2017). Interestingly, another study in yeast showed that H4H75E mutation decreases global genomic repair by impairing the recruitment of Rad4 (XPC in humans) to chromatin after UV irradiation (Selvam et al., 2019). As DDB2 preferentially binds to unmethylated nucleosomes, it is likely that H3K4me3 may promote the DDB2-XPC handover at DNA damage sites (Apelt et al., 2021). Like H3K27 acetylation, excision repair in regions marked by H3K4me3 and H3K4me1 occurs much earlier than those regions marked by repressive histone methylations (Adar et al., 2016). H3K4 methylation was also found to promote the repair of DNA double-strand breaks by the non-homologous end joining pathway (Wei et al., 2018). Whether and how H3K79 methylation and H3K4me3 are coordinated during the NER process needs to be elucidated in future studies.

## Histone Ubiquitylation and NER

Ubiquitylation is the addition of ubiquitin, which consists of 76 amino acids and exists in all eukaryotes, to a substrate protein. This process is through a reversible three-step enzymatic reaction requiring ubiquitin-activating enzymes (E1), ubiquitin-conjugating enzymes (E2), and ubiquitin ligases (E3). During the ubiquitylation, one single ubiquitin (monoubiquitylation) or a chain of ubiquitin (polyubiquitylation) can be added to the substrate protein. For polyubiquitylation, the seven lysine residues (K6, K11, K27, K29, K33, K48, K63) and N-terminal methionine (M1) in ubiquitin serve as linkage points of the ubiquitin chain (Komander and Rape, 2012). It is associated with a wide range of cellular processes such as protein degradation, DNA replication, gene transcription and DNA repair (Welchman et al., 2005). Nevertheless, only polyubiquitylation, mostly K48- and K29-linked polyubiquitylation, marks the substrate protein for degradation by the proteasome. Other polyubiquitylations and monoubiquitylations may regulate other cellular processes including NER (Miranda and Sorkin, 2007; Chauhan et al., 2021). Histone ubiquitylation occurs primarily on H2A (K119) and H2B (K20 in humans and K123 in yeast). Both H2A and H2B are mainly monoubiquitylated and involved in crosstalk with other histone modifications such as histone methylations in a variety of cellular processes (Weake and Workman, 2008). H2A ubiquitylation is generally linked to gene silencing, while H2B ubiquitylation plays a role in both repression and activation of transcription. Ubiquitylation of H2A and H2B has been shown to participate in the process of NER. Meanwhile, a subset of NER-related proteins, such as XPC (Rad4 in yeast), DDB2, CSB, UVSSA and RPB1 (the largest subunit of RNAP II), are also ubiquitylated during NER (Gillette et al., 2006; Borsos et al., 2020; Apelt et al., 2021). For example, recent studies revealed that ELOF1 is required for the ubiquitylation of RPB1 K1268, a key signal for the recruitment of downstream repair factors including UVSSA and TFIIH (van der Weegen et al., 2021). However, how ubiquitylation of NER proteins functions in NER will not be discussed in detail in this review.

In yeast, the monoubiquitylation of H2B K123, catalyzed by Rad6/Bre1 complex, is partially required for global genomic repair. The Paf1 complex, a transcription elongation factor containing five subunits, is required for the catalytic activity of Rad6/Bre1 complex (Wood et al., 2003; Tatum et al., 2011; Tatum and Li, 2011). Interestingly, ubiquitylation of H2B K123 is essential for H3K79 methylation, which is catalyzed by Dot1 and required for global genomic repair but not TCR (Tatum and Li, 2011). Thus, it is likely that H2B ubiquitylation promotes global genomic repair indirectly by enabling the recruitment of Dot1 and the subsequent methylation of H3K79. Indeed, it was revealed that H2B ubiquitylation can regulate chromatin dynamics by enhancing nucleosome stability (Chandrasekharan et al., 2009; Chandrasekharan et al., 2010). Ubiquitylation of H2B is also necessary for H3K4 methylation which is mediated by the methyltransferase Set1-COMPASS and promotes NER in a similar way to H3K79 methylation.

UV-DDB, a heterodimeric complex containing DDB1 and DDB2, is part of a big ubiquitin E3 ligase complex that recognizes damaged chromatin and ubiquitylates core histones at damaged sites (Hannah and Zhou, 2009; Sugasawa, 2009). After UV irradiation, H2A (K118 and K119) and H2B are ubiquitylated by this ubiquitin E3 ligase complex (Kapetanaki et al., 2006; Lan et al., 2012). In addition, ubiquitin ligases Ring1B (Ring2) (Wang et al., 2004; Gracheva et al., 2016) and RNF8 (Marteijn et al., 2009) can also catalyze the H2A ubiquitylation. Ring1B was found to interact with UV-DDB-CUL4 and form a stable complex to ubiquitylate H2A at an early step of damage recognition after UV irradiation (Gracheva et al., 2016). Then, ZRF1, a H2A-ubiquitin binding protein, recognizes and remodels the UV-DDB-CUL4-RING1B complex causing the assembly of the canonical UV-DDB-CUL4 complex. XPC is, then, ubiquitylated by UV-DDB-CUL4 (Sugasawa et al., 2005). In this process, ZRF1 works as a switch protein that regulates XPC ubiquitylation through remodeling of the UV-DDB-CUL4-RING1B complex (Gracheva et al., 2016). It was later discovered that NER involves chromatin reorganization and ZRF1, in combination with XPC, facilitates the relocalization of damaged chromatin to the nucleolus for repair (Chitale and Richly, 2017). In the case of RNF8-mediated H2A ubiquitylation, it occurs after the incision step of NER and RNF8 is essential for the recruitment of downstream factors 53BP1 and BRCA1 (Marteijn et al., 2009; Zhu et al., 2009). Interestingly, RNAP II stalling caused by UV-induced DNA damage triggers H2B deubiquitylation at global level through histone deubiquitylases (Ubp8 and Ubp10) and H2B ubiquitylation level restores gradually during NER in yeast and humans (Mao et al., 2014). Without H2B deubiquitylation, TCR is decreased and RNAP II degradation is increased, suggesting deubiquitylation of H2B can facilitate rescue of RNAP II stalled at UV damage sites through TCR in chromatin (Meas and Mao, 2015).

Histones H3 and H4 can also be ubiquitylated by UV-DDB-CUL4 after UV irradiation, thus destabilizing the nucleosomes and facilitating the recruitment of XPC to DNA damage sites (Wang et al., 2006).

## Histone Phosphorylation and NER

Histone phosphorylation is the addition of a phosphate group to histone residues (serine, threonine and tyrosine) by protein kinases and dephosphorylation is the removal of the phosphate group by phosphatases. The most well studied histone phosphorylation is that of the histone H2AX variant (γ-H2AX) on S139 in mammals (Rogakou et al., 1998) or S129 in yeast (Downs et al., 2000). Upon induction of DNA double strand breaks, histone H2AX is rapidly phosphorylated by ATM (ataxia telangiectasia mutated) and DNA-PKcs (Burma et al., 2001; Fernandez-Capetillo et al., 2004). In the case of UV induced γ-H2AX, the phosphorylation is mainly mediated by the kinase ATR (ataxia telangiectasia and Rad3-related) in the presence of DNA single-strand breaks (Ward and Chen, 2001; Hanasoge and Ljungman, 2007; Matsumoto et al., 2007). Histone phosphorylation reduces the positive charge of the histones, leading to a more open chromatin conformation. Unlike histone acetylation and methylation, histone phosphorylation interplays with other histone modifications and serves as a platform for recruiting factors for downstream cascade of

events, such as DNA damage checkpoint activation (Fernandez-Capetillo et al., 2002).

It was shown that γ-H2AX has no significant effect on NER in mammals and yeast (Moore et al., 2007; Revet et al., 2011). Instead, NER plays a key role in the induction of γ-H2AX by generating single-stranded DNA during the repair process (Marti et al., 2006; Hanasoge and Ljungman, 2007; Matsumoto et al., 2007). Single-stranded DNA gap intermediates produced during NER can be extended by EXO1 (exonuclease 1) and coated by RPA (replication protein A), the major eukaryotic single stranded DNA-binding protein, which then recruits ATR and other ATR signaling proteins for ATR activation (Giannattasio et al., 2010; Sertic et al., 2011; Kemp, 2019). It is also likely that the single-stranded excision products released during NER are bound by RPA and involved in ATR kinase signaling pathway (Kemp and Sancar, 2012). Moreover, R-loop formation caused by the stalling of elongating RNAP II at a DNA lesion and DNA replication fork stalling induced by UV damage can activate H2AX phosphorylation (Halicka et al., 2005; Marti et al., 2006; Tresini et al., 2015). Interestingly, other phosphorylated histones, such as H3 (S10 and T11) in mammals and H2A (S122 and T126) in yeast, are dephosphorylated after UV irradiation (Sen and De Benedetti, 2006; Moore et al., 2007; Shimada et al., 2008). Phosphorylation on other histones, including H2B (T129) in yeast, H3 (T45) in humans and H3.3 (S31) in mouse embryonic stem cells, have been identified (Lee et al., 2014; Lee et al., 2015; Martire et al., 2019). However, whether and how histone phosphorylation on these residues is involved in NER remain to be investigated.

## ATP-DEPENDENT CHROMATIN REMODELING AND NER

Besides histone modifications, ATP-dependent chromatin remodeling catalyzed by chromatin remodelers is another way to modulate chromatin structure allowing access of NER machinery to damaged DNA during repair (Nag and Smerdon, 2009; Waters et al., 2015). All the ATP-dependent chromatin remodeling complexes have a common ATPase domain and use the energy released from ATP hydrolysis to slide, eject, or restructure nucleosomes during important biological processes including chromosome assembly and segregation, DNA damage and repair, apoptosis, and cell cycle progression (Wang et al., 2007). ATP-dependent chromatin remodelers in eukaryotes are classified into four families: SWI/SNF (switch defective/sucrose nonfermenting), CHD (chromodomain helicase DNA binding), INO80 (inositol requiring 80), and ISWI (imitation switch). Even though all remodelers share a common ATPase domain, their functions are specific because each remodeler has unique protein domains (e.g., bromodomain and helicase) in their ATPase region (Clapier and Cairns, 2009).

The effect of ATP-dependent chromatin remodelers on NER was first studied in two independent *in vitro* studies. In one study, it was discovered that the *Drosophila* ACF (ATP-utilizing chromatin assembly and remodeling factor), which belongs to ISWI family, facilitates NER of (6-4)PP in the linker DNA region, but not in the nucleosome core region (Ura et al., 2001). In the other study, it was found that the yeast SWI/SNF complex enhances NER of AAF-G (acetylaminofluorene-guanine) in nucleosome core particle (Hara and Sancar, 2002). The different effects might be due to the specific functions for the two families of chromatin remodelers. ISWI remodelers maintain high order of chromatin structure by creating equal spacing between nucleosomes, while SWI/SNF remodelers rearrange nucleosomes through unwrapping, sliding, or ejecting nucleosomes (Clapier and Cairns, 2009). Similarly, the human CSB (cockayne syndrome protein B), which belongs to SWI/SNF family and is essential for TCR, was found to remodel chromatin *in vitro* (Citterio et al., 2000).

Like *in vitro* studies, one subsequent *in vivo* study in yeast showed that the SWI/SNF chromatin remodeling complex interacts with Rad4-Rad23 heterodimer to increase DNA accessibility for NER upon UV irradiation (Gong et al., 2006). In humans, SWI/SNF complex was also found to associate with XPC at DNA damage sites and promote recruitment of ATM and NER factors (e.g., XPG) in response to UV irradiation (Ray et al., 2009; Zhao et al., 2009). Rad16, another SWI/SNF chromatin remodeler, was found to promote efficient global genomic repair by increasing the occupancy of Gcn5 in chromatin and subsequent H3 acetylation through its ATPase and RING domains (Yu et al., 2011). The INO80 family of chromatin remodelers modulate chromatin structure in different ways including exchange of histone variants (e.g., H2AZ) and nucleosome sliding (Clapier et al., 2017). By using the energy from ATP hydrolysis, it can incorporate and remove histone variants in the nucleosome and create nucleosome-free regions. In humans, it was found that INO80 is recruited to UV induced DNA damage sites independent of XPC and interacts with DDB1, suggesting a role in the initiating step of NER (Jiang et al., 2010). One study, however, reported that yeast INO80 is recruited to chromatin by Rad4 upon UV irradiation and restores chromatin structure after NER (Sarkar et al., 2010). Another study in yeast showed that cells without INO80 are proficient in repair of CPDs and replication defects may contribute to UV sensitivity observed in cells lacking INO80 (Czaja et al., 2010). CHD family remodelers are primarily responsible for transcriptional repression by assembling nucleosomes, although certain CHDs in higher organisms can slide or eject nucleosomes to promote transcription (Clapier et al., 2017). It was found that human CHD1 is recruited to UV damage sites in an XPC dependent manner and mediates XPC-to-TFIIH handover to facilitate NER in chromatin (Ruthemann et al., 2017).

Recent development of NGS-based sequencing methods has enabled researchers to capture the spatial genome organization and map DNA damage formation and repair across the whole genome (Garcia-Nieto et al., 2017; Sloan et al., 2018; Li and Sancar, 2020; Sanders et al., 2020). Studies in yeast showed that the global genomic repair complex (Rad16-Rad7-Abf1), which includes SWI/SNF chromatin remodeler Rad16, binds to the boundary sites of chromosomally interacting domains (CIDs) frequently and regulates distribution of histone H3 acetylation upon UV irradiation. The global genomic repair complexes initiate nucleosome remodeling in

the vicinity of their binding sites in response to UV damage, which defines the origins of NER in chromatin (Yu et al., 2016; van Eijk et al., 2019). A recent study reported that SWI/SNF is not generally required for efficient NER and only affects NER at certain genes in yeast, while RSC (chromatin structure remodeling), another SWI/SNF family chromatin remodeler, is required for NER throughout the yeast whole genome (Bohm et al., 2021).

## CONCLUSION

NER is a highly conserved and versatile DNA damage removal pathway that counteracts challenges from a variety of DNA damaging agents. Since the basic molecular mechanism of NER has been well studied by using *in vitro* experimental system (Sancar, 2016), it becomes more and more intriguing to explore and decipher the mysteries of the NER process within the complex and dynamic molecular environment of the cell. This review is focused on our current understanding of epigenetic regulation of NER, especially on how different histone modifications affect the *in vivo* NER process in the context of chromatin. Upon DNA damage induction, a cascade of cellular events, including DNA damage checkpoint activation, histone modifications, chromatin reorganization, DNA repair, and apoptosis, would occur to deal with the assault.

In recent years, we have gained relatively better understanding of how DNA damage is recognized by NER related machinery such as UV-DDB and XPC-RAD23B-CETN2 in the chromatin environment (Apelt et al., 2021). However, how different epigenetic factors, including chromatin modifications, nucleosome positioning, chromatin remodeling, DNA modifications and non-coding RNA, are mechanistically orchestrated to give NER machinery access to DNA lesions is still unknown. These factors may interplay with each other, complicating the delicate NER process. Even for modification of histones itself, one modification may promote or repress other modification(s). The modifications on histones and non-histone proteins may indirectly regulate NER through altering gene expression profile, which increases the complexity of studying NER. Another open question is how the cellular chromatin organization is restored after the NER process. The development and application of novel research methods such as cryo-EM and third-generation sequencing would aid in our in-depth understanding of these questions.

## AUTHOR CONTRIBUTIONS

WL wrote and finalized the manuscript. KJ, TB, MAH, and LL reviewed and edited the manuscript.

## FUNDING

This work was supported by the NIH Grant R00 ES030015 (to WL).

## ACKNOWLEDGMENTS

We thank Dr. Yuan Fang for her helpful discussions on this manuscript. We thank Dr. Jinchuan Hu for his comments on this manuscript. We apologize to authors whose work could not be discussed and cited due to the space and topic constraints.

## REFERENCES

Aboussekhra, A., Biggerstaff, M., Shivji, M. K. K., Vilpo, J. A., Moncollin, V., Podust, V. N., et al. (1995). Mammalian DNA Nucleotide Excision Repair Reconstituted with Purified Protein Components. *Cell* 80 (6), 859–868. doi:10.1016/0092-8674(95)90289-9

Adar, S., Hu, J., Lieb, J. D., and Sancar, A. (2016). Genome-Wide Kinetics of DNA Excision Repair in Relation to Chromatin State and Mutagenesis. *Proc. Natl. Acad. Sci. U.S.A.* 113 (15), E2124–E2133. doi:10.1073/pnas.1603388113

Apelt, K., Lans, H., Schärer, O. D., and Luijsterburg, M. S. (2021). Nucleotide Excision Repair Leaves a Mark on Chromatin: DNA Damage Detection in Nucleosomes. *Cell. Mol. Life Sci.* 78 (24), 7925–7942. doi:10.1007/s00018-021-03984-7

Balbo Pogliano, C., Gatti, M., Rüthemann, P., Garajovà, Z., Penengo, L., and Naegeli, H. (2017). ASH1L Histone Methyltransferase Regulates the Handoff between Damage Recognition Factors in Global-Genome Nucleotide Excision Repair. *Nat. Commun.* 8 (1), 1333. doi:10.1038/s41467-017-01080-8

Battu, A., Ray, A., and Wani, A. A. (2011). ASF1A and ATM Regulate H3K56-Mediated Cell-Cycle Checkpoint Recovery in Response to UV Irradiation. *Nucleic Acids Res.* 39 (18), 7931–7945. doi:10.1093/nar/gkr523

Bohm, K. A., Hodges, A. J., Czaja, W., Selvam, K., Smerdon, M. J., Mao, P., et al. (2021). Distinct Roles for RSC and SWI/SNF Chromatin Remodelers in Genomic Excision Repair. *Genome Res.* 31 (6), 1047–1059. doi:10.1101/gr.274373.120

Borsos, B. N., Majoros, H., and Pankotai, T. (2020). Emerging Roles of Post-Translational Modifications in Nucleotide Excision Repair. *Cells* 9 (6), 1466. doi:10.3390/cells9061466

Bostelman, L. J., Keller, A. M., Albrecht, A. M., Arat, A., and Thompson, J. S. (2007). Methylation of Histone H3 Lysine-79 by Dot1p Plays Multiple Roles in the Response to UV Damage in *Saccharomyces C. DNA Repair* 6 (3), 383–395. doi:10.1016/j.dnarep.2006.12.010

Bouvier, D., Ferrand, J., Chevallier, O., Paulsen, M. T., Ljungman, M., and Polo, S. E. (2021). Dissecting Regulatory Pathways for Transcription Recovery Following DNA Damage Reveals a Non-Canonical Function of the Histone Chaperone HIRA. *Nat. Commun.* 12 (1), 3835. doi:10.1038/s41467-021-24153-1

Burma, S., Chen, B. P., Murphy, M., Kurimasa, A., and Chen, D. J. (2001). ATM Phosphorylates Histone H2AX in Response to DNA Double-Strand Breaks. *J. Biol. Chem.* 276 (45), 42462–42467. doi:10.1074/jbc.C100466200

Caron, P., Pobega, E., and Polo, S. E. (2021). A Molecular Rosetta Stone to Decipher the Impact of Chromatin Features on the Repair of Cas9-Mediated DNA Double-Strand Breaks. *Mol. Cel* 81 (10), 2059–2060. doi:10.1016/j.molcel.2021.04.024

Chandrasekharan, M. B., Huang, F., and Sun, Z.-W. (2010). Histone H2B Ubiquitination and beyond: Regulation of Nucleosome Stability, Chromatin Dynamics and the Trans-Histone H3 Methylation. *Epigenetics* 5 (6), 460–468. doi:10.4161/epi.5.6.12314

Chandrasekharan, M. B., Huang, F., and Sun, Z.-W. (2009). Ubiquitination of Histone H2B Regulates Chromatin Dynamics by Enhancing Nucleosome Stability. *Proc. Natl. Acad. Sci. U.S.A.* 106 (39), 16686–16691. doi:10.1073/pnas.0907862106

Chaudhuri, S., Wyrick, J. J., and Smerdon, M. J. (2009). Histone H3 Lys79 Methylation Is Required for Efficient Nucleotide Excision Repair in a Silenced Locus of *Saccharomyces C. Nucleic Acids Res.* 37 (5), 1690–1700. doi:10.1093/nar/gkp003

Chauhan, A. K., Sun, Y., Zhu, Q., and Wani, A. A. (2021). Timely Upstream Events Regulating Nucleotide Excision Repair by Ubiquitin-Proteasome System: Ubiquitin Guides the Way. *DNA Repair* 103, 103128. doi:10.1016/j.dnarep.2021.103128

Chitale, S., and Richly, H. (2017). Nuclear Organization of Nucleotide Excision Repair Is Mediated by RING1B Dependent H2A-Ubiquitylation. *Oncotarget* 8 (19), 30870–30887. doi:10.18632/oncotarget.16142

Citterio, E., Van Den Boom, V., Schnitzler, G., Kanaar, R., Bonte, E., Kingston, R. E., et al. (2000). ATP-dependent Chromatin Remodeling by the Cockayne Syndrome B DNA Repair-Transcription-Coupling Factor. *Mol. Cel Biol* 20 (20), 7643–7653. doi:10.1128/mcb.20.20.7643-7653.2000

Clapier, C. R., and Cairns, B. R. (2009). The Biology of Chromatin Remodeling Complexes. *Annu. Rev. Biochem.* 78, 273–304. doi:10.1146/annurev.biochem.77.062706.153223

Clapier, C. R., Iwasa, J., Cairns, B. R., and Peterson, C. L. (2017). Mechanisms of Action and Regulation of ATP-Dependent Chromatin-Remodelling Complexes. *Nat. Rev. Mol. Cel Biol* 18 (7), 407–422. doi:10.1038/nrm.2017.26

Cleaver, J. E., and Thomas, G. H. (1993). Clinical Syndromes Associated with DNA Repair Deficiency and Enhanced Sun Sensitivity. *Arch. Dermatol.* 129 (3), 348–350. doi:10.1001/archderm.1993.01680240088014

Czaja, W., Bespalov, V. A., Hinz, J. M., and Smerdon, M. J. (2010). Proficient Repair in Chromatin Remodeling Defective Ino80 Mutants of *Saccharomyces C* Highlights Replication Defects as the Main Contributor to DNA Damage Sensitivity. *DNA Repair* 9 (9), 976–984. doi:10.1016/j.dnarep.2010.06.010

Datta, A., Bagchi, S., Nag, A., Shiyanov, P., Adami, G. R., Yoon, T., et al. (2001). The P48 Subunit of the Damaged-DNA Binding Protein DDB Associates with the CBP/p300 Family of Histone Acetyltransferase. *Mutat. Research/DNA Repair* 486 (2), 89–97. doi:10.1016/s0921-8777(01)00082-9

Deem, A. K., Li, X., and Tyler, J. K. (2012). Epigenetic Regulation of Genomic Integrity. *Chromosoma* 121 (2), 131–151. doi:10.1007/s00412-011-0358-1

Dinant, C., Houtsmuller, A. B., and Vermeulen, W. (2008). Chromatin Structure and DNA Damage Repair. *Epigenetics Chromatin* 1 (1), 9. doi:10.1186/1756-8935-1-9

Downs, J. A., Lowndes, N. F., and Jackson, S. P. (2000). A Role for *Saccharomyces C* Histone H2A in DNA Repair. *Nature* 408 (6815), 1001–1004. doi:10.1038/35050000

Driscoll, R., Hudson, A., and Jackson, S. P. (2007). Yeast Rtt109 Promotes Genome Stability by Acetylating Histone H3 on Lysine 56. *Science* 315 (5812), 649–652. doi:10.1126/science.1135862

Duan, M.-R., and Smerdon, M. J. (2014). Histone H3 Lysine 14 (H3K14) Acetylation Facilitates DNA Repair in a Positioned Nucleosome by Stabilizing the Binding of the Chromatin Remodeler RSC (Remodels Structure of Chromatin). *J. Biol. Chem.* 289 (12), 8353–8363. doi:10.1074/jbc.M113.540732

Fan, W., and Luo, J. (2010). SIRT1 Regulates UV-Induced DNA Repair through Deacetylating XPA. *Mol. Cel* 39 (2), 247–258. doi:10.1016/j.molcel.2010.07.006

Fernandez-Capetillo, O., Lee, A., Nussenzweig, M., and Nussenzweig, A. (2004). H2AX: The Histone Guardian of the Genome. *DNA Repair (Amst)* 3 (8-9), 959–967. doi:10.1016/j.dnarep.2004.03.024

Fernandez-Capetillo, O., Chen, H.-T., Celeste, A., Ward, I., Romanienko, P. J., Morales, J. C., et al. (2002). DNA Damage-Induced G2-M Checkpoint Activation by Histone H2AX and 53BP1. *Nat. Cel Biol* 4 (12), 993–997. doi:10.1038/ncb884

Gale, J. M., Nissen, K. A., and Smerdon, M. J. (1987). UV-Induced Formation of Pyrimidine Dimers in Nucleosome Core DNA Is Strongly Modulated with a Period of 10.3 Bases. *Proc. Natl. Acad. Sci. U.S.A.* 84 (19), 6644–6648. doi:10.1073/pnas.84.19.6644

García-Nieto, P. E., Schwartz, E. K., King, D. A., Paulsen, J., Collas, P., Herrera, R. E., et al. (2017). Carcinogen Susceptibility Is Regulated by Genome Architecture and Predicts Cancer Mutagenesis. *EMBO J.* 36 (19), 2829–2843. doi:10.15252/embj.201796717

Geijer, M. E., Zhou, D., Selvam, K., Steurer, B., Mukherjee, C., Evers, B., et al. (2021). Elongation Factor ELOF1 Drives Transcription-Coupled Repair and Prevents Genome Instability. *Nat. Cel Biol* 23 (6), 608–619. doi:10.1038/s41556-021-00692-z

Giannattasio, M., Follonier, C., Tourrière, H., Puddu, F., Lazzaro, F., Pasero, P., et al. (2010). Exo1 Competes with Repair Synthesis, Converts NER Intermediates to Long ssDNA Gaps, and Promotes Checkpoint Activation. *Mol. Cel* 40 (1), 50–62. doi:10.1016/j.molcel.2010.09.004

Gillette, T. G., Yu, S., Zhou, Z., Waters, R., Johnston, S. A., and Reed, S. H. (2006). Distinct Functions of the Ubiquitin-Proteasome Pathway Influence Nucleotide Excision Repair. *Embo J.* 25 (11), 2529–2538. doi:10.1038/sj.emboj.7601120

Gong, F., Fahy, D., and Smerdon, M. J. (2006). Rad4-Rad23 Interaction with SWI/SNF Links ATP-Dependent Chromatin Remodeling with Nucleotide Excision Repair. *Nat. Struct. Mol. Biol.* 13 (10), 902–907. doi:10.1038/nsmb1152

Gracheva, E., Chitale, S., Wilhelm, T., Rapp, A., Byrne, J., Stadler, J., et al. (2016). ZRF1 Mediates Remodeling of E3 Ligases at DNA Lesion Sites during Nucleotide Excision Repair. *J. Cel Biol* 213 (2), 185–200. doi:10.1083/jcb.201506099

Greer, E. L., and Shi, Y. (2012). Histone Methylation: A Dynamic Mark in Health, Disease and Inheritance. *Nat. Rev. Genet.* 13 (5), 343–357. doi:10.1038/nrg3173

Gsell, C., Richly, H., Coin, F., and Naegeli, H. (2020). A Chromatin Scaffold for DNA Damage Recognition: How Histone Methyltransferases Prime Nucleosomes for Repair of Ultraviolet Light-Induced Lesions. *Nucleic Acids Res.* 48 (4), 1652–1668. doi:10.1093/nar/gkz1229

Guo, R., Chen, J., Mitchell, D. L., and Johnson, D. G. (2011). GCN5 and E2F1 Stimulate Nucleotide Excision Repair by Promoting H3K9 Acetylation at Sites of Damage. *Nucleic Acids Res.* 39 (4), 1390–1397. doi:10.1093/nar/gkq983

Guo, R., Chen, J., Zhu, F., Biswas, A. K., Berton, T. R., Mitchell, D. L., et al. (2010). E2F1 Localizes to Sites of UV-Induced DNA Damage to Enhance Nucleotide Excision Repair. *J. Biol. Chem.* 285 (25), 19308–19315. doi:10.1074/jbc.m110.121939

Halicka, H. D., Huang, X., Traganos, F., King, M. A., Dai, W., and Darzynkiewicz, Z. (2005). Histone H2AX Phosphorylation after Cell Irradiation with UV-B: Relationship to Cell Cycle Phase and Induction of Apoptosis. *Cell Cycle* 4 (2), 339–345. doi:10.4161/cc.4.2.1486

Han, J., Zhou, H., Horazdovsky, B., Zhang, K., Xu, R.-M., and Zhang, Z. (2007). Rtt109 Acetylates Histone H3 Lysine 56 and Functions in DNA Replication. *Science* 315 (5812), 653–655. doi:10.1126/science.1133234

Hanasoge, S., and Ljungman, M. (2007). H2AX Phosphorylation after UV Irradiation Is Triggered by DNA Repair Intermediates and Is Mediated by the ATR Kinase. *Carcinogenesis* 28 (11), 2298–2304. doi:10.1093/carcin/bgm157

Hanawalt, P. C., and Spivak, G. (2008). Transcription-Coupled DNA Repair: Two Decades of Progress and Surprises. *Nat. Rev. Mol. Cel Biol* 9 (12), 958–970. doi:10.1038/nrm2549

Hannah, J., and Zhou, P. (2009). Regulation of DNA Damage Response Pathways by the Cullin-RING Ubiquitin Ligases. *DNA Repair* 8 (4), 536–543. doi:10.1016/j.dnarep.2009.01.011

Hara, R., Mo, J., and Sancar, A. (2000). DNA Damage in the Nucleosome Core Is Refractory to Repair by Human Excision Nuclease. *Mol. Cel Biol* 20 (24), 9173–9181. doi:10.1128/mcb.20.24.9173-9181.2000

Hara, R., and Sancar, A. (2002). The SWI/SNF Chromatin-Remodeling Factor Stimulates Repair by Human Excision Nuclease in the Mononucleosome Core Particle. *Mol. Cel Biol* 22 (19), 6779–6787. doi:10.1128/mcb.22.19.6779-6787.2002

Hasan, S., Hassa, P. O., Imhof, R., and Hottiger, M. O. (2001). Transcription Coactivator P300 Binds PCNA and May Have a Role in DNA Repair Synthesis. *Nature* 410 (6826), 387–391. doi:10.1038/35066610

He, H., Wang, J., and Liu, T. (2017). UV-Induced RPA1 Acetylation Promotes Nucleotide Excision Repair. *Cel Rep.* 20 (9), 2010–2025. doi:10.1016/j.celrep.2017.08.016

Hodawadekar, S. C., and Marmorstein, R. (2007). Chemistry of Acetyl Transfer by Histone Modifying Enzymes: Structure, Mechanism and Implications for Effector Design. *Oncogene* 26 (37), 5528–5540. doi:10.1038/sj.onc.1210619

Hodges, A. J., Plummer, D. A., and Wyrick, J. J. (2019). NuA4 Acetyltransferase Is Required for Efficient Nucleotide Excision Repair in Yeast. *DNA Repair* 73, 91–98. doi:10.1016/j.dnarep.2018.11.006

Hoeijmakers, J. H. J. (2001). Genome Maintenance Mechanisms for Preventing Cancer. *Nature* 411 (6835), 366–374. doi:10.1038/35077232

Hu, J., Adar, S., Selby, C. P., Lieb, J. D., and Sancar, A. (2015). Genome-Wide Analysis of Human Global and Transcription-Coupled Excision Repair of UV Damage at Single-Nucleotide Resolution. *Genes Dev.* 29 (9), 948–960. doi:10.1101/gad.261271.115

Hu, J., Choi, J.-H., Gaddameedhi, S., Kemp, M. G., Reardon, J. T., and Sancar, A. (2013). Nucleotide Excision Repair in Human Cells: Fate of the Excised Oligonucleotide Carrying DNA Damage *In Vivo*. *J. Biol. Chem.* 288 (29), 20918–20926. doi:10.1074/jbc.M113.482257

Hu, J., Li, W., Adebali, O., Yang, Y., Oztas, O., Selby, C. P., et al. (2019). Genome-Wide Mapping of Nucleotide Excision Repair with XR-Seq. *Nat. Protoc.* 14 (1), 248–282. doi:10.1038/s41596-018-0093-7

Hu, J., Selby, C. P., Adar, S., Adebali, O., and Sancar, A. (2017). Molecular Mechanisms and Genomic Maps of DNA Excision Repair in *Escherichia coli* and Humans. *J. Biol. Chem.* 292 (38), 15588–15597. doi:10.1074/jbc.R117.807453

Husain, I., Van Houten, B., Thomas, D. C., Abdel-Monem, M., and Sancar, A. (1985). Effect of DNA Polymerase I and DNA Helicase II on the Turnover Rate of UvrABC Excision Nuclease. *Proc. Natl. Acad. Sci. U.S.A.* 82 (20), 6774–6778. doi:10.1073/pnas.82.20.6774

Irizar, A., Yu, Y., Reed, S. H., Louis, E. J., and Waters, R. (2010). Silenced Yeast Chromatin Is Maintained by Sir2 in Preference to Permitting Histone Acetylations for Efficient NER. *Nucleic Acids Res.* 38 (14), 4675–4686. doi:10.1093/nar/gkq242

Jacobs, S. A., and Khorasanizadeh, S. (2002). Structure of HP1 Chromodomain Bound to a Lysine 9-methylated Histone H3 Tail. *Science* 295 (5562), 2080–2083. doi:10.1126/science.1069473

Jenuwein, T., and Allis, C. D. (2001). Translating the Histone Code. *Science* 293 (5532), 1074–1080. doi:10.1126/science.1063127

Jiang, Y., Li, W., Lindsey-Boltz, L. A., Yang, Y., Li, Y., and Sancar, A. (2021). Super Hotspots and Super Coldspots in the Repair of UV-Induced DNA Damage in the Human Genome. *J. Biol. Chem.* 296, 100581. doi:10.1016/j.jbc.2021.100581

Jiang, Y., Wang, X., Bao, S., Guo, R., Johnson, D. G., Shen, X., et al. (2010). INO80 Chromatin Remodeling Complex Promotes the Removal of UV Lesions by the Nucleotide Excision Repair Pathway. *Proc. Natl. Acad. Sci. U.S.A.* 107 (40), 17274–17279. doi:10.1073/pnas.1008388107

Kakumu, E., Nakanishi, S., Shiratori, H. M., Kato, A., Kobayashi, W., Machida, S., et al. (2017). Xeroderma Pigmentosum Group C Protein Interacts with Histones: Regulation by Acetylated States of Histone H3. *Genes Cells* 22 (3), 310–327. doi:10.1111/gtc.12479

Kang, T.-H., Lindsey-Boltz, L. A., Reardon, J. T., and Sancar, A. (2010). Circadian Control of XPA and Excision Repair of Cisplatin-DNA Damage by Cryptochrome and HERC2 Ubiquitin Ligase. *Proc. Natl. Acad. Sci. U.S.A.* 107 (11), 4890–4895. doi:10.1073/pnas.0915085107

Kang, T.-H., Reardon, J. T., and Sancar, A. (2011). Regulation of Nucleotide Excision Repair Activity by Transcriptional and post-transcriptional Control of the XPA Protein. *Nucleic Acids Res.* 39 (8), 3176–3187. doi:10.1093/nar/gkq1318

Kapetanaki, M. G., Guerrero-Santoro, J., Bisi, D. C., Hsieh, C. L., Rapić-Otrin, V., and Levine, A. S. (2006). The DDB1-Cul4a DDB2 Ubiquitin Ligase Is Deficient in Xeroderma Pigmentosum Group E and Targets Histone H2A at UV-Damaged DNA Sites. *Proc. Natl. Acad. Sci. U.S.A.* 103 (8), 2588–2593. doi:10.1073/pnas.0511160103

Karakaidos, P., Karagiannis, D., and Rampias, T. (2020). Resolving DNA Damage: Epigenetic Regulation of DNA Repair. *Molecules* 25 (11), 2496. doi:10.3390/molecules25112496

Kemp, M. G. (2019). Damage Removal and gap Filling in Nucleotide Excision Repair. *Enzymes* 45, 59–97. doi:10.1016/bs.enz.2019.06.001

Kemp, M. G., Reardon, J. T., Lindsey-Boltz, L. A., and Sancar, A. (2012). Mechanism of Release and Fate of Excised Oligonucleotides during Nucleotide Excision Repair. *J. Biol. Chem.* 287 (27), 22889–22899. doi:10.1074/jbc.M112.374447

Kemp, M. G., and Sancar, A. (2012). DNA Excision Repair: Where Do All the Dimers Go? *Cell Cycle* 11 (16), 2997–3002. doi:10.4161/cc.21126

Komander, D., and Rape, M. (2012). The Ubiquitin Code. *Annu. Rev. Biochem.* 81, 203–229. doi:10.1146/annurev-biochem-060310-170328

Kouzarides, T. (2007). Chromatin Modifications and Their Function. *Cell* 128 (4), 693–705. doi:10.1016/j.cell.2007.02.005

Lan, L., Nakajima, S., Kapetanaki, M. G., Hsieh, C. L., Fagerburg, M., Thickman, K., et al. (2012). Monoubiquitinated Histone H2A Destabilizes Photolesion-Containing Nucleosomes with Concomitant Release of UV-Damaged DNA-Binding Protein E3 Ligase. *J. Biol. Chem.* 287 (15), 12036–12049. doi:10.1074/jbc.m111.307058

Lee, C.-S., Lee, K., Legube, G., and Haber, J. E. (2014). Dynamics of Yeast Histone H2A and H2B Phosphorylation in Response to a Double-Strand Break. *Nat. Struct. Mol. Biol.* 21 (1), 103–109. doi:10.1038/nsmb.2737

Lee, J.-H., Kang, B.-H., Jang, H., Kim, T. W., Choi, J., Kwak, S., et al. (2015). AKT Phosphorylates H3-Threonine 45 to Facilitate Termination of Gene Transcription in Response to DNA Damage. *Nucleic Acids Res.* 43 (9), 4505–4516. doi:10.1093/nar/gkv176

Li, G., and Reinberg, D. (2011). Chromatin Higher-Order Structures and Gene Regulation. *Curr. Opin. Genet. Dev.* 21 (2), 175–186. doi:10.1016/j.gde.2011.01.022

Li, S. (2012). Implication of Posttranslational Histone Modifications in Nucleotide Excision Repair. *Int. J. Mol. Sci.* 13 (10), 12461–12486. doi:10.3390/ijms131012461

Li, S., Zhou, M., Ze, K., Sun, X., Zhao, C., Li, Z., et al. (2020). Protective Role of Histone Deacetylase 4 from Ultraviolet Radiation-Induced DNA Lesions. *Mol. Carcinogenesis* 59 (11), 1292–1301. doi:10.1002/mc.23257

Li, W., Giles, C., and Li, S. (2014a). Insights into How Spt5 Functions in Transcription Elongation and Repressing Transcription Coupled DNA Repair. *Nucleic Acids Res.* 42 (11), 7069–7083. doi:10.1093/nar/gku333

Li, W., and Li, S. (2017). Facilitators and Repressors of Transcription-Coupled DNA Repair in *Saccharomyces C. Photochem. Photobiol.* 93 (1), 259–267. doi:10.1111/php.12655

Li, W., Liu, W., Kakoki, A., Wang, R., Adebali, O., Jiang, Y., et al. (2019). Nucleotide Excision Repair Capacity Increases during Differentiation of Human Embryonic Carcinoma Cells into Neurons and Muscle Cells. *J. Biol. Chem.* 294 (15), 5914–5922. doi:10.1074/jbc.RA119.007861

Li, W., and Sancar, A. (2020). Methodologies for Detecting Environmentally Induced DNA Damage and Repair. *Environ. Mol. Mutagen* 61, 664–679. doi:10.1002/em.22365

Li, W., Selvam, K., Ko, T., and Li, S. (2014b). Transcription Bypass of DNA Lesions Enhances Cell Survival but Attenuates Transcription Coupled DNA Repair. *Nucleic Acids Res.* 42 (21), 13242–13253. doi:10.1093/nar/gku1150

Li, W., Selvam, K., Rahman, S. A., and Li, S. (2016). Sen1, the Yeast Homolog of Human Senataxin, Plays a More Direct Role Than Rad26 in Transcription Coupled DNA Repair. *Nucleic Acids Res.* 44 (14), 6794–6802. doi:10.1093/nar/gkw428

Liu, X., and Smerdon, M. J. (2000). Nucleotide Excision Repair of the 5 S Ribosomal RNA Gene Assembled into a Nucleosome. *J. Biol. Chem.* 275 (31), 23729–23735. doi:10.1074/jbc.M002206200

Ljungman, M., Parks, L., Hulbatte, R., and Bedi, K. (2019). The Role of H3K79 Methylation in Transcription and the DNA Damage Response. *Mutat. Research/Reviews Mutat. Res.* 780, 48–54. doi:10.1016/j.mrrev.2017.11.001

Luger, K., Mäder, A. W., Richmond, R. K., Sargent, D. F., and Richmond, T. J. (1997). Crystal Structure of the Nucleosome Core Particle at 2.8 Å Resolution. *Nature* 389 (6648), 251–260. doi:10.1038/38444

Mao, P., Meas, R., Dorgan, K. M., and Smerdon, M. J. (2014). UV Damage-Induced RNA Polymerase II Stalling Stimulates H2B Deubiquitylation. *Proc. Natl. Acad. Sci. U.S.A.* 111 (35), 12811–12816. doi:10.1073/pnas.1403901111

Mao, P., Smerdon, M. J., Roberts, S. A., and Wyrick, J. J. (2016). Chromosomal Landscape of UV Damage Formation and Repair at Single-Nucleotide Resolution. *Proc. Natl. Acad. Sci. U.S.A.* 113 (32), 9057–9062. doi:10.1073/pnas.1606667113

Mao, P., and Wyrick, J. J. (2016). Emerging Roles for Histone Modifications in DNA Excision Repair. *FEMS Yeast Res.* 16 (7), fow090. doi:10.1093/femsyr/fow090

Mao, P., Wyrick, J. J., Roberts, S. A., and Smerdon, M. J. (2017). UV-Induced DNA Damage and Mutagenesis in Chromatin. *Photochem. Photobiol.* 93 (1), 216–228. doi:10.1111/php.12646

Marteijn, J. A., Bekker-Jensen, S., Mailand, N., Lans, H., Schwertman, P., Gourdin, A. M., et al. (2009). Nucleotide Excision Repair-Induced H2A Ubiquitination Is Dependent on MDC1 and RNF8 and Reveals a Universal DNA Damage Response. *J. Cel Biol* 186 (6), 835–847. doi:10.1083/jcb.200902150

Marti, T. M., Hefner, E., Feeney, L., Natale, V., and Cleaver, J. E. (2006). H2AX Phosphorylation within the G 1 Phase after UV Irradiation Depends on Nucleotide Excision Repair and Not DNA Double-Strand Breaks. *Proc. Natl. Acad. Sci. U.S.A.* 103 (26), 9891–9896. doi:10.1073/pnas.0603779103

Martire, S., Gogate, A. A., Whitmill, A., Tafessu, A., Nguyen, J., Teng, Y.-C., et al. (2019). Phosphorylation of Histone H3.3 at Serine 31 Promotes P300 Activity and Enhancer Acetylation. *Nat. Genet.* 51 (6), 941–946. doi:10.1038/s41588-019-0428-5

Matsumoto, M., Yaginuma, K., Igarashi, A., Imura, M., Hasegawa, M., Iwabuchi, K., et al. (2007). Perturbed gap-filling Synthesis in Nucleotide Excision Repair Causes Histone H2AX Phosphorylation in Human Quiescent Cells. *J. Cel Sci* 120 (Pt 6), 1104–1112. doi:10.1242/jcs.03391

Meaburn, K. J., and Misteli, T. (2007). Cell Biology: Chromosome Territories. *Nature* 445 (7126), 379–381. doi:10.1038/445379a

Meas, R., and Mao, P. (2015). Histone Ubiquitylation and its Roles in Transcription and DNA Damage Response. *DNA Repair* 36, 36–42. doi:10.1016/j.dnarep.2015.09.016

Mehrmohamadi, M., Sepehri, M. H., Nazer, N., and Norouzi, M. R. (2021). A Comparative Overview of Epigenomic Profiling Methods. *Front. Cel Dev. Biol.* 9, 714687. doi:10.3389/fcell.2021.714687

Mellon, I., Spivak, G., and Hanawalt, P. C. (1987). Selective Removal of Transcription-Blocking DNA Damage from the Transcribed Strand of the Mammalian DHFR Gene. *Cell* 51 (2), 241–249. doi:10.1016/0092-8674(87)90151-6

Miranda, M., and Sorkin, A. (2007). Regulation of Receptors and Transporters by Ubiquitination: New Insights into Surprisingly Similar Mechanisms. *Mol. Interventions* 7 (3), 157–167. doi:10.1124/mi.7.3.7

Misteli, T. (2007). Beyond the Sequence: Cellular Organization of Genome Function. *Cell* 128 (4), 787–800. doi:10.1016/j.cell.2007.01.028

Mitchell, D. L., Nguyen, T. D., and Cleaver, J. E. (1990). Nonrandom Induction of Pyrimidine-Pyrimidone (6-4) Photoproducts in Ultraviolet-Irradiated Human Chromatin. *J. Biol. Chem.* 265 (10), 5353–5356. doi:10.1016/s0021-9258(19)39363-9

Moore, J. D., Yazgan, O., Ataian, Y., and Krebs, J. E. (2007). Diverse Roles for Histone H2A Modifications in DNA Damage Response Pathways in Yeast. *Genetics* 176 (1), 15–25. doi:10.1534/genetics.106.063792

Mu, D., Park, C.-H., Matsunaga, T., Hsu, D. S., Reardon, J. T., and Sancar, A. (1995). Reconstitution of Human DNA Repair Excision Nuclease in a Highly Defined System. *J. Biol. Chem.* 270 (6), 2415–2418. doi:10.1074/jbc.270.6.2415

Nag, R., and Smerdon, M. J. (2009). Altering the Chromatin Landscape for Nucleotide Excision Repair. *Mutat. Research/Reviews Mutat. Res.* 682 (1), 13–20. doi:10.1016/j.mrrev.2009.01.002

Nishimoto, K., Niida, H., Uchida, C., Ohhata, T., Kitagawa, K., Motegi, A., et al. (2020). HDAC3 Is Required for XPC Recruitment and Nucleotide Excision Repair of DNA Damage Induced by UV Irradiation. *Mol. Cancer Res.* 18 (9), 1367–1378. doi:10.1158/1541-7786.MCR-20-0214

Oksenych, V., Zhovmer, A., Ziani, S., Mari, P.-O., Eberova, J., Nardo, T., et al. (2013). Histone Methyltransferase DOT1L Drives Recovery of Gene Expression after a Genotoxic Attack. *Plos Genet.* 9 (7), e1003611. doi:10.1371/journal.pgen.1003611

Olivieri, M., Cho, T., Álvarez-Quilón, A., Li, K., Schellenberg, M. J., Zimmermann, M., et al. (2020). A Genetic Map of the Response to DNA Damage in Human Cells. *Cell* 182 (2), 481–496. doi:10.1016/j.cell.2020.05.040

Oluwadare, O., Highsmith, M., and Cheng, J. (2019). An Overview of Methods for Reconstructing 3-D Chromosome and Genome Structures from Hi-C Data. *Biol. Proced. Online* 21, 7. doi:10.1186/s12575-019-0094-0

Palomera-Sanchez, Z., Bucio-Mendez, A., Valadez-Graham, V., Reynaud, E., and Zurita, M. (2010). Drosophila P53 Is Required to Increase the Levels of the dKDM4B Demethylase after UV-Induced DNA Damage to Demethylate Histone H3 Lysine 9. *J. Biol. Chem.* 285 (41), 31370–31379. doi:10.1074/jbc.m110.128462

Papamichos-Chronakis, M., and Peterson, C. L. (2013). Chromatin and the Genome Integrity Network. *Nat. Rev. Genet.* 14 (1), 62–75. doi:10.1038/nrg3345

Polo, S. E., Roche, D., and Almouzni, G. (2006). New Histone Incorporation Marks Sites of UV Repair in Human Cells. *Cell* 127 (3), 481–493. doi:10.1016/j.cell.2006.08.049

Prather, D., Krogan, N. J., Emili, A., Greenblatt, J. F., and Winston, F. (2005). Identification and Characterization of Elf1, a Conserved Transcription Elongation Factor in *Saccharomyces C. Mol. Cel Biol* 25 (22), 10122–10135. doi:10.1128/MCB.25.22.10122-10135.2005

Ramanathan, B., and Smerdon, M. J. (1986). Changes in Nuclear Protein Acetylation in u.v.-Damaged Human Cells. *Carcinogenesis* 7 (7), 1087–1094. doi:10.1093/carcin/7.7.1087

Ramanathan, B., and Smerdon, M. J. (1989). Enhanced DNA Repair Synthesis in Hyperacetylated Nucleosomes. *J. Biol. Chem.* 264 (19), 11026–11034. doi:10.1016/s0021-9258(18)60422-3

Ray, A., Mir, S. N., Wani, G., Zhao, Q., Battu, A., Zhu, Q., et al. (2009). Human SNF5/INI1, a Component of the Human SWI/SNF Chromatin Remodeling Complex, Promotes Nucleotide Excision Repair by Influencing ATM Recruitment and Downstream H2AX Phosphorylation. *Mol. Cel Biol* 29 (23), 6206–6219. doi:10.1128/mcb.00503-09

Revet, I., Feeney, L., Bruguera, S., Wilson, W., Dong, T. K., Oh, D. H., et al. (2011). Functional Relevance of the Histone γH2Ax in the Response to DNA Damaging Agents. *Proc. Natl. Acad. Sci. U.S.A.* 108 (21), 8663–8667. doi:10.1073/pnas.1105866108

Rogakou, E. P., Pilch, D. R., Orr, A. H., Ivanova, V. S., and Bonner, W. M. (1998). DNA Double-Stranded Breaks Induce Histone H2AX Phosphorylation on Serine 139. *J. Biol. Chem.* 273 (10), 5858–5868. doi:10.1074/jbc.273.10.5858

Roth, S. Y., Denu, J. M., and Allis, C. D. (2001). Histone Acetyltransferases. *Annu. Rev. Biochem.* 70, 81–120. doi:10.1146/annurev.biochem.70.1.81

Rubbi, C. P., and Milner, J. (2003). p53 Is a Chromatin Accessibility Factor for Nucleotide Excision Repair of DNA Damage. *Embo J.* 22 (4), 975–986. doi:10.1093/emboj/cdg082

Rüthemann, P., Balbo Pogliano, C., Codilupi, T., Garajovà, Z., and Naegeli, H. (2017). Chromatin Remodeler CHD1 Promotes XPC-To-TFIIH Handover of Nucleosomal UV Lesions in Nucleotide Excision Repair. *EMBO J.* 36 (22), 3372–3386. doi:10.15252/embj.201695742

Sancar, A. (1996). DNA Excision Repair. *Annu. Rev. Biochem.* 65, 43–81. doi:10.1146/annurev.bi.65.070196.000355

Sancar, A. (2016). Mechanisms of DNA Repair by Photolyase and Excision Nuclease (Nobel Lecture). *Angew. Chem. Int. Ed.* 55 (30), 8502–8527. doi:10.1002/anie.201601524

Sancar, A., and Rupp, W. D. (1983). A Novel Repair Enzyme: UVRABC Excision Nuclease of *Escherichia coli* Cuts a DNA Strand on Both Sides of the Damaged Region. *Cell* 33 (1), 249–260. doi:10.1016/0092-8674(83)90354-9

Sancar, A., and Tang, M.-s. (1993). Nucleotide Excision Repair. *Photochem. Photobiol.* 57 (5), 905–921. doi:10.1111/j.1751-1097.1993.tb09233.x

Sanders, J. T., Freeman, T. F., Xu, Y., Golloshi, R., Stallard, M. A., Hill, A. M., et al. (2020). Radiation-Induced DNA Damage and Repair Effects on 3D Genome Organization. *Nat. Commun.* 11 (1), 6178. doi:10.1038/s41467-020-20047-w

Sarkar, S., Kiely, R., and McHugh, P. J. (2010). The Ino80 Chromatin-Remodeling Complex Restores Chromatin Structure during UV DNA Damage Repair. *J. Cel Biol* 191 (6), 1061–1068. doi:10.1083/jcb.201006178

Schieferstein, U., and Thoma, F. (1998). Site-Specific Repair of Cyclobutane Pyrimidine Dimers in a Positioned Nucleosome by Photolyase and T4 Endonuclease V *In Vitro*. *EMBO J.* 17 (1), 306–316. doi:10.1093/emboj/17.1.306

Selby, C. P., and Sancar, A. (1993). Molecular Mechanism of Transcription-Repair Coupling. *Science* 260 (5104), 53–58. doi:10.1126/science.8465200

Selvam, K., Rahman, S. A., and Li, S. (2019). Histone H4 H75E Mutation Attenuates Global Genomic and Rad26-Independent Transcription-Coupled Nucleotide Excision Repair. *Nucleic Acids Res.* 47 (14), 7392–7401. doi:10.1093/nar/gkz453

Sen, S. P., and De Benedetti, A. (2006). TLK1B Promotes Repair of UV-Damaged DNA through Chromatin Remodeling by Asf1. *BMC Mol. Biol.* 7, 37. doi:10.1186/1471-2199-7-37

Sertic, S., Pizzi, S., Cloney, R., Lehmann, A. R., Marini, F., Plevani, P., et al. (2011). Human Exonuclease 1 Connects Nucleotide Excision Repair (NER) Processing with Checkpoint Activation in Response to UV Irradiation. *Proc. Natl. Acad. Sci. U.S.A.* 108 (33), 13647–13652. doi:10.1073/pnas.1108547108

Seto, E., and Yoshida, M. (2014). Erasers of Histone Acetylation: The Histone Deacetylase Enzymes. *Cold Spring Harbor Perspect. Biol.* 6 (4), a018713. doi:10.1101/cshperspect.a018713

Shimada, M., Niida, H., Zineldeen, D. H., Tagami, H., Tanaka, M., Saito, H., et al. (2008). Chk1 Is a Histone H3 Threonine 11 Kinase that Regulates DNA Damage-Induced Transcriptional Repression. *Cell* 132 (2), 221–232. doi:10.1016/j.cell.2007.12.013

Sloan, D. B., Broz, A. K., Sharbrough, J., and Wu, Z. (2018). Detecting Rare Mutations and DNA Damage with Sequencing-Based Methods. *Trends Biotechnol.* 36 (7), 729–740. doi:10.1016/j.tibtech.2018.02.009

Smerdon, M. J. (1991). DNA Repair and the Role of Chromatin Structure. *Curr. Opin. Cel Biol.* 3 (3), 422–428. doi:10.1016/0955-0674(91)90069-b

Smerdon, M. J., Lan, S. Y., Calza, R. E., and Reeves, R. (1982). Sodium Butyrate Stimulates DNA Repair in UV-Irradiated normal and Xeroderma Pigmentosum Human Fibroblasts. *J. Biol. Chem.* 257 (22), 13441–13447. doi:10.1016/s0021-9258(18)33468-9

Sugasawa, K., Okuda, Y., Saijo, M., Nishi, R., Matsuda, N., Chu, G., et al. (2005). UV-Induced Ubiquitylation of XPC Protein Mediated by UV-DDB-Ubiquitin Ligase Complex. *Cell* 121 (3), 387–400. doi:10.1016/j.cell.2005.02.035

Sugasawa, K. (2009). UV-DDB: A Molecular Machine Linking DNA Repair with Ubiquitination. *DNA Repair* 8 (8), 969–972. doi:10.1016/j.dnarep.2009.05.001

Tatum, D., and Li, S. (2011). Evidence that the Histone Methyltransferase Dot1 Mediates Global Genomic Repair by Methylating Histone H3 on Lysine 79. *J. Biol. Chem.* 286 (20), 17530–17535. doi:10.1074/jbc.m111.241570

Tatum, D., Li, W., Placer, M., and Li, S. (2011). Diverse Roles of RNA Polymerase II-Associated Factor 1 Complex in Different Subpathways of Nucleotide Excision Repair. *J. Biol. Chem.* 286 (35), 30304–30313. doi:10.1074/jbc.M111.252981

Teng, Y., Liu, H., Gill, H. W., Yu, Y., Waters, R., and Reed, S. H. (2008). *Saccharomyces C* Rad16 Mediates Ultraviolet-Dependent Histone H3 Acetylation Required for Efficient Global Genome Nucleotide-Excision Repair. *EMBO Rep.* 9 (1), 97–102. doi:10.1038/sj.embor.7401112

Teng, Y., Yu, Y., and Waters, R. (2002). The *Saccharomyces C* Histone Acetyltransferase Gcn5 Has a Role in the Photoreactivation and Nucleotide Excision Repair of UV-Induced Cyclobutane Pyrimidine Dimers in the MFA2 Gene. *J. Mol. Biol.* 316 (3), 489–499. doi:10.1006/jmbi.2001.5383

Tillhon, M., Cazzalini, O., Nardo, T., Necchi, D., Sommatis, S., Stivala, L. A., et al. (2012). p300/CBP Acetyl Transferases Interact with and Acetylate the Nucleotide Excision Repair Factor XPG. *DNA Repair (Amst)* 11 (10), 844–852. doi:10.1016/j.dnarep.2012.08.001

Tiwari, M., Parvez, S., and Agrawala, P. K. (2017). Role of Some Epigenetic Factors in DNA Damage Response Pathway. *Aims Genet.* 04 (1), 069–083. doi:10.3934/genet.2017.1.69

Tresini, M., Warmerdam, D. O., Kolovos, P., Snijder, L., Vrouwe, M. G., Demmers, J. A. A., et al. (2015). The Core Spliceosome as Target and Effector of Non-Canonical ATM Signalling. *Nature* 523 (7558), 53–58. doi:10.1038/nature14512

Ura, K., Araki, M., Saeki, H., Masutani, C., Ito, T., Iwai, S., et al. (2001). ATP-Dependent Chromatin Remodeling Facilitates Nucleotide Excision Repair of UV-Induced DNA Lesions in Synthetic Dinucleosomes. *EMBO J.* 20 (8), 2004–2014. doi:10.1093/emboj/20.8.2004

van der Horst, G. T. J., van Steeg, H., Berg, R. J. W., van Gool, A. J., de Wit, J., Weeda, G., et al. (1997). Defective Transcription-Coupled Repair in Cockayne Syndrome B Mice Is Associated with Skin Cancer Predisposition. *Cell* 89 (3), 425–435. doi:10.1016/s0092-8674(00)80223-8

van der Weegen, Y., de Lint, K., van den Heuvel, D., Nakazawa, Y., Mevissen, T. E. T., van Schie, J. J. M., et al. (2021). ELOF1 Is a Transcription-Coupled DNA Repair Factor that Directs RNA Polymerase II Ubiquitylation. *Nat. Cel Biol* 23 (6), 595–607. doi:10.1038/s41556-021-00688-9

van der Weegen, Y., Golan-Berman, H., Mevissen, T. E. T., Apelt, K., González-Prieto, R., Goedhart, J., et al. (2020). The Cooperative Action of CSB, CSA, and UVSSA Target TFIIH to DNA Damage-Stalled RNA Polymerase II. *Nat. Commun.* 11 (1), 2104. doi:10.1038/s41467-020-15903-8

van Eijk, P., Nandi, S. P., Yu, S., Bennett, M., Leadbitter, M., Teng, Y., et al. (2019). Nucleosome Remodeling at Origins of Global Genome-Nucleotide Excision Repair Occurs at the Boundaries of Higher-Order Chromatin Structure. *Genome Res.* 29 (1), 74–84. doi:10.1101/gr.237198.118

Wang, G. G., Allis, C. D., and Chi, P. (2007). Chromatin Remodeling and Cancer, Part II: ATP-Dependent Chromatin Remodeling. *Trends Mol. Med.* 13 (9), 373–380. doi:10.1016/j.molmed.2007.07.004

Wang, H., Wang, L., Erdjument-Bromage, H., Vidal, M., Tempst, P., Jones, R. S., et al. (2004). Role of Histone H2A Ubiquitination in Polycomb Silencing. *Nature* 431 (7010), 873–878. doi:10.1038/nature02985

Wang, H., Zhai, L., Xu, J., Joo, H.-Y., Jackson, S., Erdjument-Bromage, H., et al. (2006). Histone H3 and H4 Ubiquitylation by the CUL4-DDB-ROC1 Ubiquitin Ligase Facilitates Cellular Response to DNA Damage. *Mol. Cel* 22 (3), 383–394. doi:10.1016/j.molcel.2006.03.035

Wang, J., He, H., Chen, B., Jiang, G., Cao, L., Jiang, H., et al. (2020). Acetylation of XPF by TIP60 Facilitates XPF-ERCC1 Complex Assembly and Activation. *Nat. Commun.* 11 (1), 786. doi:10.1038/s41467-020-14564-x

Ward, I. M., and Chen, J. (2001). Histone H2AX Is Phosphorylated in an ATR-dependent Manner in Response to Replicational Stress. *J. Biol. Chem.* 276 (51), 47759–47762. doi:10.1074/jbc.C100569200

Waters, R., van Eijk, P., and Reed, S. (2015). Histone Modification and Chromatin Remodeling during NER. *DNA Repair* 36, 105–113. doi:10.1016/j.dnarep.2015.09.013

Weake, V. M., and Workman, J. L. (2008). Histone Ubiquitination: Triggering Gene Activity. *Mol. Cel* 29 (6), 653–663. doi:10.1016/j.molcel.2008.02.014

Wei, S., Li, C., Yin, Z., Wen, J., Meng, H., Xue, L., et al. (2018). Histone Methylation in DNA Repair and Clinical Practice: New Findings during the Past 5-years. *J. Cancer* 9 (12), 2072–2081. doi:10.7150/jca.23427

Welchman, R. L., Gordon, C., and Mayer, R. J. (2005). Ubiquitin and Ubiquitin-Like Proteins as Multifunctional Signals. *Nat. Rev. Mol. Cel Biol* 6 (8), 599–609. doi:10.1038/nrm1700

Wood, A., Schneider, J., Dover, J., Johnston, M., and Shilatifard, A. (2003). The Paf1 Complex Is Essential for Histone Monoubiquitination by the Rad6-Bre1 Complex, Which Signals for Histone Methylation by COMPASS and Dot1p. *J. Biol. Chem.* 278 (37), 34739–34742. doi:10.1074/jbc.c300269200

Wood, K., Tellier, M., and Murphy, S. (2018). DOT1L and H3K79 Methylation in Transcription and Genomic Stability. *Biomolecules* 8 (1), 11. doi:10.3390/biom8010011

Wood, R. D. (1997). Nucleotide Excision Repair in Mammalian Cells. *J. Biol. Chem.* 272 (38), 23465–23468. doi:10.1074/jbc.272.38.23465

Wysocki, R., Javaheri, A., Allard, S., Sha, F., Coôte´, J., and Kron, S. J. (2005). Role of Dot1-Dependent Histone H3 Methylation in G 1 and S Phase DNA Damage Checkpoint Functions of Rad9. *Mol. Cel Biol* 25 (19), 8430–8443. doi:10.1128/mcb.25.19.8430-8443.2005

Xu, J., Lahiri, I., Wang, W., Wier, A., Cianfrocco, M. A., Chong, J., et al. (2017). Structural Basis for the Initiation of Eukaryotic Transcription-Coupled DNA Repair. *Nature* 551 (7682), 653–657. doi:10.1038/nature24658

Yan, C., Dodd, T., Yu, J., Leung, B., Xu, J., Oh, J., et al. (2021). Mechanism of Rad26-Assisted Rescue of Stalled RNA Polymerase II in Transcription-Coupled Repair. *Nat. Commun.* 12 (1), 7001. doi:10.1038/s41467-021-27295-4

Yu, S., Evans, K., van Eijk, P., Bennett, M., Webster, R. M., Leadbitter, M., et al. (2016). Global Genome Nucleotide Excision Repair Is Organized into Domains that Promote Efficient DNA Repair in Chromatin. *Genome Res.* 26 (10), 1376–1387. doi:10.1101/gr.209106.116

Yu, S., Teng, Y., Waters, R., and Reed, S. H. (2011). How Chromatin Is Remodelled during DNA Repair of UV-Induced DNA Damage in *Saccharomyces C. Plos Genet.* 7 (6), e1002124. doi:10.1371/journal.pgen.1002124

Yu, Y., Deng, Y., Reed, S. H., Millar, C. B., and Waters, R. (2013). Histone Variant Htz1 Promotes Histone H3 Acetylation to Enhance Nucleotide Excision Repair in Htz1 Nucleosomes. *Nucleic Acids Res.* 41 (19), 9006–9019. doi:10.1093/nar/gkt688

Yu, Y., Teng, Y., Liu, H., Reed, S. H., and Waters, R. (2005). UV Irradiation Stimulates Histone Acetylation and Chromatin Remodeling at a Repressed Yeast Locus. *Proc. Natl. Acad. Sci. U.S.A.* 102 (24), 8650–8655. doi:10.1073/pnas.0501458102

Zhao, M., Geng, R., Guo, X., Yuan, R., Zhou, X., Zhong, Y., et al. (2017). PCAF/GCN5-Mediated Acetylation of RPA1 Promotes Nucleotide Excision Repair. *Cel Rep.* 20 (9), 1997–2009. doi:10.1016/j.celrep.2017.08.015

Zhao, Q., Wang, Q.-E., Ray, A., Wani, G., Han, C., Milum, K., et al. (2009). Modulation of Nucleotide Excision Repair by Mammalian SWI/SNF Chromatin-Remodeling Complex. *J. Biol. Chem.* 284 (44), 30424–30432. doi:10.1074/jbc.M109.044982

Zhu, B., Chen, S., Wang, H., Yin, C., Han, C., Peng, C., et al. (2018). The Protective Role of DOT1L in UV-Induced Melanomagenesis. *Nat. Commun.* 9 (1), 259. doi:10.1038/s41467-017-02687-7

Zhu, Q., Wani, G., Arab, H. H., El-Mahdy, M. A., Ray, A., and Wani, A. A. (2009). Chromatin Restoration Following Nucleotide Excision Repair Involves the Incorporation of Ubiquitinated H2A at Damaged Genomic Sites. *DNA Repair* 8 (2), 262–273. doi:10.1016/j.dnarep.2008.11.007

**Conflict of Interest:** The authors declare that the research was conducted in the absence of any commercial or financial relationships that could be construed as a potential conflict of interest.

**Publisher's Note:** All claims expressed in this article are solely those of the authors and do not necessarily represent those of their affiliated organizations, or those of the publisher, the editors and the reviewers. Any product that may be evaluated in this article, or claim that may be made by its manufacturer, is not guaranteed or endorsed by the publisher.

frontiers | Frontiers in Cell and Developmental Biology

ORIGINAL RESEARCH
published: 03 June 2022
doi: 10.3389/fcell.2022.826576

# Prolyl Isomerization-Mediated Conformational Changes Define ATR Subcellular Compartment-Specific Functions

*Himadri Biswas*[1], *Shu-Jun Zhao*[2,3], *Yetunde Makinwa*[1], *James S. Bassett*[2], *Phillip R. Musich*[4], *Jing-Yuan Liu*[2,3]* *and Yue Zou*[1]*

[1]Department of Cancer Biology, University of Toledo College of Medicine and Life Sciences, Toledo, OH, United States, [2]Department of Medicine, University of Toledo College of Medicine and Life Sciences, Toledo, OH, United States, [3]Department of Bioengineering, University of Toledo College of Engineering, Toledo, OH, United States, [4]Department of Biomedical Sciences, Quillen College of Medicine, East Tennessee State University, Johnson City, TN, United States

OPEN ACCESS

**Edited by:**
Shan Yan,
University of North Carolina at Charlotte, United States

**Reviewed by:**
Roland Stote,
Institut de Génétique et de Biologie Moléculaire et Cellulaire (IGBMC), France
Jason A. Stewart,
University of South Carolina, United States

***Correspondence:**
Jing-Yuan Liu
jingyuan.liu@utoledo.edu
Yue Zou
yue.zou@utoledo.edu

**Specialty section:**
This article was submitted to Molecular and Cellular Pathology, a section of the journal Frontiers in Cell and Developmental Biology

**Received:** 01 December 2021
**Accepted:** 26 April 2022
**Published:** 03 June 2022

**Citation:**
Biswas H, Zhao S-J Makinwa Y, Bassett JS, Musich PR, Liu J-Y and Zou Y (2022) Prolyl Isomerization-Mediated Conformational Changes Define ATR Subcellular Compartment-Specific Functions. Front. Cell Dev. Biol. 10:826576. doi: 10.3389/fcell.2022.826576

ATR is a PI3K-like kinase protein, regulating checkpoint responses to DNA damage and replication stress. Apart from its checkpoint function in the nucleus, ATR actively engages in an antiapoptotic role at mitochondria following DNA damage. The different functions of ATR in the nucleus and cytoplasm are carried out by two prolyl isomeric forms of ATR: *trans*- and *cis*-ATR, respectively. The isomerization occurs at the Pin1 Ser428-Pro429 motif of ATR. Here, we investigated the structural basis of the subcellular location-specific functions of human ATR. Using a mass spectrometry-based footprinting approach, the surface accessibility of ATR lysine residues to sulfo-NHS-LC-biotin modification was monitored and compared between the *cis*- and the *trans*-isomers. We have identified two biotin-modified lysine residues, K459 and K469, within the BH3-like domain of *cis*-ATR that were not accessible in *trans*-ATR, indicating a conformational change around the BH3 domain between *cis*- and *trans*-ATR. The conformational alteration also involved the N-terminal domain and the middle HEAT domain. Moreover, experimental results from an array of complementary assays show that *cis*-ATR with the accessible BH3 domain was able to bind to tBid while *trans*-ATR could not. In addition, both *cis*- and *trans*-ATR can directly form homodimers *via* their C-terminal domains without ATRIP, while nuclear (*trans*-ATR) in the presence of ATRIP forms dimer–dimer complexes involving both N- and C-termini of ATR and ATRIP after UV. Structural characteristics around the Ser428-Pro429 motif and the BH3 domain region are also analyzed by molecular modeling and dynamics simulation. In support, *cis* conformation was found to be significantly more energetically favorable than *trans* at the Ser428-Pro429 bond in a 20-aa wild-type ATR peptide. Taken together, our results suggest that the isomerization-induced structural changes of ATR define both its subcellular location and compartment-specific functions and play an essential role in promoting cell survival and DNA damage responses.

**Keywords: ATR, *cis*/*trans* prolyl isomerization, mass spectrometric protein footprinting, structure-function of ATR, mitochondrial ATR-tBid interaction, antiapoptosis, BH3-like domain, UV irradiation**

## INTRODUCTION

The DNA damage checkpoint pathways check genome integrity and synchronize multiple cellular pathways to establish efficient repair of DNA damage (Zhou and Elledge, 2000; Zou and Elledge, 2003). The ATM (ataxia-telangiectasia mutated) and ATR (ATM and RAD3-related) kinases mediate checkpoint pathways and represent two vital DNA damage-dependent checkpoints. Both ATM and ATR are members of the phosphoinositide 3-kinase-like related kinase family. These pathways encompass series of DNA damage sensors, signal mediators and transducers, and downstream effector molecules (Zhou and Elledge, 2000; Zou and Elledge, 2003; Sancar et al., 2004; Wu et al., 2007). The ATR-dependent checkpoint pathway contributes to anticipating replication stress and responds mainly to DNA damage caused by genotoxins such as UV irradiation (Shiloh, 2003; Zou and Elledge, 2003; Abraham, 2004; Sancar et al., 2004). After replication stress and generation of single-stranded DNA (ssDNA), RPA (replication protein A) coats the ssDNA and recruits the ATR–ATRIP complex *via* ATRIP (ATR-interacting protein). ATRIP is the nuclear partner of ATR and recruits bound ATR to the DNA damage site, where ATR is autophosphorylated at its T1989 residue (Cortez et al., 2001). This phosphorylated residue serves as a docking site for TopBP1 to substantially elevate the activation of ATR's kinase activity (Burrows and Elledge, 2008; Mordes et al., 2008; Liu et al., 2011a). Activated ATR further triggers several key downstream proteins, including p53 and other checkpoint kinases such as Chk1, causing an S-phase cell cycle arrest for the repair of the DNA damage or, apoptosis, in case of severe damage (Cortez et al., 2001; Zou and Elledge, 2003; Sancar et al., 2004; Mordes and Cortez, 2008; Mordes et al., 2008; Ciccia and Elledge, 2010; Nam and Cortez, 2011; Saldivar et al., 2017; Ma et al., 2018).

ATR that functions in the cytoplasm was found to play an important antiapoptotic role directly at the mitochondria, independent of nuclear ATR and kinase activity (Hilton et al., 2015). Except for its synthesis, ATRIP is largely absent in the cytoplasm. Contrary to nuclear ATR that always remains in the *trans*-form in a complex with ATRIP, the cytoplasmic ATR, devoid of ATRIP, exists in two prolyl isomeric forms, the *cis*- and *trans*-form. The existence of both these forms depends on a single-peptide bond orientation in ATR by prolyl isomerization. In contrast, nuclear ATR always remains in the *trans*-form in a complex with ATRIP. Pin1 regulates the balance between the *cis* and *trans* cytoplasmic form of ATR and catalyzes this conversion of *cis*-ATR to *trans*-ATR by recognizing the phosphorylated Serine 428-Proline 429 residues (pS428-P429) in the N-terminal region of ATR (Hilton et al., 2015). Albeit Pin 1 activity favors *trans*-ATR formation when it is inactivated by DAPKI kinase, in response to DNA damage, it promotes *cis*-ATR accumulation at mitochondria as *cis*-ATR is more stable in cells. Contrary to its *trans*-ATR isoform, the *cis*-ATR has an exposed BH3-like domain allowing it to bind to the pro-apoptotic tBid protein at the mitochondria (Hilton et al., 2015; Musich et al., 2017; Makinwa et al., 2020a; Makinwa et al., 2020b). This binding prevents tBid from activating Bax–Bak polymerization, which is vital for the intrinsic apoptotic pathway. Here forth, *cis*-ATR executes an antiapoptotic function that protracts the cell survival long enough to repair its damaged DNA. However, this can be a double-edged sword that can play a role in carcinogenesis. The newly discovered BH3 domain, a hallmark of apoptotic proteins, in ATR defines *cis*-ATR's role in the apoptosis pathway. However, the structural characteristics of *cis*- and *trans*-ATR and the related functions of ATR are to be characterized yet.

In this study, we determine the structural alterations of two prolyl isomeric forms of ATR, *trans*- and *cis*-ATR, using mass spectrometric protein footprinting and complementary methods. Our results demonstrate a significant conformational change at the region containing the BH3 domain between the *cis* and *trans isomeric forms of* ATR, resulting in activation or silencing of the BH3 domain as required for ATR–tBid interaction at mitochondria. In addition, we found that *cis*- and *trans*-ATR isomers form distinctly different dimers in the presence and absence of ATRIP. The *cis*-ATR forms a homodimer *via* its C-terminal domain in the cytoplasm, while the latter, in the nucleus, dimerizes *via* both C- and N-terminal domains involving ATRIP and is a heterodimer–homodimer. Our results unravel the role of ATR at mitochondria as a pro-survival protein, broadening our understanding of the cellular functions of ATR.

## EXPERIMENTAL PROCEDURES

### Cell Culture, UV Irradiation, and Antibodies

The simian virus 40-transformed human embryonic kidney (HEK) 293T cells and human colorectal carcinoma (HCT)116 $ATR^{flox/-}$ cells were maintained in DMEM (GIBCO/BRL) and McCoy's 5A media supplemented with 10% FBS and 100 units of penicillin and streptomycin/ml. UV treatments were at 40 $J/m^2$ with a 2-h recovery. ATR, p-ATR (T1989), p-53(S15), p53, and tBid antibodies were purchased from Cell Signaling.

### Protein Purification

N-terminal Flag-tagged ATR recombinant protein was isolated from HEK293T cells 48 h after transfection with pcDNA3-Flag-ATR (WT), S428A, or P429A plasmid. The cells were lysed in ice-cold lysis buffer [50 mM HEPES, pH 7.4/150 mM NaCl/1 mM EDTA/10% glycerol/1% Triton-X100, and protease inhibitors (Thermo Fischer)] for 30 min. The cell lysates were centrifuged for 10 min at 20,000 × g. The supernatants from the spun lysates were incubated at 4°C overnight with magnetic anti-FLAG M2 affinity beads (Sigma) that had been pre-equilibrated in buffer containing 50 mM HEPES, pH 7.4/150 mM NaCl. The beads were then washed once with 1 M NaCl containing 50 mM HEPES, pH 7.4 buffer and thrice with 150 mM NaCl containing 50 mM HEPES, pH 7.4. The ATR bound to beads was either used directly for pull-down experiments or eluted with 50 mM HEPES, pH 7.4 buffer containing 200 μg/ml FLAG peptide (Sigma).

### Biotin Modification and In-Gel Proteolysis

Purified ATR and mutants were modified with various molar concentrations of sulfo-NHS-LC-biotin. Typically, ATR (2 μM) was modified by adding sulfo-NHS-LC-biotin (2 mM of final

concentration) for 30 min incubation at room temperature. Modifications were quenched by the addition of 10 mM lysine, followed by purification of ATR by SDS-PAGE. The subunit bands on the gel were visualized by Coomassie blue staining, excised from the gel, and destained with water. SDS was removed by washing the gel pieces with ammonium bicarbonate, dehydrated with 100% acetonitrile, and vacuum desiccated. In-gel digestion with trypsin was performed using a ProGest robot (DigiLab). After trypsin digestion, the gel slices were washed with 25 mM ammonium bicarbonate followed by acetonitrile. Then, the gel pieces were reduced with 10 mM dithiothreitol at 60°C followed by alkylation with 50 mM iodoacetamide at RT. Thereafter, protein bands were digested overnight at 37°C with sequencing-grade trypsin (Promega). Finally, the peptide extract was dried and prepared for either MALDI-TOF or nanoLC MS/MS.

## MALDI-TOF

Peptide extracts were resuspended in 50% acetonitrile. One microliter of each peptide solution was spotted onto a Scout MALDI 384 target (Bruker Daltonics) and air-dried; 1.0 µL of α-cyano-hydroxycinnamic acid (10 mg⁄mL) in 70:30 acetonitrile: 0.1% trifluoroacetic acid was added to it. MALDI-TOF spectra were recorded by using a MALDI-TOF Biflex IV mass spectrometer (Bruker Daltonics) in positive ionization mode. Spectra of proteins and peptides were acquired in reflection mode (90–180 laser shots) in the m/z range from 500 to 3,500.

## Nano LC-MS/MS

Tryptic peptides were resuspended in 0.1% formic acid before loading onto a trapping column and eluted over a 75 µm analytical column at 350 nL/min; both columns were packed with Luna C18 resin (Phenomenex) and eluted over 40 min with a 3–40% acetonitrile gradient. The sample was analyzed by nano LC-MS/MS using a Waters NanoAcquity HPLC system interfaced to a ThermoFisher Fusion Lumos mass spectrometer. The mass spectrometer was operated in data-dependent mode, with the Orbitrap operating at 60,000 FWHM and 15,000 FWHM for MS and MS/MS, respectively. The instrument was run with a 3-s cycle for MS and MS/MS.

## Cytoplasmic and Nuclear Protein Extraction

To prepare samples for immunoprecipitation, subcellular fractionation was executed using cell lysis buffer [10 mM HEPES, pH 7.9, 10 mM KCl, 3 mM $CaCl_2$, 1.5 mM $MgCl_2$, 0.34 M sucrose, 10% glycerol, 0.1% Triton X-100, plus 1x protease, and phosphatase inhibitors (Thermo Fischer)] and a nuclear lysis buffer (50 mM Tris–HCl, pH 7.9, 140 mM NaCl, 3 mM $CaCl_2$, 1 mM EDTA, 1% NP-40, 10% glycerol, plus 1x protease, and phosphatase inhibitors). Briefly, 10 volumes of cell lysis buffer were added to one volume of packed cells. After resuspension and incubation on ice for 10 min, the cytoplasm was separated from nuclei at 500 × g for 7 min at 4°C. Isolated nuclei were washed twice with 500 µL of the nuclear wash buffer (cell lysis buffer containing 30 mM DTT) and collected by centrifugation. Collected nuclear pellets were suspended in ice-cold nuclear lysis buffer, and nuclei were lysed with rotation for 40 min at 4°C. The nuclear lysate was clarified by centrifugation at 20,000 × g for 10 min at 4°C. Lysates were mixed with SDS-loading buffer to have the final composition of 450 mM Tris–HCl, pH 8.45, 12% glycerol, 4% SDS, 0.0075% bromophenol blue, and 100 mM DTT before heating at 95°C for 5 min and protein analysis by gradient (3–8%), Tris–acetate (TA) SDS-PAGE, and Western blotting (WB). ATR isomerization was always assayed by 3–8% TA SDS-PAGE (NuPAGE, Invitrogen) and analyzed by WB.

## Immunoprecipitation Assays

To assess tBid binding to ATR, the HCT116 $ATR^{flox/-}$ cells were transfected with a plasmid construct of FLAG-ATR (wt), FLAG-ATR (S428A), or FLAG-ATR (P429A) and UV irradiated at 40 J/$m^2$ followed by a 2-h recovery before the cytoplasmic fraction (including mitochondria) were collected. FLAG-beads (Sigma) were added for pull-down overnight. Immunoprecipitated (IP) FLAG-beads were washed three times in co-immunoprecipitation (Co-IP) wash buffer (50 mM Tris–HCl, pH 7.6, 140 mM NaCl, 1 mM EDTA, 10% glycerol, and 0.2% Tween-20). Purified tBid was added for a 2 h incubation at 4°C. The FLAG-beads were washed thrice using Co-IP wash buffer, followed by suspending in 1× SDS loading buffer and boiled at 95°C for 5 min before assaying the ATR isomerization status by 3–8% TA SDS-PAGE and analyzed by WB.

## Duolink *In Situ* Proximity Ligation Assays

The Duolink protein–protein interaction assay was performed according to the manufacturer's instructions (Sigma DUO 92101). Images were captured using a Zeiss fluorescence microscope 40× objective lens. To determine ATR–Bid interactions among various ATR mutants by PLA, the HCT116 $ATR^{flox/-}$ cells were transfected with a plasmid construct of FLAG-ATR (wt), FLAG-ATR (S428A), or FLAG-ATR (P429A) and UV irradiated at 40 J/$m^2$ followed by a 2-h recovery, and PLA was performed as described by Makinwa et al. (2020a). Anti-Bid antibody (Mouse monoclonal, Santa Cruz SC-514622) at a dilution of 1:500 mixed with anti-ATR antibody (Rabbit polyclonal, Bethyl Laboratories A300-137A) at a dilution of 1:1,000 was used to determine ATR-Bid interactions. To show ATR–Bid interaction at mitochondria, the cells were probed with a mtHsp70 monoclonal antibody (Mouse monoclonal, Invitrogen MA3-028) at a dilution of 1:50 for at least 1 h at room temperature, washed with PLA wash buffer 2, and incubated with DyLight 488 goat-antimouse IgG secondary antibody (Invitrogen, 35502) at a dilution of 1:400 for 30 min at room temperature. ATR oligomerization among various ATR mutants were monitored by mixing anti-FLAG (Rabbit polyclonal, Gene Tek GTX115043) at a dilution of 1:1,000 with anti-Myc (Mouse monoclonal, Cell Signaling 9B11) at a dilution of 1:4,000. ATR: ATRIP interactions among various ATR mutants were monitored by mixing anti-FLAG (Rabbit polyclonal, Gene Tek GTX115043) at a dilution of 1:1,000 with anti-Myc (mouse monoclonal, Cell Signaling 9B11) at a dilution of 1:4,000. ATRIP dimerization was monitored by mixing anti-HA (Rabbit monoclonal, Invitrogen 2–2.2.14) at a dilution of 1:500 with anti-Myc (Mouse monoclonal, Cell signaling 9B11) at a dilution of 1:4,000. PLA

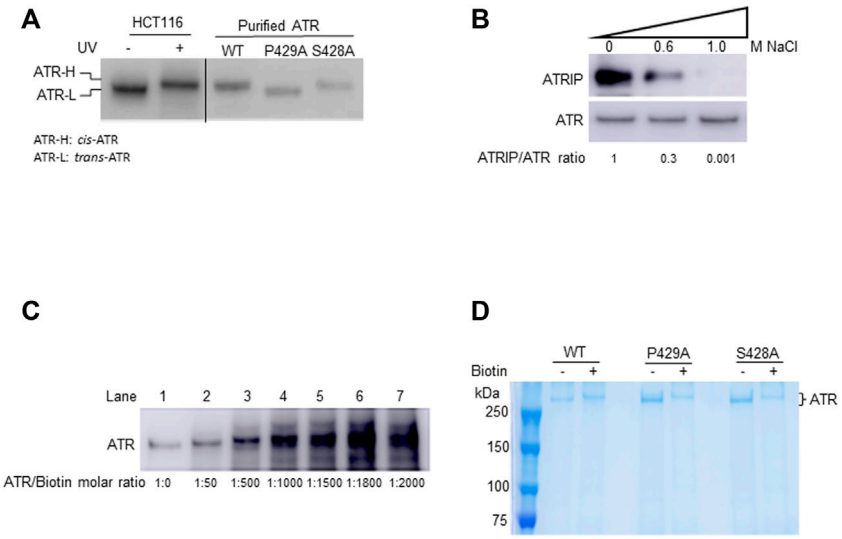


**FIGURE 1 |** In-solution biotinylation of ATR proteins. **(A)** Recombinant FLAG-ATR WT, P429A, and S428A proteins were purified from HEK293T cells. Purified WT and S428A proteins have the same electrophoretic mobility as endogenous ATR-H purified from the cytoplasmic fraction of UV-treated HCT116 cells, but P429A protein migrates as ATR-L as analyzed by Western blotting in 3–8% gradient SDS-PAGE. **(B)** FLAG-ATR protein was immunoprecipitated and washed with increasing concentrations of NaCl solution to remove bound proteins. ATRIP forms a tight complex with ATR and is efficiently removed by washing with 1M NaCl. The ATRIP/ATR ratios were normalized to the ratio at zero salt concentration. **(C)** Analysis of the mass of ATR-WT after biotinylation using increasing concentrations of sulfo-NHS-LC-biotin on 8% SDS-PAGE. ATR (2 μM) was biotinylated with sulfo-NHS-LC-biotin at different molar ratios and analyzed by Western blotting using ATR antibody. **(D)** 2 μM each of FLAG-ATR WT, P429A, and S428A proteins purified using FLAG beads, run on 8% SDS-PAGE with and without biotin (1,000 molar excess) modification, and visualized by Coomassie staining. Protein bands were excised and digested with trypsin for mass spectrometry analysis.

foci were analyzed by one-way ANOVA using GraphPad Prism 5.01 software and are reported as the average ± SD. The paired *t*-test was used to test the significance, and $p < 0.05$ is considered significant.

## *In Vitro* Kinase Activity Assay

The $ATR^{flox/-}$ cells transfected with a plasmid construct of FLAG-ATR (WT), FLAG-ATR (S428A), or FLAG-ATR (P429A) were UV treated as mentioned earlier, and cytoplasmic and nuclear lysates were prepared. Flag-ATR was IPed from cytoplasmic or nuclear extracts. The IP ATR was washed three times with PBS containing 0.05% NP40, followed by a kinase buffer wash [50 mM HEPES (pH 7.5), 150 mM NaCl, 10 mM MgCl2, 10 mM MnCl2, 2 mM DTT, 10% glycerol, 1× protease and phosphatase inhibitors, and 0.5 mM ATP]. The IP ATR was suspended in 20 μL of kinase buffer containing 0.5 mM ATP and 0.5 μg of GST-p53 protein (Boston Biochem, SP-454). The reaction was incubated at 30°C for 30 min and stopped by the addition of SDS-loading buffer. Proteins were separated by 3–8% TA SDS-PAGE and were analyzed by WB using phospho-S15 p53 antibody. IP ATR and the amount of GST-p53 in each sample were confirmed by WB.

## Molecular Modeling

The coordinates of main-chain atoms of the 20 amino acid flanking Ser428-Pro429 bond (10 residues on each side), namely, residues 419 to 438 of ATR, were acquired from the incomplete *trans* conformation ATR structure [PDB code: 5yz0 (Rao et al., 2018)]. Side chain atoms for each amino acid were added by the UCSF Chimera swapaa function (Pettersen et al., 2004). Clashes were examined and removed by experimenting with different rotamers. This generated the initial model of the wild-type ATR peptide in trans conformation. To generate the *cis* conformation, the peptide bond between Ser428-Pro429 was turned approximately 180° and then slightly adjusted to remove local clashes. Further adjustments to the side chains of the peptide were introduced by experimenting with different rotamers of affected residues to remove crowdedness or clashes. This generated the initial model of the wild-type ATR peptide in the *cis* conformation. Single-site mutagenesis of Ser428 to Ala (S428A) and Pro429 to Ala (P429A) in *cis* and *trans* conformation was generated by changing the residue at position 428 and 429 to alanine in the previously mentioned wild-type peptides, respectively. All six peptides were capped by an acetyl group on the N-terminal and by an amide group on the C-terminal to remove the charges and mimic the peptide sitting in the ATR protein.

The N-terminal ATR model that contains residue 2 to 770 was constructed similarly. The coordinates of main-chain atoms of residue 2 to 770 were acquired from *trans* conformation ATR (PDB code: 5yz0). Side-chain atoms for each amino acid were added by the UCSF Chimera swapaa function iteratively by a Python code. Clashes were examined and removed by experimenting with different rotamers. This generated the initial model of the wild-type ATR peptide in *trans* conformation. To generate the *cis* conformation, the peptide bond between Ser428-Pro429 was turned approximately 180° and then slightly adjusted to remove local clashes. In addition,

**TABLE 1 |** Identified conformational variations of ART WT, S428A, and P429A in cells or after isolation *via* FLAG-tagged immunoaffinity purification and a high salt wash.

| | Cytoplasm | | | Nucleus | | |
|---|---|---|---|---|---|---|
| ATR isomer | WT | S428A | P429A | WT | S428A | P429A |
| In cell | *Cis/trans* | *Cis* | *Trans* | *Trans* | *Trans* | *Trans* |
| Purified | *Cis* | *Cis* | *Trans* | *Cis* | *Cis* | *Trans* |

the loops containing residues 351 to 363 and residues 419 to 427 were reconstructed using ModLoop (Fiser et al., 2000) to remove clashes. Both models were capped by an amide group on the C-terminal to remove the effects of the charges, but not capped on the N-terminal to mimic the fragment sitting in the N-terminal of the full-length ATR protein.

## Molecular Dynamics Simulations and Energy Calculation

Hydrogen atoms were added, and FF14SB parameters were assigned to the protein by the tleap module of AMBER for both peptides and N-terminal ATR (Case et al., 2021). Water explicit MD simulations of the six peptides were carried out using the AMBER package. TIP3P explicit water molecules were added around each peptide 18 Å in each direction in a rectangular box, and counter ions were added to neutralize each system. Particle mesh Ewald (PME) was used to calculate the long-range electrostatic interactions, and the nonbonded cutoff was set to 8.0 Å. Each system was equilibrated by a four-step protocol before production MD simulation as previously described (Liu et al., 2011b). Restraint to the protein was removed in the 10 ns equilibrium run. A production trajectory of 400 ns employed the same condition of the final equilibration step, was run for each system. A total of 200 snapshots were collected from the last 200 ns production trajectory for total free energy calculations using the molecular mechanics-generalized Born surface area (MM-GBSA).

Water implicit MD simulations of the two N-terminal ATR were carried out by AMBER package using the Born solvation model for expedited computation. First, the structures were minimized by 500 steps of steepest descent minimization followed by 500 conjugate gradient minimizations with the restraint of 5 kcal/mol/Å$^2$ applied to the heavy atoms of the proteins. Salt concentration was set at 0.2 M. The computation of effective Born radii was set at 30 Å. Each system was heated up from 0 to 300 K gradually, with a weak restraint of 2 kcal/mol/Å$^2$ on the backbone atoms only. Restraint was then removed in the last 402 ns equilibration run without cutoff for nonbonded interactions. A production trajectory of 20 ns was run for each system using the same condition as the equilibration step. A total of 200 snapshots were collected from the 20 ns production trajectory for total free energy calculations using the molecular mechanics generalized Born surface area (MM-GBSA).

To verify the equilibrium state of each system and perform statistical analysis, total free energies of 200 frames were extracted frame-by-frame using a Python code for all simulations. Two-sided Student's *t*-test was performed by the R-package 4.1.1 (R Core Team, 2021), and a value of $p < 0.05$ was considered significant.

# RESULTS

## Protein Purification and Chemical Modification of ATR

In unstressed cells, Pin1 isomerizes ATR at p-Ser428-Pro429, converting the *cis*-Ser428-Pro429 amide bond to a *trans*-Ser428-Pro429 bond; this isomerization is dependent on the phosphorylation of Ser428 in the cytoplasm where the *cis-isoform* is the stable form in the absence of Pin1 (Hilton et al., 2015). The former is named *cis*-ATR and the latter, *trans*-ATR. As peptide bonds formed between any pair of the 19 non-proline amino acids adopt the *trans* conformation whereas proline can result in either a *cis*- or *trans*-isomer (Fischer et al., 1984; Fischer and Schmid, 1990; Hinderaker and Raines, 2003). A P429A point mutation was introduced in an ATR construct to ensure a *trans* conformation of the S428-P429A amide bond in ATR protein (ATR-L) (Hilton et al., 2015). In contrast, ATR-S428A protein was predominately *cis*-ATR (ATR-H) in the cytoplasm of cells as the serine to alanine mutation prevents the phosphorylation of ATR-Ser428 necessary for Pin1 isomerization of ATR (Hilton et al., 2015; Makinwa et al., 2020a; Makinwa et al., 2020b). In addition, purified ATR-WT protein from cells was found to be *cis*-ATR after removing Pin1 and all other ATR-interacting proteins through a high salt wash (**Figure 1A**; Hilton et al., 2015), indicating that wild-type ATR alone is naturally stable in the *cis*-isoform. The same is true for purified ATR-S428A, but purified ATR-P429A is *trans*-ATR (**Figure 1A**; Hilton et al., 2015).

In this study, recombinant ATR protein containing an N-terminal FLAG tag was overexpressed and purified from HEK293T cells. To obtain relatively pure ATR, FLAG bead-bound FLAG-ATR was washed with a high salt-containing buffer to remove proteins associated with FLAG-ATR including ATRIP 29 **Figure 1**. Analysis of the samples by Western blotting of a 3–8% gradient SDS gel shows that the purified WT and S428A ATR co-migrated with the ATR-H form, whereas P429A maintains ATR-L (**Figure 1A**). **Table 1** lists different conformational states of ATR observed in cells or after ATR purification from cells (ATRIP or any proteins associated with ATR were removed during ATR purification).

To determine differences in any surface topology of ATR (WT, P429A, and S428A), purified proteins were chemically modified at their lysine residues using sulfo-NHS-LC-biotin. Sulfo-NHS-LC-biotin derivatives is known to possess an active ester group that reacts specifically with the primary amines of proteins and/or the amino group of lysine residues, thereby forming an amide bond. For each lysine residue, this reaction increases the mass of 339.161 Da. Therefore, we first tested for the molar ratio of sulfo-NHS-LC-biotin to ATR protein. Since ATR has 175 lysine residues, it is expected that under ideal conditions all these residues can be biotinylated. This, however, assumes that all lysine residues are accessible to the biotin moiety, which is unlikely considering the tertiary structure of a protein.

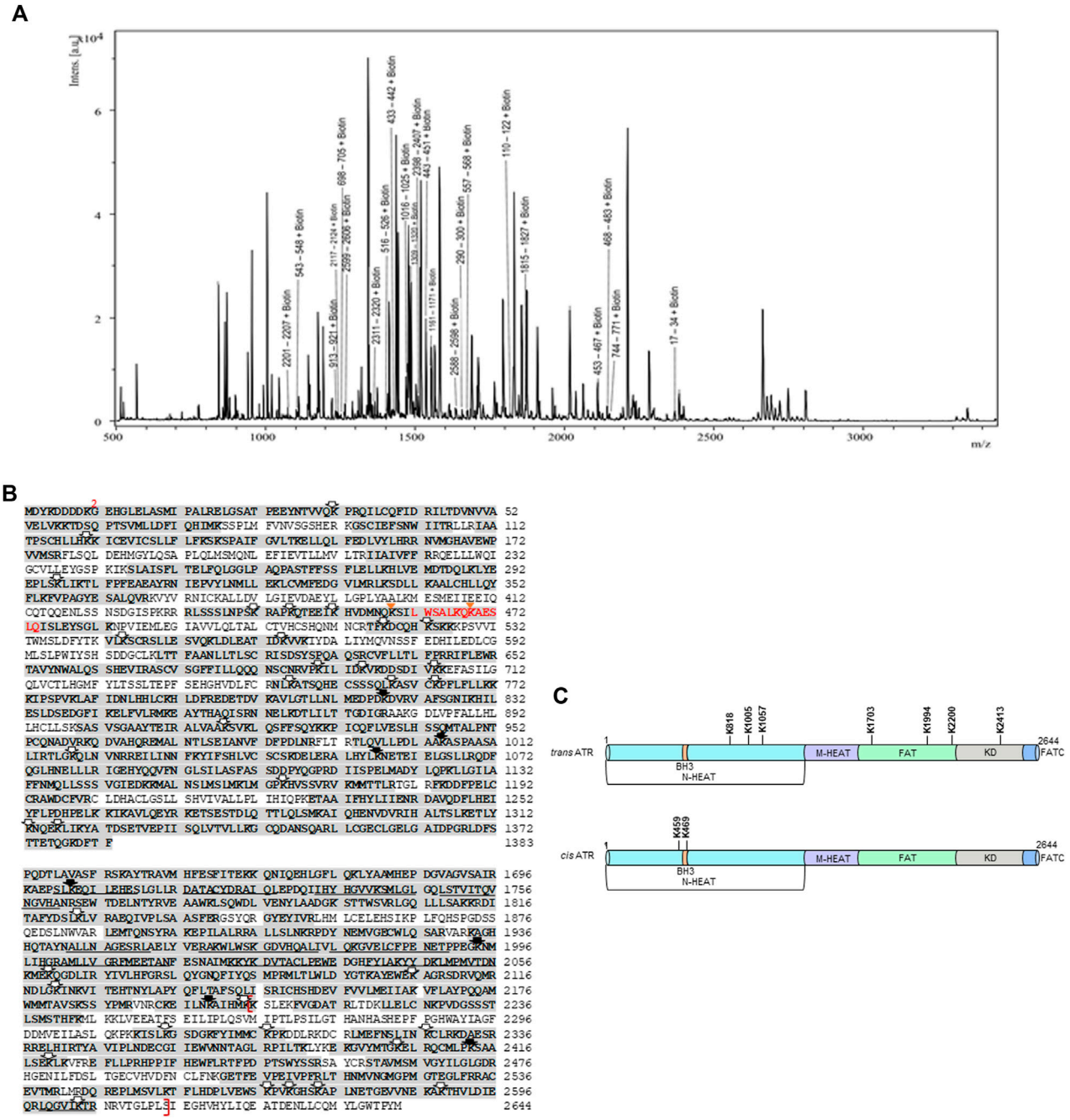


**FIGURE 2 |** MALDI-TOF and nano LC-MS/MS analysis of biotin-modified *cis*- and *trans*-ATR. **(A)** Typical MALDI-TOF mass spectrum of peptide fragments resulting from trypsin digestion of biotin-modified *cis*-ATR. **(B)** Sequence of N-HEAT, FAT, KD, and FATC domains of FLAG-tagged ATR protein. The initial methionine is part of the FLAG tag, and the first amino acid corresponding to ATR is marked as 2. Amino acid sequences corresponding to tryptic peptide fragments detected by MALDI-TOF and nano LC-MS/MS are indicated by the shading. The lysine residues modified by NHS-biotin treatment for all *trans*- and *cis*- *and WT* ATR are indicated by open arrows, whereas unique biotin-modified lysine residues were observed for *trans*-ATR (solid arrow) and *cis*- and WT ATR (gold triangle). The BH3 domain (aa461-474) is designated by red color, and the kinase domain (aa2206-2615) is enclosed in red brackets. **(C)** Summary of unique and differential biotin-modified lysine residues between *trans*- and *cis*-ATR identified by MALDI-TOF and nano LC-MS/MS in the context of the ATR structure. N-HEAT, N-terminal HEAT repeats; BH3, BH3-like domain; M-HEAT, middle HEAT repeats; FAT, FRAP, ATM, TRRAP domain; KD, kinase domain; FATC, FAT C-terminal domain.

Nevertheless, if all the 175 lysine residues are biotinylated, the calculated mass shift of the protein would be 59.35 kDa. As shown in **Figure 1C**, an increase in the concentration of the biotinylating reagent lead to an increase in the mass of the protein as demonstrated by the band shifts in SDS-PAGE (**Figure 1C**, lanes 1–4) up to a maximum of 1000-fold molar excess of

biotin (**Figure 1C**, lane 4). Further increase in concentration to 1500-fold molar excess does not result in any significant increase in the mass of the protein (**Figure 1C**, lane 5). No further increase in mass also indicates that there is a stable tertiary structure of ATR under the experimental modification conditions. Therefore, all three forms of affinity-purified FLAG-ATR proteins were modified using a 1000-fold molar excess of sulfo-NHS-LC-biotin and re-purified on SDS-PAGE (**Figure 1D**) before tryptic digestion and MALDI-TOF analysis.

## Surface Topology Analysis of Wild-Type, P429A (*trans*), and S428A (*cis*) ATR With the Biotinyl-Lysine Method and Mass Spectrometry

Chemical modification coupled with mass spectrometry has been used to probe the surface topology of proteins (Bennett et al., 2000), including proteins interacting with ATR (Shell et al., 2009). To identify biotin-modified lysines, tryptic peptides were subjected to matrix-assisted laser desorption/ionization-time-of-flight mass spectrometry (MALDI-TOF). MALDI-TOF, without chromatographic separation of the peptides, a series of peaks with a mass-to-charge ratio (m⁄z) corresponding to the tryptic peptides unfolds in a single-mass spectrum. Because the sample is known in this case, it is possible to identify the ATR peptide corresponding to each peak by calculating all possible peptide masses for tryptic digestion of ATR, including biotin modification of lysines. We determine a probability-based score, called the Ascore, which measures the probability of correct biotin-modified site localization based on the presence and intensity of site-determining ions in MS/MS spectra (**Supplementary Table S1**). A total of 185, 195, and 191 tryptic peptides with 41, 46, and 41 biotinylated lysines were identified, respectively, for WT, P429A, and S428A ATR proteins by peptide mass matching after MASCOT search. **Figure 2A** depicts a representative mass spectrum for tryptic fragments of the biotin-modified WT ATR protein. Monoisotopic resolution of the peaks allowed us to rightfully identify the tryptic fragments of ATR. **Figure 2B** illustrates the peptide fragments (bold sequences) and biotinylated lysines identified by MALDI-TOF as well as high-resolution nano LC-MS-MS analysis for ATR (WT, P429A, and S428A). We have identified seven unique biotin-modified lysine residues at K818, K1005, K1057, K1703, K1994, K2200, and K2413 for ATR P429A (ATR-L) whereas two unique biotin-modified lysines at K459 and K469 were observed for WT and S428A (ATR-H) **Figure 2C**.

## Identification of Conformational Change of the tBid-Binding Domain of *cis*/*trans*-ATR Isoform

ATR can form *cis or trans* isomers in the cytoplasm depending on Pin1, which can isomerize cis-ATR to trans-ATR. The cis-ATR, likely containing an exposed BH3 domain versus the unexposed BH3 domain in trans-ATR, is antiapoptotic at mitochondria by binding to tBid, thereby forbidding the activation of pro-apoptotic Bax. We reported previously that the BH3-like domain (aa462–474, **Figure 3A**) of ATR was required for the ATR–tBid interaction (Hilton et al., 2015). Our data showed that the P429A mutant predominantly forms the trans (ATR-L) isoform, whereas FLAG affinity-purified WT and S428A ATR mutant isoforms migrate as the cis (ATR-H) isoform (**Figure 1A**). Interestingly, mass footprinting with biotin modification revealed that WT and S428A mutant (cis-ATR) showed a conformational change over the BH3 domain where K459 and K469 were accessible to biotin modification (**Figures 3B,C**), while the P429A mutant (trans-ATR) had no such modifications. To confirm the mass spectra data, we performed a pull-down assay by incubating purified tBid protein (R & D Systems) with FLAG-immobilized ATR from cytoplasmic fractions of UV+/- treated ATRflox/− cells transfected with a plasmid construct of FLAG-ATR (WT), FLAG-ATR (S428A), or FLAG-ATR (P429A) (**Figure 3D**). The data indicate that UV irradiation led to the cis-ATR formation in the cytoplasm of cells transfected with ATR-WT construct, while ATR-P429A remains as trans-ATR and ATR-S428A as cis-ATR regardless of UV, as previously reported (Hilton et al., 2015). Furthermore, **Figure 3D** shows a very dramatic increase of tBid protein pull-down by cis-ATR rather than by trans-ATR. We also observed that in the cells the cis-ATR (ATR-S428A)–tBid interaction occurred at mitochondria regardless of UV (**Figure 3E**), while as a control, the cis-conformation of ATR-WT induced by UV led to a dramatic increase of cis-ATR–tBid interaction (**Figure 3E**). In contrast, trans-ATR (ATR-P429A) could not interact with tBid. These results show that in the presence or absence of UV irradiation tBid is associated with cis-ATR but not trans-ATR.

## Effect of *cis*/*trans* Conformational Change on ATR Dimerization

ATR dimerizes through three symmetrically arranged intermolecular contacts between the C-terminal ATR–ATR interface and also through the N-terminal ATR–ATRIP interface and the coil–coil domain of ATRIP–ATRIP dimerization ATRIP (dimer–dimer) (Rao et al., 2018). The C-terminal regions involved in ATR dimer formation are highly conserved, supporting their significance for ATR function (Rao et al., 2018). We have investigated the dimerization domain of *cis/trans* ATR through mass footprinting. Peptides that are involved in ATR dimerization were identified and are listed in **Table 2**.

Mass footprinting data can identify nearly all peptides involved in ATR dimerization for ATR (WT), P429A, and S428A mutant proteins. By use of mass footprinting, we have identified 14 peptides (all unmodified except two) at the dimeric interface for ATR P428A mutant, whereas WT and S428A mutant dimeric interface consists of 15 unmodified peptides (all unmodified except one).

We next examined whether *cis* and *trans* isoforms of ATR were oligomers in cells. ATR oligomerization was analyzed by co-expressing FLAG- and Myc-tagged ATR proteins in UV+/− treated $ATR^{flox/-}$ cells co-transfected with plasmid constructs of FLAG-ATR (WT), FLAG-ATR (S428A), or FLAG-ATR

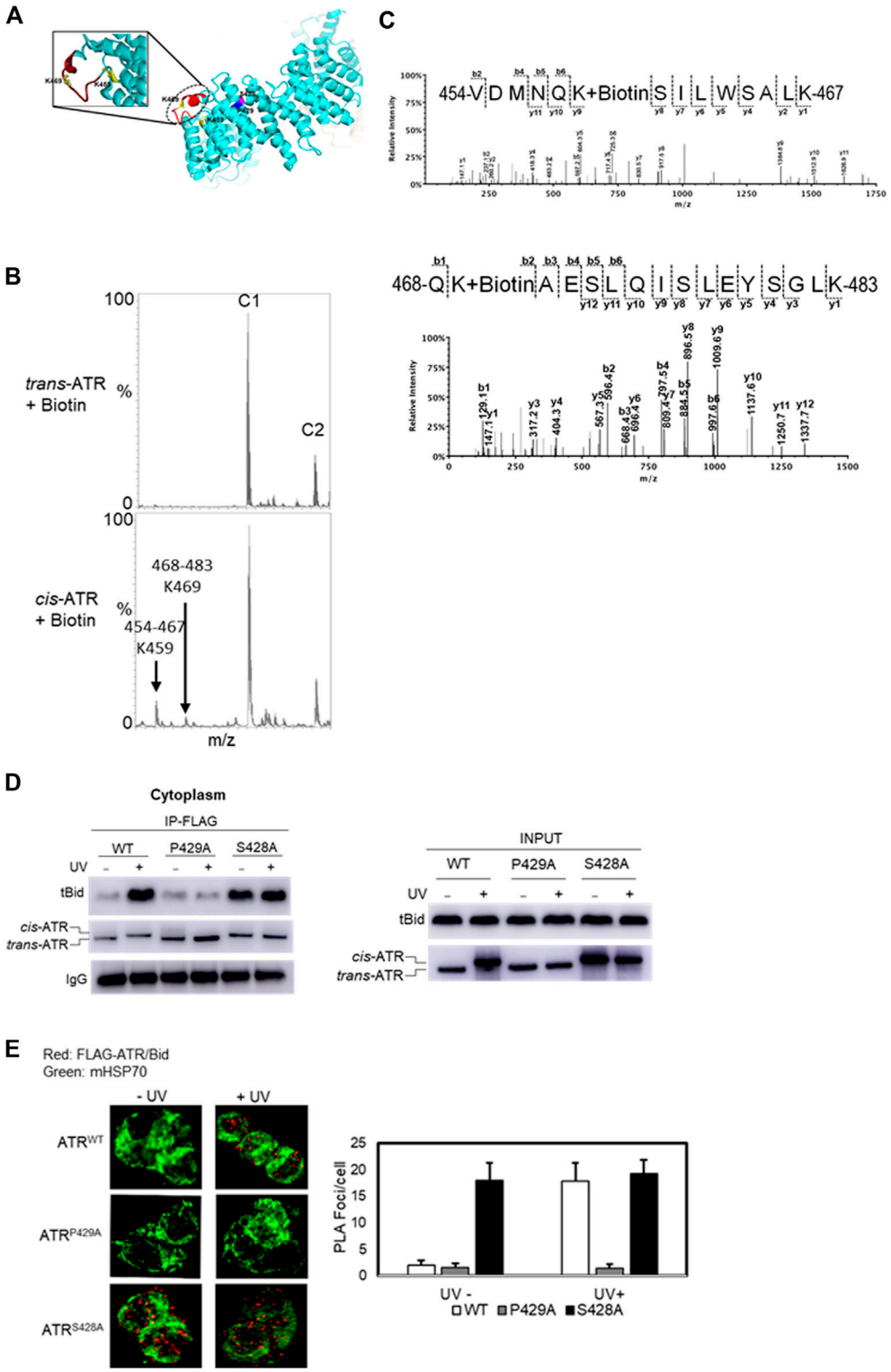


**FIGURE 3 |** Effect of *cis/trans* conformation of ATR on ATR–tBid interaction. **(A)** In ribbon diagram of ATR (PDB code 5YZ0, Rao et al., 2018), the positions of S428A and P429A mutant sites on the ATR (chain colored with cyan) structure are colored with magenta and blue, respectively. tBid interacting with the BH3 domain of ATR is shown by red color marked with a dotted circle. Biotin-modified K459 and K469 amino acids of *cis*-ATR are displayed by ball and stick. **(B)** Representative segment of MALDI-TOF data showing that K459 and K469 were readily modified with sulfo-NHS-LC-biotin in cis-ATR but were significantly protected from the modification in trans-ATR. Unmodified peaks C1 and C2 serve as controls. **(C)** Mass spectrum of identified biotin-modified Lys-459 amino acid of peptide

(*Continued*)

**FIGURE 3 |** 468QKAESLQISLEYSGLK483 and K469 amino acid of peptide 454VDMNQKSILWSALK467 of *cis*-ATR. A 147.1 Da mass increase of precursor ion and 339.1 Da increase in mass between b1, b2 and y2, y3 ions is observed for K459 and K469, respectively. **(D)** tBid interacts with the *cis* form of ATR (ATR-H). $ATR^{flox/-}$ cells were transfected with a plasmid construct of FLAG-ATR (WT), FLAG-ATR (S428A), or FLAG-ATR (P429A). *In vitro* pull-down of purified tBid protein was carried out with FLAG bead-bound ATR proteins isolated from the cytoplasmic fractions of UV- or mock-treated $ATR^{flox/-}$ cells. **(E)** Duolink PLA demonstrates that *cis*-ATR interacts with proapoptotic protein Bid. Focus stacking reveals that the UV-induced ATR–Bid interaction predominately occurs outside of the nucleus. Foci formation per cells was calculated considering an average of 50 cells, and each experiment was performed in triplicate. The bar graph represents a statistical analysis of the PLA images.

**TABLE 2 |** Identified peptides involve in ATR dimerization for ATR WT and mutant P429A and S428A proteins.

| ***Trans*-ATR** | ***Cis*-ATR** |
|---|---|
| 1696 KAEPSLKEQILEHESLGLLR 1717 | 1696 KAEPSLKEQILEHESLGLLR 1717 |
| 1716 DATACYDR 1725 | 1716 DATACYDR 1725 |
| 1724 AIQLEPDQIIHYHGVVK 1742 | 1724 AIQLEPDQIIHYHGVVK 1742 |
| 1741 SMLGLGQLSTVITQVNGVHANR 1764 | 1741 SMLGLGQLSTVITQVNGVHANR 1764 |
| 1933 AGHHQTAYNALLNAGESR 1952 | 1933 AGHHQTAYNALLNAGESR 1952 |
| 1958 AKWLWSK 1967 | 1958 AKWLWSK 1967 |
| 1966 GDVHQALIVLQK 1979 | 1966 GDVHQALIVLQK 1979 |
| 1978 GVELCFPENETPPEGkNMLIHGR 2002 | 1978 GVELCFPENETPPEGK 1995, 1994 NMLIHGR 2002 |
| 2001 AMLLVGR 2009 | 2001 AMLLVGR 2009 |
| 2008 FMEETANFESNAIMK 2024 | 2008 FMEETANFESNAIMK 2024 |
| 2023 YKDVTACLPEWEDGHFYLAK 2044 | 2023 YKDVTACLPEWEDGHFYLAK 2044 |
| 2043 YYDKLMPMVTDNK 2057 | 2043 YYDKLMPMVTDNK 2057 |
| 2598 LQGVIkTR 2607 | 2598 LQGVIkTR 2607 |

**k-biotin-modified lysine.*

(P429A) and Myc-ATR (WT), Myc-ATR (S428A), or Myc-ATR (P429A), followed by assessing ATR oligomerization by co-IP after fractionation. Immunoprecipitation of FLAG-ATR using FLAG antibodies (**Figure 4A**) demonstrates that ATR does form oligomeric complexes in cells. FLAG antibodies did not immunoprecipitate any Myc-ATR when FLAG-ATR was not expressed (**Figure 4A** cytoplasmic fraction Lane 9 and 10 and nuclear fraction Lane 9 and 10). A significant reduction in the amount of ATR-P429A-IPed HA-ATRIP in the absence of UV is likely due to the experimental variation in efficiency of HA-ATRIP construct transfection into cells. Oligomerization of *cis/trans* isoforms of ATR was further confirmed by the proximity ligation assay method by co-expressing FLAG- and Myc-tagged ATR in UV+/− treated $ATR^{flox/-}$ cells (**Figure 4B**).

## Effect of *cis/trans* Conformational Change on ATR–ATRIP Association

The conformational flexibility of ATR allows ATRIP to properly lock up the N-termini of the two ATR monomers *via* the C-termini of two ATRIP monomers toward favorable ATR–ATRIP complex formation and functional diversity (Cortez et al., 2001; Ball et al., 2005; Falck et al., 2005). To understand the effect of *cis/trans* isomerization on ATR–ATRIP association, UV+/− treated $ATR^{flox/-}$ cells were transfected with vectors encoding FLAG-ATR, Myc-ATR, and HA-ATRIP. ATR–ATRIP association was determined by FLAG-immunoprecipitation after cellular fractionation. As shown in **Figure 4A**, nuclear ATR formed a complex with ATRIP and UV irradiation enhanced the complex formation. Interestingly, little or no ATRIP was found in the cytoplasm as compared to ATRIP in the nucleus (**Figure 4A**). Thus, there was little or no cytoplasmic ATR–ATRIP complex formation. The nuclear ATR–ATRIP association for *cis/trans* ATR isoforms was confirmed further by the proximity ligation assay (**Figure 4C**).

The ATRIP–ATRIP association was assessed using the proximity ligation assay under the influence of ATR *cis/trans* isoforms. UV+/− treated $ATR^{flox/-}$ cells were co-transfected with FLAG-ATR, Myc-ATRIP, and HA-ATRIP. ATRIP oligomerization under the influence of ATR (WT, P429A, and S428A) was monitored by fluorescence microscopy (**Figure 4D**). Data suggest that ATRIP–ATRIP foci formation increased similarly by UV treatment for all ATR isoforms, which signifies the formation of stable ATR–ATRIP complexes.

## Conformational Changes Around the Kinase Domain Among ATR Mutants

Recently reported cryo-electron microscopy structural data of the human ATR–ATRIP complex reveals key components of the kinase domain related to ATR function (**Figure 3A**) (Rao et al., 2018). The PIKK regulatory domain (PRD, residues 2,483–2,597) of ATR and ATRIP (C-terminal coiled-coil domain) are both crucial for TopBP1-mediated activation. Mutation K2589E does not impair basal kinase activity of ATR but largely diminish its activation by TopBP1 (Mordes et al., 2008). Previous studies also showed that ATR undergoes autophosphorylation on residue T1989, which recruits TopBP1 for the activation of ATR (Liu et al., 2011a; Nam et al., 2011). Structural analysis reveals that residue T1989 is located on the surface of the FAT domain and is unlikely to gain access to any of the two catalytic pockets within the same ATR–ATRIP complex, suggesting *trans*-mode autophosphorylation. Since residues T1989 and K2589 both contribute to TopBP1-mediated activation of ATR, it is comprehensible that TopBP1 binds to ATR along with the dimer interface. Residue K2589 stabilizes the substrate entry groove of the kinase domain followed by a loop involved in intermolecular contacts and plays a role in the regulation of substrate entry. In sum, TopBP1 might stimulate ATR–ATRIP kinase activity by facilitating substrate access to the catalytic cavity or inducing conformational changes of the kinase domain to favor the catalytic reaction.

Our mass footprinting data uncover kinase domain assembly between ATR WT as well as the S428A and P429A mutants. All these proteins show the same peptide fragmentation pattern along the catalytic loop and the activation loop of ATR (Rao

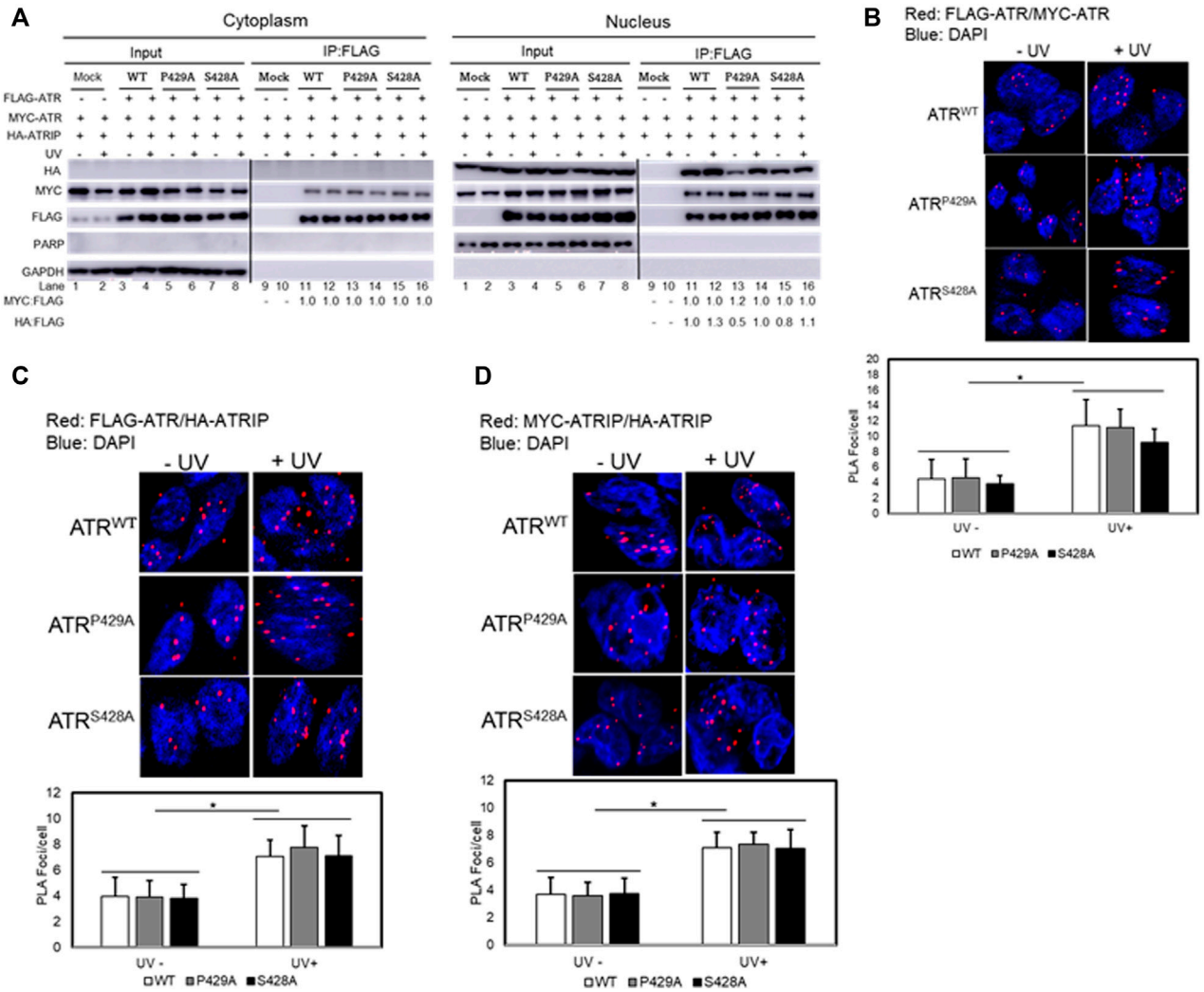


**FIGURE 4 |** Effect of *cis/trans* isomerization on ATR oligomerization and ATR–ATRIP complex formation. **(A)** Oligomerization of *trans*- and *cis*-ATR was analyzed by co-expressing vector constructs encoding FLAG-ATR, Myc-ATR, and HA-ATRIP transfected into the $ATR^{flox/-}$ cells followed by UV+/− treatments. ATR oligomerization was assessed by co-immunoprecipitation after cellular fractionation. Interestingly, no ATRIP occurred in the cytoplasm as compared to ATRIP in the nucleus. The Myc/FLAG ratios were normalized to the ratio at lane 11 (cytoplasm fraction) and HA/FLAG at lane 11 (Nuclear fraction). **(B)** PLA revealing a direct interaction between FLAG-ATR and Myc-ATR in $ATR^{flox/-}$ cells co-transfected with FLAG-ATR and Myc-ATR plasmids. The interaction was enhanced after UV irradiation at 40 J/$m^2$. A DAPI-staining overlay shows the location of the nuclei. **(C)** ATR/ATRIP complex formation was monitored using PLA by co-transfecting FLAG-ATR WT, P429A, or S428A mutant with Myc-ATRIP in $ATR^{flox/-}$ cells. **(D)** ATRIP oligomerization in the presence of FLAG-ATR WT, P429A, or S428A mutant proteins. $ATR^{flox/-}$ cells were co-transfected with Myc- and HA-ATRIP plus FLAG-ATR WT, P429A, or S428A constructs followed by UV irradiation. Oligomerization of Myc- and HA-ATRIP was monitored by PLA. Foci formation per cells was calculated considering an average of 50 cells, and each experiment was performed in triplicate. The bar graphs represent the statistical analysis of the PLA images. * stands for the *p*-value < 0.01.

et al., 2018). Residue K2859, which is important to maintain conformation at the substrate entry groove, was found to be biotin-modified for ATR WT as well as the S428A and P429A mutants. Since nuclear ATR plays an important role in DNA damage-induced checkpoint activity in association with ATRIP, we examined the checkpoint kinase activity of cytoplasmic ATR. A previous report provides evidence that phosphorylation at Ser15 is a critical event in the upregulation and functional activation of p53 during cellular stress and ATR regulates phosphorylation of Ser15 in DNA-damaged cells (Tibbetts et al., 1999). To test the phosphorylation status of p53(Ser15), ATR WT, S428A, and P429A mutant plasmid constructs were transfected into $ATR^{flox/-}$ cells. FLAG-ATR was IPed from cytoplasmic and nuclear fractions of UV+/− irradiated cells after 2-h of recovery and subjected to an *in vitro* kinase assay for phosphorylation of p53(Ser15) by ATR. All three proteins from the nucleus show the equivalent kinase activity toward p53 (**Figure 5A**), consistent with nuclear ATR, either WT, S428A, or P429A being *trans*-ATR (Hilton et al., 2015; Makinwa et al., 2020a) **Table 1**. In contrast, upon UV irradiation p53 was not phosphorylated by cytoplasmic ATR, regardless of *cis* or *trans* conformation, due to the lack of ATRIP (**Figure 5A**).

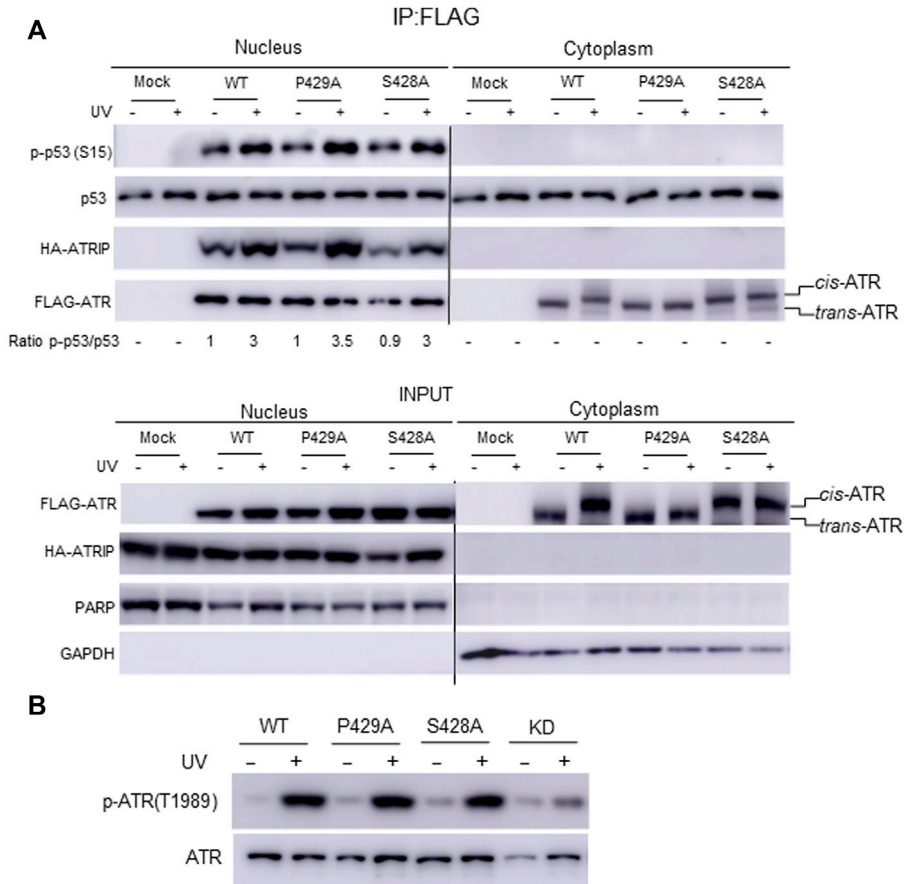


**FIGURE 5 |** Effect of *cis/trans* conformation of ATR on its kinase activity. **(A)** *In vitro* phosphorylation of purified GST-p53 was carried out to assess the checkpoint kinase activity of IPed ATR from the cytoplasmic and nuclear fractions of $ATR^{flox/-}$ cells expressing co-transfected FLAG-ATR WT, mutants P429A, or S428A plus Myc-ATRIP constructs. GST-p53 phosphorylation was monitored by Western blot using phospho-S15 p53 antibody. **(B)** Phosphorylation of ATR on T1989 was monitored to confirm the checkpoint kinase activity of ATR WT, S428A, and P429A mutant proteins in $ATR^{flox/-}$ cells after transfection with the respective plasmid construct. The nuclear fraction was collected from UV+/– irradiated cells after 2 h of recovery.

**TABLE 3 |** Calculated total free energies and components of wild-type and mutant ATR peptides (WT: NLSSNSDGIS428P429KRRRLSSSL; S428A: NLSSNSDGIA428P429KRRRLSSSL; and P429A: NLSSNSDGIS428A429KRRRLSSSL).* All values are reported in kcal/mol. *p*-values are from two-sided Student's t-test.

| Energy terms* | *Cis*-WT | | *Trans*-WT | | *Cis*-P429A | | *Trans*-P429A- | | *Cis*-S228A | | *Trans*-S428A | |
|---|---|---|---|---|---|---|---|---|---|---|---|---|
| | Mean | S.D. | Mean | S.D. | Mean | S.D. | Mean | S.D. | Mean | S.D. | Mean | S.D. |
| Bond | 64.39 | 6.94 | 62.77 | 6.61 | 61.76 | 6.44 | 60.92 | 6.72 | 62.73 | 6.98 | 63.02 | 6.70 |
| Angle | 165.05 | 9.79 | 158.48 | 9.46 | 153.17 | 10.09 | 149.53 | 9.70 | 158.96 | 10.55 | 157.95 | 10.28 |
| Dihed | 256.48 | 6.35 | 256.78 | 7.80 | 251.04 | 7.29 | 252.43 | 6.90 | 255.35 | 7.47 | 255.74 | 7.51 |
| VDW | –95.65 | 7.62 | –95.00 | 8.70 | –84.75 | 10.95 | –95.02 | 7.49 | –91.47 | 9.09 | –90.10 | 9.62 |
| ELE | –943.35 | 32.35 | –85.37 | 45.31 | –875.37 | 50.25 | –902.93 | 41.59 | –911.64 | 48.52 | –859.37 | 40.87 |
| 1–4 VDW3 | 65.9 | 3.85 | 66.04 | 3.73 | 64.93 | 3.51 | 66.04 | 3.72 | 66.47 | 3.92 | 65.92 | 3.58 |
| 1–4 EEL | 141.06 | 14.73 | 144.19 | 22.51 | 151.46 | 21.00 | 159.78 | 22.39 | 151.92 | 21.82 | 154.95 | 20.92 |
| G-Gas | –346.09 | 33.38 | –292.12 | 39.03 | –277.76 | 47.53 | –309.25 | 35.29 | –307.68 | 43.42 | –251.90 | 40.19 |
| G-Solv | –413.38 | 25.45 | –464.22 | 32.32 | –481.49 | 40.36 | –466.79 | 27.20 | –433.77 | 33.69 | –486.40 | 33.64 |
| Total | –759.47 | 15.53 | –756.34 | 15.12 | –759.26 | 15.85 | –776.04 | 15.63 | –741.45 | 15.85 | –738.29 | 14.99 |
| *p*-value | 0.042 | | | | <2.2e-16 | | | | 0.042 | | | |

* *All values are reported in kcal/mol.* p-*values are from two-sided Student's t-test.*

Interestingly, a peptide fragmentation pattern difference is observed between the ATR-P429A mutant with ATR-WT and ATR-S428A mutant. The trypsin digestion-protected peptide $^{1978}$(K)GVELCFPENETPPEGK(Biotin)NMLIHGR(A)$^{2002}$ with a biotin-modified K1994 is observed in ATR-P429A (**Table 2**). This K1994 is in very close proximity to T1989, which is at the

**TABLE 4 |** Calculated total free energies and components of N-ATR (residue 2–770) in *cis* and *trans* conformation.

| Energy terms* | Initial runs | | | | Duplicated runs | | | |
|---|---|---|---|---|---|---|---|---|
| | *Cis*-AA770 | | *Trans*-AA770 | | *Cis*-AA770 | | *Trans*-AA770 | |
| | Mean | S.D. | Mean | S.D. | Mean | S.D. | Mean | S.D. |
| Bond | 2,481.41 | 42.17 | 2,487.54 | 45.03 | 2,482.17 | 40.33 | 2,487.15 | 41.84 |
| Angle | 6,581.86 | 63.94 | 6,570.12 | 70.70 | 6,575.29 | 61.87 | 6,558.83 | 63.29 |
| Dihed | 9,774.51 | 39.64 | 9,766.92 | 38.92 | 9,803.42 | 40.60 | 9,797.98 | 42.37 |
| VDW | −5,650.77 | 54.81 | −5,358.51 | 52.50 | −5,753.14 | 61.85 | −5,387.97 | 50.02 |
| ELE | −53,120.93 | 236.72 | −52,319.35 | 209.00 | −53475.41 | 213.20 | −52,892.09 | 257.08 |
| 1–4 VDW | 2,810.94 | 23.54 | 2,822.22 | 22.24 | 2,828.29 | 22.55 | 2,816.45 | 22.17 |
| 1–4 EEl | 33,121.40 | 81.34 | 33,206.63 | 93.87 | 33,138.63 | 77.70 | 33,295.76 | 81.14 |
| G-Gas | −4,001.89 | 234.72 | −2,854.43 | 207.83 | −4,410.75 | 219.21 | −3,306.88 | 242.81 |
| G-Slov | −10,663.86 | 192.67 | −11,676.44 | 164.42 | −10,336.15 | 183.02 | −11,202.01 | 207.52 |
| Total | −14,665.75 | 86.90 | −14,530.87 | 91.30 | −14,746.90 | 92.74 | −14,508.89 | 85.09 |
| *p*-value | <2.2e-16 | | | | <2.2e-16 | | | |

ATR auto-activation site. In contrast, K1994 is not biotin modified in either WT or S428A ATR, resulting in two tryptic peptides $^{1978}$(K)GVELcFPENETPPEGK(N)$^{1995}$ and $^{1994}$(K)NMLIHGR(A)$^{2002}$. This implies that there could be a conformational alteration between *cis*-ATR (WT or S428A) and *trans*-ATR (P429A), which might affect the kinase activity of ATR. However, this effect may occur only in the cytoplasm as in the nucleus when both ATR WT and S428A are *trans*-ATR and should have the same conformation as ATR P429A. Indeed, the results in **Figure 5** indicate that the three ATR proteins, WT, S428A, and P429A, have the equivalent kinase activity in the nucleus.

Previous studies showed that ATR is transformed into a phosphorylated state after DNA damage and that a single autophosphorylation event at Thr1989 is crucial for ATR activation. Phosphorylation of Thr1989 relies on RPA, ATRIP, and ATR kinase activity. To test the autophosphorylation status at Thr1989, ATR WT, S428A, and P429A mutant plasmid constructs were transfected in ATR$^{flox/-}$ cells, and the nuclear fraction was collected from UV+/− irradiated cells after 2 h of recovery. Autophosphorylation at Thr1989 was monitored using an anti-Thr1989 phosphor ATR antibody. ATR KD version was also included as a negative control. The WB shows that there is no significant difference in autophosphorylation at Thr1989 for nuclear ATR WT and S428A mutant compared with the P429A mutant (**Figure 5B**). This is consistent with the fact that all three ATRs are always in the *trans* conformation in the nucleus. Recruitment of ATR–ATRIP to RPA-ssDNA leads to the congregation of ATR–ATRIP complexes and promotes Thr1989 phosphorylation in trans-ATR 24.

## Structural Characterization by Molecular Modeling and Computational Biology

To understand the proline isomerization of ATR at Ser428-Pro429 from the standpoint of free energies, we conducted molecular modeling and molecular dynamics (MD) simulations using the AMBER package. Due to the huge size of ATR and the incompleteness of the experimentally determined ATR structure (Rao et al., 2018), we derived 20-aa peptide with S428-P429 flanked by 9-aa on each side (NLSSNSDGISPKRRRLSSSL) in both *cis* and *trans* conformations, performed water explicit MD simulation, and calculated the total free energies for both conformations using the MM-GBSA approach. Because small peptides do not fold like protein and form rigid structures, root mean square deviation (RMSD) of the main chain atoms are greater than 3.5 Å during the simulations. To verify each system has reached its equilibrium status, we developed a Python code and extracted total free energies frame-by-frame from the MM-GBSA calculation. We then plotted and examined the data. The energies are steady and flat without further declining (**Supplementary Figure S1A**), suggesting each system is well-equilibrated. As shown in **Table 3**, the *cis* conformation of wild-type ATR is energetically more favorable than *trans* conformation with a total free energy of −759 kcal/mol vs. −756 kcal/mol. On the contrary, in the case of P429A mutant, the *cis* conformation is less stable than *trans* with a total free energy of −759 kcal/mol compared with −776 kcal/mol. This is consistent with previous findings that peptide bonds of all other 19 amino acids not involving proline favor the *trans* conformation (Zimmerman and Scheraga, 1976). However, when S428 is substituted by alanine, this trend reversed with *cis* conformation is more favorable than that with *trans* (total free energy −741 vs. −738 kcal/mol). Moreover, the aforementioned pattern of total free energies of the six types of peptides reoccurred in our duplicated runs (**Supplementary Table S2**). Therefore, the computational results fully agree with the experimental observations that *cis* conformation dominates wild-type and the S428A mutant, while *trans* conformation is preferred in the P429A mutant.

To understand if *cis*-ATR is energetically more favorable than *trans*-ATR beyond the local peptide level, we built the *cis* and *trans* models comprising residues 2–700 and performed water implicit MD simulation. Both *cis*- and *trans*-ATR are composed of helices and loops that are loosely packed, and both structures are dynamically fluctuating tremendously as indicated by the main chain RMSD value. To ensure each system has reached its equilibrium status, we extracted the total free energies frame-by-frame from the MM-GBSA calculation and examined them to be flat and steady without further declining (**Supplementary Figure**

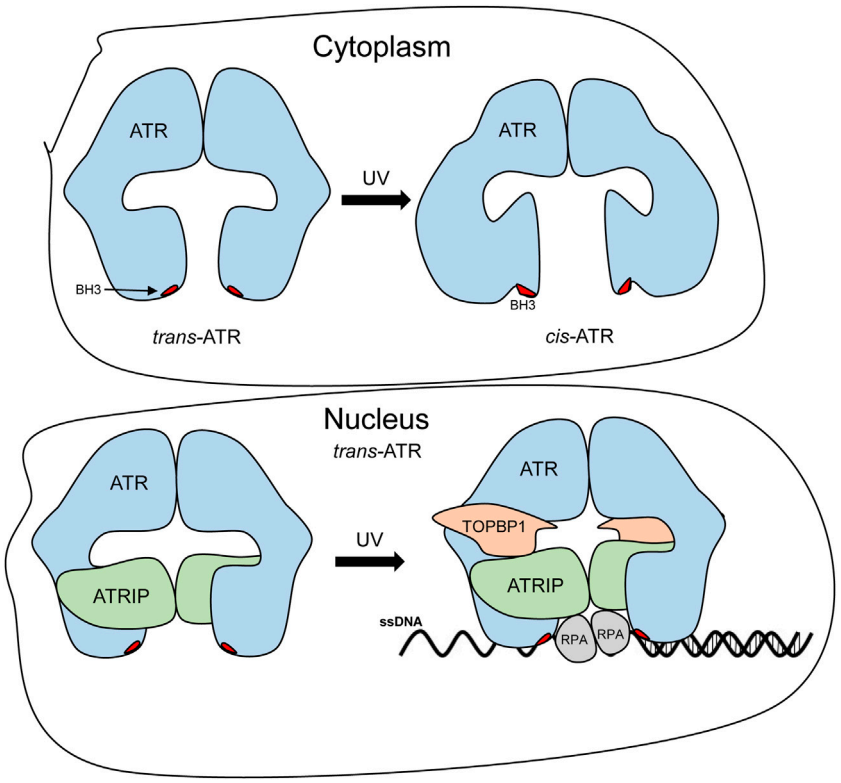


**FIGURE 6 |** Proposed prolyl isomerization-mediated conformational changes and subcellular compartment-specific functions of ATR. Mass footprinting revealed changes in the surface topology of ATR in the cytoplasm and the nucleus. After UV irradiation, cytoplasmic ATR undergoes multiple conformational changes that open up the BH3 domain and allow tBid–ATR interaction, whereas, in the nucleus, UV irradiation enhances the ATR–ATRIP association, which may help retain the *trans*-ATR conformation and allow the ATR–ATRIP complex to interact with RPA-bound ss-DNA and the subsequent binding of other ATR activators (like TOPBP1), further enhancing ATR kinase activity.

**S1B**), suggesting that the system is well-equilibrated. As shown in **Table 4**, the *cis* conformation of wild-type ATR is energetically more favorable with a total free energy of −14,666 kcal/mol vs. −14,531 kcal/mol in *trans* conformation. This is also true in duplicated runs in which *cis*-ATR has a total free energy of −14,747 kcal/mol compared with −14,509 kcal/mol of that of *trans*-ATR.

## DISCUSSION

DNA damage checkpoints and apoptosis are two dominant pathways of the DNA damage response (DDR). Moderate DNA damage activates checkpoints, leading to cell cycle arrest and DNA repair. Checkpoint activation appears to be in sync with the suppression of apoptosis, as eventually checkpoints will subside, and normal cell cycling will resume after completion of DNA repair. To this end, a balance between the levels of ATR-H (*cis*-ATR), an antiapoptotic protein, and ATR-L (*trans*-ATR), a DNA damage checkpoint kinase, is regulated in the cytoplasm. Pin1 is central to the regulation of this balance since it catalyzes the phosphorylation-dependent isomerization that converts *cis*-ATR to *trans*-ATR in the cytoplasm (Hilton et al., 2015; Makinwa et al., 2020a; Makinwa et al., 2020b). The proper balance ensures a functional and effective DNA damage response as the protection of cells from apoptosis is essential for the activities of cell cycle checkpoint arrest and DNA repair. The presented data demonstrate a structure–function mechanism by which the two pathways may work in a coordinated manner in DDR.

In this study, we demonstrated and confirmed that *cis*-ATR and *trans*-ATR are structurally different, and ATR (purified WT) is naturally stable in *cis* conformation. This is confirmed by our molecular modeling of the 20-aa peptide of ATR with Ser428-Pro429 in the middle of the sequence, and the N-terminal fragment consists of residues 2 to 770, revealing that *cis* conformation is significantly more energetically favorable than *trans* conformation in this wild-type ATR (**Table 3**, **4**). As summarized in **Figure 6**, the UV-induced *trans*-to-*cis* isomeric conversion in the cytoplasm results in a conformational change in the N-terminal and middle regions of ATR, likely exposing the BH3-like domain. Exposure of the BH3-like domain confers ATR a mitochondria-specific antiapoptotic function. Interestingly, cytoATR shows little checkpoint kinase activity, most likely due to the absence of ATRIP in the cytoplasm (**Figure 5A**). In contrast, ATR in the nucleus is known to complex with ATRIP, which renders checkpoint activity. Nuclear ATR remains

predominately in the *trans*-ATR form (**Figure 5A**). Knockdown ATRIP even does not change *trans*-ATR conformation in the nucleus (Hilton et al., 2015), implying complex formation with other ATR-interacting proteins and/or chromatins might energetically favor *trans*-ATR in the nucleus to prevent ATR from forming *cis*-ATR. Other speculative possibilities also might play a role in *cis*-to-*trans* conversion in the nucleus such as nuclear transporter proteins. These transporter proteins recognize nuclear import signal (NLS) sequences and can interact with nucleoporins to help NLS-containing proteins reach the nucleus through nuclear pore complexes (NPCs). Nuclear transporter proteins recognize sequences starting with a proline (P) and are followed by an amino acid sequence containing three to five basic residues (Lu et al., 2021). The ATR-predicted nuclear transport signal resides within the isomerization domain ($^{429}$PKRRR$^{433}$). Furthermore, although Pin1 is not involved in the nuclear ATR isomerization (Hilton et al., 2015), other types of isomerases might be involved. Finally, it is worth noting that the nuclear ATR-S428A protein shifting to *trans*-ATR is likely caused by the same mechanism that maintains wild-type ATR in the *trans*-isoform in the nucleus, and the process is probably phosphorylation-independent. ATR-S428A was generated only to make ATR phosphorylation-deficient at S428 so that Pin1 whose activity depends on the phosphorylation cannot convert *cis*-ATR to *trans*-ATR in the cytoplasm. While determination of the mechanisms is of great interest, it is out of the scope of the current study and subjected to future investigation.

In particular, our results support a structural alteration around the BH3 domain of ATR (**Figure 2B**, **Supplementary Table S1**) between *trans* and *cis*/WT ATR, making the BH3 domain in *cis*/WT ATR accessible to biotin modification and, thus, likely available for protein–protein interactions including ATR–tBid interaction (Hilton et al., 2015). In addition, conformational changes may also occur involving the N-HEAT and FAT domains.

Earlier studies showed that localization of ATR to mitochondria may occur through the binding of ATR-H to mitochondria-bound tBid *via* ATR's BH3-like domain. The binding of ATR-H to tBid leads to tBid sequestration, serving a role in preventing Bax/Bak activation. The interaction of the tBid's BH3 domain with antiapoptotic Bcl-XL protein reportedly involves the BH3, BH1, and BH2 domains from Bcl-XL by a BH3-in-groove mechanism (Chou et al., 1999; Czabotar et al., 2013). In this study, employing the protein footprinting approach, we have mapped the surface topology of *cis/trans* ATR isomers and identified two biotin-modifiable surface lysine residues around the BH3 domain at position Lys-459 and Lys-469 in the *cis*-ATR isoform (ATR-H), but the same residues are inaccessible in *trans*-ATR (**Figures 2C**, **Figure 3**). This suggests that in *cis*-ATR, the BH3 domain undergoes a conformational change which favors ATR–tBid interaction at mitochondria, which is further supported by coimmunoprecipitation and proximity ligation assays (**Figures 3D,E**).

Our mass footprinting data also reveal possible conformational changes involving N-terminal HEAT repeats (N-HEAT) and FAT domains between *trans*- and *cis*-ATR isoforms (**Figures 2B,C**). Interestingly, the middle HEAT domains (M-HEAT) in both *cis*- and *trans*-ATR remain intact after tryptic digestion (**Figure 2B**) and are not, or at least not significantly, involved in the conformational change as there were no differential biotin modifications between the M-HEAT domains of these two isomers. In contrast, the N-HEAT and FAT domains of *trans*-ATR are much more surface accessible than the same domains of *cis*-ATR (**Figure 2C**). Given that the M-HEAT domain remains the same for both isomers, a possible scenario is that in *cis*-ATR, parts of the N-HEAT and FAT domains undergo conformation changes by being folded toward each other in close contact around the M-HEAT domain, so that parts of the original accessible surface residues in both N-HEAT and FAT domains in *trans*-ATR now become inaccessible (biotin-unmodifiable). The conformational changes also may expose the hidden BH3 domain.

ATR checkpoint function is dependent on ATR–ATRIP hetero-dimeric complex formation. Through mass footprinting and coimmunoprecipitation analyses, we found that even for mitochondrial function, *cis*-ATR maintains a dimeric state *via* direct homo-dimerization of its C-terminal domains, without the involvement of ATRIP. Now one question may arise whether conformation change of *cis*-ATR diminished ATR–ATRIP complex formation in the cytoplasm. Since there is no or very little ATRIP present in the cytoplasm, it is not possible to experimentally ascertain whether *cis*-ATR can form a *cis*-ATR–ATRIP complex in the cytoplasm.

Mass footprinting data identified two interesting lysine modifications at residue 1994 which is near the ATR auto-catalytic site T1989 and another within the ATR kinase domain at residue 2,413 in *trans*-ATR but not in *cis*-ATR (**Figure 2C**). This suggests a differential conformation between *cis*- and *trans*-ATR around the FAT and kinase domains, which may affect the kinase activity of ATR. As nuclear ATR always remains in the *trans*-isoform and is ATR kinase active, it is possible that *cis*-ATR may not be kinase-active due to these structural alterations in addition to the absence of cytoplasmic ATRIP. Interestingly, we observed identical kinase activity and autophosphorylation at T1989 for all nuclear ATR WT and mutant proteins (**Figures 5A,B**). This is consistent with the fact that all nuclear ATR proteins are *trans*-ATR regardless of their state in the cytoplasm, which is also true for the ATR-S428A mutant. This may be due to the nuclear interaction with ATRIP and other ATR activator proteins, which force ATR-S428A to undergo a conformational conversion to *trans*-ATR.

Our findings provide a useful insight into how ATR regulates the mitochondrial cell death pathway and the nuclear DNA damage-signaling pathway by switching ATR between its *cis* and *trans* isomerization states.

## DATA AVAILABILITY STATEMENT

The mass spectrometry-based proteomics datasets presented in this study can be found in online repositories (Deutsch et al., 2019; Perez-Riverol et al., 2022). The names of the repository/repositories and accession number(s) can be found at: available *via* ProteomeXchange with identifier PXD031385 and 10.6019/PXD031385.

## AUTHOR CONTRIBUTIONS

HB performed most of the experiments, and S-JZ conducted most of the molecular modeling and computational biology analysis. YM, JB, and PM performed part of the experiments or computational analyses. HB wrote the draft on experimental part of the manuscript and J-YL on the computational work. PM participated in the earlier stage of the study design and manuscript preparation. HB, YZ, and J-YL performed data analyses. J-YL oversaw and directed the computational determination and related structure analyses. YZ oversaw and directed the entire study through the manuscript preparation.

## FUNDING

This work was supported by the National Institutes of Health under grants R01CA219342 to YZ and R01GM127656 to J-YL.

## ACKNOWLEDGMENTS

We are grateful to Paul Nghiem (University of Washington Medical Center) for providing the recombinant FLAG-tagged ATR expression construct. We also thank David Cortez (Vanderbilt University) for the generous gift of Myc-tagged ATR and Myc-HA-tagged ATRIP expression constructs. The authors wish to acknowledge the Ohio Supercomputer Center, Columbus OH (http://osc.edu/ark:/19495/f5s1ph73), for providing CPU time and tech support.

## SUPPLEMENTARY MATERIAL

The Supplementary Material for this article can be found online at: https://www.frontiersin.org/articles/10.3389/fcell.2022.826576/full#supplementary-material

## REFERENCES

Abraham, R. T. (2004). PI 3-kinase Related Kinases: 'big' Players in Stress-Induced Signaling Pathways. *DNA repair* 3, 883–887. doi:10.1016/j.dnarep.2004.04.002

Ball, H. L., Myers, J. S., and Cortez, D. (2005). ATRIP Binding to Replication Protein A-Single-Stranded DNA Promotes ATR-ATRIP Localization but Is Dispensable for Chk1 Phosphorylation. *MBoC* 16, 2372–2381. doi:10.1091/mbc.e04-11-1006

Bennett, K. L., Matthiesen, T., and Roepstorff, P. (2000). Probing Protein Surface Topology by Chemical Surface Labeling, Crosslinking, and Mass Spectrometry. *Methods Mol. Biol.* 146, 113–131. doi:10.1385/1-59259-045-4:113

Burrows, A. E., and Elledge, S. J. (2008). How ATR Turns on: TopBP1 Goes on ATRIP with ATR: Figure 1. *Genes Dev.* 22, 1416–1421. doi:10.1101/gad.1685108

Case, D. A., Cheatham, T. E., III, Darden, T., Gohlke, H., Luo, R., Merz, K. M., et al. (2005). The Amber Biomolecular Simulation Programs. *J. Computat. Chem.* 26, 1668–1688.

Chou, J. J., Li, H., Salvesen, G. S., Yuan, J., and Wagner, G. (1999). Solution Structure of BID, an Intracellular Amplifier of Apoptotic Signaling. *Cell* 96, 615–624. doi:10.1016/s0092-8674(00)80572-3

Ciccia, A., and Elledge, S. J. (2010). The DNA Damage Response: Making it Safe to Play with Knives. *Mol. Cell* 40, 179–204. doi:10.1016/j.molcel.2010.09.019

Cortez, D., Guntuku, S., Qin, J., and Elledge, S. J. (2001). ATR and ATRIP: Partners in Checkpoint Signaling. *Science* 294, 1713–1716. doi:10.1126/science.1065521

Czabotar, P. E., Westphal, D., Dewson, G., Ma, S., Hockings, C., Fairlie, W. D., et al. (2013). Bax Crystal Structures Reveal How BH3 Domains Activate Bax and Nucleate its Oligomerization to Induce Apoptosis. *Cell* 152, 519–531. doi:10.1016/j.cell.2012.12.031

Deutsch, E. W., Bandeira, N., Sharma, V., Perez-Riverol, Y., Carver, J. J., Kundu, D. J., et al. (2019). The ProteomeXchange Consortium in 2020: Enabling 'big Data' Approaches in Proteomics. *Nucleic Acids Res.* 48, D1145–D1152. doi:10.1093/nar/gkz984

Falck, J., Coates, J., and Jackson, S. P. (2005). Conserved Modes of Recruitment of ATM, ATR and DNA-PKcs to Sites of DNA Damage. *Nature* 434, 605–611. doi:10.1038/nature03442

Fischer, G., Bang, H., and Mech, C. (1984). Determination of Enzymatic Catalysis for the Cis-Trans-Isomerization of Peptide Binding in Proline-Containing Peptides. *Biomed. Biochim. Acta* 43, 1101–1111.

Fischer, G., and Schmid, F. X. (1990). The Mechanism of Protein Folding. Implications of *In Vitro* Refolding Models for De Novo Protein Folding and Translocation in the Cell. *Biochemistry* 29, 2205–2212. doi:10.1021/bi00461a001

Fiser, A., Do, R. K. G., and Šali, A. (2000). Modeling of Loops in Protein Structures. *Protein Sci.* 9, 1753–1773. doi:10.1110/ps.9.9.1753

Hilton, B. A., Li, Z., Musich, P. R., Wang, H., Cartwright, B. M., Serrano, M., et al. (2015). ATR Plays a Direct Antiapoptotic Role at Mitochondria, Which Is Regulated by Prolyl Isomerase Pin1. *Mol. Cell* 60, 35–46. doi:10.1016/j.molcel.2015.08.008

Hinderaker, M. P., and Raines, R. T. (2003). An Electronic Effect on Protein Structure. *Protein Sci.* 12, 1188–1194. doi:10.1110/ps.0241903

Liu, J.-Y., Li, Z., Li, H., and Zhang, J.-T. (2011). Critical Residue that Promotes Protein Dimerization: A Story of Partially Exposed Phe25 in 14-3-3σ. *J. Chem. Inf. Model.* 51, 2612–2625. doi:10.1021/ci200212y

Liu, S., Shiotani, B., Lahiri, M., Maréchal, A., Tse, A., Leung, C. C. Y., et al. (2011). ATR Autophosphorylation as a Molecular Switch for Checkpoint Activation. *Mol. Cell* 43, 192–202. doi:10.1016/j.molcel.2011.06.019

Lu, J., Wu, T., Zhang, B., Liu, S., Song, W., Qiao, J., et al. (2021). Types of Nuclear Localization Signals and Mechanisms of Protein Import into the Nucleus. *Cell Commun. Signal* 19, 60. doi:10.1186/s12964-021-00741-y

Ma, K., Wu, H., Li, P., and Li, B. (2018). LC3-II May Mediate ATR-Induced Mitophagy in Dopaminergic Neurons through SQSTM1/p62 Pathway. *Acta Biochimica Biophysica Sinica* 50, 1047–1061. doi:10.1093/abbs/gmy091

Makinwa, Y., Cartwright, B. M., Musich, P. R., Li, Z., Biswas, H., and Zou, Y. (2020). PP2A Regulates Phosphorylation-dependent Isomerization of Cytoplasmic and Mitochondrial-Associated ATR by Pin1 in DNA Damage Responses. *Front. Cell Dev. Biol.* 8, 813. doi:10.3389/fcell.2020.00813

Makinwa, Y., Musich, P. R., and Zou, Y. (2020). Phosphorylation-Dependent Pin1 Isomerization of ATR: Its Role in Regulating ATR's Anti-apoptotic Function at Mitochondria, and the Implications in Cancer. *Front. Cell Dev. Biol.* 8, 281. doi:10.3389/fcell.2020.00281

Mordes, D. A., and Cortez, D. (2008). Activation of ATR and Related PIKKs. *Cell Cycle* 7, 2809–2812. doi:10.4161/cc.7.18.6689

Mordes, D. A., Glick, G. G., Zhao, R., and Cortez, D. (2008). TopBP1 Activates ATR through ATRIP and a PIKK Regulatory Domain. *Genes Dev.* 22, 1478–1489. doi:10.1101/gad.1666208

Musich, P. R., Li, Z., and Zou, Y. (2017). Xeroderma Pigmentosa Group A (XPA), Nucleotide Excision Repair and Regulation by ATR in Response to Ultraviolet Irradiation. *Adv. Exp. Med. Biol.* 996, 41–54. doi:10.1007/978-3-319-56017-5_4

Nam, E. A., and Cortez, D. (2011). ATR Signalling: More Than Meeting at the Fork. *Biochem. J.* 436, 527–536. doi:10.1042/bj20102162

Nam, E. A., Zhao, R., Glick, G. G., Bansbach, C. E., Friedman, D. B., and Cortez, D. (2011). Thr-1989 Phosphorylation Is a Marker of Active Ataxia Telangiectasia-Mutated and Rad3-Related (ATR) Kinase. *J. Biol. Chem.* 286, 28707–28714. doi:10.1074/jbc.m111.248914

Perez-Riverol, Y., Bai, J., Bandla, C., García-Seisdedos, D., Hewapathirana, S., Kamatchinathan, S., et al. (2022). The PRIDE Database Resources in 2022: a Hub for Mass Spectrometry-Based Proteomics Evidences. *Nucleic Acids Res.* 50, D543–d552. doi:10.1093/nar/gkab1038

Pettersen, E. F., Goddard, T. D., Huang, C. C., Couch, G. S., Greenblatt, D. M., Meng, E. C., et al. (2004). UCSF Chimera?A Visualization System for Exploratory Research and Analysis. *J. Comput. Chem.* 25, 1605–1612. doi:10.1002/jcc.20084

R Core Team (2021). *R: A Language and Environment for Statistical Computing*. Vienna, Austria: R Foundation for Statistical Computing.

Rao, Q., Liu, M., Tian, Y., Wu, Z., Hao, Y., Song, L., et al. (2018). Cryo-EM Structure of Human ATR-ATRIP Complex. *Cell Res.* 28, 143–156. doi:10.1038/cr.2017.158

Saldivar, J. C., Cortez, D., and Cimprich, K. A. (2017). The Essential Kinase ATR: Ensuring Faithful Duplication of a Challenging Genome. *Nat. Rev. Mol. Cell Biol.* 18, 622–636. doi:10.1038/nrm.2017.67

Sancar, A., Lindsey-Boltz, L. A., Ünsal-Kaçmaz, K., and Linn, S. (2004). Molecular Mechanisms of Mammalian DNA Repair and the DNA Damage Checkpoints. *Annu. Rev. Biochem.* 73, 39–85. doi:10.1146/annurev.biochem.73.011303.073723

Shell, S. M., Li, Z., Shkriabai, N., Kvaratskhelia, M., Brosey, C., Serrano, M. A., et al. (2009). Checkpoint Kinase ATR Promotes Nucleotide Excision Repair of UV-Induced DNA Damage via Physical Interaction with Xeroderma Pigmentosum Group A. *J. Biol. Chem.* 284, 24213–24222. doi:10.1074/jbc.m109.000745

Shiloh, Y. (2003). ATM and Related Protein Kinases: Safeguarding Genome Integrity. *Nat. Rev. Cancer* 3, 155–168. doi:10.1038/nrc1011

Tibbetts, R. S., Brumbaugh, K. M., Williams, J. M., Sarkaria, J. N., Cliby, W. A., Shieh, S.-Y., et al. (1999). A Role for ATR in the DNA Damage-Induced Phosphorylation of P53. *Genes & Dev.* 13, 152–157. doi:10.1101/gad.13.2.152

Wu, X., Shell, S. M., Liu, Y., and Zou, Y. (2007). ATR-dependent Checkpoint Modulates XPA Nuclear Import in Response to UV Irradiation. *Oncogene* 26, 757–764. doi:10.1038/sj.onc.1209828

Zhou, B.-B. S., and Elledge, S. J. (2000). The DNA Damage Response: Putting Checkpoints in Perspective. *Nature* 408, 433–439. doi:10.1038/35044005

Zimmerman, S. S., and Scheraga, H. A. (1976). Stability of Cis, Trans, and Nonplanar Peptide Groups. *Macromolecules* 9, 408–416. doi:10.1021/ma60051a005

Zou, L., and Elledge, S. J. (2003). Sensing DNA Damage through ATRIP Recognition of RPA-ssDNA Complexes. *Science* 300, 1542–1548. doi:10.1126/science.1083430

**Conflict of Interest:** The authors declare that the research was conducted in the absence of any commercial or financial relationships that could be construed as a potential conflict of interest.

**Publisher's Note:** All claims expressed in this article are solely those of the authors and do not necessarily represent those of their affiliated organizations, or those of the publisher, the editors, and the reviewers. Any product that may be evaluated in this article, or claim that may be made by its manufacturer, is not guaranteed or endorsed by the publisher.

frontiers | Frontiers in Cell and Developmental Biology

ORIGINAL RESEARCH
published: 16 June 2022
doi: 10.3389/fcell.2022.843121

# Rad5 and Its Human Homologs, HLTF and SHPRH, Are Novel Interactors of Mismatch Repair

*Anna K. Miller[1], Guogen Mao[1], Breanna G. Knicely[1], Hannah G. Daniels[1], Christine Rahal[2], Christopher D. Putnam[2,3], Richard D. Kolodner[2,4,5,6] and Eva M. Goellner[1,7]**

[1]College of Medicine Department of Toxicology and Cancer Biology, University of Kentucky, Lexington, KY, United States, [2]Ludiwg Institute for Cancer Research San Diego, San Diego, CA, United States, [3]Department of Medicine, University of California San Diego, San Diego, CA, United States, [4]Moores-UCSD Cancer Center, San Diego, CA, United States, [5]Institute of Genomic Medicine, San Diego, CA, United States, [6]Department of Cellular and Molecular Medicine, University of California San Diego, San Diego, CA, United States, [7]Markey Cancer Center, University of Kentucky, Lexington, KY, United States

DNA mismatch repair (MMR) repairs replication errors, and MMR defects play a role in both inherited cancer predisposition syndromes and in sporadic cancers. MMR also recognizes mispairs caused by environmental and chemotherapeutic agents; however, in these cases mispair recognition leads to apoptosis and not repair. Although mutation avoidance by MMR is fairly well understood, MMR-associated proteins are still being identified. We performed a bioinformatic analysis that implicated *Saccharomyces cerevisiae* Rad5 as a candidate for interacting with the MMR proteins Msh2 and Mlh1. Rad5 is a DNA helicase and E3 ubiquitin ligase involved in post-replicative repair and damage tolerance. We confirmed both interactions and found that the Mlh1 interaction is mediated by a conserved Mlh1-interacting motif (MIP box). Despite this, we did not find a clear role for Rad5 in the canonical MMR mutation avoidance pathway. The interaction of Rad5 with Msh2 and Mlh1 is conserved in humans, although each of the Rad5 human homologs, HLTF and SHPRH, shared only one of the interactions: HLTF interacts with MSH2, and SHPRH interacts with MLH1. Moreover, depletion of SHPRH, but not HLTF, results in a mild increase in resistance to alkylating agents although not as strong as loss of MMR, suggesting gene duplication led to specialization of the MMR-protein associated roles of the human Rad5 homologs. These results provide insights into how MMR accessory factors involved in the MMR-dependent apoptotic response interact with the core MMR machinery and have important health implications into how human cells respond to environmental toxins, tumor development, and treatment choices of tumors with defects in Rad5 homologs.

**Keywords: mismatch repair (MMR), rad5, SHPRH, HLTF, alkylating agent MNNG, binding motif**

OPEN ACCESS

***Edited by:***
*Robert W. Sobol, University of South Alabama, United States*

***Reviewed by:***
*Aishwarya Prakash, University of South Alabama, United States*
*Jianfeng Li, University of South Alabama, United States*

****Correspondence:***
*Eva M. Goellner*
*egoellner@uky.edu*

***Specialty section:***
*This article was submitted to Molecular and Cellular Pathology, a section of the journal Frontiers in Cell and Developmental Biology*

***Received:*** *24 December 2021*
***Accepted:*** *16 May 2022*
***Published:*** *16 June 2022*

***Citation:***
*Miller AK, Mao G, Knicely BG, Daniels HG, Rahal C, Putnam CD, Kolodner RD and Goellner EM (2022) Rad5 and Its Human Homologs, HLTF and SHPRH, Are Novel Interactors of Mismatch Repair. Front. Cell Dev. Biol. 10:843121. doi: 10.3389/fcell.2022.843121*

## 1 INTRODUCTION

DNA mismatch repair (MMR) is the post-replicative repair pathway that repairs base-base mispairs and small insertion/deletion mispairs arising from DNA replication errors (Li, 2008; Fishel, 2015). MMR also induces apoptosis after recognizing mispairs induced by exogenous DNA damaging agents, such as $O^6$-methylguanine:thymidine mispairs that occur after exposure to $S_N1$ alkylators (Fu et al., 2012; Li et al., 2016). These lesions cannot be normally repaired by MMR as the $O^6$-methylguanine

lesion is on the template strand. Defects in the MMR result in an accumulation of mutations, which can result in altered cellular function and the development of cancers (Kolodner, 1995). Germline mutations in MMR genes are the underlying cause of the familial cancer predisposition syndrome, Lynch syndrome (Fishel et al., 1993; Lynch et al., 2015) and constitutional mismatch repair deficiency (Durno et al., 2015). Lynch syndrome predisposes individuals to several cancer types, primarily colorectal, stomach, endometrial, and ovarian cancers (de la Chapelle, 2004; Kastrinos and Stoffel, 2014), and constitutional mismatch repair deficiency is associated with many cancer types in pediatric patients (Durno et al., 2015). Somatic mutations and epigentic silencing in MMR genes are also found in a significant subset of sporadic cancers of the same subtypes (Borresen et al., 1995; Kane et al., 1997).

Mutation avoidance by eukaryotic MMR involves several steps: 1) mispair recognition by the heterodimeric MutS homologs, MSH2-MSH6 or MSH2-MSH3, 2) recruitment of the MutL homolog, MLH1-PMS2 (called Mlh1-Pms1 in *Saccharomyces cerevisiae*), 3) removal of the mispaired DNA from the daughter strand through either Exonuclease 1 (Exo1)-dependent, Rad27-dependent, or Exo1- and Rad27-independent MMR, and 4) gap-filling by the replicative polymerases, PCNA, and RFC, and 5) nick ligation (Li, 2008; Goellner et al., 2015; Fishel, 2015; Calil et al., 2021).

While the core machinery of eukaryotic DNA MMR is well defined, new MMR-interacting proteins are still being identified (Yuan et al., 2004; Li et al., 2013; Traver et al., 2015; Goellner et al., 2018; Terui et al., 2018; Rikitake et al., 2020; Calil et al., 2021). Remarkably, short peptide sequences have been identified that mediate interactions with Mlh1 (the Mlh1-interacting peptide motif or MIP box (Dherin et al., 2009)) and more recently Msh2 (the Msh2-interacting peptide motif or SHIP box (Goellner et al., 2018)). Together these motifs are involved in the interaction of *S. cerevisiae* Mlh1 with Ntg2, Sgs1, and Exo1, *S. cerevisiae* Msh2 with Exo1, Fun30, and Dpb3, and likely human MSH2 with SMARCAD1 (*S. cerevisiae* Fun30), WDHD1, and MCM9 (Dherin et al., 2009; Gueneau et al., 2013; Traver et al., 2015; Chen et al., 2016; Goellner et al., 2018). Identifying novel MMR accessory proteins and elucidating the mechanisms by which they interact with MMR will be critical to understanding mechanisms suppressing cancer development and potentially guiding cancer therapies involving DNA damaging agents.

Here we identify another novel MMR interacting partner, Rad5, that we predict to have both SHIP box and MIP box motifs. Rad5 is a helicase and E3 ubiquitin ligase involved in post-replication repair (PRR) pathways, which allow tolerance of template strand lesions that would otherwise lead to replication fork stalling (Xu et al., 2016; Gallo et al., 2019); however, Rad5 has no known role in MMR. PRR bypasses DNA template lesions via the error-prone translesion synthesis (TLS) and error-free template switching (TS) pathways (Gallo and Brown, 2019), the choice of which is in part controlled by the ubiquitination status of proliferating cell nuclear antigen (PCNA) (Gallo et al., 2019). The Rad5 E3 ligase has been associated with TS through the activity of Mms2-Ubc13-Rad5 in forming a lysine 63-linked polyubiquitination chain on PCNA (Motegi et al., 2008). However, recent studies have also identified Rad5 as a player in TLS through its interaction with the TLS protein Rev1 (Xu et al., 2016), which is consistent with the lack of epistasis of *rad5Δ* and *ubc13Δ* mutations observed in assays for genome instability (Putnam et al., 2010).

Rad5 has two known human homologs, Helicase-Like Transcription Factor (HLTF) and SNF2 Histone Linker PHD Ring Helicase (SHPRH). Both HLTF and SHPRH share the SNF2 helicase and RING finger domains with Rad5, and HLTF additionally shares the HIRAN (HIP116, Rad5 N-terminal) domain that is present N-terminal to the SNF2 helicase domain (Unk et al., 2010). Both HLTF and SHPRH have E3 ubiquitin ligase ability, both can polyubiquitinate PCNA, and HLTF can complement UV sensitivity of a *rad5Δ S. cerevisiae* strain (Unk et al., 2006; Unk et al., 2008; Masuda et al., 2012). HLTF and SHPRH also have direct but distinct roles in directing TLS- and TS-mediated PRR, and HLTF and SHPRH deletion mutants have different sensitivities to agents that cause DNA lesions (Seelinger et al., 2020). HLTF enhances TLS and inhibits SHPRH following UV damage, but MMS treatment instead causes SHPRH response and HLTF degradation (Lin et al., 2011). Loss of HLTF expression has been associated with several cancer types, including colorectal cancer (Moinova et al., 2002). Loss of SHPRH has also been associated with multiple cancers *via* 1) loss of heterozygosity of the long arm of chromosome 6, where SHPRH resides, 2) accumulation of SHPRH point mutations in melanoma and ovarian cancer-derived cell lines (Sood et al., 2003), and 3) through the protective action of a circular RNA encoding a 146 amino acid fragment of SHPRH in glioblastoma (Begum et al., 2018; Zhang et al., 2018).

In this study we confirm the predicted interactions in *S. cerevisiae* between Msh2 and Rad5 and between Mlh1 and Rad5 and verify that the Mlh1-Rad5 interaction is mediated by a MIP box. These interactions are conserved with human homologs HLTF and SHPRH. Interestingly, the Msh2-Rad5 and Mlh1-Rad5 interactions seem to have become split between the two homologs, with HLTF only binding to human MSH2 and SHPRH only binding to human MLH1. We also show that loss of SHPRH results in moderate resistance to alkylating agents. Together these data identify novel interacting partners of MMR in both yeast and humans and suggest that the SHPRH-MLH1 interaction is partially involved in an apoptotic response to damage-induced mispairs.

# 2 MATERIALS AND METHODS

## 2.1 Chemicals and Reagents

Antibodies used in this study include anti-MLH1 (Cell Signaling Technologies 3515S), MSH2 (Cell Signaling Technologies 2017S), HLTF (Fisher PA5-30173), SHPRH (Santa Cruz sc-514395), IgG (Santa Cruz sc-2025). 6-Thioguanine (6 TG) was obtained from TCI America (T0212-1G) delivered by VWR, and MNNG was obtained from Sigma-Aldrich (Cat #129941).

## 2.2 Two-Hybrid Assay

Plasmids expressing fusion proteins for yeast two-hybrid analysis were generated by Gateway cloning (Invitrogen) the gene of interest without its start codon into either the Gateway-modified bait vector, pBTM116, which encodes the LexA DNA binding domain and Trp1, or the Gateway-modified prey vector, pACT2, which encodes the GAL4 activation domain and Leu2. Bait and prey plasmids were co-transformed into the L40 *S. cerevisiae* reporter strain L40 (*MAT***a** *trp1-901 leu2-3112 his3Δ200 LYS2(4lexAop-HIS3) URA3(8lexAop-lacZ)*), in which a positive interaction of the bait and prey fusion proteins results in expression of *HIS3* and hence complementation of the *his3Δ200* mutation (Yan and Jin, 2012). Colonies were grown overnight in complete synthetic medium lacking leucine and tryptophan (CSM -Leu -Trp) to maintain plasmid selection and then 10-fold serial dilutions were spotted onto CSM -Leu -Trp control medium and CSM -Leu -Trp -His selective medium to assay for two-hybrid interactions.

## 2.3 Mutation Rate and Mutation Spectra Analysis

*S. cerevisiae* strains were grown in YPD (1% yeast extract, 2% Bacto Peptone and 2% dextrose) or in the appropriate synthetic dropout media (0.67% yeast nitrogen base without amino acids, 2% dextrose, and amino acid dropout mix at the concentration recommended by the manufacturer (US Biological) at 30 °C. All *S. cerevisiae* strains in this study were derived in the S288c strain background using standard gene deletion and pop-in, pop-out methods.

Mutator phenotypes were evaluated using the *hom3-10* frameshift reversion assay. Mutation rates were determined by fluctuation analysis using a minimum of 2 independently derived strains and 14 or more independent cultures; comparisons of mutation rates were evaluated using 95% confidence intervals.

One independent $Thr^+$ revertant was isolated per culture from fluctuation tests. Chromosomal DNA was isolated from each revertant using a Qiagen Puregene Yeast/Bact. Kit B and the *hom3-10* region were amplified by PCR using the Primer 5′-AGT TGTTTGTTGATGACTGC and Primer 5′-TTCAGAAGCTTC TTCTGGAG and sequenced with the Primer 5′-CTTTCCTGG TTCAAGCATTG using a commercial sequencing facility (Calil et al., 2021).

## 2.4 Bioinformatic Analyses

Bioinformatic analysis of potential MIP and SHIP motifs with good peptide matching scores in regions predicted to be unstructured was carried out as described previously (Goellner et al., 2018). Briefly, we determined the count of each amino acid at each position in the alignment of the SHIP boxes 1 and 2 or the MIP box from fungal Exo1 homologs. A pseudocount of 1 was added to all positions that were zero, and then the counts were converted to a fraction, $F_{k,j}$, for each amino acid $k$ at position $j$. $F_{k,j}$, values were then converted to log probabilities ($M_{k,j}$) scaled by a background model: $M_{k,j} = \log(F_{k,j}/b_k)$. The background model was calculated using the frequency of the different amino acids in the proteins encoded by the *S. cerevisiae* genome. Raw scores ($S_{raw}$) for peptides were calculated by adding up all $M_{k,j}$ values from the PSSM for each amino acid $k$ at position $j$ within the peptide sequence. We scaled the raw scores to be in the range 0–1 using the equation: $S_{scale} = (S_{raw} - S_{\min})/(S_{\max} - S_{\min})$, where $S_{\min}$ and $S_{\max}$ are the minimum and maximum scores possible for any peptide scored by the PSSM. The long-term disorder prediction score for each position in the proteins were generated using IUPRED (Dosztanyi et al., 2005), and the disorder prediction score for each peptide was calculated by averaging the scores for each of the residues in the peptide.

Identification of Rad5 homologs for the analysis of the conservation of the candidate MIP and SHIP motifs was performed by categorizing BLAST hits from each species by building a phylogenetic tree with MAFFT version 7.305 (Katoh and Standley, 2014) and PHYLIP version 3.696 (Retief, 2000) that contained all of the BLAST hits from that species with all of the *S. cerevisiae* Rad5 homologs (Chd1, Fun30, Ino80, Irc20, Irc5, Isw1, Isw2, Mot1, Rad16, Rad26, Rad5, Rad54, Rdh54, Snf2, Sth1, Swr1, and Uls1). Homologs were then assigned if the BLAST hit was on the same branch as the phylogram as only one of the *S. cerevisiae* reference sequences using the program idwtree (Goellner et al., 2018). Alignments of assigned fungal Rad5 homologs were then performed with MAFFT for analyzing conservation and building sequence logos with Seq2Logo (Thomsen and Nielsen, 2012).

## 2.5 Cell Culture

All cell lines were cultured at 5% $CO_2$ and 37°C. Hek293 and Hek293T cells were cultured in DMEM supplemented with 10% FBS (Gibco Life Technologies Corporation) and 1% Penicillin/Streptomycin (Gibco, Life Technologies). HeLa S3 cells were cultured in RPMI supplemented with 10% FBS and 1% Penicillin/Streptomycin.

## 2.6 Generation of Knockout Lines

HeLa MLH1, MSH2, HLTF, and SHPRH knockout cell lines and the HLTF and SHPRH double knockout cell line were generated by CRISPR-Cas9 technologies, using single guide RNA (sgRNA) sequences (**Table 1**) for each of the genes listed. The LentiCRISPRv2 was a gift from Feng Zhang (Addgene plasmid #52961). The plasmid was digested with BsmBI and gel purified using the QIAquick PCR purification kit according to the manufacturer's instructions. Complementary oligonucleotides (synthesized by Integrated DNA Technologies) encoding the sgRNA were then annealed and cloned into LentiCRISPRv2. Cells were then transfected with Lipofectamine 3000 (Thermo Scientific L3000008) and the cells were selected with puromycin (Promega). Single cell clones were allowed to grow up under puromycin selection and expanded. Loss of protein expression was confirmed for each clone using SDS-PAGE and western blot analysis.

## 2.7 Short-Term Cytotoxicity Assay

HEK293 cells were plated at 750,000 cells/well in a 6-well plate 24 h prior to transfection. Cells were transfected with siHLTF (Origene) or siSHPRH (Origene) alone or in combination utilizing the Lipofectamine RNAiMAX Transfection Reagent

**TABLE 1 |** sgRNA sequences for knockout cell line generation.

| Name | Forward Primer | Reverse primer |
|---|---|---|
| sgHLTF+2 | 5′-CACCGGTTGGACTACGCTATTACAC-3′ | 5′-AAACGTGTAATAGCGTAGTCCAACC-3′ |
| sgSHPRH +1 | 5′-CACCGCTGGAGGAGCACGTTTCCGT-3′ | 5′-AAACACGGAAACGTGCTCCTCCAGC-3′ |
| sgSHPRH -2 | 5′-CACCGTTGTGACAAGGGTATTCTGG-3′ | 5′-AAACCCAGAATACCCTTGTCACAAC-3′ |
| sgMLH1 -1 | 5′-CACCGTGATAGCATTAGCTGGCCGC-3′ | 5′-AAACGCGGCCAGCTAATGCTATCAC-3′ |
| sgMSH2 +4 | 5′-CACCGCTTCTATACGGCGCACGGCG-3′ | 5′-AAACCGCCGTGCGCCGTATAGAAGC-3′ |

(Invitrogen). After transfection for 24 h, the cells were seeded at 10,000 cells/well in 96-well plates, and the remaining cells were collected for protein analysis. Media was removed 24 h after seeding and cells were treated with the indicated doses of MNNG for 1 h. The media was then replaced and allowed to grow for 72 h, at which time cell viability was measured using the CellTiter 96 Aqueous One Solution Cell Proliferation Assay (MTS) kit (Promega) according to the manufacturer's instructions.

## 2.8 Long-Term Clonogenic Cytotoxicity Assay

HEK293 or HeLa S3 cells were plated in a 6-well plate 24 h prior to treatment. Cells were pre-treated with 10 μM $O^6$-benzylguanine (6-(benzyloxy-7H-purin-2-amine, Thermo Scientific, H60274-MD) for 2 h and then pulsed with MNNG or DMSO vehicle control for 1 h. Cells were then trypsinized and plated in a 6-well plate at a density of 300 cells/well for HeLa or 3,000 cells/well for HEK293 with normal media and were allowed to grow for 10 days, or until colonies of approximately 50 cells could be seen. The cells were then stained with crystal violet and the number of colonies were counted.

## 2.9 Nuclear Protein Extraction

Cells were washed with PBS, resuspended in cytoplasm extract buffer (20 mM Hepes, 10 mM KCl, 0.1 mM EDTA, 1 mM DTT, and protease inhibitor) and then chilled on ice for 10 min. 0.75% Nonidet P-40 (NP-40) lysis buffer was added and the solution was pipetted to mix followed by vortex mixing for 10 s. The cells were centrifuged at 800 x g for 3 min at 4°C to separate nuclei from cytoplasm (supernatant). The cytoplasm extract was placed in a separate tube and the nuclei pellet was resuspended in 25% sucrose/cytoplasm extraction buffer and pipetted to disperse. The cells in 25% sucrose/cytoplasm extraction buffer were underlaid with half the volume of 50% sucrose/cytoplasm extraction buffer and centrifuged at 10,000 x g for 15 min at 4°C. The supernatant was removed, and the nuclei pellet was lysed in PBE150Na (50 mM Tris-HCl at pH 7.5, 1 mM ethylenediaminetetraacetic acid (EDTA) at pH 8.0, 150 mM NaCl, 0.5% sodium deoxycholate and 1% NP-40, containing 1x complete protease inhibitor cocktail (Roche Diagnostics GmbH, Germany)). The pellet was then sonicated and centrifuged at 10,000 x g for 15 min at 4°C. The supernatant was collected as the nuclear extract.

## 2.10 Immunoprecipitation

Co-immunoprecipitations of endogenous or tagged proteins were performed using magnetic protein A/protein G beads (Thermo Scientific) followed by a conjugation step to either the IgG control or antibody of interest with BSA for 2 h followed by washes. Conjugated beads were incubated with whole cell lysate or nuclear extracts (described above) at 4°C overnight rotating followed by increasing salt washes. Beads were boiled with 6x loading buffer and samples were run on SDS-PAGE gels followed by western blot.

## 2.11 HPRT Mutagenesis Assay

The HPRT forward mutagenesis assay was performed in HeLa S3 and HeLa S3 knockout cells as described previously (Li et al., 2013). Cell lines were first cultured in hypoxanthine, aminopterin, and thymidine (HAT) supplemented media (ThermoFisher Scientific, supplied as 50x supplement) for at least five passages to clear background HPRT mutations. HAT passaged cells were seeded at $5 \times 10^5$ cells per 100 mm dish in triplicate, allowed to adhere overnight, then treated with 5 μM 6-thioguanine (6-TG). Plating efficiency of the cells was determined by culturing $5 \times 10^2$ HAT passaged cells per 100 mm dish plated in triplicate in the absence of 6-TG. The media was replaced every 2 to 3 days. After 10 days of culturing cell colonies were stained with 0.5% crystal violet in 25% methanol and the colonies containing more than 50 cells were counted. Mutation frequency was determined by calculating the median for mutant cells (number 6-TG selected colonies/$5 \times 10^5$ cells plated) and the median for plating efficiency (number untreated colonies/$5 \times 10^2$ cells plated) and dividing mutation by plating efficiency for each cell line.

## 2.12 Cell Synchronization

Cell synchronization was conducted by performing a double thymidine block in HeLa cells. The protocol for double thymidine block was adapted from a previous publication (Schroering and Williams, 2008). HeLa cells were plated and after 1 day, washed once with warmed PBS and cultured in complete medium containing 2 μM thymidine (Sigma T9250) for 18 h. The HeLa cells were washed twice with warmed PBS and released in media without thymidine for 9 h. The cells were then cultured with 2 μM thymidine for 16 h, washed once with warmed PBS and replaced with fresh media for collection at each of the times indicated for each figure. For treated cells, cells were released into complete media containing 0.2 μM MNNG or DMSO containing $O^6$-benzylguanine.

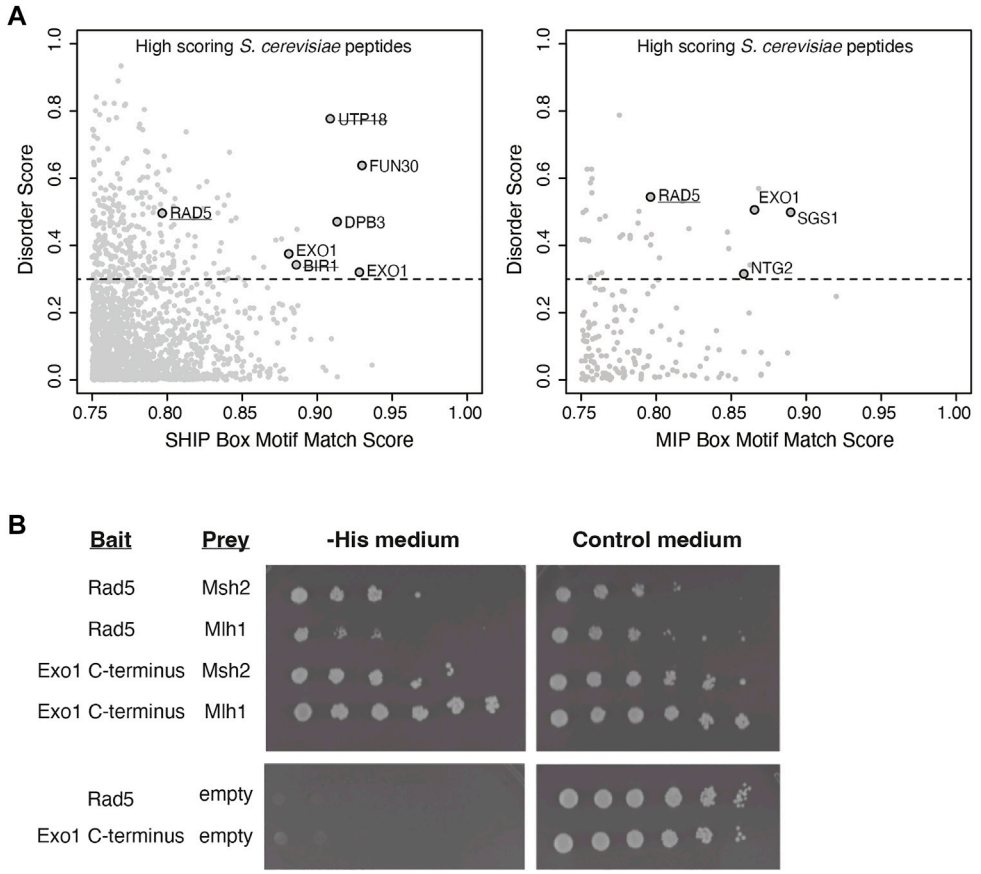


**FIGURE 1 |** Rad5 has a predicted MIP and SHIP box and interacts with Mlh1 and Msh2. **(A)** The match score of 1,745 peptides from the nuclear *S. cerevisiae* proteome with a moderate or good motif matching to either the MIP or SHIP box motif as determined from bioinformatic analysis using a position-specific scoring matrix (PSSM) are plotted against their long-range disorder predicted by IUPRED (Dosztanyi et al., 2005). Rad5 was identified in analysis for both MIP and SHIP motifs. **(B)** Yeast two-hybrid analysis shows both Msh2 and Mlh1 prey constructs interact with Rad5 bait (growth on–Leu–Trp–His selective medium as well growth on the control–Leu–Trp medium). Exo1-C terminus bait shows positive interactions with Msh2 and Mlh1 prey as a positive control. Neither Rad5 or Exo1-C terminus bait constructs autoactivate in the presence of an empty prey vector.

## 2.13 Cell Cycle Analysis

After cell synchronization using the double thymidine block, cells were trypsinized and quenched with media then centrifuged at 2,000 rpm for 5 min. The cells were then resuspended in 75% ethanol for at least 1 h at −20°C for fixation. The cells were centrifuged at 4,000 rpm for 2 min and then resuspended in PBS containing 0.25% Triton X-100 for 15 min. Cells were centrifuged at 4,000 rpm for 2 min and resuspended in PBS containing 10 μg/ml RNase A (Qiagen) and Propidium Iodide Ready Flow Reagent (ThermoFisher Scientific). Subsequent detection of the cell cycle phase distribution was accomplished by using propidium iodide for nuclear staining and detection using the BD FACSymphony A3 flow cytometer and collecting FSC, SSC, PE for propidium iodide, and BB515 for compensation with gating for single cells. The resulting data was analyzed by FlowJo software.

## 2.14 Statistical Analysis

Calculations of the mean, standard error, statistical analysis, and comparison of each set of experimental means was performed with Graphpad Prism 9.0 (Graphpad Software Inc., La Jolla, CA, United States ).

# 3 RESULTS

## 3.1 Rad5 Physically Interacts With Yeast Mlh1 and Msh2

To identify candidate MMR-interacting proteins, we computationally screened the *S. cerevisiae* proteome for proteins containing sequences resembling MIP and SHIP box motifs following our previous strategy that identified the Msh2-interacting and SHIP box-containing proteins Fun30 and Dpb3 (Goellner et al., 2018). First, the MIP motif match score and the SHIP motif match score were calculated for every 7 amino acid peptide computationally generated from the *S. cerevisiae* S288c proteome using a position-specific scoring matrix (PSSM (Stormo et al., 1982)) derived from an alignment of 301 fungal Exo1 MIP box sequences and a PSSM from an alignment of 566 fungal Exo1 SHIP box sequences. Second, high-scoring hits were filtered for proteins known to be in the nucleus or with an unknown

cellular localization. Third, the average disorder score for each peptide was determined by the averaging the long-range disorder score for the 7 amino acids of the peptides after analysis of the relevant proteins for long-range disorder with IUPRED (Dosztanyi et al., 2005). The motif match scores were then plotted against the average disorder scores (**Figure 1A**) to identify candidate peptides that matched the MIP box consensus or the SHIP box consensus and that were in disordered protein regions. These analyses identified proteins containing known functional MIP boxes (Exo1, Ntg2, Sgs1) and known functional SHIP boxes (Exo1, Fun30, Dpb3) in unstructured protein regions as well as high scoring SHIP box-like peptides in proteins previously demonstrated as not interacting with Msh2 (Utp18, Bir1) (**Figure 1A** (Goellner et al., 2018)). These analyses also implicated a candidate MIP box sequence and a candidate SHIP box sequence in the Rad5 protein.

Because this analysis suggested that Rad5 resembled Exo1, which also has both MIP and SHIP box motifs and uses both of these motifs for recruitment to MMR (Goellner et al., 2018), we sought to confirm the predicted Rad5 interactions using yeast two-hybrid analysis. We generated a bait plasmid containing *S. cerevisiae* Rad5 fused to the LexA DNA-binding domain. This plasmid, a positive control bait plasmid encoding the Exo1 C-terminus fused to LexA, or a negative control empty bait plasmid encoding only the LexA DNA-binding domain were then cotransformed into the *S. cerevisiae* tester strain L40 with prey plasmids that encoded *S. cerevisiae* Mlh1 or Msh2 fused to the Gal4 transcriptional activation domain. In the L40 tester strain, physical interaction between the bait and prey proteins drives expression of the *HIS3* gene and hence supports growth on medium lacking histidine. As expected, the yeast two-hybrid analysis revealed an interaction between the Exo1 C-terminus and both the Mlh1 and Msh2 prey vectors. The Rad5 bait plasmid also supported growth on -His medium in combination with both the Mlh1 and Msh2 prey vectors, but not the empty prey vector (**Figure 1B**), indicating that Rad5 can interact with both Mlh1 and Msh2.

## 3.2 Rad5 Binds to Mlh1 Through the MIP Box Motif

To gain insight into the Rad5 interactions with Mlh1 and Msh2, we sought to determine if these interactions were mediated through the predicted MIP box (peptide 7-EERKRFF-13) and the predicted SHIP box (peptide 30-NKESFLF-36), which are in the unstructured N-terminus of Rad5 (**Figures 2A,C**). Analysis of the conservation of these predicted motifs revealed that the predicted MIP box is extensively conserved in all fungi, whereas the predicted SHIP box is restricted to fungi in the order Saccharomycetales, which includes *S. cerevisiae* (**Figure 2B**). We and others have previously shown that mutating the conserved phenylalanine and tyrosine amino acids in these motifs to alanine disrupts the ability of these motifs to mediate interactions (Dherin et al., 2009; Goellner et al., 2018). We therefore mutated the predicted Rad5 MIP motif 7-EERKRFF-13 to 7-EERKRAA-13 (Rad5-MIPΔ) and the predicted SHIP motif 30-NKESFLF-36 to 30-NKESALA-36 (Rad5-SHIPΔ) in our Rad5 yeast two-hybrid bait plasmid. Yeast two-hybrid analysis demonstrated that the Rad5-MIPΔ mutant binds to Msh2 but not to Mlh1, indicating the Rad5-Mlh1 interaction, but not the Rad5-Msh2 interaction, is mediated by the predicted MIP box motif (**Figure 2D**). In contrast, the Rad5-SHIPΔ mutant bound to both Mlh1 and Msh2 (**Figure 2D**), indicating that the Rad5-Msh2 interaction involves another region of Rad5, an extended SHIP box that requires additional mutations to disrupt, or redundant interactions with either the putative SHIP box or another region of Rad5.

## 3.3 Loss of *RAD5* Causes a Minor Increase in Mutation Rate and a Mutation Spectrum That Is Not Representative of That Caused by a MMR Defect

Given that Rad5 binds to Msh2 and Mlh1, we investigated if loss of *RAD5* gave rise to a MMR defect in the absence of DNA damage by determining the mutation rate of a *RAD5* deletion strain with the *hom3-10* frameshift reversion assay. In the *hom3-10* assay, -1 frameshift mutations restore growth on medium lacking threonine. An *MSH2* deletion strain, which is completely deficient for MMR, had a 336-fold increase in mutation rate over the wild-type strain. However, the *rad5Δ* strain only had a 2.5-fold increase in mutation rate (**Table 2**). To determine whether this modest rate increase was representative of a defect in the canonical mutation avoidance MMR pathway, the *HOM3* gene was sequenced for 14–37 reversion isolates from each genotype (**Figure 3A**). MMR deficient strains result in almost entirely T7 → T6 frameshifts (Tishkoff et al., 1997; Flores-Rozas and Kolodner, 1998; Calil et al., 2021)), and consistent with this, 100% of the revertants from the *msh2Δ* strain were T7 → T6 frameshifts (**Figure 3B**). The wild type revertants had a wider variety of frameshift reversion mutations (only 65% T7 → T6 frameshifts), although at a much lower rate of occurrence (**Figure 3B**). The *RAD5* deletion strain had a mutation spectrum more similar to the wild-type strain with even more kinds of frameshifts observed (only 39% T7 → T6 frameshifts), which may reflect roles of *RAD5* in PRR and not MMR. Together these data suggest that loss of *RAD5* does not have a strong influence on canonical mutation avoidance pathway of MMR during unperturbed growth consistent with previous results (Johnson et al., 1992).

## 3.4 Human Homologs of Rad5, HLTF and SHPRH, Have Split Binding Between MSH2 and MLH1

To test whether the interactions identified between Rad5 and the MMR proteins are conserved in humans, we used co-

**TABLE 2 |** *hom3-10* reversion rates.

| Genotype | Strain | hom3-10 reversion rate |
|---|---|---|
| Wild type | RDKY6677 | 7.50 [4.61–8.95] x $10^{-9}$ (1) |
| *msh2Δ* | RDKY6696 | 2.52 [1.72–3.04] x $10^{-6}$ (336) |
| *rad5Δ* | RDKY6898 | 1.84 [1.27–3.06] x$10^{-8}$ (2.5) |

*Reported rates are the median rates with 95% confidence interval in square brackets. Fold increase in mutation rate is listed in parenthesis as compared to the wild-type strain. n = 14–57 independent cultures from two independently derived isolates.*

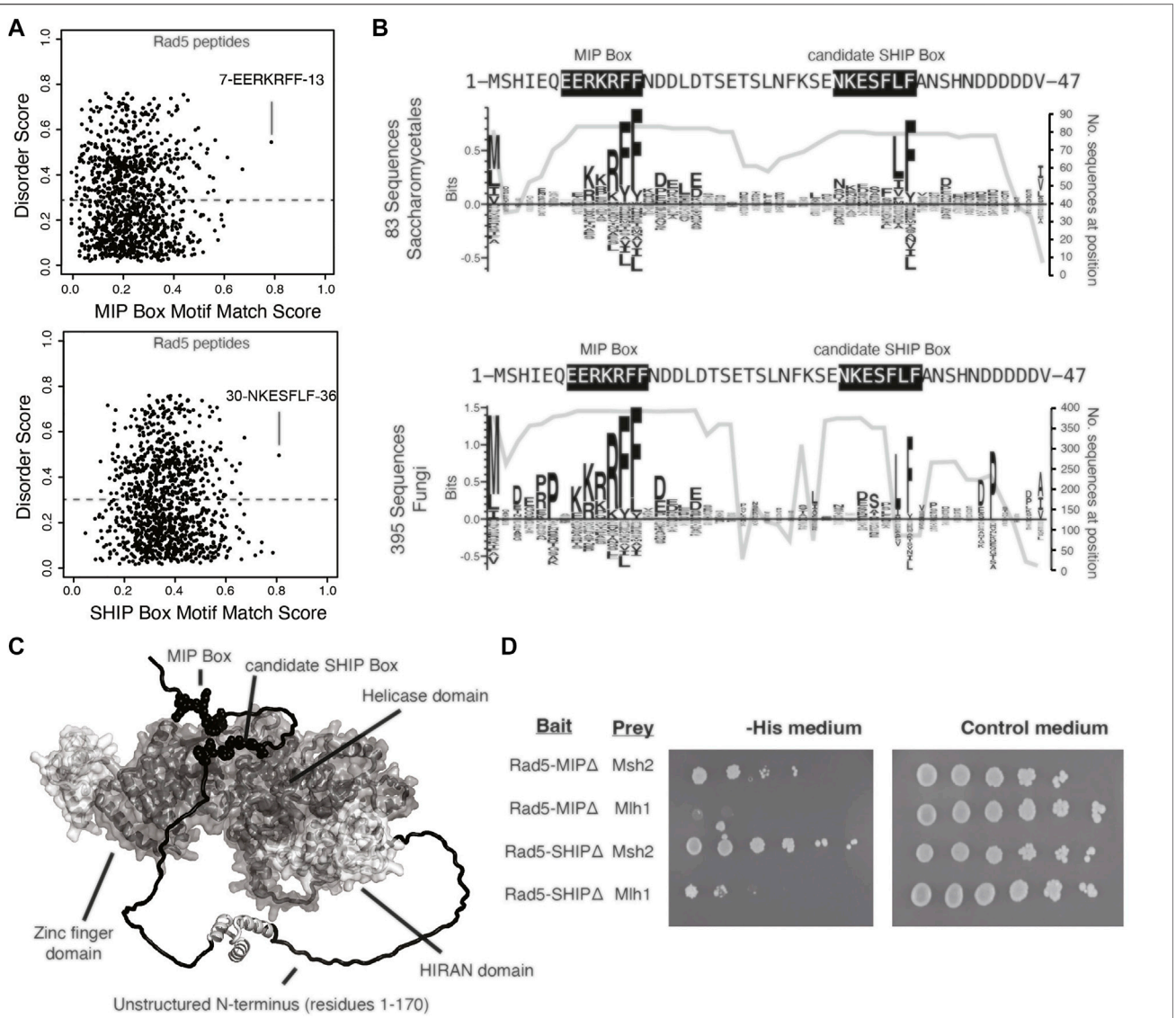


**FIGURE 2 |** Rad5 interacts with Mlh1 through a MIP box motif but does not interact with Msh2 through a SHIP box motif. **(A)** The MIP box and SHIP box motif matching scores for every 7mer peptide in *S. cerevisiae* Rad5 is plotted against the predicted disorder score, showing that the predicted MIP and SHIP boxes have the best peptide scores and are predicted to be disordered by IUPRED (Dosztanyi et al., 2005). **(B)** Sequence logos of the first 47 amino acids of *S. cerevisiae* Rad5 generated by Seq2Logo (Thomsen and Nielsen, 2012) were calculated from an alignment of 83 Saccharomycetales Rad5 sequences (top) or 395 fungal Rad5 sequences (bottom). Large letters above the zero line correspond to highly conserved residues in the alignment. The number of sequences with residues at this location is plotted underneath the sequence logo; note that the MIP box is present in almost all fungal Rad5 sequences aligned whereas the candidate SHIP box is present only in a small subset of the fungal Rad5 sequences corresponding to the Saccharomycetales (bottom). **(C)** Mapping of the predicted MIP and SHIP motifs (black spheres) onto the Alphafold2-predicted structure of *S. cerevisiae* Rad5 (Jumper et al., 2021; Varadi et al., 2022) reveals that these predicted motifs are in the unstructured N-terminus (black). **(D)** Yeast two-hybrid analysis shows that mutation of the predicted MIP box in the Rad5 bait vector retained the interaction with the Msh2 prey but resulted in a loss of interaction (indicated by no growth on selective -Leu -Trip -His medium) with the Mlh1 prey vector, whereas mutation of the predicted SHIP box in the Rad5 bait vector retained interaction with both the Msh2 and Mlh1 prey vectors.

immunoprecipitation of nuclear fraction lysates from HeLa cells to detect interactions between MMR proteins and the Rad5 human homologs, HLTF and SHPRH. HeLa cells have proficient MMR and undergo MMR-mediated apoptosis after alkylating agents (Li et al., 2013; Takeishi et al., 2020). MSH2 directly interacted with HLTF (**Figure 4A**). This interaction was stable even after DNase treatment, indicating that the co-immunoprecipation was not simply through simultaneous association with DNA (**Figure 4B**). MSH2 and HLTF interacted constitutively in basal conditions and the interaction did not change when the DNA alkylating agent MNNG was added (**Figure 4A**). No co-immunopreciptation of HLTF with MLH1 was observed under either basal or DNA damaging conditions (**Figure 4A**). In contrast, we found that SHPRH co-immunopreciptated with MLH1 under basal conditions and that the interaction was enhanced by the

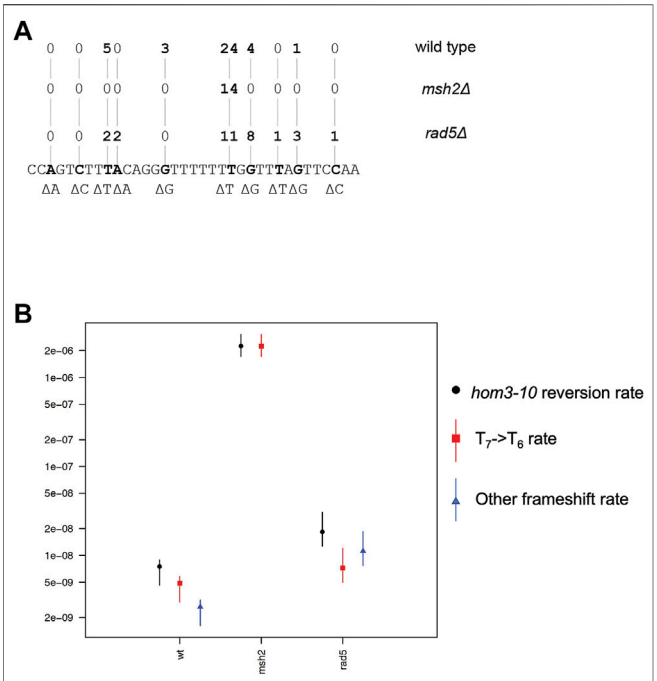


**FIGURE 3 |** Rad5 deletion strain has an altered mutation spectra from MMR deficient strains. **(A)** Spectrum of mutations selected in the *hom3-10* frameshift reversion assay that measures 1 base pair frameshifts in the modified *HOM3* gene that is required for the synthesis of threonine. 37 isolates were analyzed for the WT strain, 14 isolates were analyzed for the *msh2Δ* strain, and 28 isolates were analyzed for the *rad5Δ* strain. MMR deficient strains primarily have T7→ T6 frameshifts. MMR proficient strains have more non T7 → T6 reversion isolates. *rad5Δ* mutation spectrum resembles a WT strain more than a MMR deficient strain. **(B)** Graph of portion of overall *hom3-10* mutation rate made up of T7 → T6 reversions or non T7 → T6 reversions. Overall mutation rate for each strain is in black. Proportion of the rate represented by T7 → T6 reversion rate is in red.

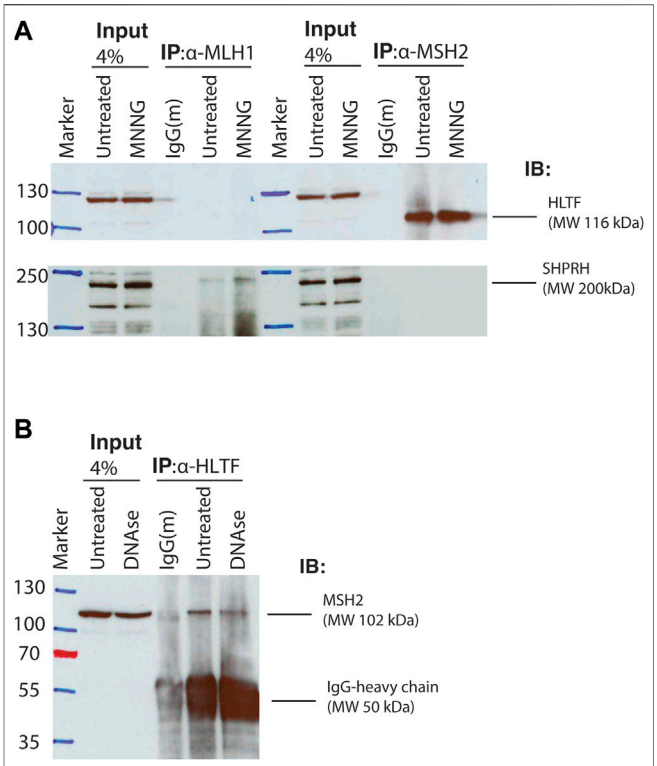


**FIGURE 4 |** Human homologs of Rad5 HLTF and SHPRH interact with MSH2 and MLH1. **(A)** HeLa cells were treated with DMSO or 30 μM MNNG and lysates were fractionated to obtain the nuclear fraction. Nuclear fractions were immunoprecipitated with either anti-MLH1 or anti-MSH2 beads and immunoblotted for either HLTF and SHPRH. HLTF co-immunoprecipitated with MSH2. Immunoprecipitated HLTF runs at the predicted molecular weight of 116 kDa, however the non-immunoprecipitated HLTF in the input lanes runs at a slightly higher MW and has several additional bands consistent with the product sheet for the ThermoFisher HLTF antibody. SHPRH co-immunoprecipitated with MLH1 and the interaction is increased after MNNG treatment. **(B)** HeLa cell nuclear lysates were treated with or without DNAse. Nuclear fractions were obtained and immunoprecipitated with anti-HLTF beads and immunoblotted for MSH2. MSH2 interacts with HLTF regardless of DNAse treatment.

presence of MNNG-induced DNA damage (**Figure 4A**). Unlike HLTF, SHPRH did not co-immunopreciptate with MSH2 under either basal or DNA damaging conditions (**Figure 4A**). Together this shows that the binding between Rad5 homologs and MMR proteins is conserved throughout evolution to human cells, and interestingly, the interactions with the core MMR proteins seem to be split between the two human Rad5 homologs.

## 3.5 HLTF Interacts Differently With Msh2 Than Other SHIP Box Containing Proteins

Given that Rad5's interaction with Msh2 could not be disrupted by mutation of the predicted SHIP box (**Figure 2**), we further investigated the human HLTF-MSH2 interaction. During the *S. cerevisiae* studies that identified the SHIP box motif, we also identified that the *msh2-M470I* mutation, which affects an amino acid in the hinge linker, disrupted the ability of Msh2 to bind to the SHIP box peptide (Goellner et al., 2018). To determine if HLTF interacted in a similar manner with MSH2, we generated the equivalent human mutation M453I in our myc-tagged MSH2 construct. We confirmed that the human mutation also disrupted SHIP box interactions by testing co-immunoprecipitation of MSH2 and MSH2-M453I with SMARCAD1 (**Figure 5A**). SMARCAD1 is the human homolog of *S. cerevisiae* Fun30; both SMARCAD1 and Fun30 contain a conserved N-terminal SHIP box. SMARCAD1 interacts with MSH2 in human and *Xenopus*, and the Fun30-Msh2 interaction in yeast is eliminated by the *msh2-M470I* mutation (Goellner et al., 2018; Terui et al., 2018; Takeishi et al., 2020). We found that SMARCAD1 interacts with wild-type MSH2 but has markedly reduced binding to the MSH2-M453I mutant (**Figure 5A**). In contrast, HLTF co-immunoprecipitated with both wild-type MSH2 and the MSH2-M453I mutant (**Figure 5B**). Taken together, evidence from both the *S. cerevisiae* Rad5-Msh2 interaction and the human HLTF-MSH2 interaction suggest that this interaction is distinct

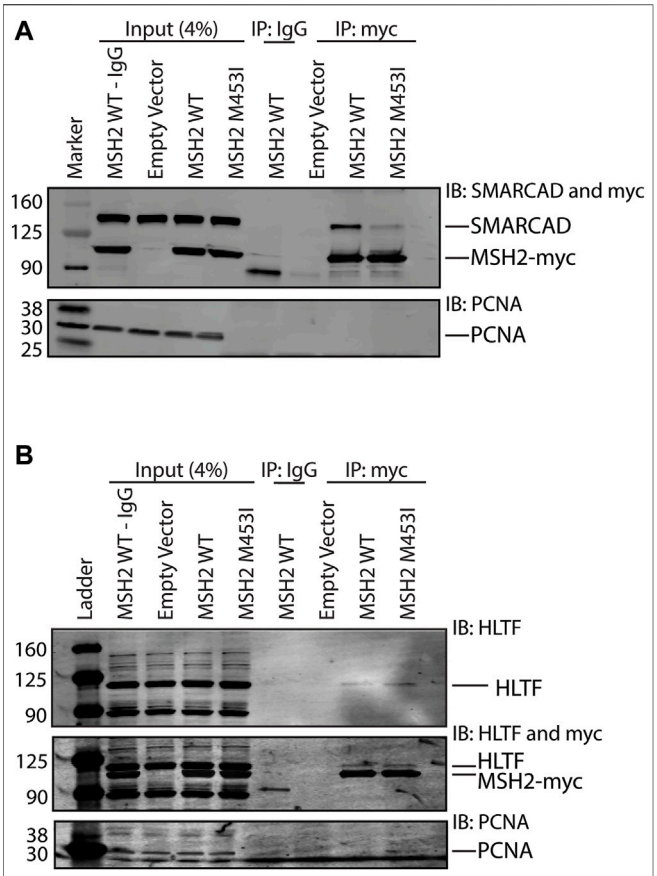


**FIGURE 5 |** HLTF retains binding with the MSH2 M453I mutation. **(A)** HEK293T cells were transfected with c-terminal Myc-FLAG tagged MSH2 WT or MSH2-M453I mutant constructs. Myc-tagged MSH2 was immunoprecipitated with anti-Myc beads and immunoblotted for SMARCAD1. SMARCAD1 co-immunoprecipitated with MSH2 WT but not the MSH2 M453I hinge region mutation. **(B)** HEK293T cells were transfected with c-terminal Myc-FLAG tagged MSH2 WT or MSH2 M453I mutant constructs and Myc-tagged MSH2 was immunoprecipitated with anti-Myc beads and immunoblotted for HLTF. HLTF co-immunoprecipitated with MSH2 WT as we observed with endogenous protein co-IPs. HLTF also co-immunoprecipitated with Msh2 M453I unlike SMARCAD1.

from those mediated by the SHIP box motif. Investigations into this mode of binding are ongoing.

## 3.6 SHPRH Interacts With MLH1 Only During S-phase

To further investigate the interaction between MLH1 and SHPRH, we looked at whether there was a cell-cycle dependency to the interaction, based on the data that the interaction is enhanced with MNNG-induced DNA damage. We first synchronized HeLa cells with a double thymidine block and followed cell cycle progression through DNA distribution by propidium idodide staining and fluorescence activated cell sorting (FACS) analysis. We carried out this experiment in the presence or absence of MNNG. After release from the double thymidine block, we observed the untreated and MNNG treated cells were beginning to move from G1 phase to S phase at 4 h and primarily in S phase by 6 h (**Figure 6A**). At the 10-h time point cells were in G2/M phase, and completed a cell cycle by 12 h (**Figure 6A**). Consistent with literature, we observed that MNNG induced a prolonged G2/M arrest occurring in the second cell cycle after treatment (24- and 36-h timepoints, **Figure 6A**) that is not observed in DMSO treated cells.

We then synchronized HeLa cells with a double thymidine block and collected nuclear lysates at the indicated time points corresponding with the cell cycle analysis above. The interaction between MLH1 and SHPRH is only observed by co-immunoprecipitation in S phase (6-h time point, **Figure 6B**), and is not detectable during G1 or G2/M.

## 3.7 Loss of SHRPH Leads to DNA Damage Resistance but Not Increased Mutation Rate

Treatment of mammalian cells with alkylating agents is known to cause MMR-mediated apoptosis in which loss of MMR activity causes increased alkylating agent resistance (Fu et al., 2012; Li et al., 2016). Given the interactions of HLTF and SHPRH with MMR proteins, we tested if loss of HLTF and/or SHPRH would similarly give rise to increased resistance to alkylation damage. To test this, we generated HeLa S3 cells in which either *MSH2*, *MLH1*, *SHPRH*, or *HLTF* was knocked out by CRISPR-Cas9. We also generated a cell line with both *SHPRH* and *HLTF* knocked out. Expression of the target proteins were totally eliminated in each cell line respectively and remained stably lost after greater than six passages (**Supplementary Figure S1**). MSH2 and MLH1 knockout cells show resistance to MNNG as previously reported for MMR deficient cells (Meikrantz et al., 1998; Fu et al., 2012) (**Figure 7A**). The HLTF and SHPRH double knock out cells showed a mild resistance to MNNG compared to the parental cells, although this did not reach the level of resistance equivalent to that of a total loss of MMR (**Figure 7B**). To determine if this phenotype was associated with a single Rad5 homolog or if it required loss of both proteins, we compared the MNNG sensitivity of the single knockout cell lines. HLTF knockout cells remained sensitive to MNNG in the clonogenic survival assay (**Figure 7C**); however, the SHPRH single knockout cell line showed moderate resistance to MNNG similar to that of the double knock out cell line (**Figure 7D**). While the resistance to MNNG was observed consistently with SHPRH loss, the cells were still markedly more sensitive to alkylating agents than cells that have totally lost MMR. Similar patterns of sensitivity to MNNG were observed for SHPRH and HLTF in a separate cell line that also has proficient MMR (HEK293) utilizing siRNA knock down of SHPRH, HLTF, or both as measured in a short-term survival MTS assay (**Supplementary Figure S2**) or long-term clonogenic assay (**Supplementary Figure S3**). This suggests that SHPRH may play a role in the promotion of apoptosis in a subset of alkylation-induced mispairs. This also demonstrates a

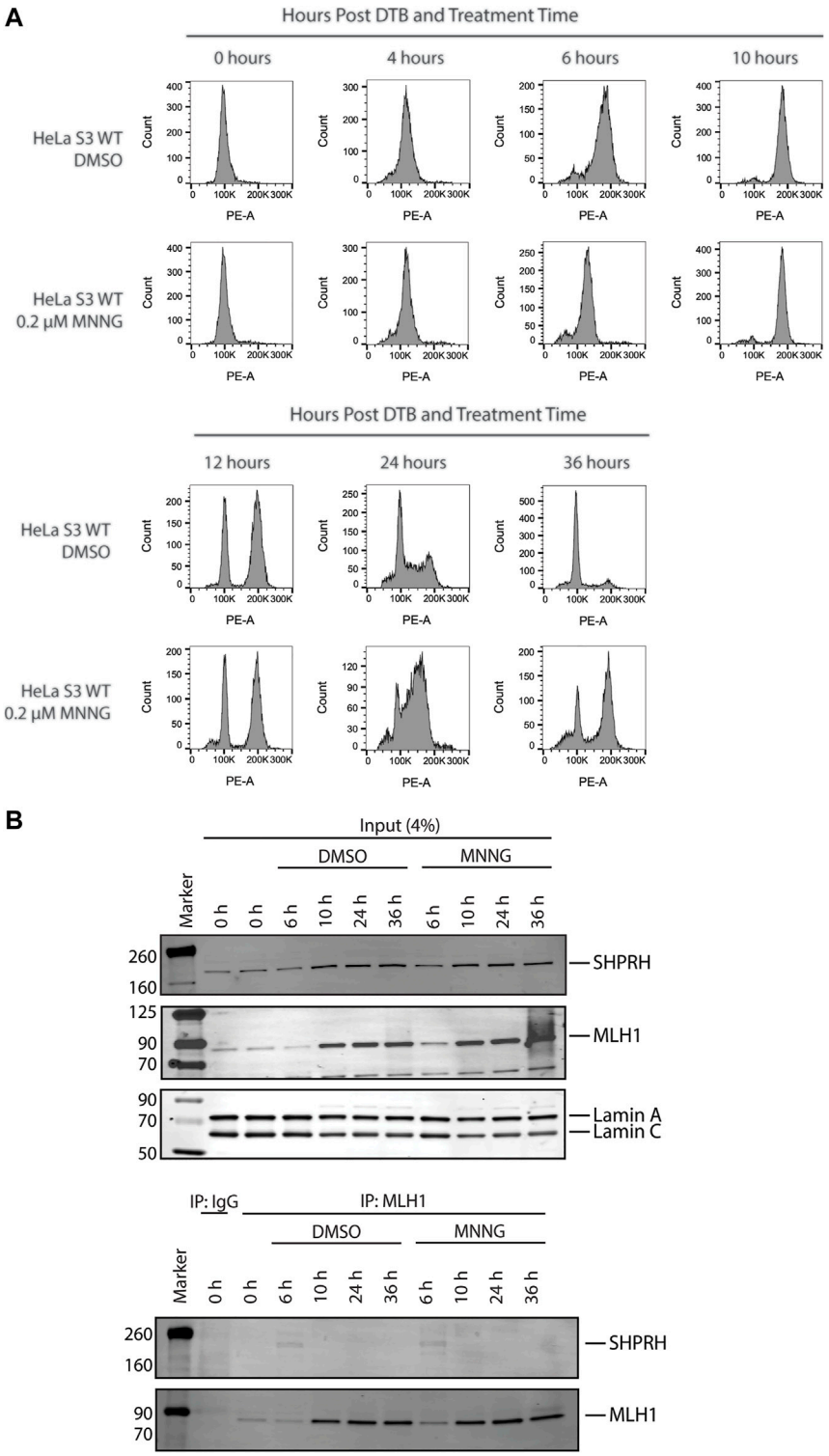


**FIGURE 6 |** SHPRH interaction with MLH1 occurs within S phase of the cell cycle. **(A)** Cell cycle progression of HeLa WT cells treated with DMSO or 0.2 μM MNNG after release from double thymidine block (DTB) synchronization. HeLa WT cells have a G2/M arrest after the second cell cycle (24 h) following treatment with MNNG. The G2/M arrest does not occur in HeLa WT cells treated with DMSO. **(B)** HeLa WT cells were synchronized in the G0/G1 cell cycle utilizing DTB synchronization. After synchronization, cells were treated with DMSO or 0.2 μM MNNG and nuclear extracts were collected at the time points indicated. Endogenous MLH1 was immunoprecipitated with anti-MLH1 beads and immunoblotted for endogenous SHPRH and MLH1. Input was probed for SHPRH, MLH1, and Lamin A/C as the loading control. SHPRH-MLH1 interaction was seen at the 6-h timepoint, which correlates with the S phase in part **(A)**.

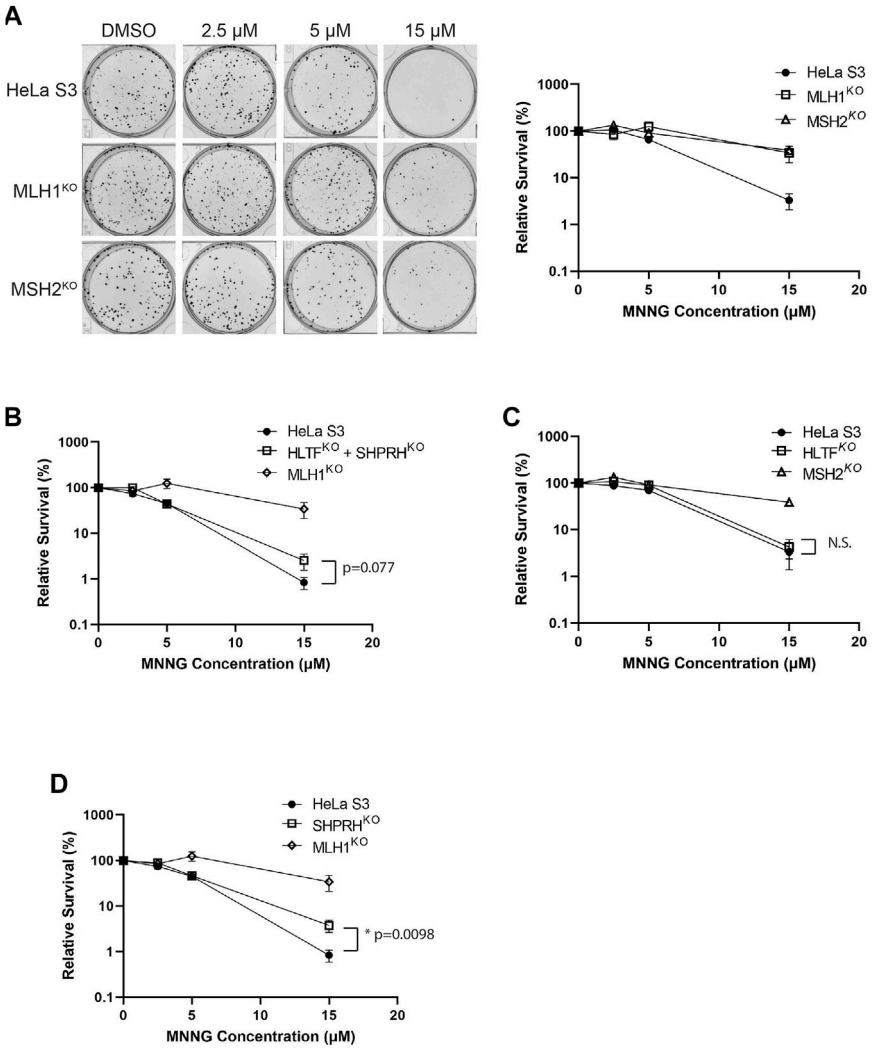


**FIGURE 7 |** Loss of SHPRH results in resistance to alkylating agents. **(A)** HeLa S3 and CRISPR MLH1 and MSH2 knockout cells were seeded into 6-well plates for 24 h followed by a 2-h pre-treatment with $O^6$-benzylguanine and a 1-h treatment of MNNG with $O^6$-benzylguanine and seeded at a low density into a 6-well plate for a clonogenic survival assay. Left panel is a representative of stained colonies. Right panel is cell viability with colony counting. Data is shown as the mean of N = 3 with 4 replicate wells each ± SEM. **(B)** HeLa S3 and CRISPR HLTF + SHPRH double knockout cells were treated the same as part A for the clonogenic survival assay. Data is shown as the mean of N = 3 with 4 replicate wells ± SEM. Survival is compared to HeLa MLH1 KO survival from part **(A)**. **(C)** HeLa S3 and CRISPR HLTF knockout cells were treated the same as part A for the clonogenic survival assay. Data is shown as the mean of N = 3 with four replicate wells ± SEM. Survival is compared to HeLa MSH2 KO survival from part **(A)**. **(D)** HeLa S3 and CRISPR SHPRH knockout cells were treated the same as part A for the clonogenic survival assay. Data is shown as the mean of N = 3 with 4 replicate wells ± SEM. Survival is compared to HeLa MLH1 KO survival from part **(A)**. Statistical significance was determined by unpaired *t*-test $^*p < 0.05$.

functional difference between the two human Rad5 homologs in regards to MMR response to alkylating damage, potentially mediated by the evolutionary split of binding partners between the two homologs (**Figure 10**).

To begin to determine the mechanisms of SHPRH involvement with the DNA MMR apoptotic response after alkylating damage, we also investigated the G2/M arrest occurring during the second cell cycle after exposure. A prolonged G2/M arrest in the second cell cycle after alkylation damage is well established phenotype for MMR-promoted apoptosis (Fu et al., 2012). Cells without MMR do not arrest or undergo apoptosis. We synchronized parental HeLa S3 cells and knock out cell lines using a double thymidine block and released after MNNG treatment. The parental cells showed the typical G2/M arrest starting at 24 h after treatment and maintained it through 48 h (**Figure 8**). The MLH1 knockout cells progressed through two normal cell cycles as reported in the literature (**Figure 8**). The HLTF knockout cells retained the G2/M arrest, consistent with their normal sensitivity to MNNG. Interestingly, the SHPRH knockout cells also retained a normal G2/M arrest despite a decreased sensitivity to MNNG (**Figure 9**). This suggests that SHPRH may play a role in the steps between G2/M arrest and the lack of resolution of the arrest that then

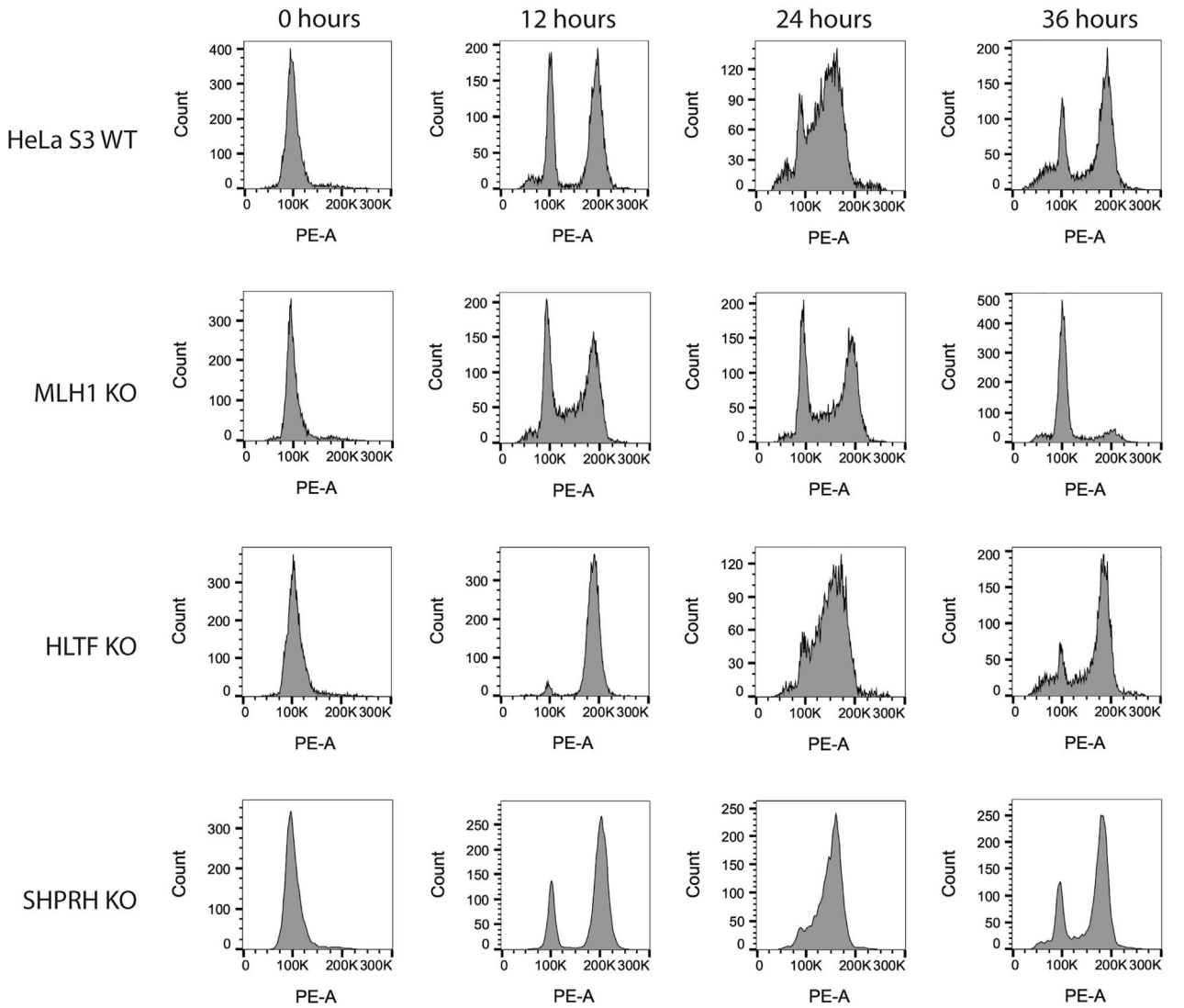


**FIGURE 8 |** HLTF and SHPRH knock out cells retain MNNG induced G2/M arrest in the second cell cycle after damage. Cell cycle FACS analysis of HeLa WT, MLH1 KO, HLTF KO, and SHPRH KO cells treated with 0.2 μM MNNG for the times indicated after DTB synchronization. HeLa WT cells have G2/M arrest after the second cell cycle (24 h). HeLa MLH1 KO cells do not have the G2/M arrest that HeLa WT cells showed. HeLa HLTF KO and SHPRH KO both have G2/M arrest similar to the HeLa WT cells.

leads to apoptosis. We also observed that untreated SHPRH knock out cells progressed through the cell cycle at a slower rate after synchronization, and that without damage they had a level of G2/M arrest (between 8 and 10 h, **Figure 9**). This was not observed in the HLTF knockout or parental HeLa cell lines (**Figure 9**). This change in cell cycle may be indicative of trouble resolving endogenous damage occurring in culture, potentially related to SHPRH's role in translesion synthesis or template switching pathways.

Given the role of SHPRH in MMR-dependent apoptosis after alkylation damage, we wanted to determine if SHPRH, unlike Rad5 in *S. cerevisiae*, acted in the canonical MMR mutation avoidance pathway. To test this in our HeLa S3 knockout cells, we used the hypoxanthine phosphoribosyl transferase (HPRT) forward mutagenesis assay, as reported by Li et al. (Li et al., 2013). The parental HeLa S3 cells had a mutation frequency less than $4.78 \times 10^{-6}$ and the MLH1 and MSH2 knockout cells had increased mutation frequency of about $2.45 \times 10^{-4}$, similar to the reported frequency for other MMR deficient cell lines (**Table 3** (Li et al., 2013)). The SHPRH knockout cells had an estimated rate about equal to the parental cell lines, without any significant colony formation observed at even at higher plating densities (**Table 3**). Together this data suggests that SHPRH

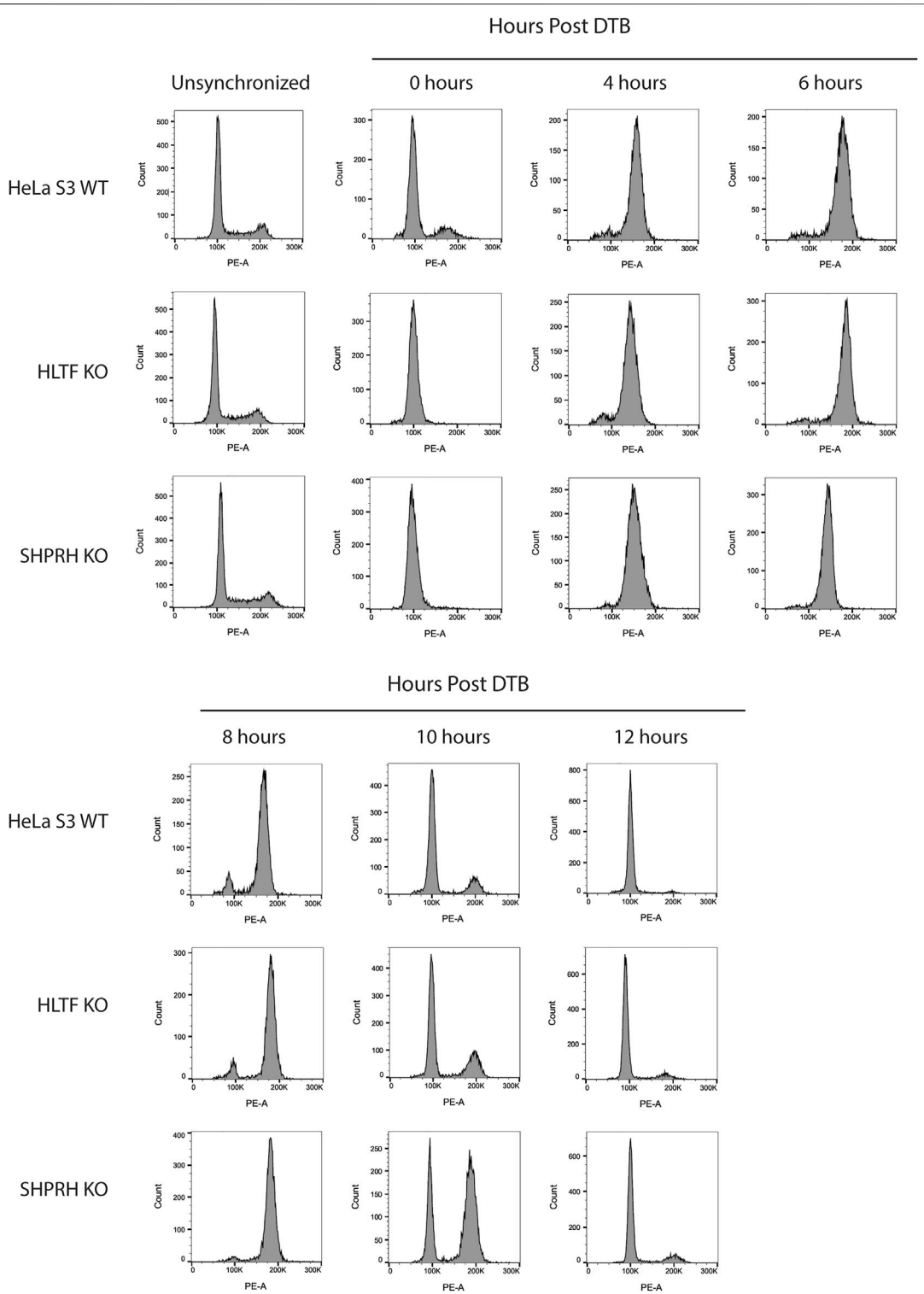


**FIGURE 9 |** SHPRH knock out cells demonstrate delayed cell cycle without exogenous damage. Cell cycle FACS analysis of HeLa WT, HLTF KO, and SHPRH KO cells after release from DTB synchronization. HeLa HLTF KO cells follow the same cell cycle progression as the HeLa WT cells. HeLa SHPRH KO cells have a slower cell cycle progression and G2/M arrest compared to the HeLa WT cells.

**TABLE 3 |** HPRT mutation frequency.

| Cell line | *HPRT* Mutation frequency |
|---|---|
| HeLa S3 | $<4.78 \times 10^{-6}$ |
| SHPRH KO | $<9.31 \times 10^{-6}$ |
| MLH1 KO | 2.44 [2.29–2.70] $\times 10^{-4}$ |
| MSH2 KO | 2.47 [1.82–3.08] $\times 10^{-4}$ |

*Reported frequency is the median frequency with 95% confidence interval in square brackets calculated as described in materials and methods. n = 6 per cell line.*

influences the MMR mediated response to alkylation-induced mispairs, but not repair of replication errors through canonical MMR.

## 4 DISCUSSION

The identification of the MIP box Mlh1-binding motif (Dherin et al., 2009) and, more recently, the SHIP box Msh2-binding motif (Goellner et al., 2018) have revealed how many proteins are recruited to sites of MMR. These proteins include those directly involved in MMR (*e.g.* Exo1) and have identified a number of other proteins whose roles in MMR and MMR-mediated processes are less well understood, including *S. cerevisiae* Ntg2, Sgs1, Fun30, and Dpb3 and human FAN1, SMARCAD1, WDHD1, and MCM9 (Dherin et al., 2009; Traver et al., 2015; Chen et al., 2016; Goellner et al., 2018; Terui et al., 2018; Takeishi et al., 2020; Goold et al., 2021; Porro et al., 2021). Here, we have used analysis of candidate MIP and SHIP box sequences to identify *S. cerevisiae* Rad5 as a MIP box-mediated Mlh1 interactor and a SHIP box-independent Msh2 interactor. These interactions are conserved through evolution to the human homologs of Rad5, HLTF, and SHPRH; however, the interaction seems to have split during evolution between the two homologs, with HLTF retaining MSH2 binding and SHPRH retaining MLH1 binding.

Why Rad5 homologs can bind to MMR proteins remains an open question. Numerous screens for mutations that cause MMR defects in *S. cerevisiae* have not identified *rad5* mutations (Huang et al., 2003; Schmidt et al., 2017). Unlike forward mutation assays like the $Can1^R$ and HPRT assays, *hom3-10* and similar frameshift reversion assays measure mutation events that are primarily specific to MMR defects (Marsischky et al., 1996; Harfe and Jinks-Robertson, 1999). Sequence analysis of the mutation spectra in MMR-deficient strains has shown that the primary *hom3-10*-reverting mutation is T7 →T6 (100%, 73 of 73 in MMR-defective genotypes; and 93%, 162 of 181 in partial MMR-defective genotypes) (Tishkoff et al., 1997; Flores-Rozas and Kolodner, 1998; Calil et al., 2021). The *rad5Δ* mutation caused only a very small increase in the *hom3-10* frameshift reversion rate, and this rate increase is attributable to a different spectrum of mutations than those expected due to an MMR defect (39% T7 →T6 frameshifts). These results suggest that Rad5 either does not play a major role in mutation avoidance by MMR, consistent with prior results (Johnson et al., 1992), or it is redundant with other MMR subpathways, similar to other MMR components such as Exo1 (Goellner et al., 2015).

To model the MMR-mediated response to $S_N1$-type alkylating agents in budding yeast, studies must be carried out in strains that have a *rad52Δmgt1Δ* double mutation background to overcome immediate repair by either direct reversal or homologous recombination pathways that are highly efficient in yeast (Cejka et al., 2005). The sensitivity of *rad5Δ* strains to replication blocking lesions specific to $S_N2$-type alkylating agents, such as MMS, has been

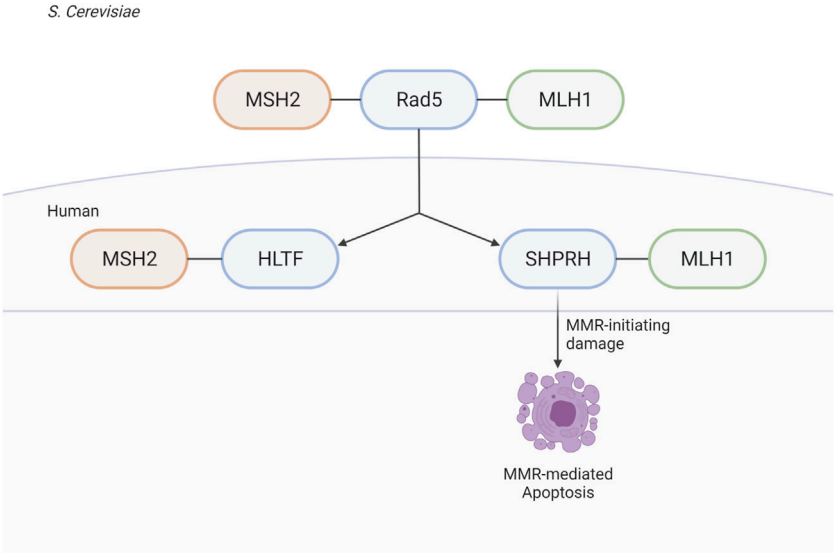


**FIGURE 10 |** Rad5 and human homologs interact with the MMR pathway. *Saccharomyces cerevisiae* helicase/E3 ligase Rad5 interacts with both key players in eukaryotic MMR, Msh2 and Mlh1. Rad5 has two human homologs, HLTF and SHPRH. Binding to the MMR pathway is conserved throughout evolution, but split between the two human homologs with HLTF binding MSH2 and SHPRH binding MLH1. SHPRH plays a role in apoptosis after alkylation damage as depletion of SHPRH results in mild resistance to MNNG. Created with BioRender.com.

heavily studied in the context of PRR (Xu et al., 2016). However, to our knowledge, few studies have looked at *rad5Δ* mutation containing strains in the context of SN1-type agents in the appropriate background to determine their impact on non-canonical MMR. Cjeka et al. did conduct a genome wide screen using the yeast deletion library in the *rad52Δmgt1Δ* genetic background and did not identify any factors beyond MMR as having a significant loss of sensitivity to MNNG (Cejka and Jiricny, 2008). However, in the same manuscript they did a second screen only in the presence of *mgt1Δ* to identify factors that may help resolve MMR mediated toxic intermediates. In this second screen *RAD5* was identified and interestingly was far more sensitive than other members of the PRR pathway (Cejka and Jiricny, 2008), suggesting that *RAD5* may be playing a unique role that we hypothesize is due to its physical interactions with MMR.

Based on these results, we have focused our efforts on understanding the role of Rad5 human homologs, HLTF and SHPRH, in non-canonical functions of MMR. Since our report that Msh2 interacts with the Fun30 helicase (SMARCAD1 in humans), another group has confirmed the human MSH2-SMARCAD1 interaction and demonstrated that SMARCAD1 KO cell lines are moderately resistant to alkylating agent-induced apoptosis likely through changes in the chromatin association of MMR proteins (Takeishi et al., 2020). Similarly, we found that depletion or knockout of SHPRH results in moderate resistance to alkylation-induced cell death, consistent with the Rad5-Mlh1 MIP box interaction and the SHPRH-MLH1 interaction. Interestingly, the SHPRH knockout lines retain the MNNG-mediated G2/M arrest but have reduced cell death. SHPRH has several functional domains, including a helicase and E3 ligase domain (Elserafy et al., 2018). Complementation studies are ongoing to determine which SHPRH domains are critical to mediating sensitivity to alkylation damage. Intriguingly, both SHPRH and SMARCAD1 are SNF2-family DNA helicases albeit with very different functions: fork reversal and nucleosome remodeling, respectively. It is currently unclear if there is any redundancy or additive effect between SHPRH and SMARCAD1 roles in influencing this pathway.

We find it especially interesting that while the interactions of both Msh2 and Mlh1 with Rad5 are conserved through evolution to the human homologs, that the binding sites seem to have been split between the two homologs (**Figure 10**). Given the differences of HLTF and SHPRH in alkylation sensitivity, it seems possible that the Msh2-Rad5 and Mlh1-Rad5 interactions have different functional roles that are retained in different Rad5 homologs after gene duplication and specialization (Ohno, 1970). An intriguing possibility, since Rad5 does not appear to act in the canonical MMR mutation avoidance pathway, is that the HLTF-MSH2 interaction acts in a separate non-canonical role of MMR such as heteroduplex rejection (Tham et al., 2016) or that MSH2 influences the role of HLTF in PRR. Several groups have shown an interaction between nuclease FAN1 and MLH1, mediated by a MIP box and an additional MLH1-interaction domain (Goold et al., 2021; Porro et al., 2021). This binding seems to influence apoptotic response to MNU and also control FAN1's role in trinucleotide repeat stabilization and interstrand cross-link repair (Rikitake et al., 2020; Porro et al., 2021). HLTF and SHPRH may be similarly impacted by MMR interactions that affect their previously identified cellular roles. Porro et al. also demonstrate that phosphorylation of the MIP box changes the association between FAN1 and MLH1, raising questions on whether the interactions between MMR proteins and Rad5 homologs may also be regulated by post-translational events.

## DATA AVAILABILITY STATEMENT

The original contributions presented in the study are included in the article/**Supplementary Material**, further inquiries can be directed to the corresponding author.

## AUTHOR CONTRIBUTIONS

EG, CP, RK, and AM conceived the overall experimental design. EG, AM, GM, BK, HD, CP, and CR collected data. CP performed bioinformatic analysis. AM and EG wrote the paper and all authors revised and modified the paper.

## FUNDING

This publication was supported by a NIH grant R00ES026653, a Markey Foundation Markey Women Strong Distinguished Researcher award, and a Phi Beta Psi Cancer Research Grant to EG and NIH R01 GM50006 to RK and support from the Ludwig Institute for Cancer Research. This publication was also supported by UK-CARES through Grant P30 ES026529 as a Career Development Award to EG. Its contents are solely the responsibility of the authors and do not necessarily represent the official views of the NIEHS. This research was supported by the Flow Cytometry and Immune Monitoring Core Shared Resource of the University of Kentucky Markey Cancer Center (P30CA177558).

## ACKNOWLEDGMENTS

The authors would like to acknowledge Amber Rohrberg and Salvatore J. Cherra III for their technical assistance and valuable discussion.

## SUPPLEMENTARY MATERIAL

The Supplementary Material for this article can be found online at: https://www.frontiersin.org/articles/10.3389/fcell.2022.843121/full#supplementary-material

**Supplementary Figure S1 |** Generation of knockout cells by CRISPR-Cas9. **(A)** Schematic of sgRNA sequence and target for generation of MSH2 knock out Hela S3 cells (top). Immunoblot of MSH2 protein levels in parental cells and selected clones after 6 continuous passages. MSH2 knockout was retained in clone 2 but re-expressed in clone 4. **(B)** Schematic of sgRNA sequence and target for generation of

HLTF knock out Hela S3 cells (top). Immunoblot of HLTF protein levels in parental cells and selected clones after 6 continuous passages. HLTF knockout was retained in clone 3 and clone 4. The double knockout cell line was made by knockout of SHPRH in the HLTF knockout background. **(C)** Schematic of sgRNA sequence and target for generation of MLH1 knock out Hela S3 cells (top). Immunoblot of MLH1 protein levels in parental cells and selected clones after 6 continuous passages. MLH1 knockout was retained in clone 3 and clone 4. **(D)** Schematic of sgRNA sequence and target for generation of SHPRH knock out Hela S3 cells (top). Immunoblot of SHPRH protein levels in parental cells and selected clones after 6 continuous passages. SHPRH knockout was retained in clone B2 and clone C3.

**Supplementary Figure S2 |** Loss of SHPRH results in resistance to alkylating agents. **(A)** HEK293 cells were co-transfected with siRNA to both HLTF and SHPRH. Cells were seeded into 96-well plates for 24 h followed by a 1-h treatment with MNNG and assayed for survival after 72 h by MTS assay. Data is shown as the mean of $N = 3 \pm$ SEM. Efficiency of knockdown for the used siRNA duplex is shown in the right panel. **(B)** HEK293 cells were transfected with siRNA to HLTF. Cells were seeded into 96-well plates for 24 h followed by a 1-h treatment with MNNG and assayed for survival after 72 h by MTS assay. Data is shown as the mean of $N = 3 \pm$ SEM. Efficiency of knockdown for the used siRNA duplex is shown in the right panel. **(C)** HEK293 cells were transfected with siRNA to SHPRH. Cells were seeded into 96-well plates for 24 h followed by a 1-h treatment with MNNG and assayed for survival after 72 h by MTS assay. Data is shown as the mean of $N = 3 \pm$ SEM. Efficiency of knockdown for the used siRNA duplex is shown in the right panel.

**Supplementary Figure S3 |** Clonogenic survival assay of HEK293 cells transfected with siSHPRH. HEK293 cells with SHPRH knocked down with siRNA were treated with indicated doses of the alkylating agent MNNG in a long-term clonogenic survival assay. HEK293 cells do not form countable colonies. Visually, siSHPRH cells have greater survival than siScrambled cells.

# REFERENCES


Begum, S., Yiu, A., Stebbing, J., and Castellano, L. (2018). Novel Tumour Suppressive Protein Encoded by Circular RNA, Circ-SHPRH, in Glioblastomas. *Oncogene* 37, 4055–4057. doi:10.1038/s41388-018-0230-3

Borresen, A.-L., Lothe, R. A., Meling, G. I., Lystad, S., Morrison, P., Lipford, J., et al. (1995). Somatic Mutations in the hMSH2 Gene in Microsatellite Unstable Colorectal Carcinomas. *Hum. Mol. Genet.* 4, 2065–2072. doi:10.1093/hmg/4.11.2065

Calil, F. A., Li, B.-Z., Torres, K. A., Nguyen, K., Bowen, N., Putnam, C. D., et al. (2021). Rad27 and Exo1 Function in Different Excision Pathways for Mismatch Repair in *Saccharomyces cerevisiae*. *Nat. Commun.* 12, 5568. doi:10.1038/s41467-021-25866-z

Cejka, P., and Jiricny, J. (2008). Interplay of DNA Repair Pathways Controls Methylation Damage Toxicity in *Saccharomyces cerevisiae*. *Genetics* 179, 1835–1844. doi:10.1534/genetics.108.089979

Cejka, P., Mojas, N., Gillet, L., Schär, P., and Jiricny, J. (2005). Homologous Recombination Rescues Mismatch-repair-dependent Cytotoxicity of S(N)1-type Methylating Agents in *S. cerevisiae*. *Curr. Biol.* 15, 1395–1400. doi:10.1016/j.cub.2005.07.032

Chen, Z., Tran, M., Tang, M., Wang, W., Gong, Z., and Chen, J. (2016). Proteomic Analysis Reveals a Novel Mutator S (MutS) Partner Involved in Mismatch Repair Pathway. *Mol. Cell. Proteomics* 15, 1299–1308. doi:10.1074/mcp.m115.056093

de la Chapelle, A. (2004). Genetic Predisposition to Colorectal Cancer. *Nat. Rev. Cancer* 4, 769–780. doi:10.1038/nrc1453

Dherin, C., Gueneau, E., Francin, M., Nunez, M., Miron, S., Liberti, S. E., et al. (2009). Characterization of a Highly Conserved Binding Site of Mlh1 Required for Exonuclease I-dependent Mismatch Repair. *Mol. Cell Biol.* 29, 907–918. doi:10.1128/mcb.00945-08

Dosztanyi, Z., Csizmok, V., Tompa, P., and Simon, I. (2005). IUPred: Web Server for the Prediction of Intrinsically Unstructured Regions of Proteins Based on Estimated Energy Content. *Bioinformatics* 21, 3433–3434. doi:10.1093/bioinformatics/bti541

Durno, C. A., Sherman, P. M., Aronson, M., Malkin, D., Hawkins, C., Bakry, D., et al. (2015). Phenotypic and Genotypic Characterisation of Biallelic Mismatch Repair Deficiency (BMMR-D) Syndrome. *Eur. J. Cancer* 51, 977–983. doi:10.1016/j.ejca.2015.02.008

Elserafy, M., Abugable, A. A., Atteya, R., and El-Khamisy, S. F. (2018). Rad5, HLTF, and SHPRH: A Fresh View of an Old Story. *Trends Genet.* 34, 574–577. doi:10.1016/j.tig.2018.04.006

Fishel, R., Lescoe, M. K., Rao, M. R. S., Copeland, N. G., Jenkins, N. A., Garber, J., et al. (1993). The Human Mutator Gene Homolog MSH2 and its Association with Hereditary Nonpolyposis Colon Cancer. *Cell* 75, 1027–1038. doi:10.1016/0092-8674(93)90546-3

Fishel, R. (2015). Mismatch Repair. *J. Biol. Chem.* 290, 26395–26403. doi:10.1074/jbc.r115.660142

Flores-Rozas, H., and Kolodner, R. D. (1998). The *Saccharomyces cerevisiae* MLH 3 Gene Functions in MSH3-dependent Suppression of Frameshift Mutations. *Proc. Natl. Acad. Sci. U.S.A.* 95, 12404–12409. doi:10.1073/pnas.95.21.12404

Fu, D., Calvo, J. A., and Samson, L. D. (2012). Balancing Repair and Tolerance of DNA Damage Caused by Alkylating Agents. *Nat. Rev. Cancer* 12, 104–120. doi:10.1038/nrc3185

Gallo, D., and Brown, G. W. (2019). Post-replication Repair: Rad5/HLTF Regulation, Activity on Undamaged Templates, and Relationship to Cancer. *Crit. Rev. Biochem. Mol. Biol.* 54, 301–332. doi:10.1080/10409238.2019.1651817

Gallo, D., Kim, T., Szakal, B., Saayman, X., Narula, A., Park, Y., et al. (2019). Rad5 Recruits Error-Prone DNA Polymerases for Mutagenic Repair of ssDNA Gaps on Undamaged Templates. *Mol. Cell* 73, 900–914. doi:10.1016/j.molcel.2019.01.001

Goellner, E. M., Putnam, C. D., Graham, W. J., Rahal, C. M., Li, B.-Z., and Kolodner, R. D. (2018). Identification of Exo1-Msh2 Interaction Motifs in DNA Mismatch Repair and New Msh2-Binding Partners. *Nat. Struct. Mol. Biol.* 25, 650–659. doi:10.1038/s41594-018-0092-y

Goellner, E. M., Putnam, C. D., and Kolodner, R. D. (2015). Exonuclease 1-dependent and Independent Mismatch Repair. *DNA repair* 32, 24–32. doi:10.1016/j.dnarep.2015.04.010

Goold, R., Hamilton, J., Menneteau, T., Flower, M., Bunting, E. L., Aldous, S. G., et al. (2021). FAN1 Controls Mismatch Repair Complex Assembly via MLH1 Retention to Stabilize CAG Repeat Expansion in Huntington's Disease. *Cell Rep.* 36, 109649. doi:10.1016/j.celrep.2021.109649

Gueneau, E., Dherin, C., Legrand, P., Tellier-Lebegue, C., Gilquin, B., Bonnesoeur, P., et al. (2013). Structure of the MutLα C-Terminal Domain Reveals How Mlh1 Contributes to Pms1 Endonuclease Site. *Nat. Struct. Mol. Biol.* 20, 461–468. doi:10.1038/nsmb.2511

Harfe, B. D., and Jinks-Robertson, S. (1999). Removal of Frameshift Intermediates by Mismatch Repair Proteins in *Saccharomyces cerevisiae*. *Mol. Cell Biol.* 19, 4766–4773. doi:10.1128/mcb.19.7.4766

Huang, M.-E., Rio, A.-G., Nicolas, A., and Kolodner, R. D. (2003). A Genomewide Screen in *Saccharomyces cerevisiae* for Genes that Suppress the Accumulation of Mutations. *Proc. Natl. Acad. Sci. U.S.A.* 100, 11529–11534. doi:10.1073/pnas.2035018100

Johnson, R. E., Henderson, S. T., Petes, T. D., Prakash, S., Bankmann, M., and Prakash, L. (1992). *Saccharomyces cerevisiae* RAD5-Encoded DNA Repair Protein Contains DNA Helicase and Zinc-Binding Sequence Motifs and Affects the Stability of Simple Repetitive Sequences in the Genome. *Mol. Cell Biol.* 12, 3807–3818. doi:10.1128/mcb.12.9.3807-3818.1992

Jumper, J., Evans, R., Pritzel, A., Green, T., Figurnov, M., Ronneberger, O., et al. (2021). Highly Accurate Protein Structure Prediction with AlphaFold. *Nature* 596, 583–589. doi:10.1038/s41586-021-03819-2

Kane, M. F., Loda, M., Gaida, G. M., Lipman, J., Mishra, R., Goldman, H., et al. (1997). Methylation of the hMLH1 Promoter Correlates with Lack of Expression of hMLH1 in Sporadic Colon Tumors and Mismatch Repair-Defective Human Tumor Cell Lines. *Cancer Res.* 57, 808–811.

Kastrinos, F., and Stoffel, E. M. (2014). The History, Genetics, and Strategies for Cancer Prevention in Lynch Syndrome. *Clin. gastroenterology hepatology official Clin. Pract. J. Am. Gastroenterological Assoc.* 12 (5), 715–727. doi:10.1016/j.cgh.2013.06.031

Katoh, K., and Standley, D. M. (2014). MAFFT: Iterative Refinement and Additional Methods. *Methods Mol. Biol.* 1079, 131–146. doi:10.1007/978-1-62703-646-7_8

Kolodner, R. D. (1995). Mismatch Repair: Mechanisms and Relationship to Cancer Susceptibility. *Trends Biochem. Sci.* 20, 397–401. doi:10.1016/s0968-0004(00)89087-8

Li, F., Mao, G., Tong, D., Huang, J., Gu, L., Yang, W., et al. (2013). The Histone Mark H3K36me3 Regulates Human DNA Mismatch Repair through its Interaction with MutSα. *Cell* 153, 590–600. doi:10.1016/j.cell.2013.03.025

Li, G.-M. (2008). Mechanisms and Functions of DNA Mismatch Repair. *Cell Res.* 18, 85–98. doi:10.1038/cr.2007.115

Li, Z., Pearlman, A. H., and Hsieh, P. (2016). DNA Mismatch Repair and the DNA Damage Response. *DNA repair* 38, 94–101. doi:10.1016/j.dnarep.2015.11.019

Lin, J.-R., Zeman, M. K., Chen, J.-Y., Yee, M.-C., and Cimprich, K. A. (2011). SHPRH and HLTF Act in a Damage-specific Manner to Coordinate Different Forms of Postreplication Repair and Prevent Mutagenesis. *Mol. Cell* 42, 237–249. doi:10.1016/j.molcel.2011.02.026

Lynch, H. T., Snyder, C. L., Shaw, T. G., Heinen, C. D., and Hitchins, M. P. (2015). Milestones of Lynch Syndrome: 1895-2015. *Nat. Rev. Cancer* 15, 181–194. doi:10.1038/nrc3878

Marsischky, G. T., Filosi, N., Kane, M. F., and Kolodner, R. (1996). Redundancy of *Saccharomyces cerevisiae* MSH3 and MSH6 in MSH2-dependent Mismatch Repair. *Genes Dev.* 10, 407–420. doi:10.1101/gad.10.4.407

Masuda, Y., Suzuki, M., Kawai, H., Hishiki, A., Hashimoto, H., Masutani, C., et al. (2012). *En Bloc* Transfer of Polyubiquitin Chains to PCNA *In Vitro* Is Mediated by Two Different Human E2-E3 Pairs. *Nucleic acids Res.* 40, 10394–10407. doi:10.1093/nar/gks763

Meikrantz, W., Bergom, M. A., Memisoglu, A., and Samson, L. (1998). O6-alkylguanine DNA Lesions Trigger Apoptosis. *Carcinogenesis* 19, 369–372. doi:10.1093/carcin/19.2.369

Moinova, H. R., Chen, W.-D., Shen, L., Smiraglia, D., Olechnowicz, J., Ravi, L., et al. (2002). HLTF Gene Silencing in Human Colon Cancer. *Proc. Natl. Acad. Sci. U.S.A.* 99, 4562–4567. doi:10.1073/pnas.062459899

Motegi, A., Liaw, H.-J., Lee, K.-Y., Roest, H. P., Maas, A., Wu, X., et al. (2008). Polyubiquitination of Proliferating Cell Nuclear Antigen by HLTF and SHPRH Prevents Genomic Instability from Stalled Replication Forks. *Proc. Natl. Acad. Sci. U.S.A.* 105, 12411–12416. doi:10.1073/pnas.0805685105

Ohno, S. (1970). *Evolution by Gene Duplication*. London, New York: Allen & Unwin, Springer-Verlag.

Porro, A., Mohiuddin, M., Zurfluh, C., Spegg, V., Dai, J., Iehl, F., et al. (2021). FAN1-MLH1 Interaction Affects Repair of DNA Interstrand Cross-Links and Slipped-CAG/CTG Repeats. *Sci. Adv.* 7, eabf7906. doi:10.1126/sciadv.abf7906

Putnam, C. D., Hayes, T. K., and Kolodner, R. D. (2010). Post-replication Repair Suppresses Duplication-Mediated Genome Instability. *PLoS Genet.* 6, e1000933. doi:10.1371/journal.pgen.1000933

Retief, J. D. (2000). Phylogenetic Analysis Using PHYLIP. *Methods Mol. Biol.* 132, 243–258. doi:10.1385/1-59259-192-2:243

Rikitake, M., Fujikane, R., Obayashi, Y., Oka, K., Ozaki, M., and Hidaka, M. (2020). MLH1-mediated Recruitment of FAN1 to Chromatin for the Induction of Apoptosis Triggered by O(6) -methylguanine. *Genes cells.* 25, 175–186. doi:10.1111/gtc.12748

Schmidt, T. T., Reyes, G., Gries, K., Ceylan, C. Ü., Sharma, S., Meurer, M., et al. (2017). Alterations in Cellular Metabolism Triggered by URA7 or GLN3 Inactivation Cause Imbalanced dNTP Pools and Increased Mutagenesis. *Proc. Natl. Acad. Sci. U. S. A.* 114, E4442–E4451. doi:10.1073/pnas.1618714114

Schroering, A. G., and Williams, K. J. (2008). Rapid Induction of Chromatin-Associated DNA Mismatch Repair Proteins after MNNG Treatment. *DNA repair* 7, 951–969. doi:10.1016/j.dnarep.2008.03.023

Seelinger, M., Søgaard, C. K., and Otterlei, M. (2020). The Human RAD5 Homologs, HLTF and SHPRH, Have Separate Functions in DNA Damage Tolerance Dependent on the DNA Lesion Type. *Biomolecules* 10, 463. doi:10.3390/biom10030463

Sood, R., Makalowska, I., Galdzicki, M., Hu, P., Eddings, E., Robbins, C. M., et al. (2003). Cloning and Characterization of a Novel Gene, SHPRH, Encoding a Conserved Putative Protein with SNF2/helicase and PHD-Finger Domains from the 6q24 Region. *Genomics* 82, 153–161. doi:10.1016/s0888-7543(03)00121-6

Stormo, G. D., Schneider, T. D., Gold, L., and Ehrenfeucht, A. (1982). Use of the 'Perceptron' Algorithm to Distinguish Translational Initiation Sites in *E. coli*. *Nucl. Acids Res.* 10, 2997–3011. doi:10.1093/nar/10.9.2997

Takeishi, Y., Fujikane, R., Rikitake, M., Obayashi, Y., Sekiguchi, M., and Hidaka, M. (2020). SMARCAD1-mediated Recruitment of the DNA Mismatch Repair Protein MutLα to MutSα on Damaged Chromatin Induces Apoptosis in Human Cells. *J. Biol. Chem.* 295, 1056–1065. doi:10.1016/s0021-9258(17)49915-7

Terui, R., Nagao, K., Kawasoe, Y., Taki, K., Higashi, T. L., Tanaka, S., et al. (2018). Nucleosomes Around a Mismatched Base Pair Are Excluded via an Msh2-dependent Reaction with the Aid of SNF2 Family ATPase Smarcad1. *Genes Dev.* 32, 806–821. doi:10.1101/gad.310995.117

Tham, K.-C., Kanaar, R., and Lebbink, J. H. G. (2016). Mismatch Repair and Homeologous Recombination. *DNA repair* 38, 75–83. doi:10.1016/j.dnarep.2015.11.010

Thomsen, M. C. F., and Nielsen, M. (2012). Seq2Logo: a Method for Construction and Visualization of Amino Acid Binding Motifs and Sequence Profiles Including Sequence Weighting, Pseudo Counts and Two-Sided Representation of Amino Acid Enrichment and Depletion. *Nucleic acids Res.* 40, W281–W287. doi:10.1093/nar/gks469

Tishkoff, D. X., Filosi, N., Gaida, G. M., and Kolodner, R. D. (1997). A Novel Mutation Avoidance Mechanism Dependent on *S. cerevisiae* RAD27 Is Distinct from DNA Mismatch Repair. *Cell* 88, 253–263. doi:10.1016/s0092-8674(00)81846-2

Traver, S., Coulombe, P., Peiffer, I., Hutchins, J. R. A., Kitzmann, M., Latreille, D., et al. (2015). MCM9 Is Required for Mammalian DNA Mismatch Repair. *Mol. Cell* 59, 831–839. doi:10.1016/j.molcel.2015.07.010

Unk, I., Hajdú, I., Blastyák, A., and Haracska, L. (2010). Role of Yeast Rad5 and its Human Orthologs, HLTF and SHPRH in DNA Damage Tolerance. *DNA repair* 9, 257–267. doi:10.1016/j.dnarep.2009.12.013

Unk, I., Hajdú, I., Fátyol, K., Hurwitz, J., Yoon, J.-H., Prakash, L., et al. (2008). Human HLTF Functions as a Ubiquitin Ligase for Proliferating Cell Nuclear Antigen Polyubiquitination. *Proc. Natl. Acad. Sci. U.S.A.* 105, 3768–3773. doi:10.1073/pnas.0800563105

Unk, I., Hajdú, I., Fátyol, K., Szakál, B., Blastyák, A., Bermudez, V., et al. (2006). Human SHPRH Is a Ubiquitin Ligase for Mms2-ubc13-dependent Polyubiquitylation of Proliferating Cell Nuclear Antigen. *Proc. Natl. Acad. Sci. U.S.A.* 103, 18107–18112. doi:10.1073/pnas.0608595103

Varadi, M., Anyango, S., Deshpande, M., Nair, S., Natassia, C., Yordanova, G., et al. (2022). AlphaFold Protein Structure Database: Massively Expanding the Structural Coverage of Protein-Sequence Space with High-Accuracy Models. *Nucleic acids Res.* 50, D439–D444. doi:10.1093/nar/gkab1061

Xu, X., Lin, A., Zhou, C., Blackwell, S. R., Zhang, Y., Wang, Z., et al. (2016). Involvement of Budding Yeast Rad5 in Translesion DNA Synthesis through Physical Interaction with Rev1. *Nucleic Acids Res.* 44, 5231–5245. doi:10.1093/nar/gkw183

Yan, D., and Jin, Y. (2012). Regulation of DLK-1 Kinase Activity by Calcium-Mediated Dissociation from an Inhibitory Isoform. *Neuron* 76, 534–548. doi:10.1016/j.neuron.2012.08.043

Yuan, F., Gu, L., Guo, S., Wang, C., and Li, G.-M. (2004). Evidence for Involvement of HMGB1 Protein in Human DNA Mismatch Repair. *J. Biol. Chem.* 279, 20935–20940. doi:10.1074/jbc.m401931200

Zhang, M., Huang, N., Yang, X., Luo, J., Yan, S., Xiao, F., et al. (2018). A Novel Protein Encoded by the Circular Form of the SHPRH Gene Suppresses Glioma Tumorigenesis. *Oncogene* 37, 1805–1814. doi:10.1038/s41388-017-0019-9

**Conflict of Interest:** The authors declare that the research was conducted in the absence of any commercial or financial relationships that could be construed as a potential conflict of interest.

**Publisher's Note:** All claims expressed in this article are solely those of the authors and do not necessarily represent those of their affiliated organizations, or those of the publisher, the editors and the reviewers. Any product that may be evaluated in this article, or claim that may be made by its manufacturer, is not guaranteed or endorsed by the publisher.

frontiers | Frontiers in Cell and Developmental Biology

ORIGINAL RESEARCH
published: 21 June 2022
doi: 10.3389/fcell.2022.831741

# The C-Terminal Domain of Y-Box Binding Protein 1 Exhibits Structure-Specific Binding to Poly(ADP-Ribose), Which Regulates PARP1 Activity

*Konstantin N. Naumenko[1†], Mariya V. Sukhanova[1†], Loic Hamon[2], Tatyana A. Kurgina[1,3], Rashid O. Anarbaev[1,3], Aswin Mangerich[4], David Pastré[2] and Olga I. Lavrik[1,3]**

[1]LBCE, Institute Chemical Biology and Fundamental Medicine (ICBFM), Novosibirsk, Russia, [2]SABNP, Univ Evry, INSERM U1204, Université Paris-Saclay, Evry, France, [3]Department of Natural Sciences, Novosibirsk State University, Novosibirsk, Russia, [4]Department of Biology, Molecular Toxicology Group, University of Konstanz, Konstanz, Germany

OPEN ACCESS

**Edited by:**
Robert W. Sobol,
University of South Alabama,
United States

**Reviewed by:**
Valentyn Oksenych,
University of Oslo, Norway
Kate Saville,
University of South Alabama,
United States

***Correspondence:**
Olga I. Lavrik
lavrik@niboch.nsc.ru

[†]These authors have contributed equally to this work

**Specialty section:**
This article was submitted to Molecular and Cellular Pathology, a section of the journal Frontiers in Cell and Developmental Biology

**Received:** 08 December 2021
**Accepted:** 25 May 2022
**Published:** 21 June 2022

**Citation:**
Naumenko KN, Sukhanova MV, Hamon L, Kurgina TA, Anarbaev RO, Mangerich A, Pastré D and Lavrik OI (2022) The C-Terminal Domain of Y-Box Binding Protein 1 Exhibits Structure-Specific Binding to Poly(ADP-Ribose), Which Regulates PARP1 Activity. Front. Cell Dev. Biol. 10:831741. doi: 10.3389/fcell.2022.831741

Y-box-binding protein 1 (YB-1) is a multifunctional protein involved in the regulation of gene expression. Recent studies showed that in addition to its role in the RNA and DNA metabolism, YB-1 is involved in the regulation of PARP1 activity, which catalyzes poly(ADP-ribose) [PAR] synthesis under genotoxic stress through auto-poly(ADP-ribosyl)ation or protein trans-poly(ADP-ribosyl)ation. Nonetheless, the exact mechanism by which YB-1 regulates PAR synthesis remains to be determined. YB-1 contains a disordered Ala/Pro-rich N-terminal domain, a cold shock domain, and an intrinsically disordered C-terminal domain (CTD) carrying four clusters of positively charged amino acid residues. Here, we examined the functional role of the disordered CTD of YB-1 in PAR binding and in the regulation of PARP1-driven PAR synthesis *in vitro*. We demonstrated that the rate of PARP1-dependent synthesis of PAR is higher in the presence of YB-1 and is tightly controlled by the interaction between YB-1 CTD and PAR. Moreover, YB-1 acts as an effective cofactor in the PAR synthesis catalyzed by the PARP1 point mutants that generate various PAR polymeric structures, namely, short hypo- or hyperbranched polymers. We showed that either a decrease in chain length or an increase in branching frequency of PAR affect its binding affinity for YB-1 and YB-1–mediated stimulation of PARP1 enzymatic activity. These results provide important insight into the mechanism underlying the regulation of PARP1 activity by PAR-binding proteins containing disordered regions with clusters of positively charged amino acid residues, suggesting that YB-1 CTD-like domains may be considered PAR "readers" just as other known PAR-binding modules.

**Keywords: Y-box binding protein 1, PARP1, trans-poly(ADP-ribosyl) ation, poly(ADP-ribose), disordered C-terminal domain**

## INTRODUCTION

YB-1 is a multifunctional RNA-binding protein mainly involved in RNA metabolism and other processes related to the maintenance of genome stability in animals (Mordovkina et al., 2020; Sangermano et al., 2020). Initially, YB-1 was identified as an RNA-binding protein implicated in the regulation of transcription and RNA metabolism (Eliseeva et al., 2011). YB-1 has mainly a cytoplasmic localization and is reported to associate with cytoplasmic ribonucleoprotein (mRNP) granules (Nekrasov et al., 2003; Skabkin et al., 2004). On the other hand, YB-1 displays a nuclear localization in aggressive types of cancer resistant to chemotherapy which influences the sensitivity of cancer cells to anticancer drugs and the efficiency of chemotherapy (Bargou et al., 1997; Shibahara et al., 2001; Matsumoto and Bay, 2005; Kosnopfel et al., 2014; Bates et al., 2020). In addition, the translocation of YB-1 from the cytoplasm to nucleus has been reported, mainly, upon treatment with a DNA-damaging drug; these data support the idea that YB-1 has nuclear-specific functions in cancer cells (Stein et al., 2001; Fujita et al., 2005; Sorokin et al., 2005). YB-1 actions in the cytoplasm are predominantly associated with mRNA metabolism (Budkina et al., 2020), while the nuclear function of YB-1—in addition to its described role as a transcription factor—remains to be elucidated (Sangermano et al., 2020). The participation of YB-1 in DNA repair was recently suggested because of its interactions with damaged DNA and several repair proteins identified in in vitro studies using recombinant proteins and cells (Hasegawa et al., 1991; Ise et al., 1999; Das et al., 2007; Gao et al., 2009; Fomina et al., 2015; Alemasova et al., 2016; Alemasova et al., 2017). A possible mechanism by which YB-1 is connected with DNA repair and genome stability could be its interaction with PARP1 (Alemasova et al., 2015), which is a key DNA repair–regulatory protein (Chaudhuri and Nussenzweig, 2017; Lavrik, 2020). PARP1 is a member of the ADP-ribosyltransferases diphtheria toxin-like family [ARTDs, also known as poly(ADP-ribose) polymerases (PARPs)], which catalyze the transfer of ADP-ribose units from $NAD^+$ onto amino acid residues (aa) of target proteins resulting in their mono- or poly (ADP-ribosyl)ation (MARylation or PARylation) (Lüscher et al., 2021). PARP1 is well known primarily as a DNA base excision factor and a single-strand break repair factor that is recruited to DNA damage and forms DNA repair foci, facilitating the repair process (Hanzlikova et al., 2017; Polo et al., 2019; Lavrik, 2020). PARP1 activates upon binding to damaged DNA thereby resulting in the synthesis of a PAR and a covalent modification of itself and other nuclear proteins (Alemasova and Lavrik, 2019). PAR synthesis is considered a local signal at sites of DNA damage, which could attract proteins through noncovalent PAR binding or/and modulate a protein's function *via* the covalent modification of the protein with PAR (d'Amours et al., 1999; Teloni et al., 2015). In recent years, some proteins modulating PARP1 enzymatic activity were identified (Ouararhni et al., 2006; Masaoka et al., 2012; Sun, X. et al., 2016; Gibbs-Seymour et al., 2016); thus, PARP1-interacting and PAR-binding partners are under intensive investigation (Dasovich et al., 2021; Kliza et al., 2021). In this context, YB-1 is an attractive candidate for a PARP1-interacting partner because YB-1 is a target for the covalent PARylation (trans-PARylation) by PARP1 and shows noncovalent binding to PAR *in vitro* (Alemasova et al., 2015; Alemasova et al., 2019). Both poly- and mono-(ADP-ribosyl) ation of YB-1 by PARP1, PARP2, PARP10, or PARP14 were revealed in proteomic studies of the ADP-ribosylome in various cell lines (Gagne et al., 2012; Carter-O'Connell et al., 2014; Carter-O'Connell et al., 2016; Zhen et al., 2017; Kalesh et al., 2019). Our previous research indicates that YB-1 modulates PARP1 activity and can be trans-PARylated *in vitro* (Alemasova et al., 2015; Alemasova et al., 2018; Naumenko et al., 2020). Besides, the regulation of PARP1 activity by YB-1 depends on the formation of PARP1–YB-1 complexes with damaged DNA and YB-1 interaction with PAR, which is accompanied by a decrease in the average PAR polymer size formed during PARP1 auto-PARylation (Naumenko et al., 2020). The effect of YB-1 on PARP1 activity appears to be related to the ability of this protein to bind both PAR and damaged DNA (Naumenko et al., 2020). YB-1 consists of a disordered alanine/proline-rich (AP) domain, a cold-shock domain (CSD), and a long disordered C-terminal domain (CTD) carrying clusters of negatively and positively charged residues ~30 aa each (Eliseeva et al., 2011). Structurally, the CSD is similar to the oligonucleotide/oligosaccharide-binding fold (OB-fold), contains RNA-binding motifs RNP-1 and RNP-2, and participates in specific interaction with RNA and sequence-independent binding to single- or double-stranded DNA (Tanabe, Y., 2015, Ise, T 1999; Bouvet et al., 1995b). The CTD is involved in nonspecific nucleic-acid binding and seems to mainly stabilize the protein–nucleic acid interactions (Kloks et al., 2002; Kim et al., 2013). PAR is regarded as a nucleic-acid–like polymer and has variable chain length reaching 200 or more ADP-ribose units (Althaus and Richter, 1987; Alvarez-Gonzalez et al., 1987). Additionally, the PAR polymer has either linear or branched structure (Hayashi et al., 1983). In contrast to DNA (or RNA), PAR has a ribose-phosphate-phosphate-ribose backbone and contains two negative charges per nucleotide unit thus being more acidic than DNA or RNA (Alvarez-Gonzalez and Jacobson, 1987). RNA/DNA-binding proteins can directly interact with PAR, and PAR-binding modules in these proteins often overlap with DNA/RNA-binding domains, which can be structured or disordered (Teloni and Altmeyer, 2015). Accordingly, both the CSD and CTD of YB-1 are involved in DNA/RNA binding and may interact with PAR. Our previous studies have revealed that the CTD of YB-1 is implicated in the regulation of PARP1 activity, namely, a deletion of the CTD abrogates both YB-1–dependent stimulation of PARP1 and YB-1 trans-PARylation (Naumenko et al., 2020). These results suggest that the CTD is required for the YB-1 binding to PAR or formation of YB-1–PARP1–DNA complexes, thereby affecting the PARP1 activity.

In the present study, we tested the hypothesis of YB-1 binding to PAR and DNA *via* a charge-dependent mechanism. We demonstrated a strong correlation between the positive charge of the YB-1 CTD and its ability to bind PAR and damaged DNA and to be trans-PARylated. The data showed that the deletion of

basic aa 230–324 in the CTD severely reduces YB-1 binding to PAR and has only a modest impact on binding affinity for DNA. The deletion of three positively charged amino acids clusters in the YB-1 CTD caused a loss of 1) YB-1 binding to PAR and to damaged DNA and 2) YB-1 trans-PARylation by PARP1. Furthermore, PAR structural features such as branching and chain length were found to influence noncovalent binding of YB-1 and to have a strong influence on YB-1 trans-PARylation. Thus, the CTD can be considered a specific PAR-interacting module that is capable of binding to a wide range of PAR polymer structures having various polymer lengths and frequencies of branching.

# MATERIALS AND METHODS

## Chemicals

Radioactive [$\alpha$-$^{32}$P] ATP was produced in the Laboratory of Biotechnology at ICBFM (Siberian Branch of Russian Academy of Sciences [SB RAS], Novosibirsk, Russia). Oligodeoxynucleotides were synthesized by Biosset (Russia) and the Laboratory of Biomedical Chemistry at ICBFM (SB RAS, Novosibirsk, Russia). $NAD^+$ and $\beta$-nicotinamide mononucleotide were purchased from Sigma-Aldrich (United States, catalog # 481911 and N3501, respectively), whereas reagents for buffer and electrophoresis components from Sigma-Aldrich, United States (Tris, catalog #T6791; BSA, catalog # A9418; EDTA, catalog #E5134; HEPES, catalog #H3375), PanReacAppliChem, Germany (acrylamide/bis-acrylamide, catalog # A1089/A3636; Urea catalog # A1049), Molecular Group (DTT, catalog # 19733320), Merk (NaCl, catalog # 106404).

## Plasmid Construction

Plasmid pET-3-1-YB-1 containing full length (FL) cDNA of rabbit *YB-1* is a generous gift from Drs. L.P. Ovchinnikov and D.A. Kretov (Institute of Protein Research RAS, Moscow, Russia). PCR products containing the full-length YB-1–coding sequence or a sequence encoding a truncated form of YB-1 (consisting of aa 1–184, 1–230, or 1–279) were cloned into the pLate-31 plasmid vector according to the recommended protocol (ThermoFisher, United States, catalog #K1271). The sequences of mutant genes were confirmed at the SB RAS Genomics Core Facility (ICBFM SB RAS, Novosibirsk, Russia).

Plasmid pET32a-hPARP-1-His is a kind gift from Dr. M. Satoh (Université Laval, Québec, Canada). Mutation Y986S, Y986H, or G972R within the *PARP1* coding sequence was generated by site-directed mutagenesis with Q5-polymerase (New England Biolabs, United States, catalog #M0491S). The sequences of mutant *PARP1* genes were confirmed at the SB RAS Genomics Core Facility.

## Protein Expression and Purification

Recombinant YB-1 and its mutants [YB-1 ($\Delta$1), YB-1 ($\Delta$1-2), or YB-1 ($\Delta$1-2-3)] were overexpressed in *Escherichia coli* BL21 (DE3) and purified. YB-1 was purified by Ni-NTA affinity chromatography (GE Healthcare United States, catalog # GE17-5255-01), Mono-S chromatography (GE Healthcare, United States catalog # GE17-5168-01), and Superdex 16/600 chromatography (GE Healthcare, United States, catalog # GE28-9893-35) as described earlier (Alemasova et al., 2017). YB-1 mutants were purified by Ni-NTA and Mono-S chromatography.

Recombinant wild-type (wt) PARP1 and mutants PARP1$^{Y986S}$, PARP1$^{Y986H}$, and PARP1$^{G972R}$ were overexpressed in *E. coli* Rosetta (DE3)pLysS (Novogen, catalog # 70956-3) and purified by Ni-NTA agarose (GE Healthcare United States, catalog # GE17-5255-01) affinity chromatography, HiTrap Heparin High Performance (GE Healthcare, United States, catalog # GE17-0407-01) affinity chromatography, and deoxyribonucleic acid–cellulose (single-stranded calf thymus DNA) (Sigma-Aldrich, United States, catalog #D8273) affinity chromatography as described previously (Sukhanova et al., 2004).

Yeast nicotinamide mononucleotide adenylyltransferase (NMNAT) was kindly provided by Dr. S.I. Shram (Institute of Molecular Genetic Russian Academy of Science, Moscow, Russia).

## DNA Substrates

A fluorescein (FAM)-labeled DNA duplex (Nick) was obtained by hybridization of 5′-FAM- CCGCTATTTCAACCCTTTGCA GTCCCAGAAGG-3′ with complementary oligonucleotides (5′-GGCGATAAAGTTGGG-3′ and 5′-pAAACGTCAGGGTCTTCC-3′) in a 1.0:1.5:1.5 ratio. The oligonucleotide mixture was incubated for 5 min at 95°C and then slowly cooled to room temperature.

A damaged pBR322 plasmid (New England BioLabs, Catalog #N3033L) was prepared by heat and acid treatment in combination with apurinic/apyrimidinic endonuclease 1 (APE1)-catalyzed cleavage of apurinic/apyrimidinic sites (Sukhanova et al., 2004).

## Preparation of Protein-free poly(ADP-Ribose) [PAR]

[$^{32}$P]NAD labeled on the adenylate phosphate was synthesized using [$\alpha^{32}$P]ATP (3000 Ci/mmol) and $\beta$-nicotinamide mononucleotide in a reaction catalyzed by NMNAT as described elsewhere (Alemasova et al., 2015). [$^{32}$P]-labeled PAR was synthesized in a 200 µL reaction mixture consisting of 50 mM Tris-HCl pH 8.0, 40 mM NaCl, 1 mM dithiothreitol (DTT), 5 mM $MgCl_2$, 100 nM Nick, 200 nM PARP1 (or 500 nM PARP1$^{Y986S}$, PARP1$^{Y986H}$, or PARP1$^{G972R}$), and 10 µM [$^{32}$P] $NAD^+$ (20 µCi). The mixture was incubated at 37°C for 30 min. After that, DNA was removed by DNase I (New England BioLabs, Catalog #M0303L) treatment. The poly (ADP-ribosyl)ated PARP1 was incubated with 0.1 M NaOH at 37°C for 40 min, and then pH was adjusted to 7.5 with 0.1 M HCl. PAR was isolated from the resulting sample by phenol:chloroform:isoamyl alcohol (25:24:1) (Sigma-Aldrich, catalog #P2069) extraction and purified by ethanol precipitation. Resultant PAR samples were analyzed by electrophoresis in a denaturing urea 20% polyacrylamide gel with subsequent phosphorimaging. [$^{32}$P]-labeled–PAR concentration was estimated as the amount of monomeric ADP-ribose

incorporated into a polymer. [$^{32}$P]NAD$^+$ signal intensity (arbitrary units, a.u.) was used as a standard. The amounts of [$^{32}$P]PAR produced were calculated by acquiring the signals from PAR resolved by the urea polyacrylamide gel electrophoresis (PAGE).

## A Radioactive Assay of PARP1 Activity and Protein Trans- and Auto-PARylation

To calculate the initial rates of PAR synthesis in the reaction catalyzed by PARP1 (or its mutants) in the presence or absence of YB-1 full length (FL) (or its mutants), the kinetics of [$^{32}$P]-labeled–ADP-ribose incorporation into an acid-insoluble precipitate were assayed with [$^{32}$P]NAD$^+$ as a substrate. The reaction mixtures consisted of 50 mM Tris-HCl pH 8.0, 40 mM NaCl, 1 mM DTT, 100 μg/ml BSA, 10 mM EDTA, 100 nM PARP1 wt [or PARP1$^{Y986S}$, PARP1$^{Y986H}$, or PARP1$^{G972R}$], 0.5–2.5 μM YB-1(FL) or 2.0 μM mutant YB-1, and 0.5 $OD_{260}$/ml DNase I–activated calf thymus DNA ($DNA_{act}$). The reaction components were mixed on ice. The reactions were initiated by the addition of NAD$^+$ (0.4 μCi [$^{32}$P]NAD$^+$) to a final concentration of 20 μM. The mixtures were incubated at 30°C, 5 μl aliquots were taken at 1, 3, 5 and 10 min. The reactions were stopped by placing aliquots dropwise on Whatman 1 paper filters preimpregnated with 10% trichloroacetic acid (TCA). The PARylated proteins were precipitated on filters in the presence of TCA. To remove unreacted NAD$^+$, the filters were washed four times with 5% TCA, then TCA was removed by means of 96% ethanol, and the filters were dried. [$^{32}$P]-labeled–ADP-ribose incorporation into the acid-insoluble material (PARylated proteins) was quantified by radioautography using Typhoon FLA 7000 (GE Healthcare, United States). The data were plotted ($p$ versus t) and fitted by logistic Equation 1:

$$[P] = [P_{max}] \cdot \left(1 - e^{-kt}\right) \quad (1)$$

$$v = \frac{d[P]}{dt} = k \cdot [P_{max}] \cdot e^{-kt} \quad (2)$$

$$v_0 = \left.\frac{d[P]}{dt}\right|_{t=0} = k \cdot [P_{max}] \quad (3)$$

where $p$ is product PARP1-(ADP-ribose)n, $P_{max}$ is maximum synthesis product concentration at $t_\infty$, $t$ is time, k is first-order rate constant. Calculated kinetic parameters, [$P_{max}$] and k, can be used to calculate the initial rate of the reaction (Equation 3).

The protein PARylation assay was performed in reaction mixtures composed of 50 mM Tris-HCl pH 8.0, 40 mM NaCl, mM DTT, 100 μg/ml BSA, 10 mM EDTA, 100 nM PARP1 wt (or PARP1$^{Y986S}$, PARP1$^{Y986H}$, or PARP1$^{G972R}$), 0.5–2.5 μM YB-1(FL) [or 2 μM YB-1 (Δ1), YB-1 (Δ1-2), or YB-1 (Δ1-2-3)], and 0.5 $OD_{260}$/ml activated DNA. The reactions were initiated by the addition of NAD$^+$ (0.4 μCi [$^{32}$P]NAD$^+$) to a final concentration of 20 μM and were allowed to proceed at 30°C for 10 min. The reactions were stopped by the addition of SDS sample loading buffer and heating for 1.5 min at 97°C and were analyzed by denaturing SDS-PAGE as described elsewhere (Laemmli, 1970). Bands of proteins labeled with [$^{32}$P]ADP-ribose were visualized and quantified by phosphorimaging on Typhoon FLA 7000 (GE Healthcare, United States) and in the Quantity One Basic software.

## Evaluation of Half-Maximal Effective Concentrations ($EC_{50}$) of YB-1–PAR Complexes

Complexes of YB-1(FL) or one of its mutants with PAR were subjected to an electrophoretic mobility shift assay (EMSA). The reaction was carried out in a mixture composed of 50 mM Tris-HCl pH 8.0, 40 mM NaCl, 1 mM DTT, 100 μg/ml BSA, 60 nM [$^{32}$P]PAR (estimated by the calculation of the [$^{32}$P]ADP-ribose amount incorporated into the polymer), and various concentrations of YB-1(FL) or its mutants. The reaction mixtures were incubated at 37°C for 5 min. Loading buffer consisting of 20% glycerol and 0.015% bromophenol blue was then added to the samples. Nondenaturing PAGE in a 5% gel (acrylamide/bis-acrylamide at 37.5:1) was performed for the analysis of complexes PAR–YB-1(FL) and PAR-YB-1 (Δ1), 10% PAGE (acrylamide/bis-acrylamide at 75:1) for the analysis of complexes PAR–YB-1 (Δ1-2) and PAR–YB-1 (Δ1-2-3), and 10% PAGE (acrylamide/bis-acrylamide at 75:1) for the analysis of complexes PAR$^{Y986S}$–YB-1(FL), PAR$^{Y986H}$–YB-1(FL), and PAR$^{G972R}$–YB-1(FL) in TBE buffer at 4°C followed by phosphorimaging on a Typhoon FLA 9500 Biomolecular Imager (GE Healthcare). Bound- and unbound-PAR signals were quantified in the Quantity One Basic software. The data were fitted to an equation using the SigmaPlot software.

## Fluorescence Anisotropy Measurements of the Binding of YB-1 or its Mutants to DNA

The anisotropy measurements were performed at 25°C on a CLARIOstar multifunctional microplate reader and in the MARS Data Analysis Software (BMG LABTECH GmbH, Germany). Excitation wavelength was 482 nm (the 482-16 filter plus dichroic filter LP504), and emission wavelength was 530 nm (530-40 filter). The binding reactions were conducted in Corning black 384-well polystyrene assay plates. Reaction mixtures consisting of a buffer (50 mM Tris-HCl pH 8.0, 40 mM NaCl, 1 mM DTT, and 100 μg/ml BSA), 0–6000 nM YB-1(FL) [or YB-1 (Δ1), YB-1 (Δ1-2), or 0–20000 nM YB-1 (Δ1-2-3)], and 50 nM FAM-labeled Nick were prepared on ice.

The data were plotted (F versus C) and fitted to a four-parameter logistic equation:

$$F = F_0 + (F_{max} - F_0) \div \left[1 + \left[\frac{EC_{50}}{C}\right]^n\right]$$

where F is the measured anisotropy (mA) of a solution containing the FAM-labeled DNA at a given concentration (C) of YB-1 protein, $F_0$ represents anisotropy of a solution of the labeled DNA alone, $F_{max}$ is anisotropy of the DNA saturated with YB-1, $EC_{50}$ denotes the concentration of protein at which $F = (F_{max}–F_0)/2$, and n is the Hill coefficient.

## Dynamic Light Scattering Measurement of the Size Distribution of PARylated PARP1 and its Mutants

These measurements were performed to determine the hydrodynamic radius ($R_h$) of PARylated molecules. All DLS

measurements were conducted as described previously (Vasil'eva et al., 2019). PARylation reactions were carried out directly in a quartz cuvette used for DLS measurements. The reaction mixture (25 μL) was composed of 25 mM HEPES-NaOH pH 7.5, 100 mM NaCl, 1 mM DTT, 10 mM $MgCl_2$, 2.5 μM Nick, and 2.5 μM PARP1 wt (or $PARP1^{Y986S}$, $PARP1^{Y986H}$ or $PARP1^{G972R}$). Samples were equilibrated for 1 min and then the auto-PARylation reactions were initiated by the addition of $NAD^+$ to a final concentration of 1 mM. $R_h$ measurement was performed every 3 min after the PARylation reaction initiation. After 40-min incubation, the reaction was stopped by the addition of EDTA to a final concentration of 10 mM, and $R_h$ was measured in the EDTA-treated sample.

$R_h$ of the particles was calculated *via* the Stokes–Einstein equation under the assumption of the spherical shape of the PARylated molecules:

$$R_h = \frac{k \cdot T}{6 \cdot \pi \cdot \eta \cdot D}$$

where D is the diffusion coefficient determined by DLS, k denotes Boltzmann's constant, T is absolute temperature, and η represents solvent viscosity assumed here to be the viscosity of water containing buffer components at 25°C.

## Atomic Force Microscopy Experiments and Image Analysis

For experiments with the auto-PARylation of PARP1 wt or its mutants ($PARP1^{Y986S}$ and $PARP1^{Y986H}$), 40 nM PARP1 was incubated with 10 ng/μL pBR plasmid in a buffer (50 mM Tris-HCl pH 8.0, 25 mM NaCl, 10 mM $MgCl_2$, and 1 mM DTT). The reactions were initiated by the addition of $NAD^+$ to a final concentration of 0.25 mM followed by incubation for 1 h at 37°C. Next, the samples were diluted 10-fold with AFM deposition buffer (12.5 mM HEPES-NaOH pH 8.0, 12.5 mM KCl, and 1 mM DTT) and immediately deposited on a mica surface. For AFM imaging, the samples were processed as described before (Sukhanova et al., 2016). After that, the mica surface was rinsed with a 0.02% uranyl acetate solution, rapidly rinsed with pure water (Millipore), and air-dried before AFM imaging in ambient air (Révet et al., 1998) by means of Nanoscope V Multimode 8 (Bruker, Santa-Barbara, CA, United States) in peakforce tapping (PFT) mode with Scanasyst-Air probes (Bruker). In this experiment, continuous force–distance curves were recorded at 2048 × 2048 pixels and a line rate of 1.5 Hz, and the tip was oscillated in the vertical direction with an amplitude of 100–300 nm at low frequency (1–2 kHz).

# RESULTS

## Truncation of C-Terminal Domain of YB-1 Impairs PAR Binding

Two possible mechanisms have been proposed to explain YB-1–dependent regulation of PARP1 activity: {1} formation of a heterotrimeric PARP1–YB-1–damaged DNA complex, where YB-1 is a predominant target of PARylation, and {2} formation of a YB-1 complex with PAR covalently attached to PARP, where again YB-1 is the main target of the modification (Naumenko et al., 2020). In both cases, the interaction of YB-1 with damaged DNA or PAR influences the regulation of PARylation reactions. Previously, we showed that the CTD is essential for the control of PARP1 activity by YB-1 *in vitro*, whereas the AP-CSD fragment has only a minor influence on PARP1 activity (Naumenko et al., 2020). Therefore, we hypothesized here that efficient formation of a YB-1–PAR or YB-1–damaged DNA complex depends on the positively charged clusters within the CTD. The CTD has been reported to play an important part in the regulation of YB-1 interaction with DNA and RNA, regulation of YB-1 protein–protein interactions, and control over the formation of YB-1 multimers (Tafuri and Wolffe, 1992; Murray, 1994; Bouvet et al., 1995a; Pisarev et al., 2002; Kretov et al., 2019). Nevertheless, general involvement of the CTD in PAR binding is not understood completely. The disordered YB-1 CTD, aa 130–324, is the largest domain of YB-1 which contains four clusters of positively charged residues (aa 136–156, 184–205, 230–251, and 279–296; **Figure 1**). We propose that through electrostatic interactions, positively charged amino acids can contribute to the YB-1 binding to DNA and PAR. Therefore, deletion of these clusters should influence the formation of stable complexes between YB-1 and PAR (or DNA) and reduce the efficiency of YB-1 interaction with these molecules. To assess the contribution of the CTD positively charged clusters to the binding of YB-1 to PAR and DNA, truncated mutants of YB-1 were prepared in this work. These mutants contain deletions of one [YB-1 (Δ1)], two [YB-1 (Δ1-2)], or three [YB-1 (Δ1-2-3)] positively charged clusters in the YB-1 CTD (**Figure 1**). Characteristics of the binding of YB-1(FL) or its deletion mutants to a protein-free PAR polymer were compared by the EMSA (**Figure 2**; **Supplementary Figure S1**: Gel shift).

There was no significant difference in the PAR binding affinity only in the comparison between the YB-1 (Δ1) mutant and YB-1(FL). By contrast, the deletion of two or three positively charged clusters in the C terminus dramatically reduced the ability of YB-1 to bind PAR (**Figure 2**). $EC_{50}$ values of interactions YB-1(FL)–PAR and YB-1 (Δ1)–PAR were two-to four-fold lower (~500 nM) than those of YB-1 (Δ1-2)–PAR (1164 nM) and YB-1 (Δ1-2-3)–PAR (2081 nM). The data suggested that a deletion of at least two positively charged clusters (aa 231–304) in the YB-1 CTD significantly reduces its binding to PAR.

Truncations of the CTD can also weaken YB-1's DNA-binding affinity (Tanabe et al., 2015). To address this point, the efficiency of the binding of YB-1(FL) or its deletion mutants to DNA was measured by fluorescence anisotropy measurements (**Figure 3**). The gradual truncation of the CTD affected the YB-1–DNA interactions by weakening YB-1 binding affinity for DNA. Thus, YB-1 and its mutants bind to DNA with $EC_{50}$ values ranging from 1100 to 3100 nM, and the YB-1 (Δ1-2-3) mutant possesses ~3-fold weaker affinity for DNA than YB-1 (FL) does.

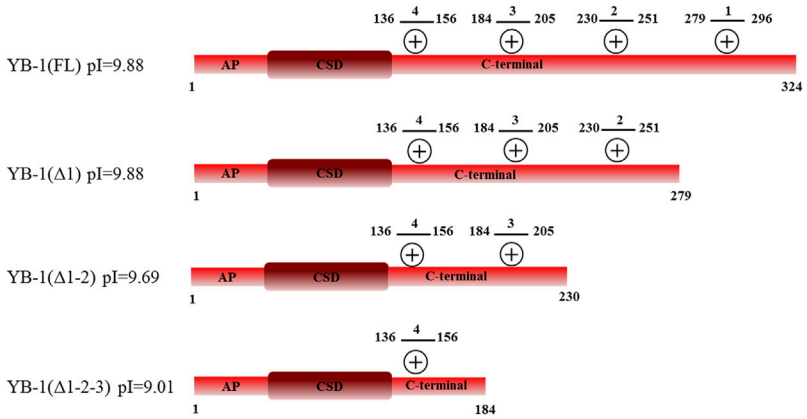


**FIGURE 1 |** Domain structure of YB-1(FL) and its C-terminal deletion mutants: YB-1 (Δ1), YB-1 (Δ1-2), and YB-1 (Δ1-2-3). Designations: alanine/proline-rich (AP) domain, cold-shock domain (CSD), C-terminal domain (CTD) carrying four clusters ($1_{279-296}$, $2_{230-251}$, $3_{184-205}$, $4_{136-156}$) of positively charged residues (+).

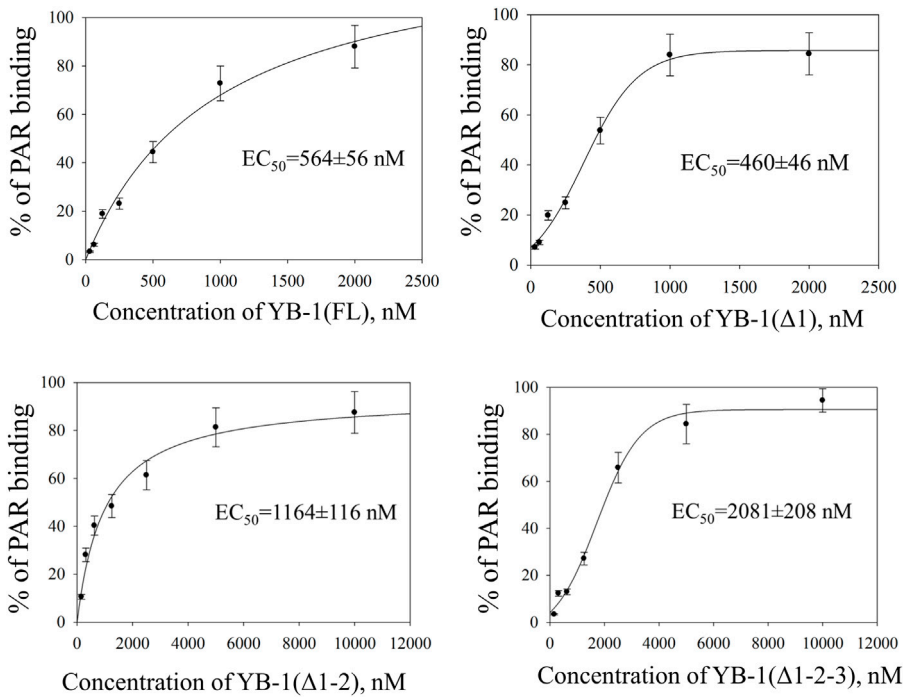


**FIGURE 2 |** CTD shortening weakens YB-1 affinity for PAR. Graphs show quantification of EMSA data (**Supplementary Figure S1**) and represent the mean values of three independent experiments with error bars (±SD). The binding parameters ($EC_{50}$) of YB-1 interaction with PAR was determined as YB-1 concentration resulting in 50% substrate binding. $EC_{50}$ values are the mean (±SD) of three independent experiments. The reaction mixtures contained 60 nM [$^{32}$P]-labeled PAR and YB-1(FL) or its C-terminal deletion mutants at the indicated concentrations.

These data meant that the CTD truncation in YB-1 correlates with attenuation of PAR-binding affinity; in addition, the shortest mutant, YB-1 (Δ1-2-3), also has a much weaker DNA-binding ability in comparison with YB-1 (FL). Moreover, a deletion of two positively charged clusters in the CTD drastically impaired YB-1 binding to PAR, although YB-1 (Δ1-2) still possesses a DNA-binding ability similar to that of the full-length protein.

## Truncation of C-Terminal Domain of YB-1 Decreases the Level of Trans-PARylation of YB-1

Our previous studies have shown that YB-1 stimulates the PAR synthesis catalyzed by PARP1 (Carter-O'Connell et al., 2018; Naumenko et al., 2020). To determine whether our data on YB-1 binding to PAR or DNA are consistent with the influence of YB-1 on PARP1 activity, we analyzed this activity in the presence of

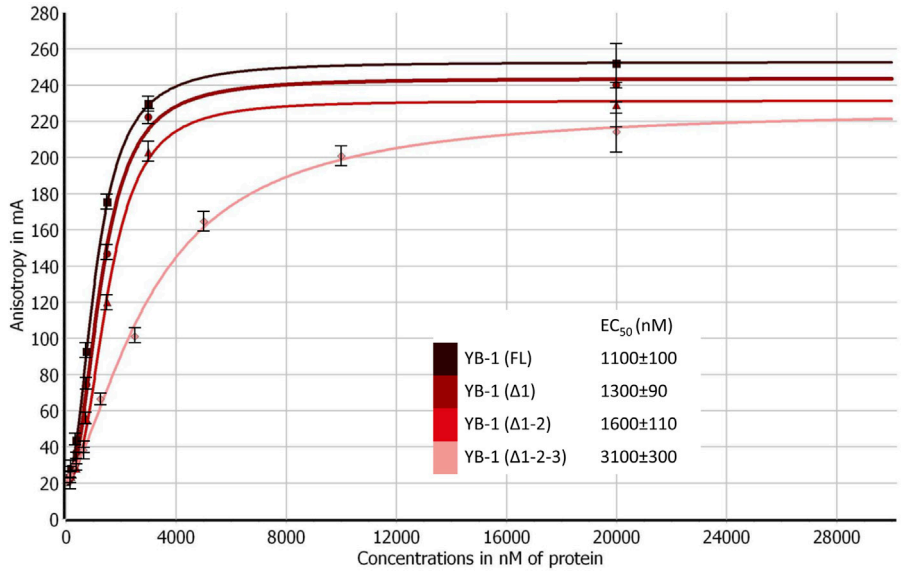


**FIGURE 3 |** CTD shortening weakens YB-1 affinity for damaged DNA. Titrations of FAM-labeled DNA with YB-1(FL) or one of its deletion mutants. The reaction mixtures contained 50 nM FAM-labeled DNA duplex and either YB-1(FL) or one of its C-terminal deletion mutants as indicated. Graphs represent the mean values of three independent experiments with error bars representing ± SD. $EC_{50}$ values are the mean (±SD) of at least three independent experiments.

either YB-1(FL) or one of its deletion mutants: YB-1 (Δ1), YB-1 (Δ1-2), or YB-1 (Δ1-2-3) (**Figures 4**, **5**). First, we estimated PARP1 activity and protein PARylation at various concentrations of YB-1(FL) (**Figure 4**). A higher concentration of YB-1 caused ~ 6.5-fold acceleration of the initial rate of PAR synthesis, accompanied by an increase in both PARP1 auto-PARylation and YB-1 trans-modification (**Figures 4B,C**). These results are consistent with our previous data (Chen et al., 2018; Naumenko et al., 2020).

Next, we tested whether C-terminally truncated forms of YB-1 affect the PARylation reactions catalyzed by PARP1, namely the rates of PAR synthesis and protein PARylation (**Figure 5**). The stimulatory effect of YB-1 on PARP1 activity diminished with gradual shortening of the CTD in YB-1 (**Figure 5B**). Additionally, YB-1 mutants with truncated CTD yielded substantially lower levels of trans-PARylation (**Figures 5C,D**).

Although the presence of YB-1 (Δ1-2) caused only moderate stimulation of PARP1 activity and this mutant yielded only a low level of trans-PARylation, the YB-1 (Δ1-2-3) mutant had no noticeable effect on PARP1 activity and manifested no trans-PARylation (**Figures 5B,C**).

Consequently, the partial CTD deletion in YB-1 affects the interaction of YB-1 with both PAR and DNA and attenuates the stimulatory effect of YB-1 on overall PAR synthesis and own trans-PARylation. In particular, the YB-1 (Δ1-2-3) mutant has a weak affinity for PAR and DNA (**Figures 2**, **3**) and fails to stimulate PARP1 activity. This mutant cannot be trans-PARylated either (**Figure 5**). This finding confirms the importance of the positively charged region of the CTD for PAR and DNA binding by YB-1 and for the regulation of PARylation reactions.

Together with our previous results showing that PARP1 regulation with YB-1 depends on the presence of DNA and formation of ternary complex of PARP1-DNA-YB-1 (Naumenko et al., 2020), these data provide further support of significant contribution of YB-1 interaction with PAR in regulation of PARP1 activity.

## The Affinity of YB-1 for PAR Depends on the Length and Frequency of Branching of the Polymer

Our data indicated that the stimulation of PARP1 activity by YB-1 is affected by the removal of three positively charged clusters in the CTD; for instance, YB-1 (Δ1-2-3) showed weaker binding affinity for PAR (**Figure 2**) and its trans-PARylation was not detectable (**Figure 5**). This result suggested that YB-1–PAR interactions play a pivotal part in the regulation of PARP1 by YB-1 and in YB-1 trans-PARylation reactions. PAR is a nucleic-acid–like polymer composed of ADP-ribose monomers, but in contrast to DNA or RNA, this polymer is known to have branched structures with branching points occurring every 20–50 ADP-ribose units, and its monomers have a twice higher negative charge (Althaus and Richter, 1987). Both the branching frequency of PAR polymers and chain length affect noncovalent protein binding and PAR polymer stability *in vitro* as well as PAR-dependent protein localization and reorganization on nuclear structures in the cell (Panzeter et al., 1992; Fahrer et al., 2007; Fahrer et al., 2010; Aberle et al., 2020; Rudolph et al., 2021). Furthermore, PAR branching frequency is reported to vary during different phases of the DNA damage–induced PARylation reaction, implying biological relevance of PAR structure (Aberle et al., 2020). Taking into account that the YB-1–PAR noncovalent interactions *via* the CTD make YB-1 a target for trans-PARylation (**Figures 2**, **5**), the different chain length and

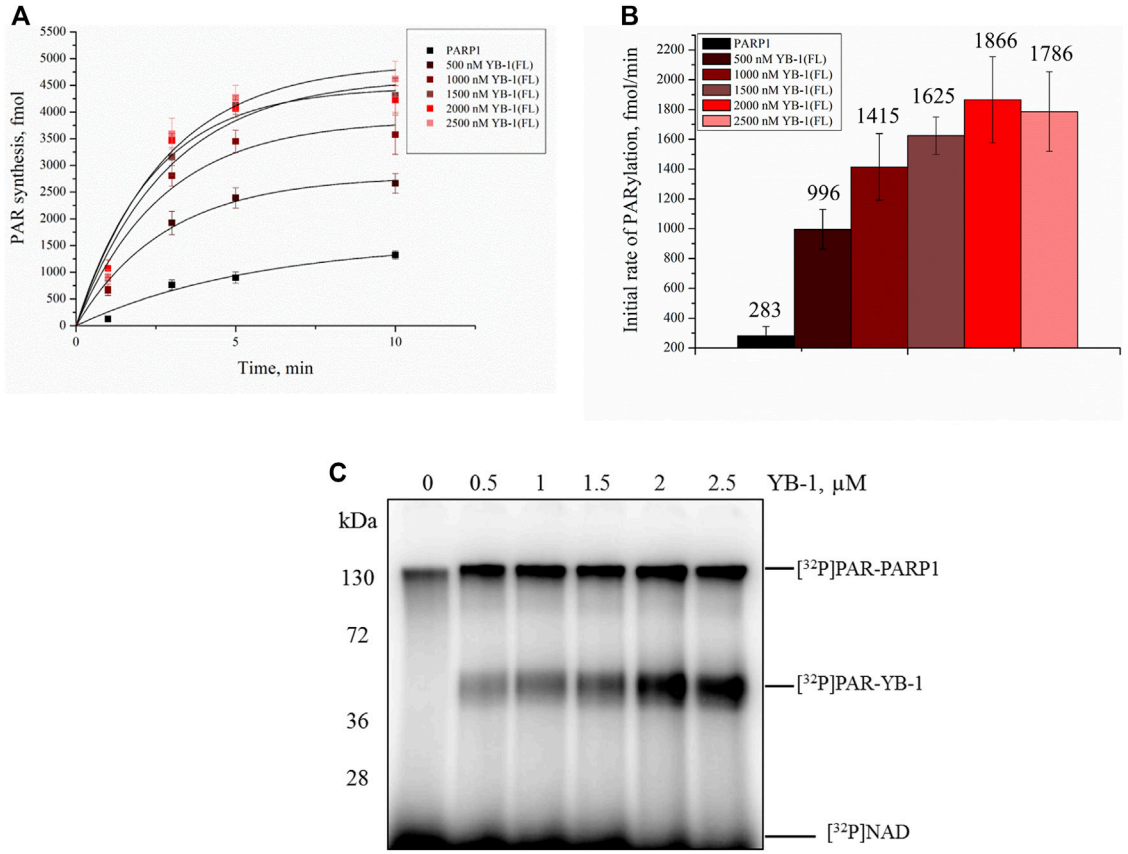


**FIGURE 4 |** YB-1 increases the rate of PAR synthesis by PARP-1 and the PARylation level of protein targets (PARP-1 and YB-1). **(A)** Kinetics of PAR synthesis catalyzed by PARP1 in the absence or presence of various concentrations of YB-1(FL). Graphs represent the mean values of three independent experiments with error bars representing ± SD. **(B)** Initial rates of PAR synthesis estimated in the presence of various concentrations of YB-1(FL). PARP1 at 100 nM was incubated with 0.5 $OD_{260}$/ml $DNA_{act}$, 20 μM $NAD^+$, and [$^{32}$P]NAD (0.4 μCi) in the presence of 0.5–2.5 μM YB-1(FL) as indicated. [$^{32}$P]PAR-modified proteins were precipitated with TCA and quantified radiographically. The initial rates (fmol/min) were determined from a direct analysis of progressive curve **(A)** which yields $P_{max}$ and k (Equations 1 and 3), and represent the mean ± SD of three independent measurements. **(C)** PARP1 auto-PARylation and YB-1 trans-PARylation detected by SDS-PAGE and subsequent phosphorimaging. The reaction mixtures were composed of 100 nM PARP1, 0.5 $OD_{260}$/ml $DNA_{act}$, 0.5–2.5 μM YB-1 (or its mutant as indicated), 20 μM $NAD^+$, and [$^{32}$P]NAD (0.4 μCi).

branching frequency of PAR could regulate YB-1–PARP1 functional interactions. To clarify the influence of PAR structure on YB-1–dependent regulation of PARP1 activity, we used single-point mutants of PARP1 that synthesize short ($PARP1^{Y986S}$), short hyperbranched ($PARP1^{Y986H}$), or short hypobranched ($PARP1^{G972R}$) PAR polymers (Rolli et al., 1997). Previously, the characteristics of PAR polymers produced by these PARP1 mutants have been determined by PAGE, two-dimensional thin-layer chromatography, HPLC and UPLC-MS/MS analysis (Rolli et al., 1997; Aberle et al., 2020). To test the enzymatic activity of the PARP1 mutants, we performed a PAGE-based assay of PARPs' auto-PARylation and of PAR polymers (**Supplementary Figure S2**). Additionally, AFM was carried out to analyze morphological features of the auto-PARylated proteins [PARP1 wt, $PARP1^{Y986S}$, and $PARP1^{Y986H}$; **Figure 6**]. AFM imaging of PARP1 wt or its mutant ($PARP1^{Y986S}$, $PARP1^{Y986H}$, or $PARP1^{G972R}$) after incubation with a DNA substrate in the presence of $NAD^+$ was conducted next. PARP1's and its mutants' activation that was detected at the single-molecule level allowed us to analyze the morphology of the PAR polymers synthesized by these proteins (**Figure 6**). We noticed that these point mutations of PARP1 are accompanied by alterations in the shape and size of auto-PARylated PARP1 molecules detected by AFM. In general, the wild-type PARylated PARP1 molecules were larger than the mutant proteins' molecules. This finding is in agreement with biochemical data indicating that all these mutations of PARP1 lead to synthesis of shorter chain length of PAR compared with the wild type (Rolli et al., 1997; Aberle et al., 2020). The AFM images revealed that PARylated PARP1 wt has star-shaped structure (**Figure 6A**), whereas automodified $PARP1^{Y986S}$ has indeterminate shape and a much smaller size and PAR (**Figure 6C**). PARylated molecules of $PARP1^{Y986H}$ synthesizing hyperbranched PAR look like small sphere-like structures with highly packed polymer chains (**Figure 6B**). We did not observe noticeable features of the morphology between autoPARylated $PARP1^{Y986S}$ and $PARP1^{G972R}$, the shape and size of these molecules were similar (**Figure 6C** and **Supplementary Figure**

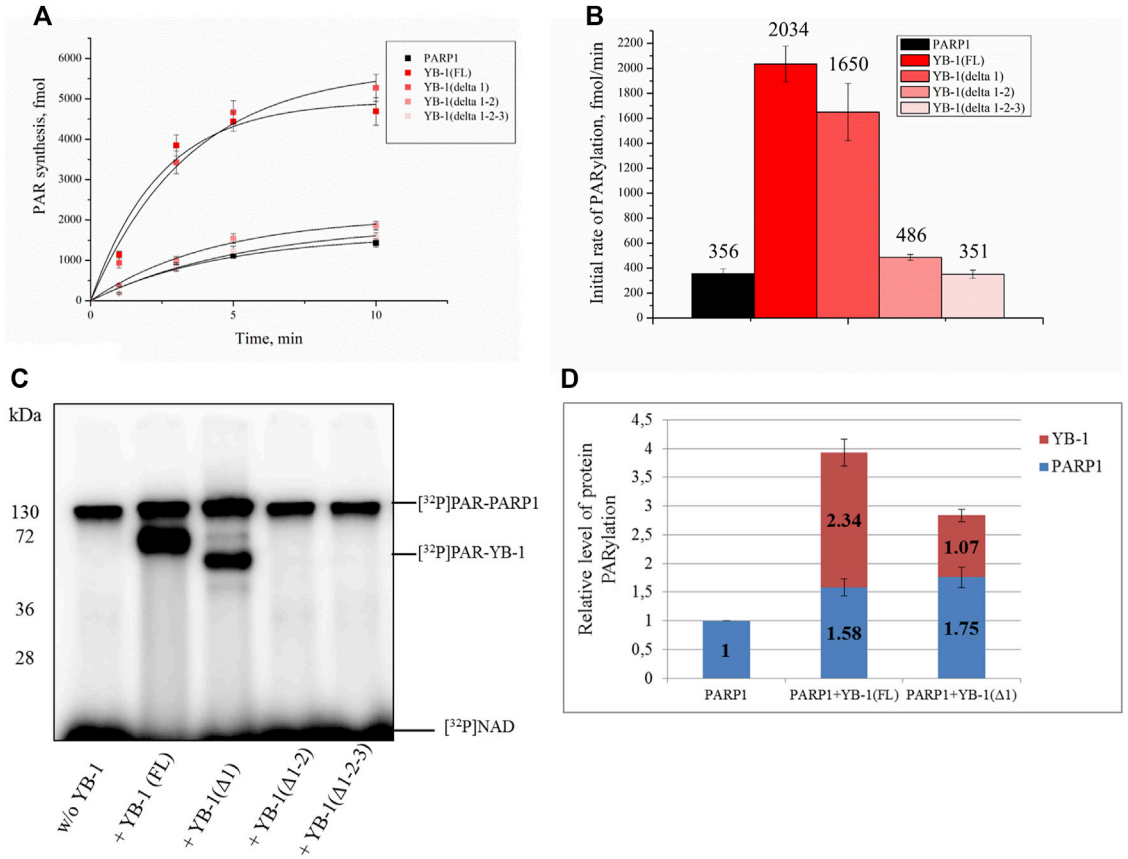


**FIGURE 5 |** A positively charged region of the YB-1 CTD is required for the stimulation of PARP1 activity and YB-1 trans-PARylation. **(A)** Kinetics of the PAR synthesis catalyzed by PARP1 in the absence or presence of YB-1(FL) or its deletion mutants. Graphs represent the mean values of three independent experiments with error bars representing ± SD. **(B)** The initial rates of PAR synthesis estimated in the presence of either YB-1(FL) or one of its deletion mutants. PARP1 at 100 nM was incubated with 0.5 $OD_{260}$/ml $DNA_{act}$, 20 μM $NAD^+$, and [$^{32}$P]NAD (0.4 μCi) in the presence of 2.0 μM YB-1(FL), YB-1 (Δ1), YB-1 (Δ1-2), or YB-1 (Δ1-2-3) as indicated. [$^{32}$P]PAR-modified proteins were precipitated with TCA and quantified radiographically. The initial rates (fmol/min) were determined from a direct analysis of progressive curve **(A)** which yields $P_{max}$ and k (Equations 1 and 3), and represent the mean ± SD of three independent measurements. **(C)** PARP1 auto-PARylation and trans-PARylation of YB-1 mutants detected after SDS-PAGE with phosphorimaging. The reaction mixtures contained 100 nM PARP1, 2 μM YB-1(FL) or its mutant as indicated, 20 μM $NAD^+$ [$^{32}$P]NAD (0.4 μCi), and 0.5 $OD_{260}$/ml $DNA_{act}$. **(D)** The diagram presents relative levels of PARP1 auto-PARylation and YB-1 trans-PARylation (the mean ± SD of three independent experiments). The relative protein PARylation levels were normalized to the auto-PARylation data on PARP1 alone.

**S3**). Thus, the synthesis of the highly branched PAR by $PARP1^{Y986H}$ gives rise to PARylated molecules with compact globular structure. This finding suggests that these PARP1 point mutants and PARP1 wt produce clearly distinct types of PARylated molecules in solution.

We also estimated the size of auto-PARylated proteins by DLS measurements of Rh of modified PARP1 wt and its mutants ($PARP1^{Y986S}$ and $PARP1^{Y986H}$) (**Figure 7**). Under our reaction conditions, DLS measurements showed $R_h$ values of ~10 nm for PARP1 and its mutants before the initiation of PARylation (**Figure 7A**). The activation of PARP1 wt and its mutants as detected by DLS enabled us to measure the average $R_h$ values of the PARylated proteins after the incubation with DNA and $NAD^+$ (**Figure 7C**). PARylation of proteins expanded their size and accordingly increased $R_h$ (10–18–26 nm; **Figures 7A,C**). For example, $R_h$ of ~26 nm was registered for auto-PARylated PARP1 wt, and $R_h$ of 22.6 and 18.5 nm for automodified mutants $PARP1^{Y986H}$ and $PARP1^{Y986S}$, respectively (**Figure 7C**). Thus, the $R_h$ values of PARylated proteins were substantially higher than the respective value measured for proteins before the initiation of PAR synthesis (**Figures 7A,C**). In addition, the increase in $R_h$ values of PARylated proteins shows different extent for PARP1 wt and its mutants. For mutants, 1.5- and 2.3-fold increase of $R_h$ values was observed upon PARylation of $PARP1^{Y986S}$ and $PARP1^{Y986H}$, respectively, whereas 2.6-fold increase of $R_h$ values was detected after PARylation of PARP1 wt, that is consistent with the synthesis of shorter PAR chain by the mutants. Thus, both AFM images and DLS measurements indicate morphological differences between the wild type and mutant PARylated PARP1 molecules.

The variation of PAR structure and PARylated protein morphology may have an influence on the efficiency of YB-1 binding to PAR formed through PARP1 automodification and on

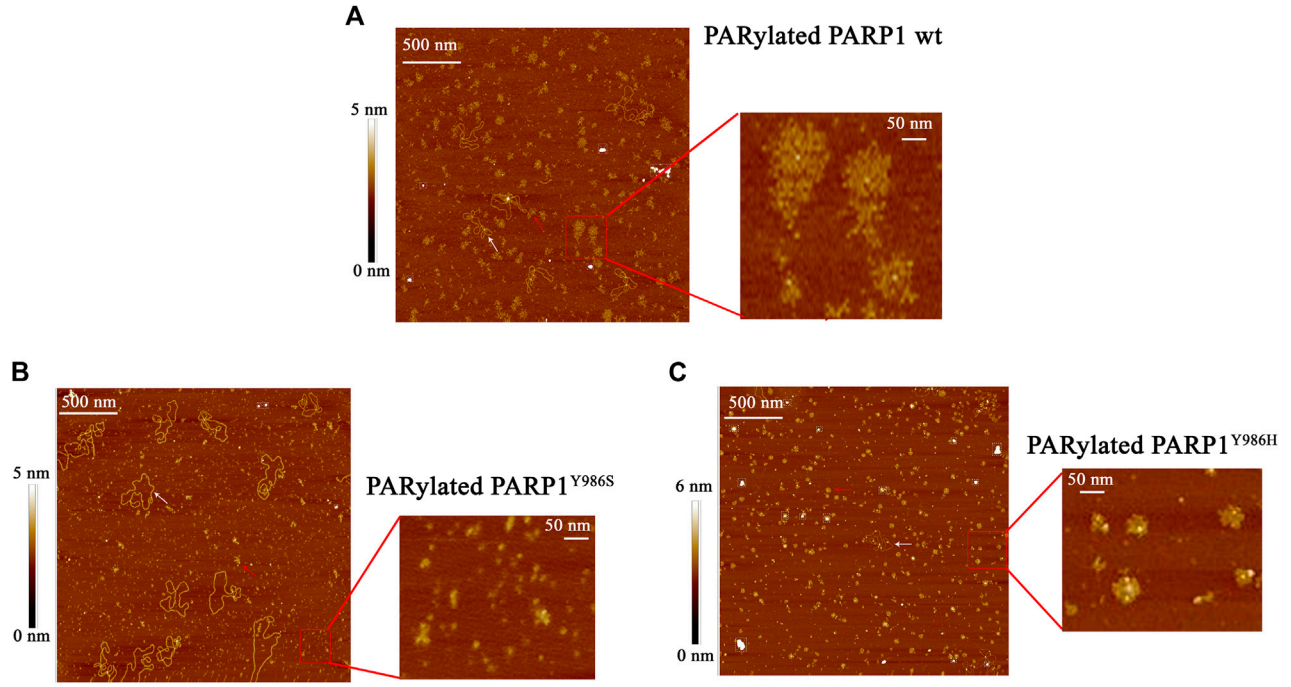


**FIGURE 6 |** AFM visualization of the shape of PAR polymers synthesized by PARP1 wt **(A)** or its mutants: PARP1$^{Y986H}$ **(B)** or PARP1$^{Y986S}$ **(C)**. The large scale of AFM images illustrate auto-PARylation of PARP1 and its mutants, red rectangle shows the higher magnification image of modified molecules. White arrows indicate plasmid DNA molecules, and red arrows point to PARylated proteins. Scale bar: 500 nm; Z scale: 5 nm (for PARP1 wt and PARP1$^{Y986S}$) and 6 nm (for PARP1$^{Y986H}$).

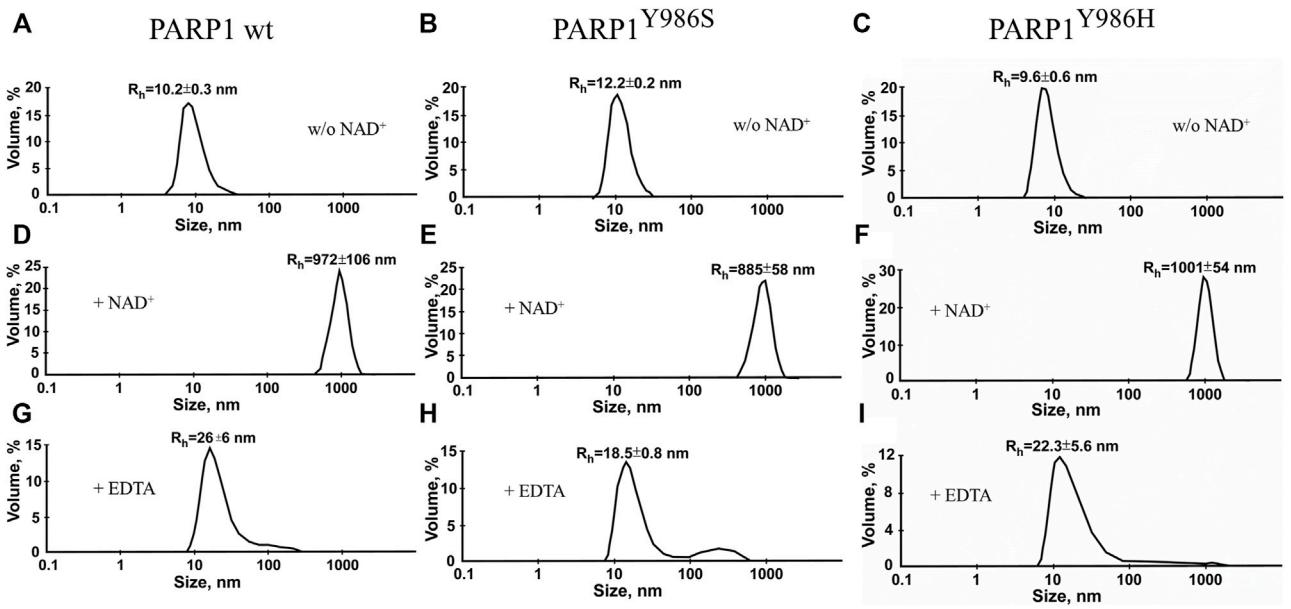


**FIGURE 7 |** Volume-weighted size distributions of PARylated PARP1 wt and its mutants as determined by DLS. $R_h$ values were measured for individual proteins **(A)** immediately after 40-min incubation with $NAD^+$ and DNA **(B)** or after EDTA addition intended to disrupt aggregates of PARylated proteins stabilized with $Mg^{2+}$ **(C).** The reaction mixtures contained 2.5 μM PARP1 or its mutant, 2.5 μM DNA (Nick), 10 mM $MgCl_2$ and 1 mM $NAD^+$ (where indicated). Aggregation of autoPARylated PARP1 during PAR synthesis is mediated by $Mg^{2+}$ ions, which stabilize intermolecular contact between adjacent PARylated molecules (Vasil'eva et al., 2019). To disrupt automodified PARP1 assemblies stabilized by $Mg^{2+}$ **(B)** EDTA (to a final concentration of 10 mM) was added to detect the real size of PARylated molecules **(C)**. $R_h$ values are the mean (±SD) of three independent experiments.

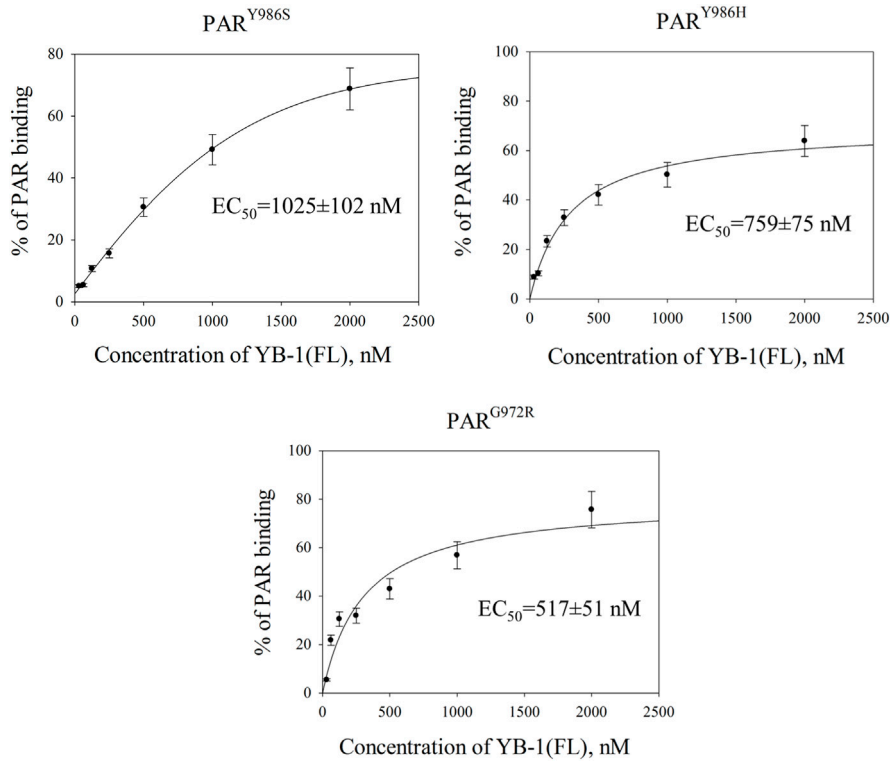


**FIGURE 8 |** YB-1 affinity for protein-free PAR polymers synthesized by PARP1 mutants. Graphs show quantification of EMSA data (**Supplementary Figure S4**) and represent the mean values of three independent experiments with error bars (±SD). The binding parameters (EC50) of YB-1 interaction with PAR was determined as YB-1 concentration resulting in 50% substrate binding. $EC_{50}$ values are the mean (±SD) of three independent experiments. The reaction mixtures contained 60 nM [$^{32}$P]-labeled PAR and YB-1 (FL) at the indicated concentrations.

the effects of YB-1 on PARP1 activity. To test this hypothesis, first we employed an EMSA to compare YB-1 binding to protein-free PARs produced by PARP1$^{Y986S}$ (PAR$^{Y986S}$), PARP1$^{Y986H}$ (PAR$^{Y986H}$), and PARP1$^{G972R}$ (PAR$^{G972R}$); **Figure 8**; **Supplementary Figure S2**. In contrast to PARP1 wt generating long PAR polymers with regular branching, mutants PARP1$^{Y986S}$, PARP1$^{G972R}$, and PARP1$^{Y986H}$ were shown to produce shorter PAR polymers; besides, PARP1$^{G972R}$ and PARP1$^{Y986H}$ synthesize hypo- or hyperbranched PAR, respectively (Rolli et al., 1997; Aberle et al., 2020).

The $EC_{50}$ values of YB-1(FL)–PAR complexes were estimated from the EMSA data obtained at various YB-1(FL) concentrations and a fixed PAR concentration (**Figure 8**; **Supplementary Figure S4**). For PAR produced by PARP1 mutants, $EC_{50}$ values varied from 1025 to 517 nM and were substantial higher in the case of PAR$^{Y986S}$ and PAR$^{Y986H}$ polymers than the values for the PAR synthesized by PARP1 wt (~564 nM; **Figures 2**, **8**). Thus, YB-1 binds with higher affinity to long regularly branched PAR than to the short regularly branched (PAR$^{Y986S}$) or short hyperbranched (PAR$^{Y986H}$) polymer but has comparable binding-affinities for the PAR produced by PARP1 wt and short hypobranched PAR$^{G972R}$ (**Figures 2**, **8**).

These results meant that YB-1 can bind different protein-free PAR molecules; at the same time, PAR structure, namely length and branching frequency, clearly affect YB-1's PAR-binding efficiency.

## YB-1 Stimulates the Activity of PARP1 Mutants Synthesizing Highly Branched or Short PAR Polymers

Next, we investigated what happens to these differences in YB-1 binding to short, long, and hypo- and hyperbranched polymers when PAR is covalently attached to PARP1, namely, how YB-1 could influence activity of PARP1 mutants producing different types of PAR and having clear differences in morphological structure of automodified molecules (**Figures 6**, **7C**). To address this question, we tested these PARP1 mutants' activities in the presence of YB-1(FL) (**Figure 9**). Under our reaction conditions in the PARP1 wt activity assay, the overall rate of PAR synthesis catalyzed by these mutants was lower than that of the wt enzyme (**Figure 9A**). The addition of YB-1 stimulated the activity of PARP1 mutants thereby increasing the rate of PAR synthesis by 2.5-, 4.5-, or 2.5-fold for PARP1$^{Y986S}$, PARP1$^{G972R}$ and PARP1$^{Y986H}$, respectively (**Figure 9B**). The data also revealed that trans-PARylation of YB-1 occurred with all PARP1 mutants (**Figure 9C**). Of note, in the case of PARP1$^{Y986S}$ and PARP1$^{G972R}$, the level of YB-1

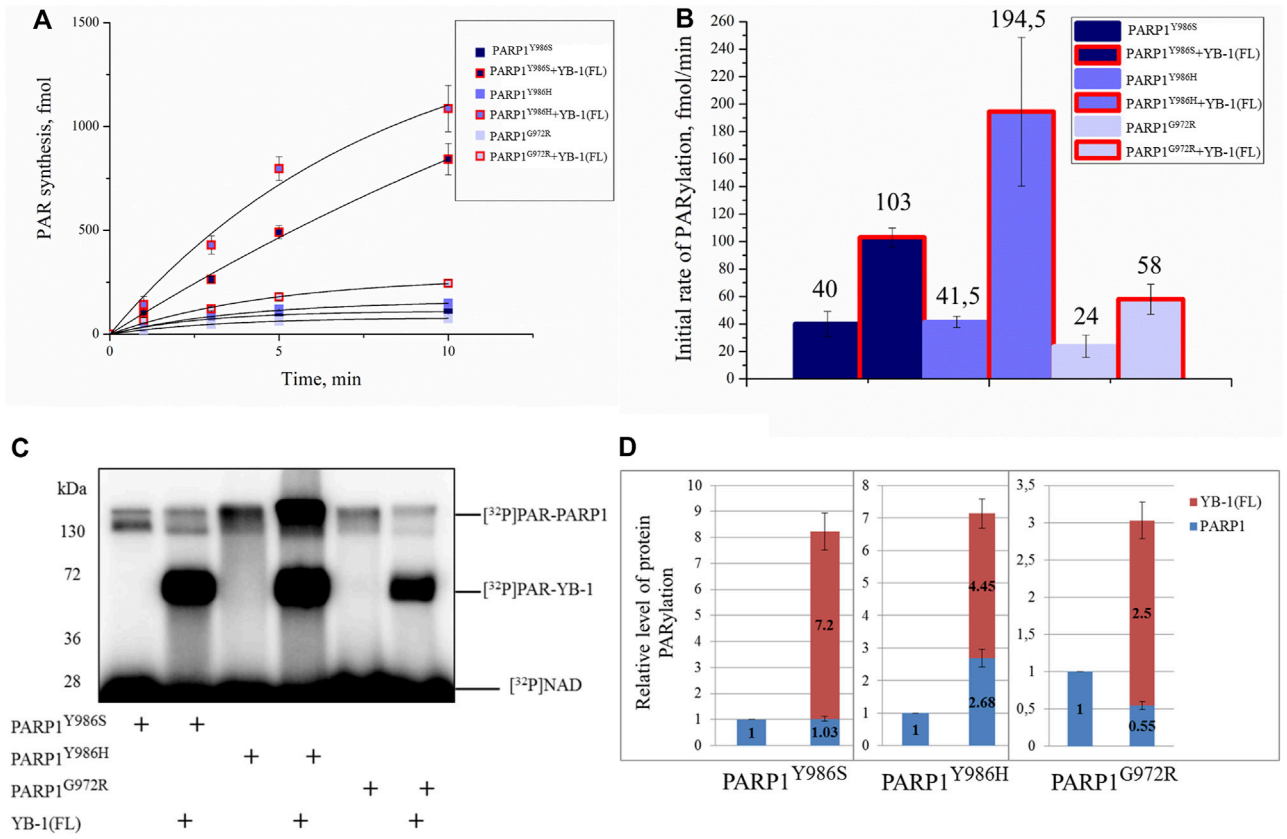


**FIGURE 9 |** YB-1 stimulates the activity of PARP1 point mutants. **(A)** The kinetics of PAR synthesis catalyzed by PARP1 in the absence or presence of YB-1(FL) or its deletion mutants. Graphs represent the mean values of three independent experiments with error bars representing ± SD. **(B)** Initial rates of PAR synthesis estimated in the presence of YB-1(FL). PARP1 mutants at 100 nM were incubated with 0.5 $OD_{260}$/ml $DNA_{act}$, 20 μM $NAD^+$, and [$^{32}$P]NAD (0.4 μCi) in the presence of 2.0 μM YB-1 as indicated. [$^{32}$P]PAR-modified proteins were precipitated with TCA and counted. The initial rates (fmol/min) were determined from a direct analysis of progressive curve **(A)** which yields $P_{max}$ and k (Equations 1 and 3), and represent the mean ± SD of three independent measurements. **(C)** Auto-PARylation of PARP1 mutants and YB-1 trans-PARylation according to SDS-PAGE and phosphorimaging. The reaction mixtures consisted of 100 nM PARP1, 2.0 μM YB-1, 20 μM $NAD^+$ [$^{32}$P]NAD (0.4 μCi), and 0.5 $OD_{260}$/ml $DNA_{act}$. **(D)** The diagrams present relative magnitude of PARP1 auto-PARylation and of YB-1 trans-PARylation (the mean of three independent experiments). The relative levels of PARylated proteins were normalized to the autoPARylated PARP1 mutant alone.

PARylation was significantly higher than the level of PARP1 auto-PARylation, reaching up to 87% of total protein modification (**Figure 9D**). One could say that PAR–YB-1 interactions are influenced by the structure of PAR attached to PARP1 (its length and frequency of branching), which affects the strength of stimulation of overall PAR synthesis and the ratio of YB-1 trans-PARylation to PARP1 auto-PARylation. Indeed, with mutants $PARP1^{Y986S}$ and $PARP1^{G972R}$ producing short PAR, we observed a YB-1–dependent increase in the PAR synthesis rate—that was similar to that seen with PARP1 wt—but a much higher level of YB-1 trans-PARylation (83 and 87%, respectively). With the $PARP1^{Y986H}$ mutant producing hyperbranched PAR, YB-1 had a moderate effect on the rate of PAR synthesis, and the level of its trans-PARylation was comparable with that observed in the reaction catalyzed by PARP1 wt (~60%; **Figure 5D**). Thus, PAR structure represents an important determinant for the stimulation of PARP1 activity with YB-1, because this parameter determines the level of YB-1 trans-PARylation, which plays a key role in the stimulation of PARP1 activity by increasing the overall PAR product yield.

## DISCUSSION

YB-1 has emerged as a key regulator of cell metabolism and performs diverse biological functions, including modulation of gene transcription, mRNA translation, chromatin modification, cell proliferation, and a stress response (Mordovkina et al., 2020; Sangermano et al., 2020). Moreover, YB-1 protein expression is upregulated in human cancers including breast, prostate, and ovarian cancers and melanoma and can correlate with aggressive tumor cell phenotypes and tumor formation and progression (Sangermano et al., 2020). YB-1 is thought to be a multifunctional protein capable of binding to single- or double-stranded DNA or RNA and can interact with proteins taking part in various metabolic pathways including gene transcription, mRNA translation, DNA repair, and control of cell cycle progression parameters (Skabkin et al., 2006). Our recent data show that aside from these functions, YB-1 can be involved in the regulation of activity of PARP1, which is a key player in DNA repair (Alemasova et al., 2018; Naumenko et al., 2020). PARP1 acts primarily as a sensor of DNA strand breaks and forms DNA

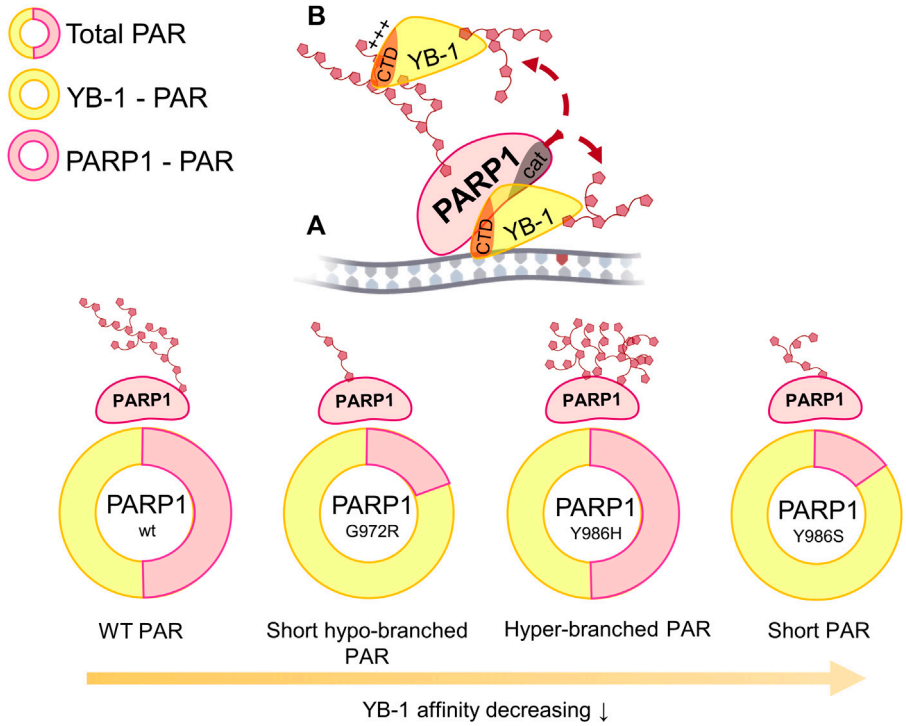


**FIGURE 10 |** The influence of various lengths and branching frequencies of the PAR synthesized by PARP1 point mutants (Y986H, Y986S, and G972R) on the YB-1 affinity to PAR, the magnitude of PARP1 auto-PARylation (highlighted in rosy) and YB-1 trans-PARylation (highlighted in yellow) during the stimulation of PARP1 activity in ternary complex "PARP1–YB-1–damaged DNA" **(A)** as well as during the interaction of YB-1 with PAR *via* its C-terminal domain (CTD; **(B)**.

repair foci *via* local synthesis of PAR at DNA damage sites (Satoh and Lindahl, 1992; Caldecott, 2014). To date, approximately 1500 proteins have been identified as acceptors of the covalent PARylation performed by PARP1, and many of these proteins are also PAR-binding factors, so-called "readers" of PAR (Tanabe et al., 2015; Ayyappan et al., 2021). Accordingly, PARP1 activity appears to be regulated by proteins both *via* the assembly of protein–protein complexes on damaged DNA and/or by PAR binding that results in trans-PARylation of target proteins, a decrease or increase in the magnitude of PARP1 auto-PARylation, and a switch of PARP1 specificity from auto-PARylation to trans-PARylation (Alemasova and Lavrik., 2019). This notion suggests that other proteins can regulate the "PAR-code" including PARP1 auto-PARylation and protein trans-PARylation patterns and PAR polymer structure (Luo and Kraus, 2012; Alemasova and Lavrik., 2019; Reber et al., 2021). A number of proteins that cooperate with PARP1 and are targeted by PARylation contain a highly basic intrinsically disordered protein region, implying an important role of such a region in PAR binding (Fischbach et al., 2018; Singatulina et al., 2019; Krüger et al., 2019; Rank, 2019). Among them, more than 100 RNA-binding proteins have considerable PAR-binding affinity and are PARylated in a cellular context (Gagne et al., 2008; Jungmichel et al., 2013; Zhang et al., 2013; Daniels et al., 2014). So far, only a few proteins have been shown to regulate the PARP1 activity and PAR-dependent processes *in vitro* and *in vivo* (Krietsch et al., 2012; Altmeyer et al., 2015; Sun et al., 2016; Singatulina et al., 2019). Expectedly, the regulation of PARP1 activity by RNA-binding proteins is being actively investigated (Bock et al., 2015; Singatulina et al., 2019; Leung 2020). RNA-binding proteins usually contain an RNA recognition motif (RRM), RG/RGG repeats, and serine/arginine-rich (SR), lysine-and-arginine-rich (KR), and/or arginine/glycine-rich (RG/RGG) repeats (Corley et al., 2020); all these regions possess both RNA- and PAR-binding properties (Teloni and Altmeyer, 2015). Herein, we report that the CTD of YB-1 plays a critical role in the binding of YB-1 to PAR and is required for YB-1–driven regulation of PARP1 activity. The CTD is the largest region of YB-1 and mediates protein–protein and protein–nucleic acid interactions and is essential for the function of this protein *in vivo* (Mordovkina et al., 2020), but the participation of the CTD in the regulation of PARP1-related reactions is poorly understood. The CTD has a disordered structure and predominantly contains clusters of basic amino acid residues, which are followed by clusters of acidic residues termed a charged zipper (**Figure 1**). On the basis of our previous findings, the regulation of PARP1 by YB-1 was expected to depend on the formation of two types of complexes mediated by YB-1 interaction with DNA in a ternary complex with PARP1 and by an interaction with PAR during PARP1 auto-PARylation (Naumenko et al., 2020). We also supposed that the YB-1 CTD plays a central role in the regulation of PARylation reactions because its deletion inhibits YB-1–dependent stimulation of PAR synthesis and YB-1 trans-PARylation (Alemasova et al., 2018; Naumenko et al., 2020). Assuming that the CTD is a key module with regards to PAR binding, a direct participation of clusters of

basic amino acid residues from the YB-1 CTD in PAR recognition was hypothesized in the present work. Here we were able to show that clusters of positively charged residues within the CTD are necessary for YB-1 interaction with PAR. Our results revealed that the reduced PAR-binding activity of YB-1 mutants (featuring a deletion of two positively charged clusters in the CTD) correlates well with diminished trans-PARylation (**Figures 2**, **5**). Thus, the noncovalent YB-1–PAR interaction and covalent YB-1 trans-PARylation are tightly linked within these processes, and the CTD may be regarded as a key module for PAR binding and regulation of PARP1 auto-PARylation by YB-1. We also found that YB-1 stimulates the activities of mutant PARP1 proteins that produce short branched PAR (i.e., PARP1$^{Y986S}$), short hyperbranched PAR (PARP1$^{Y986H}$), or short hypobranched PAR (i.e., PARP1$^{G972R}$) (**Figure 9**), implying that YB-1 modulates PARP1 activity in the context of diverse PAR structures. At the same time, the size (i.e., number of ADP-ribose units) and shape (i.e., branching frequency) of protein-free PAR affect YB-1 binding affinity for the polymers, and these PAR characteristics greatly influence the ratio of PARP1 auto-PARylation to trans-PARylation of YB-1 in case of PARP1 mutants. For example, PARP1$^{Y986S}$ and PARP1$^{G972R}$ produce short-chain PAR and predominantly catalyze YB-1 trans-PARylation.

It should be noted that the level of YB-1 trans-PARylation is only moderately affected by the type of damaged DNA structure (Naumenko et al., 2020), whereas the PAR structure affects the trans-modification of this protein (**Figure 9**).

To sum up the current results, we propose a model where the PAR structure formed during PARP1 auto-PARylation plays an important role in YB-1–PAR complex formation, YB-1 trans-PARylation, and PARP1 auto-PARylation (**Figure 10**). For instance, PAR structure and the YB-1 interaction with PAR should contribute primarily to the regulation of YB-1 trans-PARylation by changing the efficiency of YB-1 trans-modification and hence the stimulation of PAR synthesis by an exchange between PARylated and non-PARylated YB-1 molecules, in line with the model suggested by us earlier (Naumenko et al., 2020). This notion suggests that YB-1 may be viewed as "PAR-code" regulating the factors that interact with PAR and thereby influences PARP1 activity (Reber and Mangerich, 2021). The observed patterns of PAR synthesis may be extrapolated to PARP1's protein partners containing PAR-binding disordered regions with clusters of positively charged amino acid residues.

## DATA AVAILABILITY STATEMENT

The original contributions presented in the study are included in the article/**Supplementary Material**, further inquiries can be directed to the corresponding author.

## AUTHOR CONTRIBUTIONS

OL contributed to the conceptualization and design of the study. KN, TK, LH, RA, and MS carried out the experiments and analyzed the data. MS, OL, KN, and RA prepared the figures and wrote the first draft of the manuscript. AM, DP, and LH provided intellectual input and edited the manuscript. All the authors have read and approved the submitted version.

## FUNDING

The work was supported by the Russian Science Foundation Grant Number 20-14-00086, Russian Foundation for Basic Research grant number 20-34-90095 (fluorescence anisotropy experiments) and by the Program of Fundamental Scientific Research of the State Academies of Sciences project #121031300041-4 (expression and purification of recombinant proteins).

## ACKNOWLEDGMENTS

The authors are grateful to S. N. Khodyreva (ICBFM SB RAS), S. I. Shram (Institute of Molecular Genetic RAS, Moscow), and D. A. Kretov (Institute of Protein Research RAS, Moscow, Russia) for APE1, NMNAT, and for YB-1–encoding plasmid pET-3-1-YB-1 (wt), respectively. We gratefully acknowledge UEVE Université Paris-Saclay and Genopole EVRY for constant support of Laboratoire Structure-Activité des Biomolécules Normales et Pathologiques. English-language–editing services were provided by "shevchuk-editing.com".

## SUPPLEMENTARY MATERIAL

The Supplementary Material for this article can be found online at: https://www.frontiersin.org/articles/10.3389/fcell.2022.831741/full#supplementary-material

## REFERENCES

Aberle, L., Krüger, A., Reber, J. M., Lippmann, M., Hufnagel, M., Schmalz, M., et al. (2020). PARP1 Catalytic Variants Reveal Branching and Chain Length-specific Functions of poly(ADP-Ribose) in Cellular Physiology and Stress Response. *Nucleic Acids Res.* 48, 10015–10033. doi:10.1093/nar/gkaa590

Alemasova, E. E., and Lavrik, O. I. (2019). Poly(ADP-ribosyl)ation by PARP1: Reaction Mechanism and Regulatory Proteins. *Nucleic Acids Res.* 47, 3811–3827. doi:10.1093/nar/gkz120

Alemasova, E. E., Moor, N. A., Naumenko, K. N., Kutuzov, M. M., Sukhanova, M. V., Pestryakov, P. E., et al. (2016). Y-box-binding Protein 1 as a Non-canonical Factor of Base Excision Repair. *Biochimica Biophysica Acta (BBA) - Proteins Proteomics* 1864, 1631–1640. doi:10.1016/j.bbapap.2016.08.012

Alemasova, E. E., Naumenko, K. N., Kurgina, T. A., Anarbaev, R. O., and Lavrik, O. I. (2018). The Multifunctional Protein YB-1 Potentiates PARP1 Activity and Decreases the Efficiency of PARP1 Inhibitors. *Oncotarget* 9, 23349–23365. doi:10.18632/oncotarget.25158

Alemasova, E. E., Naumenko, K. N., Pestryakov, P. E., and Lavrik, O. I. (2017). Production, Purification of the Recombinant Analog of Y-Box-Binding Protein

and its Interaction with poly(ADP-Ribose), RNA, Single- and Double-Stranded DNAs. *Biopolym. Cell* 33, 214–220. doi:10.7124/bc.000954

Alemasova, E. E., Pestryakov, P. E., Sukhanova, M. V., Kretov, D. A., Moor, N. A., Curmi, P. A., et al. (2015). Poly(ADP-ribosyl)ation as a New Posttranslational Modification of YB-1. *Biochimie* 119, 36–44. doi:10.1016/j.biochi.2015.10.008

Althaus, F., and Richter, C. (1987). *ADP-ribosylation of Proteins*. Berlin, Heidelberg: Springer.

Altmeyer, M., Neelsen, K. J., Teloni, F., Pozdnyakova, I., Pellegrino, S., Grøfte, M., et al. (2015). Liquid Demixing of Intrinsically Disordered Proteins Is Seeded by poly(ADP-Ribose). *Nat. Commun.* 6, 8088. doi:10.1038/ncomms9088

Alvarez-Gonzalez, R., and Jacobson, M. K. (1987). Characterization of Polymers of Adenosine Diphosphate Ribose Generated *In Vitro* and *In Vivo*. *Biochemistry* 26, 3218–3224. doi:10.1021/bi00385a042

Ayyappan, V., Wat, R., Barber, C., Vivelo, C. A., Gauch, K., Visanpattanasin, P., et al. (2021). ADPriboDB 2.0: an Updated Database of ADP-Ribosylated Proteins. *Nucleic Acids Res.* 49, D261–D265. doi:10.1093/nar/gkaa941

Bargou, R. C., Jürchott, K., Wagener, C., Bergmann, S., Metzner, S., Bommert, K., et al. (1997). Nuclear Localization and Increased Levels of Transcription Factor YB-1 in Primary Human Breast Cancers Are Associated with Intrinsic MDR1 Gene Expression. *Nat. Med.* 3, 447–450. doi:10.1038/nm0497-447

Bates, M., Boland, A., McDermott, N., and Marignol, L. (2020). YB-1: The Key to Personalised Prostate Cancer Management? *Cancer Lett.* 490, 66–75. doi:10.1016/j.canlet.2020.07.006

Bock, F. J., Todorova, T. T., and Chang, P. (2015). RNA Regulation by Poly(ADP-Ribose) Polymerases. *Mol. Cell* 58, 959–969. doi:10.1016/j.molcel.2015.01.037

Bouvet, P., Matsumoto, K., and Wolffe, A. P. (1995a). Sequence-specific RNA Recognition by the Xenopus Y-Box Proteins. An Essential Role for the Cold Shock Domain. *J. Biol. Chem.* 270, 28297–28303. doi:10.1074/jbc.270.47.28297

Bouvet, P., Matsumoto, K., and Wolffe, A. P. (1995b). Sequence-specific RNA Recognition by the Xenopus Y-Box Proteins. An Essential Role for the Cold Shock Domain. *J. Biol. Chem.* 270, 28297–28303. doi:10.1074/jbc.270.47.28297

Budkina, K. S., Zlobin, N. E., Kononova, S. V., Ovchinnikov, L. P., and Babakov, A. V. (2020). Cold Shock Domain Proteins: Structure and Interaction with Nucleic Acids. *Biochem. Mosc.* 85, 1–19. doi:10.1134/s0006297920140011

Caldecott, K. W. (2014). Protein ADP-Ribosylation and the Cellular Response to DNA Strand Breaks. *DNA Repair* 19, 108–113. doi:10.1016/j.dnarep.2014.03.021

Carter-O'Connell, I., Jin, H., Morgan, R. K., David, L. L., and Cohen, M. S. (2014). Engineering the Substrate Specificity of ADP-Ribosyltransferases for Identifying Direct Protein Targets. *J. Am. Chem. Soc.* 136, 5201–5204. doi:10.1021/ja412897a

Carter-O'Connell, I., Jin, H., Morgan, R. K., Zaja, R., David, L. L., Ahel, I., et al. (2016). Identifying Family-member-specific Targets of Mono-ARTDs by Using a Chemical Genetics Approach. *Cell Rep.* 14, 621–631. doi:10.1016/j.celrep.2015.12.045

Carter-O'Connell, I., Vermehren-Schmaedick, A., Jin, H., Morgan, R. K., David, L. L., and Cohen, M. S. (2018). Combining Chemical Genetics with Proximity-dependent Labeling Reveals Cellular Targets of Poly(ADP-Ribose) Polymerase 14 (PARP14). *ACS Chem. Biol.* 13, 2841–2848. doi:10.1021/acschembio.8b00567

Chen, Q., Kassab, M. A., Dantzer, F., and Yu, X. (2018). PARP2 Mediates Branched Poly ADP-Ribosylation in Response to DNA Damage. *Nat. Commun.* 9, 3233. doi:10.1038/s41467-018-05588-5

Corley, M., Burns, M. C., and Yeo, G. W. (2020). How RNA-Binding Proteins Interact with RNA: Molecules and Mechanisms. *Mol. Cell* 78, 9–29. doi:10.1016/j.molcel.2020.03.011

d'Amours, D., Desnoyers, S., d'Silva, I., and Poirier, G. G. (1999). Poly(ADP-ribosyl)ation Reactions in the Regulation of Nuclear Functions. *Biochem. J.* 342, 249–268. doi:10.1042/bj3420249

Daniels, C. M., Ong, S.-E., and Leung, A. K. L. (2014). Phosphoproteomic Approach to Characterize Protein Mono- and poly(ADP-Ribosyl)ation Sites from Cells. *J. Proteome Res.* 13, 3510–3522. doi:10.1021/pr401032q

Das, S., Chattopadhyay, R., Bhakat, K. K., Boldogh, I., Kohno, K., Prasad, R., et al. (2007). Stimulation of NEIL2-Mediated Oxidized Base Excision Repair via YB-1 Interaction during Oxidative Stress. *J. Biol. Chem.* 282, 28474–28484. doi:10.1074/jbc.m704672200

Dasovich, M., Beckett, M. Q., Bailey, S., Ong, S.-E., Greenberg, M. M., and Leung, A. K. L. (2021). Identifying poly(ADP-Ribose)-Binding Proteins with Photoaffinity-Based Proteomics. *J. Am. Chem. Soc.* 143, 3037–3042. doi:10.1021/jacs.0c12246

Eliseeva, I. A., Kim, E. R., Guryanov, S. G., Ovchinnikov, L. P., and Lyabin, D. N. (2011). Y-box-binding Protein 1 (YB-1) and its Functions. *Biochem. Mosc.* 76, 1402–1433. doi:10.1134/s0006297911130049

Fahrer, J., Kranaster, R., Altmeyer, M., Marx, A., and Bürkle, A. (2007). Quantitative Analysis of the Binding Affinity of poly(ADP-Ribose) to Specific Binding Proteins as a Function of Chain Length. *Nucleic Acids Res.* 35, e143. doi:10.1093/nar/gkm944

Fahrer, J., Popp, O., Malanga, M., Beneke, S., Markovitz, D. M., Ferrando-May, E., et al. (2010). High-affinity Interaction of poly(ADP-Ribose) and the Human DEK Oncoprotein Depends upon Chain Length. *Biochemistry* 49, 7119–7130. doi:10.1021/bi1004365

Fischbach, A., Krüger, A., Hampp, S., Assmann, G., Rank, L., Hufnagel, M., et al. (2018). The C-Terminal Domain of P53 Orchestrates the Interplay between Non-covalent and Covalent poly(ADP-Ribosyl)ation of P53 by PARP1. *Nucleic Acids Res.* 46, 804–822. doi:10.1093/nar/gkx1205

Fomina, E. E., Pestryakov, P. E., Maltseva, E. A., Petruseva, I. O., Kretov, D. A., Ovchinnikov, L. P., et al. (2015). Y-box Binding Protein 1 (YB-1) Promotes Detection of DNA Bulky Lesions by XPC-Hr23b Factor. *Biochem. Mosc.* 80, 219–227. doi:10.1134/s000629791502008x

Fujita, T., Ito, K.-i., Izumi, H., Kimura, M., Sano, M., Nakagomi, H., et al. (2005). Increased Nuclear Localization of Transcription Factor Y-Box Binding Protein 1 Accompanied by Up-Regulation of P-Glycoprotein in Breast Cancer Pretreated with Paclitaxel. *Clin. Cancer Res.* 11, 8837–8844. doi:10.1158/1078-0432.ccr-05-0945

Gagné, J.-P., Isabelle, M., Lo, K. S., Bourassa, S., Hendzel, M. J., Dawson, V. L., et al. (2008). Proteome-wide Identification of poly(ADP-Ribose) Binding Proteins and poly(ADP-Ribose)-Associated Protein Complexes. *Nucleic Acids Res.* 36, 6959–6976. doi:10.1093/nar/gkn771

Gagné, J.-P., Pic, É., Isabelle, M., Krietsch, J., Éthier, C., Paquet, É., et al. (2012). Quantitative Proteomics Profiling of the poly(ADP-Ribose)-Related Response to Genotoxic Stress. *Nucleic Acids Res.* 40, 7788–7805. doi:10.1093/nar/gks486

Gao, Y., Fotovati, A., Lee, C., Wang, M., Cote, G., Guns, E., et al. (2009). Inhibition of Y-Box Binding Protein-1 Slows the Growth of Glioblastoma Multiforme and Sensitizes to Temozolomide Independent O6-Methylguanine-DNA Methyltransferase. *Mol. Cancer Ther.* 8, 3276–3284. doi:10.1158/1535-7163.mct-09-0478

Gibbs-Seymour, I., Fontana, P., Rack, J. G. M., and Ahel, I. (2016). HPF1/C4orf27 Is a PARP-1-Interacting Protein that Regulates PARP-1 ADP-Ribosylation Activity. *Mol. Cell* 62, 432–442. doi:10.1016/j.molcel.2016.03.008

Hanzlikova, H., Gittens, W., Krejcikova, K., Zeng, Z., and Caldecott, K. W. (2017). Overlapping Roles for PARP1 and PARP2 in the Recruitment of Endogenous XRCC1 and PNKP into Oxidized Chromatin. *Nucleic Acids Res.* 45, 2546–2557. doi:10.1093/nar/gkw1246

Hasegawa, S. L., Doetsch, P. W., Hamilton, K. K., Martin, A. M., Okenquist, S. A., Lenz, J., et al. (1991). DNA Binding Properties of YB-1 and dbpA: Binding to Doublestranded, Single-Stranded, and Abasic Site Containing DNAs. *Nucl. Acids Res.* 19, 4915–4920. doi:10.1093/nar/19.18.4915

Hayashi, K., Tanaka, M., Shimada, T., Miwa, M., and Sugimura, T. (1983). Size and Shape of poly(ADP-Ribose): Examination by Gel Filtration, Gel Electrophoresis and Electron Microscopy. *Biochem. Biophysical Res. Commun.* 112, 102–107. doi:10.1016/0006-291x(83)91803-x

Ise, T., Nagatani, G., Imamura, T., Kato, K., Takano, H., Nomoto, M., et al. (1999). Transcription Factor Y-Box Binding Protein 1 Binds Preferentially to Cisplatin-Modified DNA and Interacts with Proliferating Cell Nuclear Antigen. *Cancer Res.* 59, 342–346.

Jungmichel, S., Rosenthal, F., Altmeyer, M., Lukas, J., Hottiger, M. O., and Nielsen, M. L. (2013). Proteome-wide Identification of poly(ADP-Ribosyl)ation Targets in Different Genotoxic Stress Responses. *Mol. Cell* 52, 272–285. doi:10.1016/j.molcel.2013.08.026

Kalesh, K., Lukauskas, S., Borg, A. J., Snijders, A. P., Ayyappan, V., Leung, A. K. L., et al. (2019). An Integrated Chemical Proteomics Approach for Quantitative Profiling of Intracellular ADP-Ribosylation. *Sci. Rep.* 9, 6655. doi:10.1038/s41598-019-43154-1

Kim, E. R., Selyutina, A. A., Buldakov, I. A., Evdokimova, V., Ovchinnikov, L. P., and Sorokin, A. V. (2013). The Proteolytic YB-1 Fragment Interacts with DNA

Repair Machinery and Enhances Survival during DNA Damaging Stress. *Cell cycle* 12, 3791–3803. doi:10.4161/cc.26670

Kliza, K. W., Liu, Q., Roosenboom, L. W. M., Jansen, P. W. T. C., Filippov, D. V., and Vermeulen, M. (2021). Reading ADP-Ribosylation Signaling Using Chemical Biology and Interaction Proteomics. *Mol. Cell* 81, 4552–4567. doi:10.1016/j.molcel.2021.08.037

Kloks, C. P. A. M., Spronk, C. A. E. M., Lasonder, E., Hoffmann, A., Vuister, G. W., Grzesiek, S., et al. (2002). The Solution Structure and DNA-Binding Properties of the Cold-Shock Domain of the Human Y-Box Protein YB-1. *J. Mol. Biol.* 316, 317–326. doi:10.1006/jmbi.2001.5334

Kosnopfel, C., Sinnberg, T., and Schittek, B. (2014). Y-Box Binding Protein 1 - A Prognostic Marker and Target in Tumour Therapy. *Eur. J. Cell Biol.* 93, 61–70. doi:10.1016/j.ejcb.2013.11.007

Kretov, D. A., Clément, M.-J., Lambert, G., Durand, D., Lyabin, D. N., Bollot, G., et al. (2019). YB-1, an Abundant Core mRNA-Binding Protein, Has the Capacity to Form an RNA Nucleoprotein Filament: a Structural Analysis. *Nucleic Acids Res.* 47, 3127–3141. doi:10.1093/nar/gky1303

Krietsch, J., Caron, M.-C., Gagné, J.-P., Ethier, C., Vignard, J., Vincent, M., et al. (2012). PARP Activation Regulates the RNA-Binding Protein NONO in the DNA Damage Response to DNA Double-Strand Breaks. *Nucleic Acids Res.* 40, 10287–10301. doi:10.1093/nar/gks798

Krüger, A., Stier, A., Fischbach, A., Bürkle, A., Hauser, K., and Mangerich, A. (2019). Interactions of P53 with poly(ADP-Ribose) and DNA Induce Distinct Changes in Protein Structure as Revealed by ATR-FTIR Spectroscopy. *Nucleic Acids Res.* 47, 4843–4858. doi:10.1093/nar/gkz175

Laemmli, U. K. (1970). Cleavage of Structural Proteins during the Assembly of the Head of Bacteriophage T4. *Nature* 227, 680–685. doi:10.1038/227680a0

Lavrik, O. I. (2020). PARPs' Impact on Base Excision DNA Repair. *DNA Repair* 93, 102911. doi:10.1016/j.dnarep.2020.102911

Leung, A. K. L. (2020). Poly(ADP-ribose): a Dynamic Trigger for Biomolecular Condensate Formation. *Trends Cell Biol.* 30, 370–383. doi:10.1016/j.tcb.2020.02.002

Lindahl, T., and Andersson, A. (1972). Rate of Chain Breakage at Apurinic Sites in Double-Stranded Deoxyribonucleic Acid. *Biochemistry* 11, 3618–3623. doi:10.1021/bi00769a019

Luo, X., and Kraus, W. L. (2012). On PAR with PARP: Cellular Stress Signaling through poly(ADP-Ribose) and PARP-1. *Genes Dev.* 26, 417–432. doi:10.1101/gad.183509.111

Lüscher, B., Ahel, I., Altmeyer, M., Ashworth, A., Bai, P., Chang, P., et al. (2021). ADP-ribosyltransferases, an Update on Function and Nomenclature. *FEBS J.* doi:10.1111/febs.16142

Masaoka, A., Gassman, N. R., Kedar, P. S., Prasad, R., Hou, E. W., Horton, J. K., et al. (2012). HMGN1 Protein Regulates Poly(ADP-Ribose) Polymerase-1 (PARP-1) Self-PARylation in Mouse Fibroblasts. *J. Biol. Chem.* 287, 27648–27658. doi:10.1074/jbc.m112.370759

Matsumoto, K., and Bay, B. H. (2005). Significance of the Y-Box Proteins in Human Cancers. *J. Mol. Genet. Med.* 1, 11–17. doi:10.4172/1747-0862.1000005

Mordovkina, D., Lyabin, D. N., Smolin, E. A., Sogorina, E. M., Ovchinnikov, L. P., and Eliseeva, I. (2020). Y-box Binding Proteins in mRNP Assembly, Translation, and Stability Control. *Biomolecules* 10, 591. doi:10.3390/biom10040591

Murray, M. T. (1994). Nucleic Acid-Binding Properties of the Xenopus Oocyte Y Box Protein mRNP3+4. *Biochemistry* 33, 13910–13917. doi:10.1021/bi00250a046

Naegeli, H., and Althaus, F. R. (1991). Regulation of poly(ADP-Ribose) Polymerase. Histone-specific Adaptations of Reaction Products. *J. Biol. Chem.* 266, 10596–10601. doi:10.1016/s0021-9258(18)99265-3

Naumenko, K. N., Sukhanova, M. V., Hamon, L., Kurgina, T. A., Alemasova, E. E., Kutuzov, M. M., et al. (2020). Regulation of Poly(ADP-Ribose) Polymerase 1 Activity by Y-Box-Binding Protein 1. *Biomolecules* 10, 1325. doi:10.3390/biom10091325

Nekrasov, M. P., Ivshina, M. P., Chernov, K. G., Kovrigina, E. A., Evdokimova, V. M., Thomas, A. A. M., et al. (2003). The mRNA-binding Protein YB-1 (P50) Prevents Association of the Eukaryotic Initiation Factor eIF4G with mRNA and Inhibits Protein Synthesis at the Initiation Stage. *J. Biol. Chem.* 278, 13936–13943. doi:10.1074/jbc.m209145200

Ouararhni, K., Hadj-Slimane, R., Ait-Si-Ali, S., Robin, P., Mietton, F., Harel-Bellan, A., et al. (2006). The Histone Variant mH2A1.1 Interferes with Transcription by Down-Regulating PARP-1 Enzymatic Activity. *Genes Dev.* 20, 3324–3336. doi:10.1101/gad.396106

Panzeter, P. L., Realini, C. A., and Althaus, F. R. (1992). Noncovalent Interactions of Poly(adenosine Diphosphate Ribose) with Histones. *Biochemistry* 31, 1379–1385. doi:10.1021/bi00120a014

Pisarev, A. V., Skabkin, M. A., Thomas, A. A., Merrick, W. C., Ovchinnikov, L. P., and Shatsky, I. N. (2002). Positive and Negative Effects of the Major Mammalian Messenger Ribonucleoprotein P50 on Binding of 40 S Ribosomal Subunits to the Initiation Codon of β-Globin mRNA. *J. Biol. Chem.* 277, 15445–15451. doi:10.1074/jbc.m111954200

Polo, L. M., Xu, Y., Hornyak, P., Garces, F., Zeng, Z., Hailstone, R., et al. (2019). Efficient Single-Strand Break Repair Requires Binding to Both poly(ADP-Ribose) and DNA by the Central BRCT Domain of XRCC1. *Cell Rep.* 26, 573–581. doi:10.1016/j.celrep.2018.12.082

Rank, L. (2019). *Cellular Characterization of PARP1 Variants with Altered Enzymatic Activities [dissertation/doctoral Thesis]*. Konstanz: University of Konstanz.

Ray Chaudhuri, A., and Nussenzweig, A. (2017). The Multifaceted Roles of PARP1 in DNA Repair and Chromatin Remodelling. *Nat. Rev. Mol. Cell Biol.* 18, 610–621. doi:10.1038/nrm.2017.53

Reber, J. M., and Mangerich, A. (2021). Why Structure and Chain Length Matter: on the Biological Significance Underlying the Structural Heterogeneity of poly(ADP-Ribose). *Nucleic Acids Res.* 49, 8432–8448. doi:10.1093/nar/gkab618

Rolli, V., O'Farrell, M., Ménissier-de Murcia, J., and de Murcia, G. (1997). Random Mutagenesis of the Poly(ADP-Ribose) Polymerase Catalytic Domain Reveals Amino Acids Involved in Polymer Branching. *Biochemistry* 36, 12147–12154. doi:10.1021/bi971055p

Rudolph, J., Roberts, G., Muthurajan, U. M., and Luger, K. (2021). HPF1 and Nucleosomes Mediate a Dramatic Switch in Activity of PARP1 from Polymerase to Hydrolase. *Elife* 10, e65773. doi:10.7554/eLife.65773

Sangermano, F., Delicato, A., and Calabrò, V. (2020). Y Box Binding Protein 1 (YB-1) Oncoprotein at the Hub of DNA Proliferation, Damage and Cancer Progression. *Biochimie* 179, 205–216. doi:10.1016/j.biochi.2020.10.004

Satoh, M. S., and Lindahl, T. (1992). Role of poly(ADP-Ribose) Formation in DNA Repair. *Nature* 356, 356–358. doi:10.1038/356356a0

Shibahara, K., Sugio, K., Osaki, T., Uchiumi, T., Maehara, Y., Kohno, K., et al. (2001). Nuclear Expression of the Y-Box Binding Protein, YB-1, as a Novel Marker of Disease Progression in Non-small Cell Lung Cancer. *Clin. Cancer Res.* 7, 3151–3155.

Skabkin, M. A., Kiselyova, O., Chernov, K., Sorokin, A., Dubrovin, E., Yaminsky, I., et al. (2004). Structural Organization of mRNA Complexes with Major Core mRNP Protein YB-1. *Nucleic Acids Res.* 32, 5621–5635. doi:10.1093/nar/gkh889

Skabkin, M. A., Lyabin, D. N., and Ovchinnikov, L. P. (2006). Nonspecific and Specific Interactions of Y-Box-Binding Protein 1 (YB-1) with mRNA and Posttranscriptional Regulation of Protein Synthesis in Animal Cells. *Mol. Biol.* 40, 551–563. doi:10.1134/s0026893306040078

Sorokin, A. V., Selyutina, A. A., Skabkin, M. A., Guryanov, S. G., Nazimov, I. V., Richard, C., et al. (2005). Proteasome-mediated Cleavage of the Y-Box-Binding Protein 1 Is Linked to DNA-Damage Stress Response. *EMBO J.* 24, 3602–3612. doi:10.1038/sj.emboj.7600830

Stein, U., Jürchott, K., Walther, W., Bergmann, S., Schlag, P. M., and Royer, H.-D. (2001). Hyperthermia-induced Nuclear Translocation of Transcription Factor YB-1 Leads to Enhanced Expression of Multidrug Resistance-Related ABC Transporters. *J. Biol. Chem.* 276, 28562–28569. doi:10.1074/jbc.m100311200

Sukhanova, M. V., Khodyreva, S. N., and Lavrik, O. I. (2004). Poly(ADP-ribose) Polymerase-1 Inhibits Strand-Displacement Synthesis of DNA Catalyzed by DNA Polymerase β. *Biochem. Mosc.* 69, 558–568. doi:10.1023/b:biry.0000029855.68502.fa

Sun, X., Fu, K., Hodgson, A., Wier, E. M., Wen, M. G., Kamenyeva, O., et al. (2016). Sam68 Is Required for DNA Damage Responses via Regulating poly(ADP-Ribosyl)ation. *PLoS Biol.* 14, e1002543. doi:10.1371/journal.pbio.1002543

Tafuri, S. R., and Wolffe, A. P. (1992). DNA Binding, Multimerization, and Transcription Stimulation by the Xenopus Y Box Proteins *In Vitro*. *New Biol.* 4, 349–359.

Tanabe, Y., Nagatoishi, S., and Tsumoto, K. (2015). Thermodynamic Characterization of the Interaction between the Human Y-Box Binding Protein YB-1 and Nucleic Acids. *Mol. Biosyst.* 11, 2441–2448. doi:10.1039/c5mb00184f

Teloni, F., and Altmeyer, M. (2015). Readers of poly(ADP-Ribose): Designed to Be Fit for Purpose. *Nucleic Acids Res.* 44, 993–1006. doi:10.1093/nar/gkv1383

Vasil'eva, I. A., Anarbaev, R. O., Moor, N. A., and Lavrik, O. I. (2019). Dynamic Light Scattering Study of Base Excision DNA Repair Proteins and Their Complexes. *Biochimica Biophysica Acta (BBA) - Proteins Proteomics* 1867, 297–305. doi:10.1016/j.bbapap.2018.10.009

Zhang, Y., Wang, J., Ding, M., and Yu, Y. (2013). Site-specific Characterization of the Asp- and Glu-ADP-Ribosylated Proteome. *Nat. Methods.* 10, 981–984. doi:10.1038/nmeth.2603

Zhen, Y., Zhang, Y., and Yu, Y. (2017). A Cell-line-specific Atlas of PARP-Mediated Protein Asp/Glu-ADP-Ribosylation in Breast Cancer. *Cell Rep.* 21, 2326–2337. doi:10.1016/j.celrep.2017.10.106

**Conflict of Interest:** The authors declare that the research was conducted in the absence of any commercial or financial relationships that could be construed as a potential conflict of interest.

frontiers | Frontiers in Cell and Developmental Biology

TYPE Original Research
PUBLISHED 22 July 2022
DOI 10.3389/fcell.2022.893806



OPEN ACCESS

EDITED BY
Shan Yan,
University of North Carolina at Charlotte, United States

REVIEWED BY
Tribhuwan Yadav,
Massachusetts General Hospital and Harvard Medical School, United States
Yuan Liu,
Florida International University, United States

*CORRESPONDENCE
Aishwarya Prakash,
aprakash@southalabama.edu

SPECIALTY SECTION
This article was submitted to Molecular and Cellular Pathology, a section of the journal Frontiers in Cell and Developmental Biology

RECEIVED 10 March 2022
ACCEPTED 01 July 2022
PUBLISHED 22 July 2022

CITATION
Sharma N, Thompson MK, Arrington JF, Terry DM, Chakravarthy S, Prevelige PE and Prakash A (2022), Novel interaction interfaces mediate the interaction between the NEIL1 DNA glycosylase and mitochondrial transcription factor A. *Front. Cell Dev. Biol.* 10:893806. doi: 10.3389/fcell.2022.893806



# Novel interaction interfaces mediate the interaction between the NEIL1 DNA glycosylase and mitochondrial transcription factor A

Nidhi Sharma[1], Marlo K. Thompson[1], Jennifer F. Arrington[1], Dava M. Terry[1], Srinivas Chakravarthy[2], Peter E. Prevelige[3] and Aishwarya Prakash[1]*

[1]Department of Biochemistry and Molecular Biology, Mitchell Cancer Institute, University of South Alabama, Mobile, AL, United States, [2]Advanced Photon Source, Illinois Institute of Technology, Chicago, IL, United States, [3]Department of Microbiology, University of Alabama at Birmingham, Birmingham, AL, United States

The maintenance of human mitochondrial DNA (mtDNA) is critical for proper cellular function as damage to mtDNA, if left unrepaired, can lead to a diverse array of pathologies. Of the pathways identified to participate in DNA repair within the mitochondria, base excision repair (BER) is the most extensively studied. Protein-protein interactions drive the step-by-step coordination required for the successful completion of this pathway and are important for crosstalk with other mitochondrial factors involved in genome maintenance. Human NEIL1 is one of seven DNA glycosylases that initiates BER in both the nuclear and mitochondrial compartments. In the current work, we scrutinized the interaction between NEIL1 and mitochondrial transcription factor A (TFAM), a protein that is essential for various aspects of mtDNA metabolism. We note, for the first time, that both the N- and C- terminal domains of NEIL1 interact with TFAM revealing a unique NEIL1 protein-binding interface. The interaction between the two proteins, as observed biochemically, appears to be transient and is most apparent at concentrations of low salt. The presence of DNA (or RNA) also positively influences the interaction between the two proteins, and molar mass estimates indicate that duplex DNA is required for complex formation at higher salt concentrations. Hydrogen deuterium exchange mass spectrometry data reveal that both proteins exchange less deuterium upon DNA binding, indicative of an interaction, and the addition of NEIL1 to the TFAM-DNA complex alters the interaction landscape. The transcriptional activity of TFAM appears to be independent of NEIL1 expression under normal cellular conditions, however, in the presence of DNA damage, we observe a significant reduction in the mRNA expression of TFAM-transcribed mitochondrial genes in the absence of NEIL1. Overall, our data indicate that the interaction between NEIL1 and TFAM can be modulated by local environment such as salt concentrations, protein availability, the presence of nucleic acids, as well as the presence of DNA damage.

KEYWORDS

base excision repair (BER), NEIL1 DNA glycosylase, mitochondrial transcription factor A (TFAM), small angle X-ray scattering (SAXS), HDX-MS (hydrogen–deuterium exchange mass-spectrometry)

## Introduction

Maintaining the integrity of the 16.5 kb circular human mitochondrial genome is essential for proper cellular function as mitochondrial DNA (mtDNA) encodes for 13 polypeptides, 22 tRNAs, and two rRNAs that are required for the generation of ATP *via* oxidative phosphorylation (OXPHOS) (Anderson et al., 1981). Mitochondria rely heavily upon nuclear-encoded proteins for genome maintenance. The mitochondrial proteome comprises some ~1,500 proteins that are transported to the organelle *via* different import mechanisms (Endo et al., 2011; Wiedemann and Pfanner, 2017; Ruan et al., 2020). Much like its nuclear counterpart, mtDNA is also subjected to damage from various endogenous and exogenous sources that leads to genome instability and various pathologies, including neurodegenerative disorders, metabolic dysfunction, and some cancers (Copeland and Longley, 2014; Van Houten et al., 2016; Rahman and Copeland, 2019). MtDNA molecules were originally thought to be especially prone to damage by reactive oxygen species (ROS) owing to their lack of protection from nucleosomes as well as their location proximal to sites of OXPHOS within the mitochondrial inner membrane; however, this assumption has recently been contested as mtDNA are compacted into nucleoid complexes (further discussed below) and ROS appear to be concentrated within the mitochondrial cristae (Yakes and Van Houten, 1997; Anson et al., 2000; Lim et al., 2005; Kauppila and Stewart, 2015). However, to cope with mtDNA damage, several nuclear-encoded repair factors that participate in multiple DNA repair pathways have been identified in the mitochondria. Of these, the mitochondrial base excision repair (mtBER) pathway appears to be the major pathway involved with the removal of small, non-bulky lesions that arise in the DNA (Fromme and Verdine, 2004; Szczesny et al., 2008; Wallace et al., 2012; Krokan and Bjoras, 2013; Prakash and Doublié, 2015). Several nuclear BER enzymes have been implicated in the repair of mtDNA, including seven of the eleven known mammalian DNA glycosylases that initiate BER, end processing enzymes such as polynucleotide kinase phosphate (PNKP), DNA polymerases such as polymerase beta (Polβ) that are needed to fill in the gap generated, and DNA ligase III needed to seal the gap (Prakash and Doublié, 2015; Saki and Prakash, 2017; Baptiste et al., 2021).

The NEIL1 enzyme is a bifunctional DNA glycosylase that possesses both glycosylase and lyase functions and is involved with the removal of oxidized DNA bases such as thymine glycol, 5-hydroxy uracil, the ring-opened formamidopyrimidine (Fapy) lesions, as well as the further oxidation products of 8-oxo guanine (8-oxoG), namely spiroiminodihydantoin (Sp) and guanidinohydantoin (Gh) that result in an abasic (AP) site (Krishnamurthy et al., 2008; Zhao et al., 2010; Prakash et al., 2012; Vik et al., 2012; Minko et al., 2020; Yeo et al., 2021). NEIL1 also possesses lyase activity by which it can incise the DNA backbone at AP sites. Crystal structures of NEIL1 unliganded and bound to DNA containing oxidized DNA lesions have provided valuable insight into the enzymatic and lesion recognition activity of the enzyme (Doublié et al., 2004; Zhu et al., 2016; Liu et al., 2021). Notably, the structures of NEIL1 lacked a large region of disorder at the C-terminal end of the protein. Previously, we and others have shown that this disordered tail of NEIL1 comprising 100 amino acid residues (aa 290–390) participates in the interaction with its binding partners, including the homotrimeric proliferating cellular nuclear antigen (PCNA), flap endonuclease 1 (FEN-1), heterotrimeric replication protein A (RPA), the Werner Syndrome RecQ like helicase (WRN helicase), and mitochondrial single stranded DNA binding protein (mtSSB) (Das et al., 2007; Dou et al., 2008; Hegde et al., 2008; Theriot et al., 2010; Prakash et al., 2017; Sharma et al., 2018).

Unlike nuclear DNA that is packaged into nucleosomes, mtDNA is packaged into nucleo-protein structures called nucleoids, which are approximately 110 nm in size based on high-resolution techniques (Kukat et al., 2011; Bogenhagen, 2012; Campbell et al., 2012; Farge and Falkenberg, 2019). The mitochondrial transcription factor A (TFAM) protein, a major component of mitochondrial nucleoids was originally thought to be sufficient for the higher-order organization of the mitochondrial genome and is also required to initiate transcription from the light and heavy strand promoter regions of mtDNA (Alam et al., 2003; Kaufman et al., 2007; Kukat et al., 2015). However, recent reports [reviewed in (Mishmar et al., 2019)] implicate nuclear factors such as MOF in the binding and regulation of higher-order genome organization within the mitochondrion, suggesting a more complex scenario involving nuclear-mitochondrial crosstalk. Although current experimental strategies limit the examination of the exact composition of the mitochondrial nucleoid, several other proteins, including mtSSB, the mtDNA replicative polymerase gamma (POLG), and the twinkle helicase, are associated with the mitochondrial nucleoid (Bogenhagen et al., 2008).

Evidence for the participation of TFAM in mtBER was provided by studies indicating the ability of TFAM to bind to 8-oxoG while inhibiting BER enzymes, including 8-oxoG DNA glycosylase (OGG1), uracil-DNA glycosylase (UDG), and apurinic endonuclease 1 (APE1) (Canugovi et al., 2010). TFAM was further implicated in the cleavage of AP sites to yield single-strand breaks in the DNA (Xu et al., 2019). Given the substrate overlap between NEIL1 and TFAM and the likely close proximity of NEIL1 to the mitochondrial nucleoid, in the current

manuscript, we report for the first time an interaction between NEIL1 and TFAM *via* unique interaction interfaces. While the interaction between the two proteins appears to be transient and dependent upon the presence of DNA, we noted that NEIL1 can interact with TFAM using multiple regions within both its N- and C- termini. This finding is novel and represents a deviation from previous observations that suggest the interaction domain of NEIL1 resides solely within its C-terminal disordered tail. Here, we use orthogonal approaches including far-western analysis, pull-down studies, small-angle X-ray scattering (SAXS), multi-angle light scattering (MALS), and hydrogen deuterium exchange mass spectrometry (HDX-MS), to probe the interaction between the two proteins. Our data collectively suggest that the interaction between NEIL1 and TFAM is transient and can be enhanced by modulating the local environment such as salt concentration, protein availability, and the presence of DNA or RNA. Furthermore, the importance of the interaction between the two proteins is underscored by the observation that NEIL1 is required for the transcription of mitochondrial genes under conditions of cellular stress.

# Experimental approach

## Plasmids, DNA, and RNA oligonucleotides

The bacterial expression plasmid containing C-terminal His-tagged NEIL1 (pET30a) was obtained from the laboratories of Dr. Sylvie Doublié and Dr. Susan Wallace (University of Vermont, United States). The plasmid containing the ORF for full-length TFAM was a kind gift from Dr. Robert Sobol (University of South Alabama, United States). The TFAM DNA sequence lacking the mitochondrial targeting sequence was amplified from this plasmid and subcloned into a pET30a vector. The *E. coli* expression plasmids containing the full-length (FL) NEIL1-FL, C-terminal truncated polypeptides (Δ40, Δ56, Δ78, and Δ100), and GST fused C-terminal regions (289–389, 289–349, 312–389, and 312–349) were synthesized as described previously (Das et al., 2007; Prakash et al., 2017; Sharma et al., 2018). The Flag peptide sequence was included at the C-terminus of both NEIL1-FL and TFAM in the pET30a background using primers containing the Flag nucleotide sequence by traditional cloning methods with restriction enzyme digestion.

The duplex oligonucleotide substrate used in these studies is a 22-nt oligomer 5′-ATTCAACCAA**X**AGCCCTGGCCG-3′ with a complementary oligomer 5′-CGGCCAGGGCTATTG GTTGAAT-3′. The X represents either tetrahydrofuran, an abasic site analog (specific DNA; SD), or thymine (nonspecific DNA; NSD). The oligos were ordered from Integrated DNA Technologies Inc. (IDT, Coralville, IA) and PAGE purified. For optimal annealing, equimolar mixtures of the oligomers were heated at 94°C for 2 min, then slowly cooled to room temperature. A 22-nt single-stranded RNA oligonucleotide with the sequence 5′-rArUrUrCrArArCrCrArA**Xr**ArGrCrCrCrUrGrGrCrCrG-3′ was synthesized by IDT for use in the affinity pull-down experiments.

## Overexpression and purification of NEIL1 and TFAM

TFAM was overexpressed and purified as described previously (Ngo et al., 2011). NEIL1-FL, the C-terminal truncated polypeptides, and the GST fused NEIL1 C-terminal regions were overexpressed and purified as described previously (Sharma et al., 2018). Briefly, protein expression was induced by 0.4–1 mM IPTG at 18–25°C in the Rosetta 2 *E. coli* expression strain. Bacterial pellets were lysed using sonication, and the resulting cell debris was discarded after centrifugation at 25,000 × g for 1 h. Protein purification was performed using affinity chromatography (Talon beads or Glutathione S Sepharose) following the manufacturer's protocol (Clontech Laboratories, Inc., Mountain View, CA; and Millipore-Sigma, St. Louis, MO). The proteins were further purified using a HiTrap SPFF ion exchange column and Superdex 200 Increase 10/300 GL size exclusion column (Cytiva). The purified fractions were concentrated and stored at -80°C until further use.

## Far-western analysis

Far-western analysis was performed as described previously (Prakash et al., 2017). Briefly, proteins (50 pmol of the NEIL1 polypeptides, bovine serum albumin, and glutathione S-transferase; 1 pmol TFAM) were separated by 12% SDS-PAGE, transferred to a PVDF membrane (BioRad), treated with 6M guanidine HCl in PBS containing 1 mM DTT, and then gradually refolded with successive dilutions of guanidine HCl in PBS containing 1 mM DTT. The membranes were then blocked for 3 h with 5% milk in PBS at 4°C and incubated with purified TFAM (1 pmol/ml) overnight. Immunoblot analysis was performed using an anti-TFAM antibody (Cell signaling #7495) at 1:1,000 dilution in 5% BSA in PBST.

## Affinity pull-down using Flag-tagged recombinant protein

Affinity pull-down experiments were performed using C-terminal Flag-tagged purified NEIL1 or TFAM in wash buffer containing 50 mM Tris-HCl pH 7.5, 10% glycerol, and 50–300 mM NaCl/KCl. Briefly, 1.25/2.5 nM each of NEIL1, TFAM, and specific DNA or RNA were mixed in a final volume of 400 µl in wash buffer and incubated on ice for 1 h. The mixture was then added to 20 µl Anti-FLAG M2 Magnetic Beads (#M8823 Millipore Sigma), pre-equilibrated with wash buffer, and tumbled end over end for 2 h at 4°C. The beads were then washed with 250 µl wash buffer three times, followed by elution using 3X Flag peptide (#F4799 Millipore

Sigma). The samples were analyzed *via* SDS-PAGE. For analysis of complex formation in the presence of Benzonase Nuclease (Millipore-Sigma catalog #E1014) where indicated, 125 units of Benzonase Nuclease (at 250 units/µl) was added to the proteins prior to complex formation.

## Complex formation and size exclusion chromatography

The NEIL1-TFAM complex was prepared by mixing both proteins in a 1:1 M ratio in a buffer containing 20 mM HEPES (pH 7.5), 300 mM NaCl, 10% (v/v) glycerol, and 1 mM DTT. The complex was incubated on ice for 1 h prior to size exclusion chromatography (SEC) analysis. The ternary complex of TFAM-NEIL1-DNA was prepared by mixing each in a 1:1:1 M ratio followed by incubation on ice for 1 h. The SEC was performed with a Superdex 200 column using a buffer containing 20 mM HEPES (pH 7.5), 300 mM NaCl, 10% (v/v) glycerol, and 1 mM DTT. The NEIL1-DNA and TFAM-DNA complexes were prepared by mixing the proteins and the DNA in a 1:1 M ratio and incubated for 1 h on ice prior to loading onto the SEC column. The column was calibrated with blue dextran (to determine the void volume) and three standards of known molecular weights (MW) using Gel Filtration LMW Calibration Kit (Cytiva # 28403841).

## Small-angle X-ray scattering and multi-angle light scattering

SEC-MALS-SAXS/SEC-SAXS data were collected at beamline 18-ID (BioCAT) of the Advanced Photon Source (APS) at Argonne National Laboratory. All experiments were performed in the buffer containing 25 mM HEPES pH 7.4, 300 mM NaCl, 5% glycerol, and 1 mM DTT. Samples for data collection included individual proteins (NEIL1-FL and TFAM), the NEIL1-TFAM complex, protein-DNA complexes (NEIL1-DNA and TFAM-DNA), and the ternary complex (TFAM-NEIL1-DNA) at concentrations of 7–11 mg/ml (190 µM each) at 300 µl volume. The samples were loaded onto an in-line SEC column (Superdex 200 10/300) coupled to a MALS detector (DAWN Helios II, Wyatt Technologies) and a SAXS flow cell. At a flow rate of 0.7 ml/min, 0.5 s exposures were acquired every 1 s. The SEC-SAXS data files were processed in BioXTAS RAW (version 2.1.0) using evolving factor analysis (EFA) to extract scattering profiles for each component in overlapping peaks (Meisburger et al., 2016; Hopkins et al., 2017). Forward scattering intensity ($I_0$) and radius of gyration ($R_g$) were determined using Guinier fit (Konarev et al., 2003). The Kratky plots were normalized against Rg using BioXTAS RAW. Scattering curves were further analyzed using GNOM for the calculation of $I_0$, $R_g$, distance distribution P(r), maximum dimension ($D_{max}$), Porod volume ($V_\rho$), and excluded volume ($V_e$) (Svergun, 1992). The MW values were estimated using volume of correlation, Porod volume, ATSAS datclass/ShapeandSize, and Bayesian estimation methods (Rambo and Tainer, 2013; Franke et al., 2018; Hajizadeh et al., 2018; Piiadov et al., 2019). Absolute molar mass values were also calculated from MALS for comparison with the SAXS MW estimates using the ASTRA software (Wyatt Technologies).

## Hydrogen deuterium exchange-mass spectrometry

HDX-MS experiments were performed on a Synapt G2-Si (Waters Corp.) and a Leap HD/X-PAL (Trajan) fluidics system. The proteins and DNA were mixed in an equimolar ratio at a concentration of 100 µM and incubated for 1 h in a buffer containing 50 mM Tris-HCl pH 7.5, 10% glycerol, 100 mM NaCl, and 1 mM DTT. Deuterium exchange was initiated by diluting the samples 10X to a final concentration of 10 µM in an equivalent buffer made with $D_2O$ at 20°C. After incubation of protein samples for different time points (15, 30, 60, 90 s, 3, 10, and 30 m), the exchange reaction was stopped, and in-solution digestion (2 min at 2°C) was initiated by 10X dilution into 0.3 mg/ml pepsin in 100 mM potassium phosphate buffer pH 2.5. Non-deuterated protein samples for control measurements were also prepared following the same protocol except for the deuterium exchange step. All reactions were performed in triplicate. Peptide trapping and desalting were carried out using a Waters VanGuard BEH Pre-column 2.1 × 5 mm, and separation was achieved using a Waters BEH C18 reverse-phase column 1.7 µm 1.0 × 50 mm with all liquid chromatography (LC) carried out using a Waters Acquity LC system. Thirty pmol of digested peptides were loaded, trapped, and washed using a 0.1% formic acid solution at 0.1 ml/min, and subsequent separation was carried out using a 14 min 5%–40% acetonitrile gradient at a flow rate of 70 µl/min. Peptide identification was performed by acquiring and processing the $MS^E$ data acquired for non-deuterated samples using ProteinLynx Global Server v3.0.1 (PLGS, Waters Corporation). The level of deuterium exchange was examined using HDExaminer software (Sierra Analytics). Significant uptake changes were shown using volcano plots by a confidence threshold of a $p$ value of <0.05, and figures were created using VolcaNoseR (Goedhart and Luijsterburg, 2020). The protein structure figures were prepared using PyMOL (The PyMOL Molecular Graphics System, Version 1.7.6.2 Schrödinger, LLC). Protein-DNA interactions from the PDB files were extracted using the DNAproDB database (Sagendorf et al., 2020), and figures were created with BioRender.com.

## Cell culture and cell viability assay

Wild-type (WT) and NEIL1 knockout (KO) Hap1 cell lines were kindly provided by Dr. Magnar Bjørås (Norwegian

University of Science and Technology (NTNU), Norway). Cells were cultured in IMDM media supplemented with 10% FBS and 1X penicillin and streptomycin at 37°C and 5% $CO_2$. NEIL1 KO cell lines were validated using western blot analysis. WT and NEIL1 KO Hap1 cells from a 10 cm dish were collected by scraping in cell lytic M (Millipore Sigma) and lysed by agitation at 4°C. Cell debris were pelleted by centrifugation at 16,900 × g for 15 min at 4°C and whole cell extract was collected. 50 µg of protein was loaded, separated by SDS-PAGE, and transferred to a PVDF membrane (Biorad). The membrane was probed using a NEIL1 rabbit polyclonal antibody (1:1000; Proteintech #12145-1-AP). PCNA (D3H8P) XP rabbit monoclonal antibody (1:1,000; Cell Signaling #13110S) was used as loading control. An ECL anti-rabbit IgG secondary antibody conjugated to HRP (1:10,000; GE Healthcare NA934V) and WesternBright ECL HRP substrate (Advansta Inc) were used to visualize antibody binding using a BioRad ChemiDoc imager. Cell viability upon methyl methanesulfonate (MMS) treatment was assessed using a resazurin-based fluorescence assay as described previously (D'Arcy et al., 2019). Briefly, cells were seeded (10,000 cells/well) in costar black 96-well clear bottom plates. After 24 h, media containing MMS was added to final concentrations of 1, 3, 10, 30, 100, and 300 µM, 1, 3, 10, and 30 mM by serial dilution. Following 72 h, resazurin solution was added to a final concentration of 120 µM and incubated for 4 h. The relative fluorescence was measured at 540 ± 20 nm excitation and 620 ± 20 nm emission on a Tecan Infinite M1000 Pro multimode plate reader. Non-linear regression analysis [(Inhibitor) vs. response] was performed using GraphPad Prism 8.

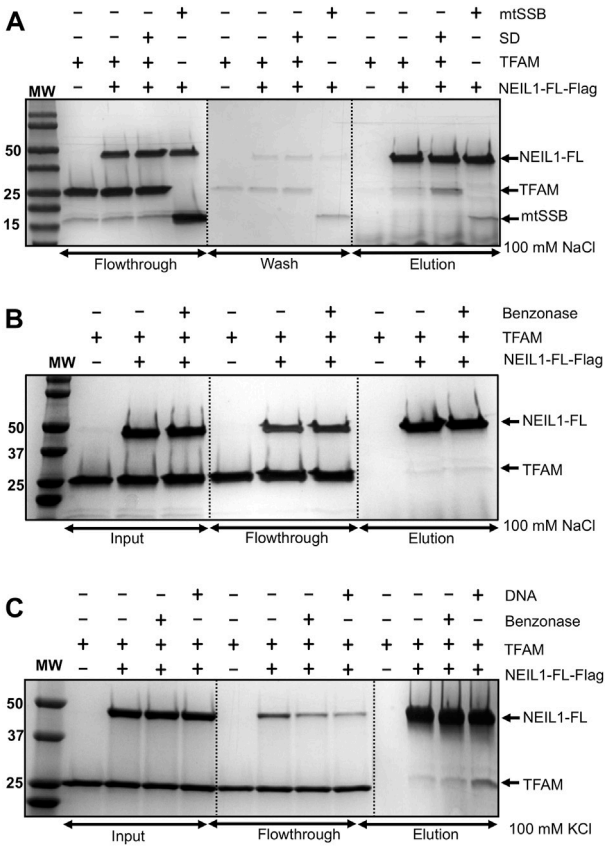


FIGURE 1
Affinity pull-down experiments reveal an interaction between recombinantly purified NEIL1 and TFAM. **(A)** Flag-tagged, full-length NEIL1 (NEIL1-FL) was used to pull down TFAM in the presence and absence of a specific DNA (SD) sequence containing an abasic site in a buffer containing 100 mM NaCl. TFAM was observed in the elution fractions in both the presence and absence of SD. mtSSB was used as a positive control as we previously documented the interaction between NEIL1 and mtSSB. **(B)** The purified proteins were treated with Benzonase prior to complex formation to eliminate nucleic acid contamination followed by the pull-down experiment. TFAM was observed in elution fractions containing either 100 mM NaCl in the buffer, or 100 mM KCl in the buffer **(C)** in the both Benzonase treated or non-treated samples indicating that there is a direct interaction between the two proteins.

## Quantitative real-time PCR and estimation of mtDNA copy number

cDNA was prepared from each cell line, with or without treatment with 125 µM MMS for 72 h, using the TaqMan™ Gene Expression Cells-to-CT™ Kit (#4399002). mRNA expression of four human mitochondrial genes *CYB*, *ND1*, *CO1*, and *RNR1* was determined by quantitative real-time PCR using the TaqMan Fast Universal Master Mix (2X; catalog no. 4352042) and TaqMan Gene Expression Assay probes from Life Technologies (*MT-CYB*, Hs02596867_s1; *MT-ND1*; Hs02596873_s1; *MT-CO1*, Hs02596864_g1; *MT-RNR1*, Hs02596859_g1). The reactions were performed using QuantStudio Pro 7 (Applied Biosystems) RT-PCR system, and analysis of mRNA expression was performed as per the instruction of the manufacturer (ΔΔCT method). Transcript quantities were normalized to GAPDH (Hs02758991_g1) as a reference gene transcript.

The absolute and relative mtDNA copy number was estimated for the Hap1 WT and NEIL1 KO cells using Absolute Human Mitochondrial DNA Copy Number Quantification qPCR Assay Kit (ScienCell Research Laboratories #8948) following the manufacturer's protocol. Briefly, genomic DNA (gDNA) was isolated using GeneJET Genomic DNA Purification Kit (ThermoFisher Scientific #K0721), and 2.5 ng gDNA was used to quantify mtDNA copy number with mtDNA specific primer sets in QuantStudio Pro 7 (Applied Biosystems) RT-PCR system. A reference genomic DNA in the kit was used to calculate the absolute and relative mtDNA copy number. A total of three to four biological replicates were analyzed for these experiments with each experiment performed in triplicate. Statistical analysis was performed using Student's t-test in GraphPad Prism version 8.1.0 for MAC OS X (GraphPad Software, San Diego, California United States, www.graphpad.com).

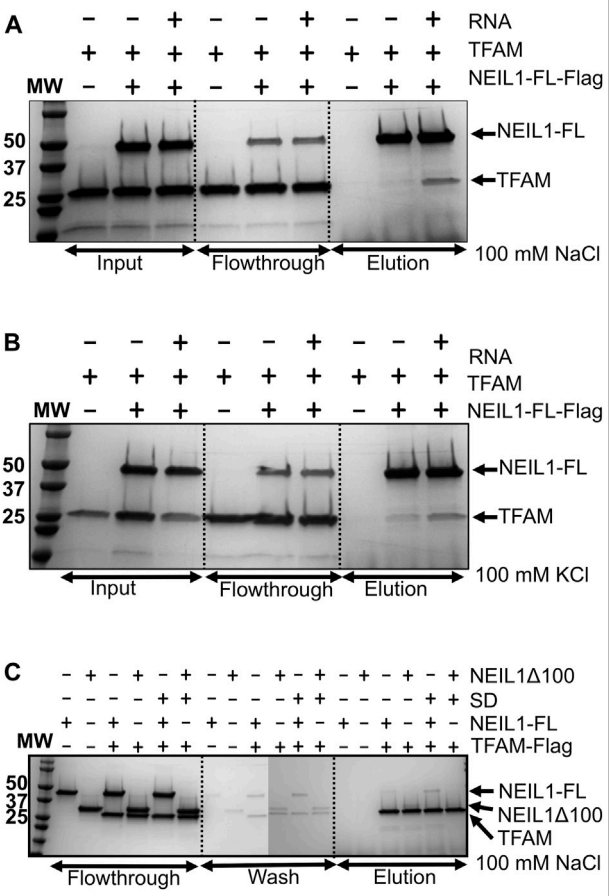


FIGURE 2
Affinity pull-down experiments display an interaction between NEIL1 and TFAM using recombinantly purified proteins. **(A)** Flag tagged NEIL1 was used to pull down TFAM in the presence of RNA in a buffer containing 100 mM NaCl. TFAM is observed in the elution fractions in the absence and presence of RNA. **(B)** Flag tagged NEIL1 was used to pull down TFAM in the presence of RNA in a buffer containing 100 mM KCl. Under these conditions, TFAM is also observed in the elution fractions in the absence and presence of RNA. **(C)** The reverse pull-down experiment using Flag-tagged TFAM was performed. Full-length NEIL1 (NEIL1-FL) and a truncated NEIL1 enzyme lacking 100 residues from disordered C-terminal region (NEIL1-Δ100) were observed in the elution fractions in the presence and absence of DNA. Non-specific binding of untagged TFAM, NEIL1-FL, and NEIL1-Δ100 with Flag beads was not detected as shown in elution fractions when the interaction partner is absent.

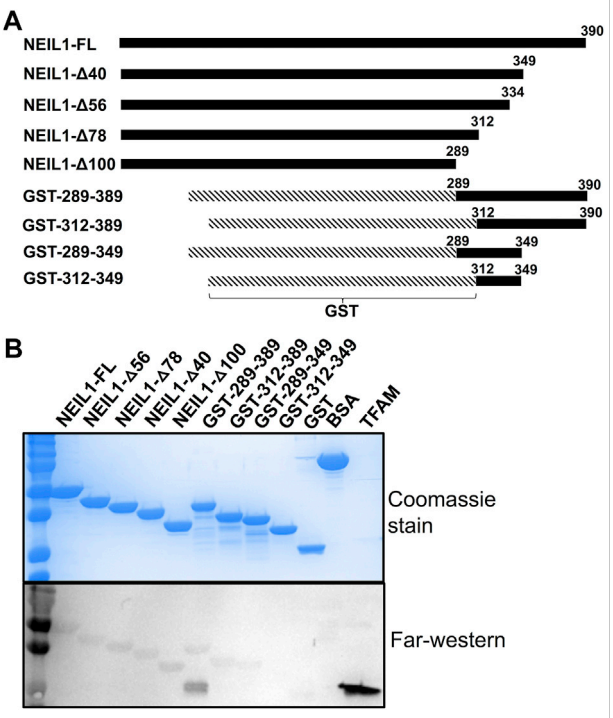


FIGURE 3
Far-western analysis indicates that NEIL1 interacts with TFAM via multiple binding sites present at both the N- and C-terminal domains. **(A)** A map of the His-tagged polypeptides of NEIL1 lacking portions of the C-terminal disordered tail and the GST-tagged C-terminal polypeptides of NEIL1 lacking the N-terminal portion of the enzyme. **(B)** Far-western analysis to determine the minimal region of NEIL1 required for interaction with TFAM. All proteins used in this study were expressed in *E. coli*, purified to homogeneity, and verified by sodium dodecyl sulfate-polyacrylamide gel electrophoresis (SDS-PAGE) analysis stained with Coomassie blue. 50 pmol of NEIL1 and the truncated enzymes, bovine serum albumin (negative control), glutathione S-transferase (negative control), and 1 pmol of TFAM (positive control) were loaded onto the gel. Far-western analysis was performed where proteins were transferred to a PVDF membrane, denatured, slowly renatured on the membrane, incubated with 10 pmol/ml purified TFAM, and probed with an anti-TFAM antibody to detect an interaction.

# Results

## Mapping the interaction between NEIL1 and TFAM, *in vitro*

The interaction of NEIL1 with downstream BER factors, as well as with proteins involved with other aspects of DNA metabolism, is essential for the efficient repair of DNA lesions (Hegde et al., 2012). NEIL1's function has been associated with mitochondrial genome maintenance, as demonstrated by previous work by our group and others (Hu et al., 2005; Vartanian et al., 2006; Sampath et al., 2011; Sharma et al., 2018). In preliminary experiments, using affinity pull-down assays from mammalian cells followed by mass-spectrometry, we identified peptides belonging to interacting partners of NEIL1 including TFAM and mtSSB (data not shown). We previously reported and mapped an interaction between NEIL1 and mtSSB using biochemical and structural approaches (Sharma et al., 2018). In the current manuscript, using recombinantly purified Flag-tagged NEIL1 or TFAM, we

show that NEIL1 and TFAM likely interact weakly at concentrations of low salt between 50–100 mM NaCl or 50–150 mM KCl, while a slight interaction was observed at higher salt concentrations (>300 mM NaCl) both in the presence and absence of a 22-mer specific DNA (SD) or RNA substrate containing an abasic site analog (Figures 1A–C, Figures 2A–B; Supplementary Figures S1–S5). We also performed similar experiments in the presence of Benzonase to probe a direct interaction between the two proteins in the absence of any nucleic acid binding partners and noted that the presence of Benzonase did not alter binding between the two proteins (Figures 1B,C). These results indicate that the interaction between NEIL1 and TFAM is most likely transient and can be manipulated by altering the interacting environment where lower salt conditions are favored. Interestingly, we also observed an interaction between TFAM and a truncated polypeptide of NEIL1 that lacks the C-terminal protein interaction domain (called NEIL1Δ100), both in the presence and absence of DNA, indicating that interaction with TFAM is not limited to the residues within the putative protein-binding disordered C-terminal tail of NEIL1 (Figure 2C).

To further identify the region of NEIL1 that binds to TFAM, we employed far-western analysis using purified recombinant histidine-tagged full-length NEIL1 (NEIL1-FL) and the truncated polypeptides of NEIL1, with the indicated number of residues deleted: NEIL1-Δ40, NEIL1-Δ56, NEIL1-Δ78, and NEIL1-Δ100 (Figures 3A,B top panel). We also expressed and purified GST-tagged NEIL1 polypeptides containing regions of the disordered C-terminus, amino acids 289–390, 289–349, 312–390, and 312–349 (Figures 3A,B top panel) and performed far-western analysis as described previously (Hegde et al., 2012; Prakash et al., 2017). BSA and GST alone were used as negative controls. The membrane with the refolded FL and truncated NEIL1 proteins was incubated with purified TFAM and then probed with an antibody against TFAM. Interestingly, our results indicate that purified TFAM interacts with the N-terminal regions of NEIL1, including the protein that lacks the protein interaction domain (100 residues) (Figure 3B, bottom panel). A slight interaction with TFAM was also observed with the C-terminal polypeptides of NEIL1 except for one that comprised residues 312–349. This indicates that NEIL1 interacts with TFAM *via* multiple binding sites that are present at its N- as well as C-terminal domains, a result that is divergent from past observations with its other binding partners, including mtSSB and the proliferating cell nuclear antigen (PCNA) where NEIL1 interactions were exclusively observed within the disordered C-terminal tail (Prakash et al., 2017; Sharma et al., 2018). Replicates of the far-western analysis are displayed in Supplementary Figure S6.

## Complex formation between NEIL1 and TFAM observed *via* SEC, MALS, and SAXS

From our past experience with recombinant NEIL1, we observed that the protein is unstable and prone to aggregation when subjected to multiple freeze-thaw cycles upon long-term storage. Furthermore, for structural studies involving solution scattering methods where we require milligram amounts of purified protein, we noted that NEIL1 was prone to precipitation at higher concentrations in the presence of a buffer containing lower concentrations of sodium chloride (<100 mM NaCl). Even though complex formation between NEIL1 and TFAM is favored at lower salt conditions, for the SEC studies we used buffer containing 300 mM NaCl to attempt to isolate a protein-protein complex in the presence of DNA. We used a calibrated Superdex 200 column and documented the MW of each eluting species (Supplementary Table S1). We first analyzed the proteins alone to determine their individual retention volumes and calculated the MW values based on a standard curve. NEIL1-FL (theoretical mass of 44.75 kDa) elutes as a single peak with a MW of 49.1 kDa on the SEC column (Supplementary Figure S7A; Supplementary Table S1). The theoretical MW of a full-length TFAM monomer (lacking the N-terminal mitochondrial targeting sequence or MTS) is 25.6 kDa, and on the SEC column TFAM elutes as a single peak with a MW estimate of 39.9 kDa (Supplementary Figure S7A; Supplementary Table S1). The higher MW values calculated from our SEC experiments for the proteins is likely because of their elongated shape that results from the region of disorder within the C-terminal domain of unliganded NEIL1 (residues 290–390) (Doublié et al., 2004; Hegde et al., 2010) and high intrinsic flexibility observed in unliganded TFAM (Rubio-Cosials et al., 2011). When combined, a mixture of NEIL1 and TFAM elutes as two separate peaks at their respective retention volumes, indicating that the two proteins likely do not form a complex that can be isolated under solvent conditions containing 300 mM NaCl (Supplementary Figure S7A; Supplementary Table S1). Next, we performed SEC analysis of the two proteins in the presence of the specific (SD) or non-specific DNA (NSD) substrates. The NEIL1-SD and -NSD complexes elute at a MW value of 52.8 kDa, and the TFAM-DNA complexes elute at ~45 kDa (45.4 for SD and 43.6 for NSD; Supplementary Figures S7B,C; Supplementary Table S1). The SEC data obtained for the ternary complex (TFAM-NEIL1-DNA) was inconclusive, as we did not observe a clear separate peak at a higher retention volume for the complex (Supplementary Figures S7D–F; Supplementary Table S1). However, given the likely transient nature of these interactions, there may be a small fraction representative of a ternary complex present in the equilibrated mixture of TFAM-NEIL1-DNA, which cannot be deciphered by SEC under our current conditions. We therefore sought to determine the absolute molar mass and the stoichiometry of binding using SEC-MALS-SAXS methods where samples are loaded onto an SEC Superdex 200 column with an exclusion limit of 600 kDa, followed by a UV detector, MALS detector (DAWN Helios II, Wyatt Technologies), and a SAXS flow cell.

SEC-MALS-SAXS data were collected at beamline 18-ID (BioCAT) of the advanced photon source (APS) at Argonne National Laboratory. All measurements were performed in a buffer containing 25 mM HEPES pH 7.4, 5% glycerol, 300 mM NaCl, and 1 mM DTT, which we used previously to scrutinize the NEIL1-mtSSB complex (Sharma et al., 2018). We collected SEC-MALS-SAXS data either in duplicate or triplicate for the proteins individually, protein-DNA complexes (including both SD and NSD), and the protein-protein-DNA ternary complexes where the SEC profiles (top left panels) and SAXS analyses (top right and bottom panels) are displayed in Supplementary Figures S8A–I. The absolute molar mass and MW values calculated by MALS and SAXS are tabulated in Supplementary Table S2. For the ternary complex (TFAM-NEIL1-SD), we collected SEC-SAXS data in triplicate and the data are consistent between two of the three runs. For simplicity, values obtained from run 1 are displayed in Supplementary Table S2. For some of the NEIL1-containing samples, we were able to estimate molar mass values from MALS for only one of the three runs owing to aggregation in solution, as observed in the scattering curves obtained from SAXS analysis (Supplementary Table S2; Supplementary Figures S8A,C). For each sample, we performed evolving factor analysis (EFA) to extract individual components from SEC-SAXS peaks, which revealed multiple overlapping components (*comp*) in solution for some of the samples (Supplementary Table S2). For each scattering species, we observe a distinct profile where the scattering intensity is plotted as a function of momentum transfer (Supplementary Figures S8A–I; Top right Panels). An upward trend at low q-values is observed in samples containing NEIL1 alone and NEIL1-TFAM, which is representative of some aggregation of NEIL1 within the samples. The estimated values of forward scattering intensity [$I$ (0)], radius of gyration ($R_g$), and maximum particle dimension ($D_{max}$) from Guinier analysis or pairwise distance distribution, $P(r)$, analysis are summarized in Supplementary Table S2. $P(r)$ analysis for both unliganded NEIL1 and TFAM display a curve with an elongated tail that results in large $D_{max}$ values of 152 Å and 140 Å, respectively, similar to values we and others reported for these proteins (Rubio-Cosials et al., 2011; Prakash et al., 2017; Rubio-Cosials et al., 2018; Sharma et al., 2018) (Supplementary Figures S8A,B; bottom left panels). The large $D_{max}$ values represent a likely elongated shape for these unliganded proteins that result from intrinsic flexibility and the presence of multiple conformations of varying dimensions in solution. This pronounced flexibility is also observed in the Kratky plots for the individual proteins where the plot either does not fully converge to the q axis at high q values or converges at larger q values when compared to the bound proteins described below (Supplementary Figures S8A,B; bottom right panels). When combined, the two proteins NEIL1 and TFAM elute as separate peaks as observed by the SEC profile collected prior to MALS and SAXS, and the $D_{max}$ values and Kratky plots are similar to those obtained for the unliganded proteins alone (Supplementary Figure S8C). For the NEIL1-SD/-NSD and TFAM-SD/-NSD complexes, we observe lower $D_{max}$ values (126/115 Å for NEIL1-SD/-NSD and 89/95 Å for TFAM-SD/-NSD) in comparison to the unliganded proteins (152 Å for NEIL1; 140 Å for TFAM) suggesting that binding to DNA changes the conformation of the proteins, likely stabilizing them and causing them to be more globular in nature (Supplementary Table S2; Supplementary Figures S8D–G; bottom left panels). Kratky analysis for the proteins bound to DNA display bell-shaped curves characteristic of less flexible, globular molecules (Supplementary Figures S8D–G; bottom right panels). EFA for the ternary complex containing TFAM-NEIL1-SD/-NSD reveals multiple components in solution with $D_{max}$ values of 148 Å and 154 Å that best correspond to the TFAM-NEIL1-SD and -NSD complexes, respectively, indicative of a larger linear dimension for the ternary complexes relative to the protein species (Supplementary Table S2; Supplementary Figures S8H,I; bottom left panels). Kratky plots for the ternary complexes are bell-shaped and converge to the q-axis at lower q-values when compared with the proteins alone (Supplementary Figures S8H,I; Bottom right panels).

In summary, corroborating our SEC results, in the absence of DNA, a mixture of NEIL1 and TFAM did not form a complex as indicated by two separate eluting species with MW values corresponding to the individual proteins. However, in the presence of DNA, we observe complex formation as indicated by a peak with a higher molar mass of 91.2 kDa obtained by MALS (Supplementary Table S2. This value could correspond to a ternary complex of TFAM-NEIL1-DNA at either a stoichiometric ratio of 1:1:1 (theoretical MW 83.9 kDa) or 1:1:2 (theoretical MW 97.5 kDa). These results indicate that NEIL1 and TFAM form a ternary complex only in the presence of DNA under our current solvent conditions.

## HDX-MS to identify peptides at the interaction interface

We used HDX-MS, a powerful technique that provides information regarding protein folding, stability, conformational dynamics, and ligand binding, to probe the interaction between NEIL1 and TFAM in the presence of DNA. With HDX-MS we can measure the rate of deuterium uptake when amide hydrogens present in the protein backbone are exposed to deuterated solvent ($D_2O$) and exchanged. Well-folded, buried, stable, secondary structural elements of a protein are typically protected from HDX; however, flexible regions and solvent-exposed residues readily take up deuterium. Similarly, upon protein-protein or protein-ligand binding, interaction interfaces are also protected from HDX. To our knowledge, this technique has not been previously used to scrutinize NEIL1, TFAM, or their binding to interacting partners thus presenting a novel methodology to scrutinize these complexes. We therefore systematically analyzed the binding of the specific

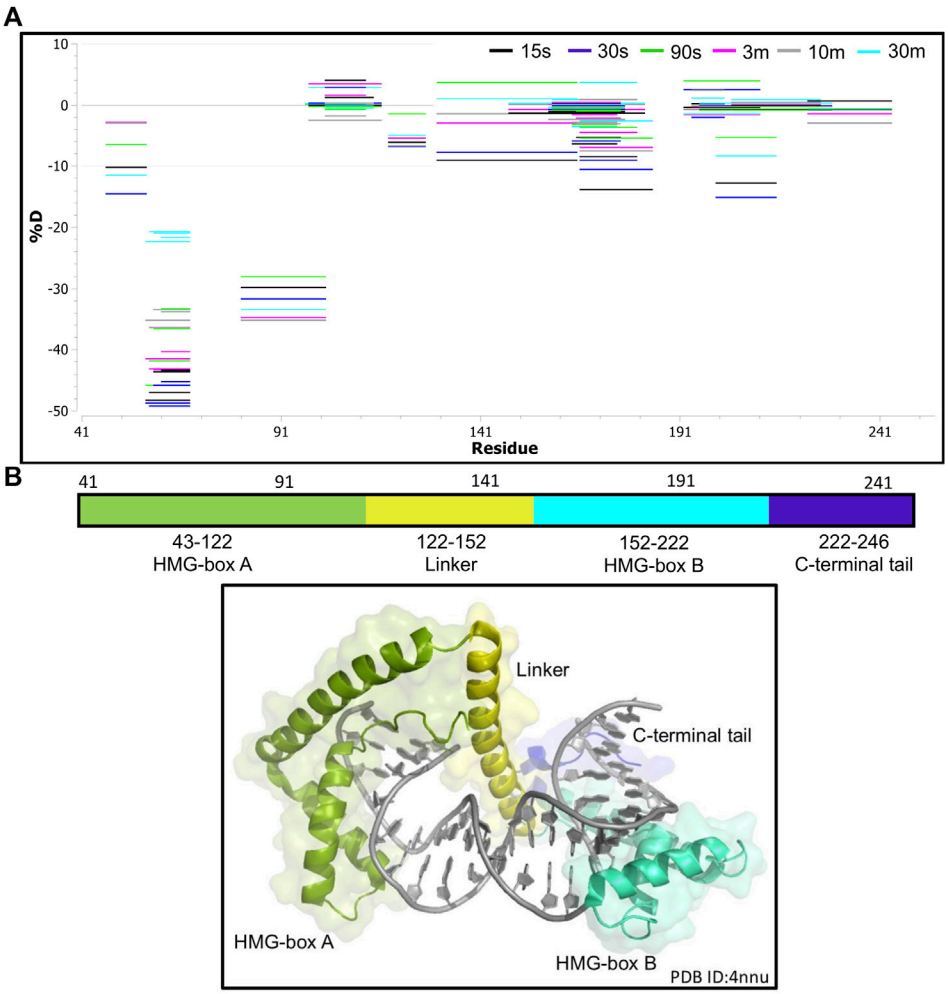


FIGURE 4
Hydrogen-deuterium exchange of the TFAM-DNA complex reveals the regions of TFAM involved with DNA binding. **(A)** Woods plot representing the distribution of TFAM regions displaying differential levels of solvent protection in the presence of DNA. Percent change in deuteration for peptides after various time points (15 s–30 m) between TFAM and the TFAM-DNA complex, where a negative percentage indicates less deuteration and more protection due to complex formation with the DNA. Each horizontal line in the plot represents an individual peptide with residue range on the *X*-axis and deuteration level i.e., level of protection on the *Y*-axis. **(B)** The domain map and cartoon representation of the crystal structure of the TFAM-DNA complex (PDB ID:4nnu) are displayed. In the structure, the DNA is colored grey and each region is color-matched to the domain map above.

DNA substrate containing an abasic site analog to NEIL1 and TFAM individually as well as in a complex comprising both proteins. Given the lower concentration of samples required for this technique, we were able to use the buffer containing 100 mM NaCl for these experiments. Both NEIL1 and TFAM bind to double-stranded DNA substrates with nanomolar affinities where Kd's measured for the NEIL1-DNA complex range from 2–29 nM (Odell et al., 2010; Prakash et al., 2016; Schomacher et al., 2016; Kladova et al., 2019) depending on the lesion and the DNA substrate, and Kd's measured for TFAM range from 4–7 nM (Gangelhoff et al., 2009; Malarkey et al., 2012; Ngo et al., 2014; Brown et al., 2015; Ramachandran et al., 2017; Cuppari et al., 2019). Prior knowledge of protein-DNA binding and residues involved with the interactions is obtained from published crystal structures of the TFAM-DNA and NEIL1-DNA complexes (Ngo et al., 2014; Zhu et al., 2016). We systematically collected HDX-MS data for the TFAM and NEIL1 proteins individually, the respective protein-DNA complexes, and lastly, the TFAM-NEIL1-DNA complex. For each of our samples, we obtained near-complete peptide coverage where the coverage for the TFAM samples ranged between 84.58%–94.86%, whereas the NEIL1 samples displayed a coverage of 98.74% (Supplementary Figures S9, S10).

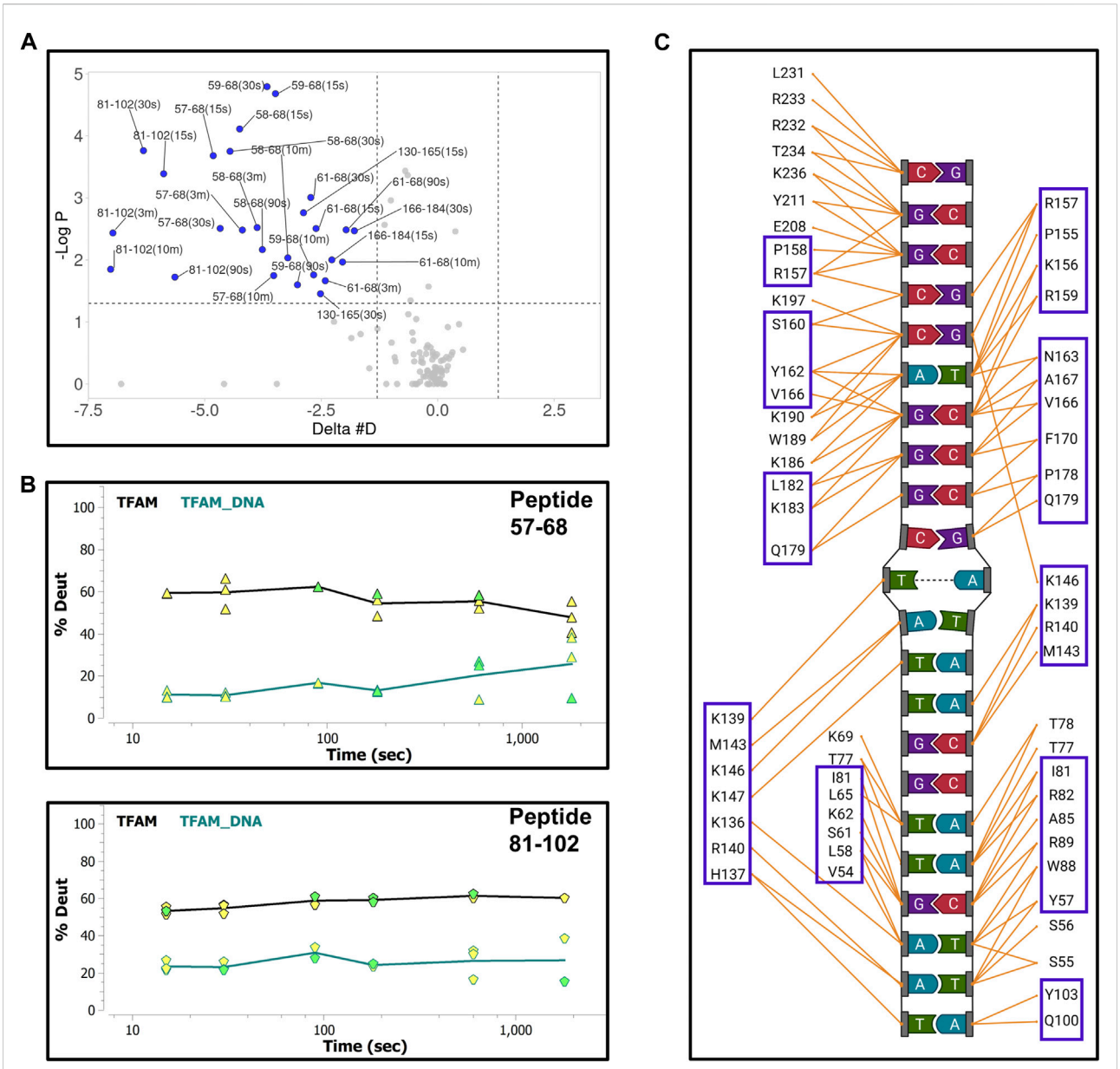


FIGURE 5
Hydrogen-deuterium exchange of the TFAM-DNA complex reveals the regions of TFAM involved with DNA binding. **(A)** Volcano plot quantifying the significant change in deuteron uptake for each peptide at a given time point. The upper left quadrant of the plot displays peptides (solid blue circles) with a significant decrease in deuteron uptake of the TFAM-DNA complex relative to TFAM alone. This significance is based on two statistical tests performed by the HDExaminer software where the first is a *p*-value test with a significance cutoff value of <0.05 (i.e., at a confidence level of 95%) and the second is based on whether the difference value on the *X*-axis (Delta #D) is greater than the replicate variance across all of the data within each specific data set as determined by the program. **(B)** Representative uptake plots are shown from the HDX-MS time course for peptides 57–68 and 81–102 that are significantly different between the TFAM-DNA and TFAM samples based on the volcano plot in **(A)**. **(C)** Interaction map showing TFAM residues that interact with DNA in the crystal structure of the TFAM-DNA complex (PDB ID:4nnu). Blue boxes represent residues within peptides that display a significant decrease in deuteration observed in the volcano plot.

First, we collected HDX-MS data of the TFAM-DNA complex over varying time points (from 15 s to 30 m), which reveal protection of certain regions within TFAM as indicated by a decrease in deuteration uptake (Woods plot, Figure 4A). We observe a decrease in deuterium exchange for the peptides present in the regions corresponding to high mobility group (HMG) box A (residues 43–122) and HMG-box B (residues 152–222) with an up to 50% decrease for box A and 20% for box B. We noted a ~10% decrease in deuterium exchange for the peptides within the linker region (residues 122–152) and the

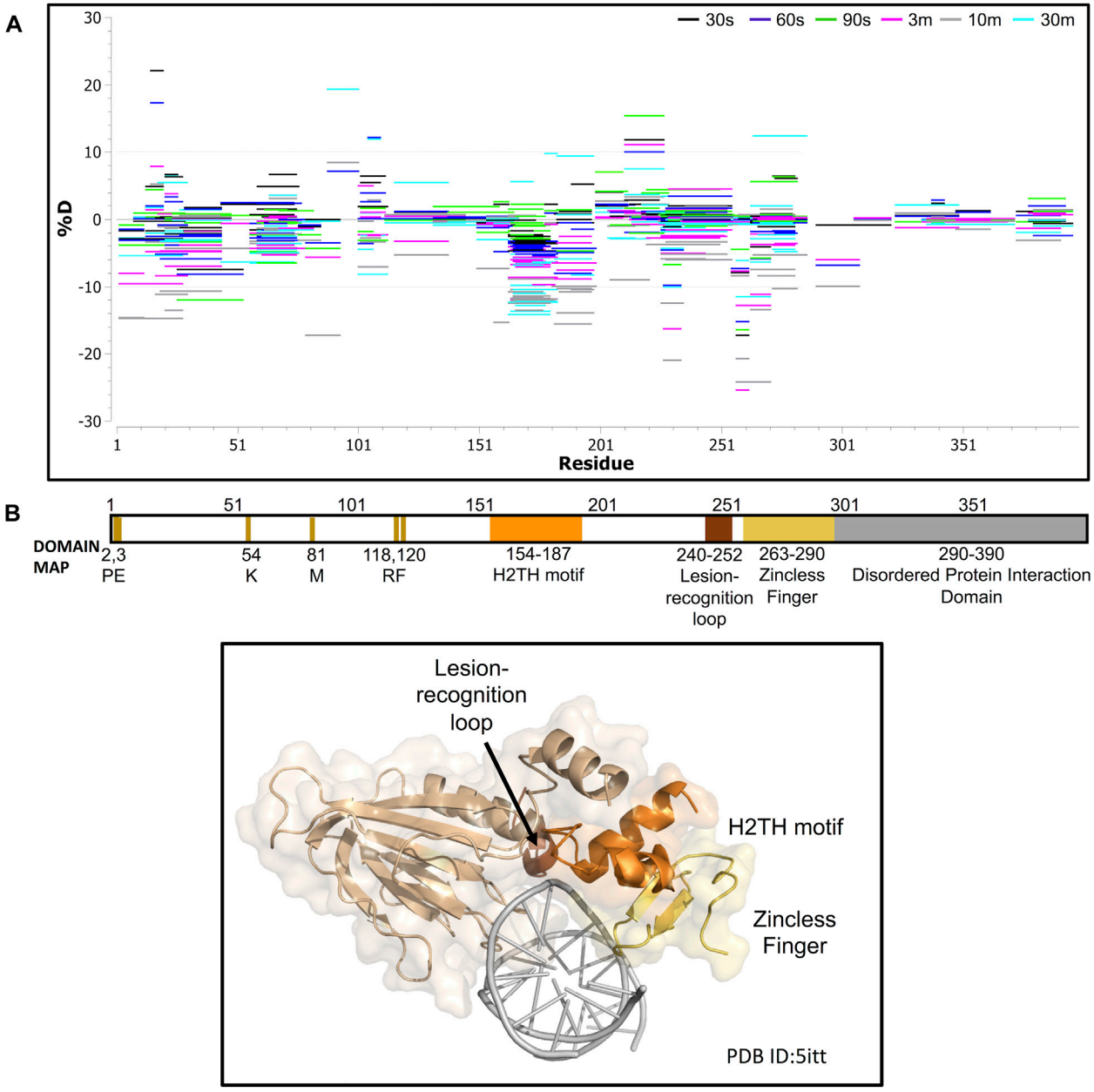


FIGURE 6
Hydrogen-deuterium exchange experiments for the NEIL1-DNA complex reveals regions of NEIL1 involved with DNA binding. **(A)** Woods plot representing the distribution of NEIL1 regions displaying differential levels of solvent protection in the presence of DNA. Percent change in deuteration for peptides after various time points (30 s–30 m) between NEIL1 and the NEIL1-DNA complex, where a negative percentage indicates less deuteration and more protection as a result of complex formation between NEIL1 and the DNA. Each horizontal line in the plot represents an individual peptide with residue range on the X-axis and deuteration level i.e., level of protection on the *Y*-axis. **(B)** Domain map and cartoon representation of crystal structure of NEIL1-DNA complex (PDB ID:5itt) are displayed. The active site and void-filling residues, and DNA binding motifs are indicated in the domain map. In the structure, the DNA is colored grey, and each region is color-matched to the domain map above.

C-terminal tail (residues 222–246). These results are consistent with the available structural data for DNA bound TFAM [PDB ID:4nnu, (Ngo et al., 2014)] where the two HMG boxes A and B are mainly involved with DNA binding in addition to some interactions mediated by the linker region (Figure 4B). Four main peptides comprising residues 57–68, 81–102, 130–165, and 166–184 display a significant decrease in deuteration uptake at various time points ($p$-value of <0.05; Figure 5A). Uptake plots for these peptides (Figure 5B) display a consistent decrease in deuteration upon DNA binding. Based on available structural

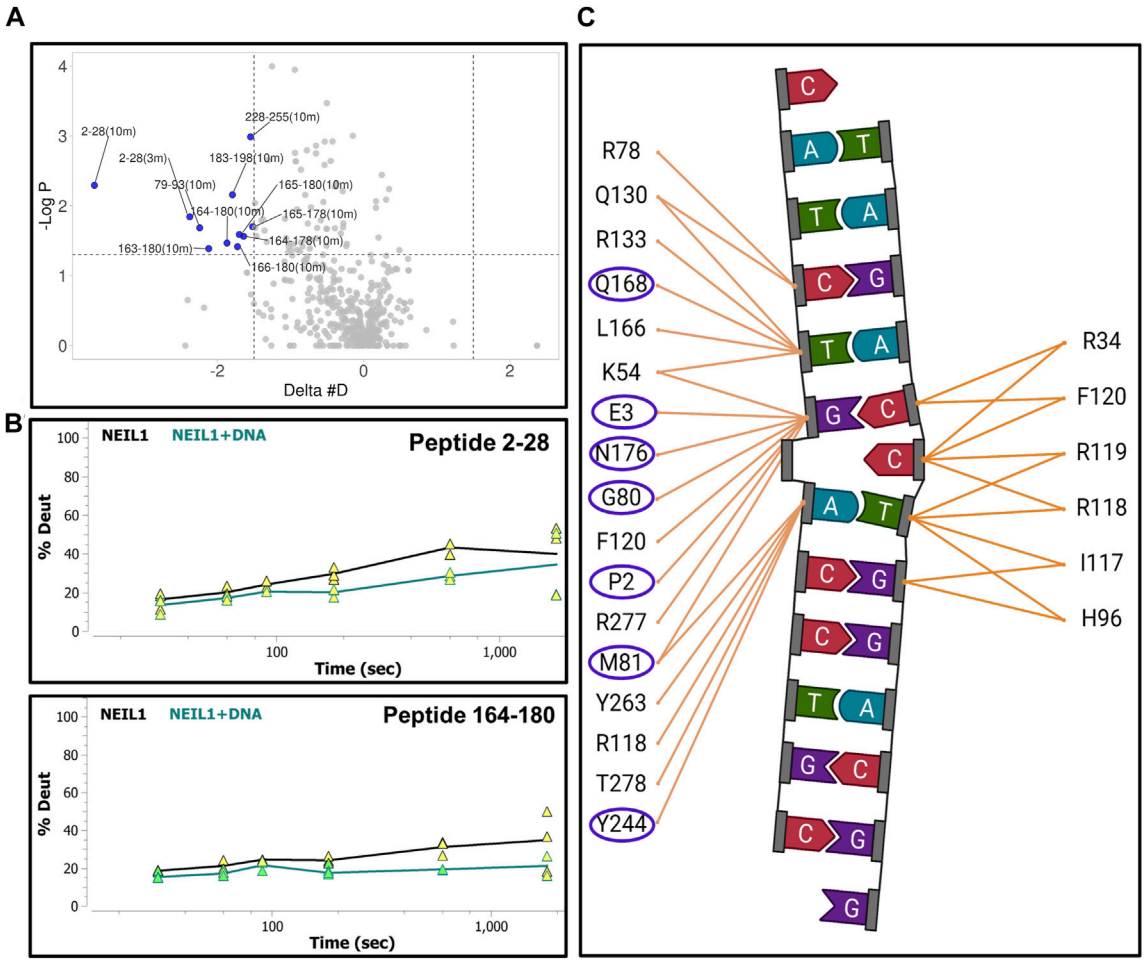


FIGURE 7
Hydrogen-deuterium exchange experiments for the NEIL1-DNA complex reveals regions of NEIL1 involved with DNA binding. **(A)** Volcano plot quantifying the significant change in deuteron uptake for each peptide at a given time point. The upper left quadrant displays peptides (solid blue circles) at various time points, representing a significant decrease in deuteron uptake upon DNA binding to NEIL1 relative to NEIL1 alone at a *p*-value of <0.05 (please refer to the legend for Figure 5A for a detailed description of the statistical tests used). **(B)** Representative uptake plots are shown from the HDX-MS time course for two of the significant peptides, 2–28 and 164–180, that lie within the significant quadrant in panel **(A)** above. **(C)** Interaction map showing NEIL1 residues that interact with the DNA in the crystal structure of the NEIL1-DNA complex (PDB ID:5itt). The residues within the blue oval circles indicate those present in peptides with a significant decrease in deuteration, as observed in the volcano plot.

data, these peptides harbor residues L58 and I81 within HMG-box A and N163, P178, and L182 in HMG-box B, which are involved in the intercalation of the DNA minor groove (Ngo et al., 2014). Residues identified from our HDX-MS data that reside within the four peptides (57–68, 81–102, 130–165, and 166–184) are present in the interaction interface of the TFAM-DNA complex (Figure 5C).

We next collected HDX-MS data over a time course (from 30 s to 30 m) for the complex between NEIL1 and DNA, and observed protection at various regions upon DNA binding as indicated by an up to 25% decrease in deuterium uptake (Woods plot; Figure 6A). These regions mainly cluster within the N-terminal domain, harboring the active site residues P2, E3, and K54, and the void-filling residues M81, R118, and F120. We also observed protection at the DNA binding helix-two-turns-helix (H2TH) motif (residues 154–187) and the zincless finger motif (residues 260–293; Figures 6A,B). Peptides that display a significant decrease in deuterium uptake with a confidence *p*-value of <0.05 upon DNA binding lie within regions 2–28, 79–93, 163–180, 183–198, and 228–255 (Volcano analysis, Figure 7A). The uptake plots for these regions show a consistent decrease in deuteration with an additional region identified between residues 256–271, which also display protection upon DNA binding (Figure 7B). The available crystal structures of NEIL1 bound to DNA provide clear confirmation that the peptides that display protection upon

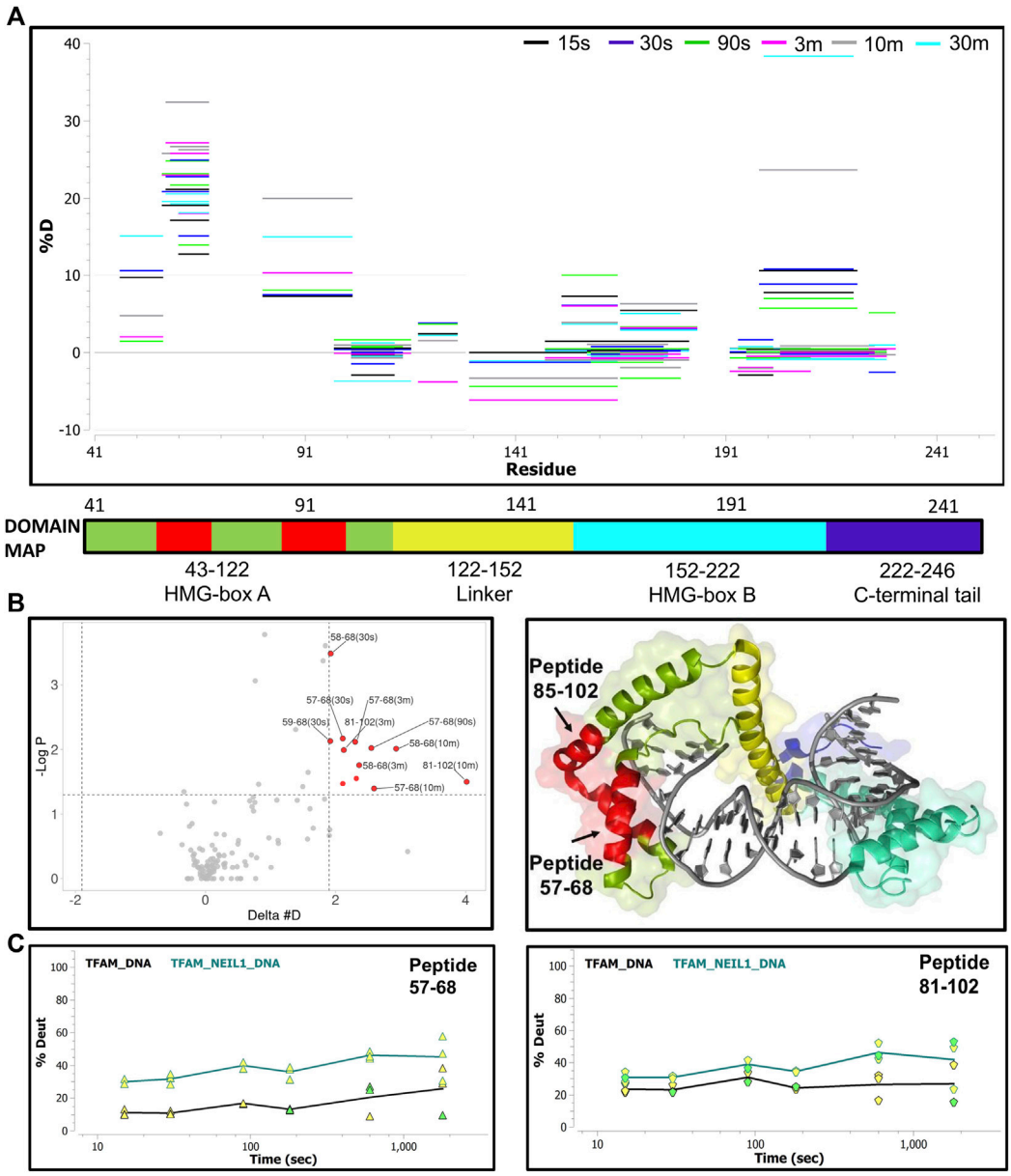


FIGURE 8
Hydrogen-deuterium exchange analysis of the TFAM-DNA and TFAM-NEIL1-DNA complexes reveals putative TFAM regions that interact with NEIL1 in the presence of DNA. **(A)** Woods plot representing percent change in deuteration for peptides after various time points (15 s–30 m) between the TFAM-DNA and TFAM-NEIL1-DNA complexes, where a positive percentage indicates more deuteration and less protection observed when NEIL1 is present within the TFAM-NEIL1-DNA complex. Each horizontal line in the plot represents an individual peptide with residue range on the *X*-axis and deuteration level i.e., level of protection on the *Y*-axis. **(B)** Volcano plot displaying TFAM peptides with a statistically significant increase in deuteration ($p$-value < 0.05; please refer to the legend for Figure 5A for a detailed description of the statistical tests used) in the TFAM-NEIL1-DNA complex indicated as solid red circles (left panel). On the right panel, the peptides with a significant increase in deuteration are mapped on the crystal structure of the TFAM-DNA complex (PDB ID:4nnu) and are highlighted in red. The domain map above also displays the two regions (red) that show the greatest difference in deuterium uptake upon the addition of NEIL1. **(C)** Representative uptake plots are shown from the HDX-MS time course for peptides 57–68 and 81–102 that lie within the significance quadrant of the volcano plot in **(B)**.

DNA binding identified by our HDX-MS data are present within the interaction interface of the NEIL1-DNA complex (Figure 7C).

Lastly, we collected HDX-MS data for a sample containing equimolar ratios of TFAM, NEIL1, and DNA at various time points (15 s–30 m) and compared it to the data obtained with the

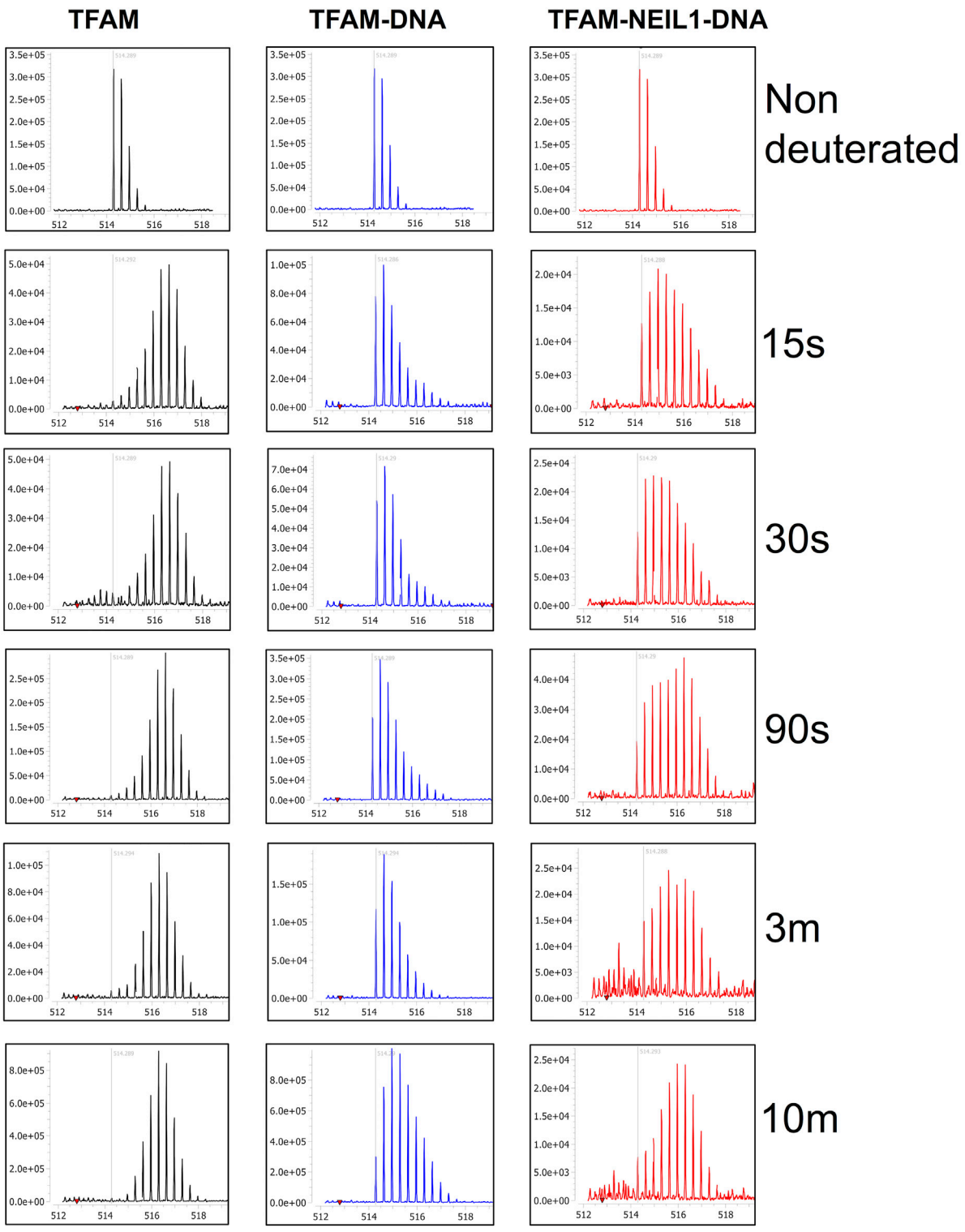


FIGURE 9
Isotopic mass distribution spectra reveal bimodal deuterium exchange upon the addition of NEIL1 to the TFAM-DNA complex. Isotopic mass distribution spectra from representative HDX-MS experiments for the peptide containing TFAM residues 57–68 at various time points as indicated (15 s–10 m). The distribution pattern for TFAM alone (black) displays greater deuterium exchange when compared to the TFAM-DNA complex (blue), which appears to exchange less deuterium. The addition of NEIL1 to the sample mixture (TFAM-NEIL1-DNA complex; red) reveals a bimodal isotopic mass distribution, which likely results from the presence of multiple species (protein-protein; protein-DNA; protein-protein-DNA; or protein alone) within the sample. The grey line within each plot indicates an *m/z* value of 514.29 corresponding to the non-deuterated peptide.

TFAM-DNA sample. Surprisingly, upon the addition of NEIL1, we observed an increase in deuterium uptake for TFAM peptides that are clustered within HMG-box A (with an up to 30% increase) and HMG-box B (with ~10% increase; Figure 8A). However, only two regions display a significant increase ($p$-value of <0.05) in deuterium uptake, which includes residues 57–68 and 81–102 that are present in HMG-box A (Figure 8B). The peptide uptake plots for the two TFAM regions also show a consistent increase in deuterium exchange when NEIL1 is present in the TFAM-NEIL1-DNA sample (Figure 8C).

To probe the origin of the increased exchange upon the addition of NEIL1, we interrogated the isotopic distribution present in the raw data. Protection of TFAM residues 57–68 upon DNA binding is evidenced by comparison of the left and middle panels of Figure 9. In the absence of DNA, the isotopic distribution is shifted towards higher mass (rightward) at early times, whereas, in the presence of DNA the shift is substantially delayed, indicating protection upon DNA binding. When NEIL1 is added to the TFAM-DNA mixture, the isotopic distribution is broadened and appears to be a superposition of the distribution patterns for unbound and DNA-bound TFAM (Figure 9; right panels). This broadened, or bimodal, pattern is indicative of the presence of both protected and unprotected TFAM molecules in solution (Supplementary Figure S11).

## DNA damage by methyl methanesulfonate decreases the transcriptional activity of TFAM in the absence of NEIL1

To assess the functional impact and the biological role of the interaction between NEIL1 and TFAM, we tested the impact of NEIL1 on the transcriptional activity of TFAM. For these experiments, we used human Hap1 cells where the expression of NEIL1 is either ablated (NEIL1 KO) or unaltered (NEIL1 WT; Supplementary Figure S12A, verified *via* western blotting). Transcriptional activity of TFAM can be monitored by measuring the steady-state mRNA transcript levels of four mitochondrial genes encoding Cytochrome b (*CYB*), NADH dehydrogenase subunit 1 (*ND1*), Cytochrome c oxidase I (*CO1*), and 12S ribosomal RNA (*RNR1*) (Bonekamp et al., 2021). Quantitative reverse transcription PCR (qRT-PCR) analysis for the *CYB*, *ND1*, *CO1*, and *RNR1* genes reveals no significant difference between the WT and NEIL1 KO cells in the absence of any DNA damage indicating that the presence or absence of NEIL1 does not deter the transcriptional activity of TFAM under normal cellular function (Figure 10A, left). To ensure that differences in mtDNA copy number did not influence the qRT-PCR results above, we assessed relative mtDNA copy number and noted no differences between the NEIL1 WT and KO Hap1 cell lines (Figure 10A, right).

Next, we studied the extent to which DNA damage induced by methyl methanesulfonate (MMS) alters the transcriptional activity of TFAM in the presence and absence of NEIL1. We selected the alkylating agent for our studies as the N-glycosyl bond is rendered weak by base alkylation thereby leading to the generation of AP sites, which is a good substrate for both NEIL1 and TFAM (Lindahl, 1993; Friedberg et al., 2005; Vik et al., 2012; Xu et al., 2019). We treated the NEIL1 WT and KO Hap1 cells with an empirically determined concentration (125 μM; Supplementary Figure S12B) of MMS for 3 days and assessed the transcriptional activity of TFAM *via* qRT-PCR as described above. Interestingly, the mRNA expression of all four mitochondrial genes was significantly reduced in the absence of NEIL1 upon MMS treatment (Figure 10B, left), suggesting that NEIL1 is essential for the efficient transcription of mitochondrial genes by TFAM in the presence of DNA damage resulting from MMS. In addition, we did not note any difference in the mtDNA copy number between the NEIL1 WT and KO Hap1 cell lines upon MMS treatment indicating that our results were not altered due to differences in mtDNA copy number (Figure 10B, right).

# Discussion

It is estimated that over 80% of proteins do not function in isolation, but rather work in complexes with other proteins or co-factors to accomplish their roles (Berggard et al., 2007; Rao et al., 2014). As such, the study of protein-protein interactions is essential for understanding cellular processes. These interactions can be either highly stable and permanent or transient and dynamic. While stable interactions are required for macromolecular assemblies like ribosomes to perform their function, transient interactions are important to carry out various signaling and regulatory processes (Acuner Ozbabacan et al., 2011), lending importance to our current endeavor to scrutinize the interaction between NEIL1 and TFAM. While classical biochemical methods used to detect protein-protein interactions can identify robust and stable protein complexes, it is technically challenging to detect interactions between weakly bound, transient protein complexes *in vivo* and *in vitro*. Therefore, choosing appropriate methods that can carefully recognize these dynamic interactions is of the utmost importance. While BER can be thought of as a highly-coordinated, step-wise process involving excision, removal, and restoration of a damaged DNA base, several other factors also mediate the otherwise simplified process. These include and are not limited to protein-protein interactions, post-translational modifications of BER enzymes, and the type of DNA damage (Carter and Parsons, 2016; Moor and Lavrik, 2018). While we and others have provided evidence for the interaction of NEIL1 with several nuclear factors including PCNA, RFC, and RPA (Dou et al., 2008; Theriot et al., 2010; Hegde et al., 2015; Prakash et al., 2017; Sharma et al., 2018), the interaction of

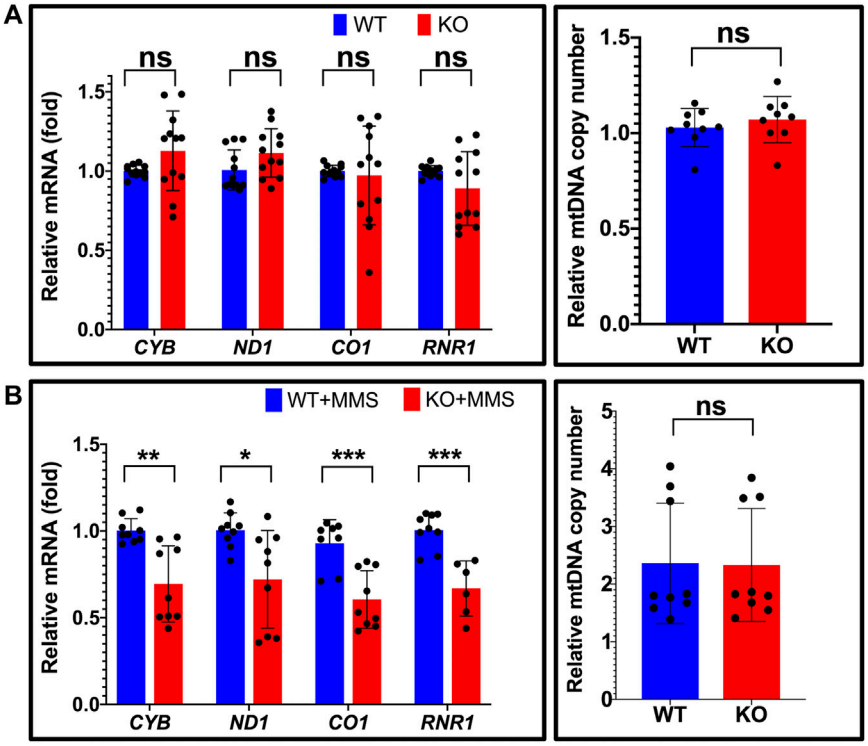


FIGURE 10
Estimation of relative mitochondrial mRNA expression reveals that NEIL1 is necessary for efficient transcription by TFAM upon DNA damage. **(A)** Left, the relative mRNA expression of four mitochondrial genes encoding Cytochrome b (*CYB*), NADH dehydrogenase subunit 1 (*ND1*), Cytochrome c oxidase I (*CO1*), and 12S ribosomal RNA (*RNR1*) were estimated by qRT-PCR in untreated Hap1 cell lines where the expression of NEIL1 is either intact (i.e., wild-type, WT) or knocked out (i.e., KO). Right, estimation of mitochondrial copy number by qPCR in the WT and KO cell lines. **(B)** Left, the relative mRNA expression of the above four mitochondrial genes in the WT and KO Hap1 cells treated with 125 μM MMS for 3 days prior to gene expression analysis. Right, estimation of mitochondrial copy number by qPCR in the WT and KO cell lines after MMS treatment. Statistical analysis was performed in GraphPad Prism using a Student's t-test where ns, not significant; *$p < 0.05$; **$p < 0.01$; and ***$p < 0.001$.

NEIL1 with mitochondrial proteins remains underreported. Reports that this enzyme is post-translationally modified by phosphorylation and acetylation have also been described, where we showed that no change in enzyme function was attributed to phosphorylation events *in vitro*, and Mitra and colleagues indicated that acetylation of the enzyme at lysine residues 296–298 is important for nuclear localization and binding to chromatin (Prakash et al., 2016; Sengupta et al., 2018). However, the role of these modifications within the mitochondrion has thus far not been evaluated and requires scrutiny.

Our efforts to study the interactome of NEIL1 within the context of the mitochondrion have been impeded owing to challenges such as low endogenous cellular levels of NEIL1 and even lower levels of the enzyme within the mitochondrion, as well as the lack of specificity of commercially available antibodies. NEIL1 is typically involved with the recognition and removal of oxidized DNA bases where the frequency at which these lesions occur within the mitochondrion remains to be elucidated; however, the enzyme likely processes oxidized lesions when they occur within mtDNA (Hailer et al., 2005; Krishnamurthy et al., 2008; Albelazi et al., 2019; Han et al., 2019). In this current study, we employed an orthogonal *in vitro* approach to study the interaction between NEIL1 and mitochondrial TFAM in the presence of an abasic site containing DNA duplex that is a favored substrate by both proteins and propose a model for this interaction (Figure 11). In one scenario, when TFAM, NEIL1, and DNA are combined in a 1:1:1 M ratio, we propose that both NEIL1 and TFAM can individually bind to half of the available DNA, leaving some amount of protein unbound. In this tug-of-war model, the two proteins do not interact even in the presence of DNA, but instead compete for the DNA. We also propose a second model, which we refer to as the complex formation model, where a portion of both proteins interact in the presence or absence of DNA forming a complex. Species containing protein-DNA binary complexes or unbound-protein/DNA are also possible in this scenario. To distinguish between these two proposed models, we present data from affinity pull-down experiments, far western studies, SEC-MALS coupled to SAXS, and HDX-MS. Our data

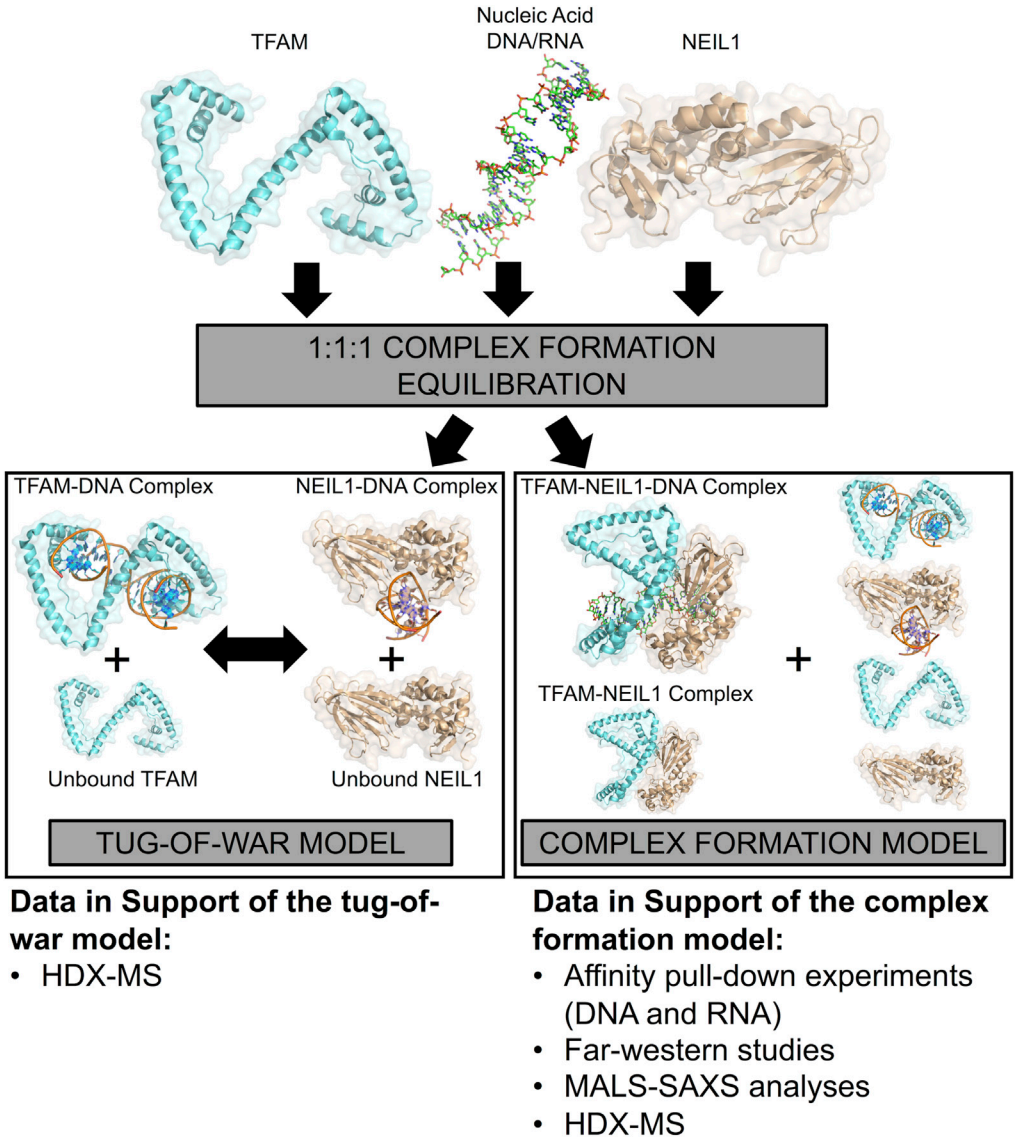


FIGURE 11
A model representing the interaction between NEIL1 and TFAM in the presence and absence of nucleic acid binding partners. Two scenarios are possible, when NEIL1, TFAM, and DNA are mixed in a 1:1:1 M ratio. In the tug-of-war model, the two proteins compete to form protein-DNA complexes, whereas, in the complex formation model, a small fraction of both proteins interact in the presence and absence of DNA, forming a complex. Species containing protein-DNA complexes or unbound-protein/DNA are also possible in this scenario. The HDX-MS data alone are insufficient to distinguish between the two proposed models but support for the complex formation model is also provided by pull-down, far-western, MALS, and SAXS analyses.

indicate that the two proteins appear to interact weakly in the absence of DNA, whereas the presence of DNA favorably alters the interaction landscape. Furthermore, we noted that the interaction can be regulated by changing the buffer conditions, effectively modulating the local binding environment as observed in our affinity pull-down studies where lowering the salt concentration in the buffer favors an interaction. The stoichiometry of the complexes as determined using absolute molar mass values from MALS analysis suggest that larger ternary TFAM-NEIL1-DNA complexes form in the presence of DNA. We further scrutinized the impact of complex formation using HDX-MS, and while this technique does not provide us with atomic resolution structures like NMR, X-ray crystallography, or cryo-electron microscopy, it offers valuable information regarding the conformational dynamics of the protein-DNA binary complexes or protein-protein-DNA ternary complexes studied here (Narang et al., 2020). From our HDX-MS data, it is difficult to distinguish

between the tug-of-war model and the complex formation model as the two models present similar species in solution as observed by a bimodal distribution of TFAM peptides upon the addition of NEIL1 within the TFAM-NEIL1-DNA sample; however, evidence from other techniques presented herein favor the complex formation model (Figure 11). We also note that the activity of TFAM is not negatively impacted by the presence (or absence) of NEIL1 under normal cellular conditions. However, we observed aberrant TFAM transcriptional activity upon treatment with MMS in the absence of NEIL1. MMS is a damaging agent which generates primarily 7-methylguanine (7meG) and 3-methlyladenine (3meA) (Beranek, 1990) and while the monofunctional alkyladenine DNA glycosylase (AAG) can excise alkylated bases within the mitochondrion, abasic sites are generated in the process, which are substrates for both NEIL1 and TFAM (van Loon and Samson, 2013; Montaldo et al., 2019). While there is no direct evidence for the involvement of NEIL1 in the repair of 7meG or 3meA, NEIL1 is known to excise other methylated bases such as 2,6-diamino-4-hydroxy-5N-methyl formamidopyrimidine (Fapy-7meG) which could form spontaneously from 7meG in alkaline environments such as that found in the mitochondria (Gates et al., 2004; Prakash et al., 2014). Future work involving mechanistic insight into the interaction between NEIL1 and TFAM in the presence of a panel of oxidative stressors as well as other DNA damaging agents specific to mitochondrial DNA, is warranted.

## Data availability statement

The original contributions presented in the study are included in the article/Supplementary Material, further inquiries can be directed to the corresponding author.

## Author contributions

AP conceptualized the project. NS, PP, and AP designed the experiments. NS, SC, and PP performed the experiments. MT, JA, and DT assisted with the various aspects of the data collection. NS, AP, and PP analyzed the data. NS, AP, and MT prepared the figures. NS and AP wrote the manuscript. All authors have read and approved the submitted version.

## Funding

NS and AP were supported in part by a grant from the National Institutes of Environmental Health Sciences (NIEHS), Outstanding New Environmental Scientist (ONES) R01 grant #R01ES030084 to AP, and AP is also supported by an NIEHS R35 subcontract grant #R35ES031708 to Dr. Joann Sweasy (University of Arizona). Startup funds provided by the University of South Alabama Health Mitchell Cancer Institute are also acknowledged. This research used resources of the Advanced Photon Source, a U.S. Department of Energy (DOE) Office of Science User Facility operated for the DOE Office of Science by Argonne National Laboratory under Contract No. DE-AC02-06CH11357. This project was supported by grant P41 GM103622 from the National Institute of General Medical Sciences of the National Institutes of Health. The content is solely the responsibility of the authors and does not necessarily reflect the official views of the National Institute of General Medical Sciences or the National Institutes of Health.

## Conflict of interest

The authors declare that the research was conducted in the absence of any commercial or financial relationships that could be construed as a potential conflict of interest.

## Publisher's note



## Acknowledgments

We would like to acknowledge Drs. Bill Copeland and Matthew Longley at the NIEHS for their advice, suggestions, and assistance with troubleshooting various aspects of the initial experimental design. We also thank Dr. Robert W. Sobol for providing necessary reagents and advice for the successful completion of the qRT-PCR assays.

## Supplementary material

The Supplementary Material for this article can be found online at: https://www.frontiersin.org/articles/10.3389/fcell.2022.893806/full#supplementary-material

# References


Acuner Ozbabacan, S. E., Engin, H. B., Gursoy, A., and Keskin, O. (2011). Transient protein-protein interactions. *Protein Eng. Des. Sel.* 24, 635–648. doi:10.1093/protein/gzr025

Alam, T. I., Kanki, T., Muta, T., Ukaji, K., Abe, Y., Nakayama, H., et al. (2003). Human mitochondrial DNA is packaged with TFAM. *Nucleic Acids Res.* 31, 1640–1645. doi:10.1093/nar/gkg251

Albelazi, M. S., Martin, P. R., Mohammed, S., Mutti, L., Parsons, J. L., Elder, R. H., et al. (2019). The biochemical role of the human NEIL1 and NEIL3 DNA glycosylases on model DNA replication forks. *Genes (Basel)* 10, 315. doi:10.3390/genes10040315

Anderson, S., Bankier, A. T., Barrell, B. G., De Bruijn, M. H., Coulson, A. R., Drouin, J., et al. (1981). Sequence and organization of the human mitochondrial genome. *Nature* 290, 457–465. doi:10.1038/290457a0

Anson, R. M., Hudson, E., and Bohr, V. A. (2000). Mitochondrial endogenous oxidative damage has been overestimated. *FASEB J.* 14, 355–360. doi:10.1096/fasebj.14.2.355

Baptiste, B. A., Baringer, S. L., Kulikowicz, T., Sommers, J. A., Croteau, D. L., Brosh, R. M., JR., et al. (2021). DNA polymerase beta outperforms DNA polymerase gamma in key mitochondrial base excision repair activities. *DNA Repair (Amst)* 99, 103050. doi:10.1016/j.dnarep.2021.103050

Beranek, D. T. (1990). Distribution of methyl and ethyl adducts following alkylation with monofunctional alkylating agents. *Mutat. Res.* 231, 11–30. doi:10.1016/0027-5107(90)90173-2

Berggard, T., Linse, S., and James, P. (2007). Methods for the detection and analysis of protein-protein interactions. *Proteomics* 7, 2833–2842. doi:10.1002/pmic.200700131

Bogenhagen, D. F. (2012). Mitochondrial DNA nucleoid structure. *Biochim. Biophys. Acta* 1819, 914–920. doi:10.1016/j.bbagrm.2011.11.005

Bogenhagen, D. F., Rousseau, D., and Burke, S. (2008). The layered structure of human mitochondrial DNA nucleoids. *J. Biol. Chem.* 283, 3665–3675. doi:10.1074/jbc.M708444200

Bonekamp, N. A., Jiang, M., Motori, E., Garcia Villegas, R., Koolmeister, C., Atanassov, I., et al. (2021). High levels of TFAM repress mammalian mitochondrial DNA transcription *in vivo*. *Life Sci. Alliance* 4, e202101034. doi:10.26508/lsa.202101034

Brown, T. A., Tkachuk, A. N., and Clayton, D. A. (2015). Mitochondrial transcription factor A (TFAM) binds to RNA containing 4-way junctions and mitochondrial tRNA. *PLoS One* 10, e0142436. doi:10.1371/journal.pone.0142436

Campbell, C. T., Kolesar, J. E., and Kaufman, B. A. (2012). Mitochondrial transcription factor A regulates mitochondrial transcription initiation, DNA packaging, and genome copy number. *Biochim. Biophys. Acta* 1819, 921–929. doi:10.1016/j.bbagrm.2012.03.002

Canugovi, C., Maynard, S., Bayne, A. C., Sykora, P., Tian, J., De Souza-Pinto, N. C., et al. (2010). The mitochondrial transcription factor A functions in mitochondrial base excision repair. *DNA Repair (Amst)* 9, 1080–1089. doi:10.1016/j.dnarep.2010.07.009

Carter, R. J., and Parsons, J. L. (2016). Base excision repair, a pathway regulated by posttranslational modifications. *Mol. Cell. Biol.* 36, 1426–1437. doi:10.1128/MCB.00030-16

Copeland, W. C., and Longley, M. J. (2014). Mitochondrial genome maintenance in health and disease. *DNA Repair (Amst)* 19, 190–198. doi:10.1016/j.dnarep.2014.03.010

Cuppari, A., Fernandez-Millan, P., Battistini, F., Tarres-Sole, A., Lyonnais, S., Iruela, G., et al. (2019). DNA specificities modulate the binding of human transcription factor A to mitochondrial DNA control region. *Nucleic Acids Res.* 47, 6519–6537. doi:10.1093/nar/gkz406

D'Arcy, B. M., Swingle, M. R., Papke, C. M., Abney, K. A., Bouska, E. S., Prakash, A., et al. (2019). The antitumor drug LB-100 is a catalytic inhibitor of protein phosphatase 2A (PPP2CA) and 5 (PPP5C) coordinating with the active-site catalytic metals in PPP5C. *Mol. Cancer Ther.* 18, 556–566. doi:10.1158/1535-7163.MCT-17-1143

Das, A., Boldogh, I., Lee, J. W., Harrigan, J. A., Hegde, M. L., Piotrowski, J., et al. (2007). The human Werner syndrome protein stimulates repair of oxidative DNA base damage by the DNA glycosylase NEIL1. *J. Biol. Chem.* 282, 26591–26602. doi:10.1074/jbc.M703343200

Dou, H., Theriot, C. A., Das, A., Hegde, M. L., Matsumoto, Y., Boldogh, I., et al. (2008). Interaction of the human DNA glycosylase NEIL1 with proliferating cell nuclear antigen. The potential for replication-associated repair of oxidized bases in mammalian genomes. *J. Biol. Chem.* 283, 3130–3140. doi:10.1074/jbc.M709186200

Doublié, S., Bandaru, V., Bond, J. P., and Wallace, S. S. (2004). The crystal structure of human endonuclease VIII-like 1 (NEIL1) reveals a zincless finger motif required for glycosylase activity. *Proc. Natl. Acad. Sci. U. S. A.* 101, 10284–10289. doi:10.1073/pnas.0402051101

Endo, T., Yamano, K., and Kawano, S. (2011). Structural insight into the mitochondrial protein import system. *Biochim. Biophys. Acta* 1808, 955–970. doi:10.1016/j.bbamem.2010.07.018

Farge, G., and Falkenberg, M. (2019). Organization of DNA in mammalian mitochondria. *Int. J. Mol. Sci.* 20, 2770. doi:10.3390/ijms20112770

Franke, D., Jeffries, C. M., and Svergun, D. I. (2018). Machine learning methods for X-ray scattering data analysis from biomacromolecular solutions. *Biophys. J.* 114, 2485–2492. doi:10.1016/j.bpj.2018.04.018

Friedberg, E. C., Walker, G. C., Siede, W., and Wood, R. D. (2005). *DNA repair and mutagenesis*. USA: American Society for Microbiology Press.

Fromme, J. C., and Verdine, G. L. (2004). Base excision repair. *Adv. Protein Chem.* 69, 1–41. doi:10.1016/S0065-3233(04)69001-2

Gangelhoff, T. A., Mungalachetty, P. S., Nix, J. C., and Churchill, M. E. (2009). Structural analysis and DNA binding of the HMG domains of the human mitochondrial transcription factor A. *Nucleic Acids Res.* 37, 3153–3164. doi:10.1093/nar/gkp157

Gates, K. S., Nooner, T., and Dutta, S. (2004). Biologically relevant chemical reactions of N7-alkylguanine residues in DNA. *Chem. Res. Toxicol.* 17, 839–856. doi:10.1021/tx049965c

Goedhart, J., and Luijsterburg, M. S. (2020). VolcaNoseR is a web app for creating, exploring, labeling and sharing volcano plots. *Sci. Rep.* 10, 20560. doi:10.1038/s41598-020-76603-3

Hailer, M. K., Slade, P. G., Martin, B. D., Rosenquist, T. A., and Sugden, K. D. (2005). Recognition of the oxidized lesions spiroiminodihydantoin and guanidinohydantoin in DNA by the mammalian base excision repair glycosylases NEIL1 and NEIL2. *DNA Repair (Amst)* 4, 41–50. doi:10.1016/j.dnarep.2004.07.006

Hajizadeh, N. R., Franke, D., Jeffries, C. M., and Svergun, D. I. (2018). Consensus Bayesian assessment of protein molecular mass from solution X-ray scattering data. *Sci. Rep.* 8, 7204. doi:10.1038/s41598-018-25355-2

Han, D., Schomacher, L., Schule, K. M., Mallick, M., Musheev, M. U., Karaulanov, E., et al. (2019). NEIL1 and NEIL2 DNA glycosylases protect neural crest development against mitochondrial oxidative stress. *Elife* 8, e49044. doi:10.7554/eLife.49044

Hegde, M. L., Hazra, T. K., and Mitra, S. (2010). Functions of disordered regions in mammalian early base excision repair proteins. *Cell. Mol. Life Sci.* 67, 3573–3587. doi:10.1007/s00018-010-0485-5

Hegde, M. L., Hegde, P. M., Arijit, D., Boldogh, I., and Mitra, S. (2012). Human DNA glycosylase NEIL1's interactions with downstream repair proteins is critical for efficient repair of oxidized DNA base damage and enhanced cell survival. *Biomolecules* 2, 564–578. doi:10.3390/biom2040564

Hegde, M. L., Theriot, C. A., Das, A., Hegde, P. M., Guo, Z., Gary, R. K., et al. (2008). Physical and functional interaction between human oxidized base-specific DNA glycosylase NEIL1 and flap endonuclease 1. *J. Biol. Chem.* 283, 27028–27037. doi:10.1074/jbc.M802712200

Hegde, P. M., Dutta, A., Sengupta, S., Mitra, J., Adhikari, S., Tomkinson, A. E., et al. (2015). The C-terminal domain (ctd) of human DNA glycosylase NEIL1 is required for forming BERosome repair complex with DNA replication proteins at the replicating genome: Dominant negative function of the ctd. *J. Biol. Chem.* 290, 20919–20933. doi:10.1074/jbc.M115.642918

Hopkins, J. B., Gillilan, R. E., and Skou, S. (2017). BioXTAS RAW: Improvements to a free open-source program for small-angle X-ray scattering data reduction and analysis. *J. Appl. Crystallogr.* 50, 1545–1553. doi:10.1107/S1600576717011438

Hu, J., De Souza-Pinto, N. C., Haraguchi, K., Hogue, B. A., Jaruga, P., Greenberg, M. M., et al. (2005). Repair of formamidopyrimidines in DNA involves different glycosylases: Role of the OGG1, NTH1, and NEIL1 enzymes. *J. Biol. Chem.* 280, 40544–40551. doi:10.1074/jbc.M508772200

Kaufman, B. A., Durisic, N., Mativetsky, J. M., Costantino, S., Hancock, M. A., Grutter, P., et al. (2007). The mitochondrial transcription factor TFAM coordinates the assembly of multiple DNA molecules into nucleoid-like structures. *Mol. Biol. Cell* 18, 3225–3236. doi:10.1091/mbc.e07-05-0404

Kauppila, J. H., and Stewart, J. B. (2015). Mitochondrial DNA: Radically free of free-radical driven mutations. *Biochim. Biophys. Acta* 1847, 1354–1361. doi:10.1016/j.bbabio.2015.06.001

Kladova, O. A., Grin, I. R., Fedorova, O. S., Kuznetsov, N. A., and Zharkov, D. O. (2019). Conformational dynamics of damage processing by human DNA glycosylase NEIL1. *J. Mol. Biol.* 431, 1098–1112. doi:10.1016/j.jmb.2019.01.030

Konarev, P. V., Volkov, V. V., Sokolova, A. V., Koch, M. H., and Svergun, D. I. (2003). Primus: A windows PC-based system for small-angle scattering data analysis. *J. Appl. Crystallogr.* 36, 1277–1282. doi:10.1107/s0021889803012779

Krishnamurthy, N., Zhao, X., Burrows, C. J., and David, S. S. (2008). Superior removal of hydantoin lesions relative to other oxidized bases by the human DNA glycosylase hNEIL1. *Biochemistry* 47, 7137–7146. doi:10.1021/bi800160s

Krokan, H. E., and Bjoras, M. (2013). Base excision repair. *Cold Spring Harb. Perspect. Biol.* 5, a012583. doi:10.1101/cshperspect.a012583

Kukat, C., Davies, K. M., Wurm, C. A., Spahr, H., Bonekamp, N. A., Kuhl, I., et al. (2015). Cross-strand binding of TFAM to a single mtDNA molecule forms the mitochondrial nucleoid. *Proc. Natl. Acad. Sci. U. S. A.* 112, 11288–11293. doi:10.1073/pnas.1512131112

Kukat, C., Wurm, C. A., Spahr, H., Falkenberg, M., Larsson, N. G., Jakobs, S., et al. (2011). Super-resolution microscopy reveals that mammalian mitochondrial nucleoids have a uniform size and frequently contain a single copy of mtDNA. *Proc. Natl. Acad. Sci. U. S. A.* 108, 13534–13539. doi:10.1073/pnas.1109263108

Lim, K. S., Jeyaseelan, K., Whiteman, M., Jenner, A., and Halliwell, B. (2005). Oxidative damage in mitochondrial DNA is not extensive. *Ann. N. Y. Acad. Sci.* 1042, 210–220. doi:10.1196/annals.1338.023

Lindahl, T. (1993). Instability and decay of the primary structure of DNA. *nature* 362, 709–715. doi:10.1038/362709a0

Liu, M., Zhang, J., Zhu, C., Zhang, X., Xiao, W., Yan, Y., et al. (2021). DNA repair glycosylase hNEIL1 triages damaged bases via competing interaction modes. *Nat. Commun.* 12, 4108. doi:10.1038/s41467-021-24431-y

Malarkey, C. S., Bestwick, M., Kuhlwilm, J. E., Shadel, G. S., and Churchill, M. E. (2012). Transcriptional activation by mitochondrial transcription factor A involves preferential distortion of promoter DNA. *Nucleic Acids Res.* 40, 614–624. doi:10.1093/nar/gkr787

Meisburger, S. P., Taylor, A. B., Khan, C. A., Zhang, S., Fitzpatrick, P. F., Ando, N., et al. (2016). Domain movements upon activation of phenylalanine hydroxylase characterized by crystallography and chromatography-coupled small-angle X-ray scattering. *J. Am. Chem. Soc.* 138, 6506–6516. doi:10.1021/jacs.6b01563

Minko, I. G., Vartanian, V. L., Tozaki, N. N., Coskun, E., Coskun, S. H., Jaruga, P., et al. (2020). Recognition of DNA adducts by edited and unedited forms of DNA glycosylase NEIL1. *DNA Repair (Amst)* 85, 102741. doi:10.1016/j.dnarep.2019.102741

Mishmar, D., Levin, R., Naeem, M. M., and Sondheimer, N. (2019). Higher order organization of the mtDNA: Beyond mitochondrial transcription factor A. *Front. Genet.* 10, 1285. doi:10.3389/fgene.2019.01285

Montaldo, N. P., Bordin, D. L., Brambilla, A., Rosinger, M., Fordyce Martin, S. L., Bjoras, K. O., et al. (2019). Alkyladenine DNA glycosylase associates with transcription elongation to coordinate DNA repair with gene expression. *Nat. Commun.* 10, 5460. doi:10.1038/s41467-019-13394-w

Moor, N. A., and Lavrik, O. I. (2018). Protein-protein interactions in DNA base excision repair. *Biochemistry.* 83, 411–422. doi:10.1134/S0006297918040120

Narang, D., Lento, C., and D, J. W. (2020). HDX-MS: An analytical tool to capture protein motion in action. *Biomedicines* 8, 224. doi:10.3390/biomedicines8070224

Ngo, H. B., Kaiser, J. T., and Chan, D. C. (2011). The mitochondrial transcription and packaging factor Tfam imposes a U-turn on mitochondrial DNA. *Nat. Struct. Mol. Biol.* 18, 1290–1296. doi:10.1038/nsmb.2159

Ngo, H. B., Lovely, G. A., Phillips, R., and Chan, D. C. (2014). Distinct structural features of TFAM drive mitochondrial DNA packaging versus transcriptional activation. *Nat. Commun.* 5, 3077. doi:10.1038/ncomms4077

Odell, I. D., Newick, K., Heintz, N. H., Wallace, S. S., and Pederson, D. S. (2010). Non-specific DNA binding interferes with the efficient excision of oxidative lesions from chromatin by the human DNA glycosylase, NEIL1. *DNA Repair (Amst)* 9, 134–143. doi:10.1016/j.dnarep.2009.11.005

Piiadov, V., Ares De Araujo, E., Oliveira Neto, M., Craievich, A. F., and Polikarpov, I. (2019). SAXSMoW 2.0: Online calculator of the molecular weight of proteins in dilute solution from experimental SAXS data measured on a relative scale. *Protein Sci.* 28, 454–463. doi:10.1002/pro.3528

Prakash, A., Cao, V. B., and Doublie, S. (2016). Phosphorylation sites identified in the NEIL1 DNA glycosylase are potential targets for the JNK1 kinase. *PLoS One* 11, e0157860. doi:10.1371/journal.pone.0157860

Prakash, A., Carroll, B. L., Sweasy, J. B., Wallace, S. S., and Doublie, S. (2014). Genome and cancer single nucleotide polymorphisms of the human NEIL1 DNA glycosylase: Activity, structure, and the effect of editing. *DNA Repair (Amst)* 14, 17–26. doi:10.1016/j.dnarep.2013.12.003

Prakash, A., and Doublié, S. (2015). Base excision repair in the mitochondria. *J. Cell. Biochem.* 116, 1490–1499. doi:10.1002/jcb.25103

Prakash, A., Doublie, S., and Wallace, S. S. (2012). The fpg/nei family of DNA glycosylases: Substrates, structures, and search for damage. *Prog. Mol. Biol. Transl. Sci.* 110, 71–91. doi:10.1016/B978-0-12-387665-2.00004-3

Prakash, A., Moharana, K., Wallace, S. S., and Doublié, S. (2017). Destabilization of the PCNA trimer mediated by its interaction with the NEIL1 DNA glycosylase. *Nucleic Acids Res.* 45, 2897–2909. doi:10.1093/nar/gkw1282

Rahman, S., and Copeland, W. C. (2019). POLG-related disorders and their neurological manifestations. *Nat. Rev. Neurol.* 15, 40–52. doi:10.1038/s41582-018-0101-0

Ramachandran, A., Basu, U., Sultana, S., Nandakumar, D., and Patel, S. S. (2017). Human mitochondrial transcription factors TFAM and TFB2M work synergistically in promoter melting during transcription initiation. *Nucleic Acids Res.* 45, 861–874. doi:10.1093/nar/gkw1157

Rambo, R. P., and Tainer, J. A. (2013). Accurate assessment of mass, models and resolution by small-angle scattering. *Nature* 496, 477–481. doi:10.1038/nature12070

Rao, V. S., Srinivas, K., Sujini, G. N., and Kumar, G. N. (2014). Protein-protein interaction detection: Methods and analysis. *Int. J. Proteomics* 2014, 147648. doi:10.1155/2014/147648

Ruan, L., Wang, Y., Zhang, X., Tomaszewski, A., Mcnamara, J. T., Li, R., et al. (2020). Mitochondria-associated proteostasis. *Annu. Rev. Biophys.* 49, 41–67. doi:10.1146/annurev-biophys-121219-081604

Rubio-Cosials, A., Battistini, F., Gansen, A., Cuppari, A., Bernado, P., Orozco, M., et al. (2018). Protein flexibility and synergy of HMG domains underlie U-turn bending of DNA by TFAM in solution. *Biophys. J.* 114, 2386–2396. doi:10.1016/j.bpj.2017.11.3743

Rubio-Cosials, A., Sidow, J. F., Jimenez-Menendez, N., Fernandez-Millan, P., Montoya, J., Jacobs, H. T., et al. (2011). Human mitochondrial transcription factor A induces a U-turn structure in the light strand promoter. *Nat. Struct. Mol. Biol.* 18, 1281–1289. doi:10.1038/nsmb.2160

Sagendorf, J. M., Markarian, N., Berman, H. M., and Rohs, R. (2020). DNAproDB: An expanded database and web-based tool for structural analysis of DNA-protein complexes. *Nucleic Acids Res.* 48, D277–D287. doi:10.1093/nar/gkz889

Saki, M., and Prakash, A. (2017). DNA damage related crosstalk between the nucleus and mitochondria. *Free Radic. Biol. Med.* 107, 216–227. doi:10.1016/j.freeradbiomed.2016.11.050

Sampath, H., Batra, A. K., Vartanian, V., Carmical, J. R., Prusak, D., King, I. B., et al. (2011). Variable penetrance of metabolic phenotypes and development of high-fat diet-induced adiposity in NEIL1-deficient mice. *Am. J. Physiol. Endocrinol. Metab.* 300, E724–E734. doi:10.1152/ajpendo.00387.2010

Schomacher, L., Han, D., Musheev, M. U., Arab, K., Kienhofer, S., Von Seggern, A., et al. (2016). Neil DNA glycosylases promote substrate turnover by Tdg during DNA demethylation. *Nat. Struct. Mol. Biol.* 23, 116–124. doi:10.1038/nsmb.3151

Sengupta, S., Yang, C., Hegde, M. L., Hegde, P. M., Mitra, J., Pandey, A., et al. (2018). Acetylation of oxidized base repair-initiating NEIL1 DNA glycosylase required for chromatin-bound repair complex formation in the human genome increases cellular resistance to oxidative stress. *DNA Repair (Amst)* 66-67, 1–10. doi:10.1016/j.dnarep.2018.04.001

Sharma, N., Chakravarthy, S., Longley, M. J., Copeland, W. C., and Prakash, A. (2018). The C-terminal tail of the NEIL1 DNA glycosylase interacts with the human mitochondrial single-stranded DNA binding protein. *DNA Repair (Amst)* 65, 11–19. doi:10.1016/j.dnarep.2018.02.012

Svergun, D. (1992). Determination of the regularization parameter in indirect-transform methods using perceptual criteria. *J. Appl. Crystallogr.* 25, 495–503. doi:10.1107/s0021889892001663

Szczesny, B., Tann, A. W., Longley, M. J., Copeland, W. C., and Mitra, S. (2008). Long patch base excision repair in mammalian mitochondrial genomes. *J. Biol. Chem.* 283, 26349–26356. doi:10.1074/jbc.M803491200

Theriot, C. A., Hegde, M. L., Hazra, T. K., and Mitra, S. (2010). RPA physically interacts with the human DNA glycosylase NEIL1 to regulate excision of oxidative DNA base damage in primer-template structures. *DNA Repair (Amst)* 9, 643–652. doi:10.1016/j.dnarep.2010.02.014

Van Houten, B., Hunter, S. E., and Meyer, J. N. (2016). Mitochondrial DNA damage induced autophagy, cell death, and disease. *Front. Biosci.* 21, 42–54. doi:10.2741/4375

van Loon, B., and Samson, L. D. (2013). Alkyladenine DNA glycosylase (AAG) localizes to mitochondria and interacts with mitochondrial single-stranded binding protein (mtSSB). *DNA Repair (Amst)* 12, 177–187. doi:10.1016/j.dnarep.2012.11.009

Vartanian, V., Lowell, B., Minko, I. G., Wood, T. G., Ceci, J. D., George, S., et al. (2006). The metabolic syndrome resulting from a knockout of the NEIL1 DNA glycosylase. *Proc. Natl. Acad. Sci. U. S. A.* 103, 1864–1869. doi:10.1073/pnas.0507444103

Vik, E. S., Alseth, I., Forsbring, M., Helle, I. H., Morland, I., Luna, L., et al. (2012). Biochemical mapping of human NEIL1 DNA glycosylase and AP lyase activities. *DNA Repair (Amst)* 11, 766–773. doi:10.1016/j.dnarep.2012.07.002

Wallace, S. S., Murphy, D. L., and Sweasy, J. B. (2012). Base excision repair and cancer. *Cancer Lett.* 327, 73–89. doi:10.1016/j.canlet.2011.12.038

Wiedemann, N., and Pfanner, N. (2017). Mitochondrial machineries for protein import and assembly. *Annu. Rev. Biochem.* 86, 685–714. doi:10.1146/annurev-biochem-060815-014352

Xu, W., Boyd, R. M., Tree, M. O., Samkari, F., and Zhao, L. (2019). Mitochondrial transcription factor A promotes DNA strand cleavage at abasic sites. *Proc. Natl. Acad. Sci. U. S. A.* 116, 17792–17799. doi:10.1073/pnas.1911252116

Yakes, F. M., and Van Houten, B. (1997). Mitochondrial DNA damage is more extensive and persists longer than nuclear DNA damage in human cells following oxidative stress. *Proc. Natl. Acad. Sci. U. S. A.* 94, 514–519. doi:10.1073/pnas.94.2.514

Yeo, J., Lotsof, E. R., Anderson-Steele, B. M., and David, S. S. (2021). RNA editing of the human DNA glycosylase NEIL1 alters its removal of 5-hydroxyuracil lesions in DNA. *Biochemistry* 60, 1485–1497. doi:10.1021/acs.biochem.1c00062

Zhao, X., Krishnamurthy, N., Burrows, C. J., and David, S. S. (2010). Mutation versus repair: NEIL1 removal of hydantoin lesions in single-stranded, bulge, bubble, and duplex DNA contexts. *Biochemistry* 49, 1658–1666. doi:10.1021/bi901852q

Zhu, C., Lu, L., Zhang, J., Yue, Z., Song, J., Zong, S., et al. (2016). Tautomerization-dependent recognition and excision of oxidation damage in base-excision DNA repair. *Proc. Natl. Acad. Sci. U. S. A.* 113, 7792–7797. doi:10.1073/pnas.1604591113

# Advantages of publishing in Frontiers

**OPEN ACCESS**
Articles are free to read for greatest visibility and readership

**FAST PUBLICATION**
Around 90 days from submission to decision

**HIGH QUALITY PEER-REVIEW**
Rigorous, collaborative, and constructive peer-review

**TRANSPARENT PEER-REVIEW**
Editors and reviewers acknowledged by name on published articles

**Frontiers**
Avenue du Tribunal-Fédéral 34
1005 Lausanne | Switzerland

**Visit us:** www.frontiersin.org
**Contact us:** frontiersin.org/about/contact

**REPRODUCIBILITY OF RESEARCH**
Support open data and methods to enhance research reproducibility

**DIGITAL PUBLISHING**
Articles designed for optimal readership across devices

**FOLLOW US**
@frontiersin

**IMPACT METRICS**
Advanced article metrics track visibility across digital media

**EXTENSIVE PROMOTION**
Marketing and promotion of impactful research

**LOOP RESEARCH NETWORK**
Our network increases your article's readership